Charles University in Prague
Faculty of Mathematics and Physics

DOCTORAL THESIS

Marián Vlček

Investigation of defects in quasicrystals

Department of Low Temperature Physics

Supervisor of the doctoral thesis: doc. Mgr. Jakub Čížek, Ph.D.
Study programme: Physics
Specialization: Physics of Condensed Matter and Materials Research

Prague 2015

I would like to show my gratitude to my supervisor, doc. Mgr. Jakub Čížek, Ph.D., whose guidance, support and valuable advices enabled me to develop an understanding of the subject.

Marián Vlček

I declare that I carried out this doctoral thesis independently, and only with the cited sources, literature and other professional sources.

I understand that my work relates to the rights and obligations under the Act No. 121/2000 Coll., the Copyright Act, as amended, in particular the fact that the Charles University in Prague has the right to conclude a license agreement on the use of this work as a school work pursuant to Section 60 paragraph 1 of the Copyright Act.

In Prague date 30.6.2015

Marián Vlček

Název práce: Studium defektů v kvazikrystalech

Autor: Marián Vlček

Katedra: Katedra fyziky nízkých teplot

Vedoucí disertační práce: doc. Mgr. Jakub Čížek, Ph.D., Katedra fyziky nízkých teplot

Abstrakt: V predloženej práci boli pomocou spektroskopie doby života pozitrónov a koincidenčnej spektroskopie Dopplerovského rozšírenia anihilačného píku študované zliatiny WE43 s prídavkom zinku a ternárne zliatiny Mg-Zn-Y. V týchto zliatinách bola nedávno zistená prítomnosť ikosahedrálnej fázy $Mg_3Zn_6Y_1$ s kvázikryštalickou štruktúrou, čo pritiahlo pozornosť výskumníkov. Spektroskopia doby života pozitrónov preukázala prítomnosť unikátnych vakanciám podobných defektov na rozhraní ikosahedrálnej fázy a horčíkovej matrice, ktoré sú charakteristické pre horčíkové zliatiny obsahujúce ikosahedrálnu fázu. Tepelné spracovanie skúmaných zliatin vedie k významným zmenám morfológie hraničných fáz. Keďže vakanciám podobné defekty spojené s ikosahedrálnou fázou sa vyskytujú na jej rozhraní s horčíkovou matricou, zmeny v morfológii ikosahedrálnej fázy vedú k výrazným zmenám koncentrácie týchto defektov.

Ďalej boli skúmané vzorky pripravené uhlovým pretláčaním kanálom rovnakého prierezu. Typy defektov prítomné v týchto zliatinách a ich teplotná stabilita bola určená pomocou spektroskopie doby života pozitrónov a merania tvrdosti počas izochronného žíhania. Fázové transformácie v odliatych zliatinách a vzorkách deformovaných uhlovým pretláčaním kanálom rovnakého prierezu boli skúmané pomocou *in situ* merania diffrakcie röntgenového žiarenia a diferenčnej skenovacej kalorimetrie.

Klíčová slova: kvazikryštály, defekty, horčíkové zliatiny, anihilácia pozitrónov

Title: Investigation of defects in quasicrystals

Author: Marián Vlček

Department: Department of Low Temperature Physics

Supervisor: doc. Mgr. Jakub Čížek, Ph.D., Department of Low Temperature Physics

Abstract: In the present work defects in WE43-based alloys modified by addition of Zn and ternary Mg-Zn-Y alloys were studied by positron lifetime spectroscopy and coincidence measurement of Doppler-broadening of annihilation radiation. Icosahedral phase $Mg_3Zn_6Y_1$ with quasicrystalline structure was recently observed in Mg-Zn-Y system and attracts great attention of researchers due to its unique properties. Positron lifetime spectroscopy revealed that positrons are trapped at a special kind of vacancy-like defects located at interfaces between the Mg matrix and icosahedral phase in the studied alloys. Heat treatment of studied alloys leads to marked changes in the morphology of secondary phases. Since the vacancy-like defects are located at the surface of icosahedral phase, heat treatment significantly influences their concentration.

Samples processed by equal-channel angular pressing were investigated to elucidate the influence of ultra-fined-grained structure on types of defects present in the studied alloys. The temperature stability of the ultra-fined-grained structure was studied by positron lifetime spectroscopy and microhardness measurements of isochronally annealed samples. Phase transformations were examined by *in situ* X-ray diffraction and differential scanning calorimetry in the as-cast alloys as well as the samples deformed by equal-channel angular pressing.

Keywords: quasicrystals, defects, Mg-alloys, positron annihilation

Contents

1. Introduction

Quasicrystals have peculiar structure which exhibits some features of both crystalline and amorphous materials. Their structure is ordered but at the same time it lacks the translation symmetry. Quasicrystals exhibit high strength, hardness and brittleness due to low density of dislocations and their low mobility. In addition, they have low surface energy, high abrasion and corrosion resistance and show highly isotropic elastic properties.

Most of the discovered quasicrystals were prepared as a single phase materials. However, quasicrystalline precipitates in magnesium alloys with zinc and rare earth alloying elements were recently observed. Unique structure of these precipitates may create new types of defects which are not present in the conventional magnesium alloys.

Positron annihilation spectroscopy represents a group of well-established experimental techniques suitable for investigation of open-volume defects in condensed matter. Positron lifetime spectroscopy is employed to identify the types of defects and to quantify their concentrations. Complementary technique called coincidence spectroscopy of Doppler broadening of annihilation radiation is used to characterize the chemical composition in the vicinity of open-volume defects. Complex information about the defects in studied materials can be obtained by combination of these two experimental methods.

In the present work, the samples of magnesium alloys containing icosahedral phase were examined in the as cast condition, after various heat treatments and also after severe plastic deformation induced by equal-channel angular pressing. Investigations by positron lifetime spectroscopy and coincidence Doppler broadening spectroscopy were performed to elucidate the influence of heat treatment and ultra-fine-grained structure on defects in the studied alloys.

Positron annihilation techniques were combined with scanning electron microscopy, X-ray diffraction and microhardness measurements to provide a complete picture of physical processes taking place in the studied samples. Phase transformations of intermetallic phases were investigated by *in situ* X-ray diffraction of synchrotron radiation and differential scanning calorimetry.

2. Physical principles of positron annihilation spectroscopy

2.1 Positron source

In laboratory practice, positrons are commonly generated by radioisotopes undergoing β^+ decay. These radioisotope decay according to the equation

$$ {}^A_Z X \rightarrow {}^A_{Z-1} X' + e^+ + \nu . \tag{2.1} $$

During the β^+ decay, the nucleus ${}^A_Z X$ simultaneously emits positron e^+ and neutrino ν and decays to nucleus ${}^A_{Z-1} X'$. Positrons emited by β^+ decay exhibit continuous energy spectrum of kinetic energies. Typical end-point energies are in the range of hundreds keV to several MeV.

Decay scheme of ^{22}Na which is the most often used positron source in positron annihilation spectroscopy is shown in figure 2.1. The end-point energy of positrons emitted by ^{22}Na radioisotope is $E_{max} = 0.545$ MeV and their mean kinetic energy is $\sim$ 270 keV.

The decay of ^{22}Na radioisotope produces the daughter ^{22}Ne nucleus in excited state which subsequently de-excites by emission of γ ray, so-called start photon, with characteristic energy of 1274 keV. The name is derived from the fact that the lifetime of the excited ^{22}Ne level is only a few ps (see figure 2.1), therefore the start photon is emitted practically simultaneously with positron and denotes the time when the positron was born.

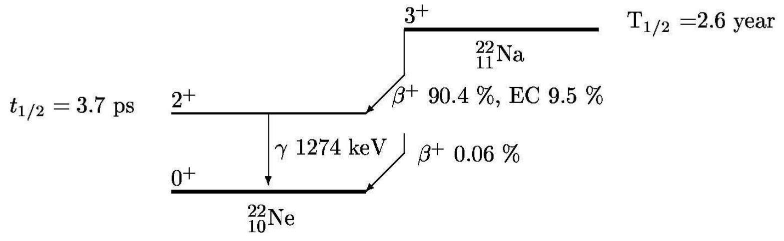

Figure 2.1: Decay scheme of the radioisotope ^{22}Na.

2.2 Thermalization of positrons

Positron penetrating into condensed matter quickly loses its initial kinetic energy until it reaches thermal energy of $\sim \frac{3}{2}kT$ (i.e. 0.039 eV at room temperature) [1].

This process is called positron thermalization. Positrons lose their energy by excitation of core electrons at high energies (above $\sim$ 100 eV), while at lower energies (100-0.1 eV) scattering by conduction electrons becomes dominant. Finally, at energies below 0.1 eV scattering on phonons is the prevailing mechanism of energy loss. Thermalization of positron in condensed mater usually takes several ps. On the other hand, typical positron lifetimes in condensed matter are in the order of hundreds ps. Hence, the thermalization time of positron is approximately two orders of magnitude shorter than the positron lifetime in condensed matter and can be neglected in most circumstances.

Velocity of positron in thermal equilibrium is governed by the classic Maxwell-Boltzmann distribution which states that the mean square velocity of positron is

$$v_+ \equiv \sqrt{\langle v^2 \rangle} = \sqrt{\frac{3kT}{m^*}}, \tag{2.2}$$

where k is the Boltzmann constant, T temperature and m^* is the effective positron mass. The value of the latter quantity is usually $m^* \simeq 1.5m$, where m is the rest mass of positron. The effective positron mass reflects the interaction of positron with condensed matter medium and includes contribution of phonons, positron band structure and electron-positron interaction. The mean square velocity of positron can be expressed as

$$v_+[\mathrm{nm/ps}] \simeq 5.5\sqrt{T}. \tag{2.3}$$

2.3 Positron implantation profile

Penetration of positrons emitted by a β^+ source with mean energy in order of hundreds keV into condensed matter can be described by an empirical implantation profile [2]

$$P(x) = \alpha_+ e^{-\alpha_+ x}, \tag{2.4}$$

where $P(x)$ is probability that positron penetrates into depth x under surface of sample. The mean penetration depth can be calculated using the expression

$$\frac{1}{\alpha_+}[\mathrm{cm}] \simeq \frac{E_{max}^{1.4}[\mathrm{MeV}]}{16\varrho[\mathrm{g}\cdot\mathrm{cm}^{-3}]}, \tag{2.5}$$

where E_{max} is the end-point energy of β^+ source and ϱ is density of sample. In metals, the mean penetration depth of positrons emitted by ^{22}Na source ranges from 10 to 500 μm. Therefore, positrons emitted by ^{22}Na source probe bulk properties of the sample.

2.4 Positron states in condensed matter

Thermalized positrons are scattered almost exclusively by phonons and in the classical approximation positrons perform a random isotropic diffusion motion in material. The momentum distribution of positrons does not change further after thermalization. Scattering by phonons leads to temperature dependence of the positron diffusion coefficient [3]

$$D_+ \sim \frac{1}{\sqrt{T}}. \tag{2.6}$$

The positron diffusion coefficient typically falls into the range from 0.1 to 2 cm^{2}s^{-1} at room temperature. The mean free path of a thermalized positron is

$$l_+ = v_+ \tau_{ph}, \tag{2.7}$$

where τ_{ph} is the relaxation time of phonon scattering. The mean free path of positron in metals is usually in the order of nanometers.

During its lifetime positron explores mean volume of $\lambda_+^2 L_+$ in the sample. The quantity λ_+ is the positron wavelength and L_+ is the mean diffusion length of positron. The wavelength of a thermalized positron can be calculated as

$$\lambda_+[\mathrm{nm}] = \frac{2\pi\hbar}{m^* v_+} \simeq 5.2\sqrt{\frac{293[\mathrm{K}]}{T[\mathrm{K}]}}. \tag{2.8}$$

The mean diffusion length L_+ is defined as the mean distance which positrons travel from the point of their thermalization to the place of annihilation during their lifetime τ_I. It can be expressed as

$$L_+ = \sqrt{D_+ \tau_I}. \tag{2.9}$$

The mean positron diffusion length in metals is in the order of hundreds nanometers. Hence, volume explored by a positron during its lifetime in the sample contains about 10^7 atoms.

The positron wavelength λ_+ in condensed matter is always larger than the interatomic distance. Therefore, positrons in condensed matter behave as waves and we speak about delocalized or free positrons. The annihilation rate of positrons in condensed is proportional to overlap of the electron and positron density [4]

$$\lambda = \pi r_e^2 c \hat{n}_-, \tag{2.10}$$

where r_e is the classical electron radius, c is the velocity of light and

$$\hat{n}_- = \int n_+(\boldsymbol{r}) n_-(\boldsymbol{r}) \gamma(n_-) \mathrm{d}^3\boldsymbol{r}, \tag{2.11}$$

where $n_+(\mathbf{r})$ is the positron density, $n_-(\mathbf{r})$ is the electron density and $\gamma(n_-)$ is the enhancement factor.

The electron density $n_-(\mathbf{r})$ is a sum of squares of electron wavefunctions $\psi_-(\mathbf{r})$ over all occupied states below the Fermi level E_F

$$n_-(\mathbf{r}) = \sum_{e_i \leq E_F} [\psi_-(\mathbf{r})]^2, \tag{2.12}$$

where e_i represents the energy eigenvalue of the ith-level.

Commonly used positron β^+ sources have activity in the order of one MBq, i.e. they emit on average one positron per microsecond. Since this time scale is much longer than typical positron lifetime in condensed matter, there is only one positron at certain time in the sample. Therefore, the positron density $n_+(\mathbf{r})$ is simply a square of the positron wavefunction

$$n_+(\mathbf{r}) = [\psi_+(\mathbf{r})]^2. \tag{2.13}$$

Attractive Coulombic interaction between positron and electrons induces enhancement of the electron density around the positron site. This effects is especially pronounced in metals where local enhancement of the valence electron density leads to a significant increase in the positron annihilation rate. The enhancement factor $\gamma(n_-)$, which is a function of the electron density, is introduced to take this effect into account.

Therefore, the quantity $\hat{n}_-$ can be understood as the effective electron density which affects positron. Inverse of the annihilation rate is called positron lifetime

$$\tau = \frac{1}{\lambda}. \tag{2.14}$$

Typical values of positron lifetime are in range from 100 to 300 ps for delocalized positrons in metals.

Positrons are positively charged, therefore, they are electrostatically repelled by positive ions in crystal lattice. Hence, open-volume defects, e.g. vacancies and clusters of vacancies, represent regions with lower potential for positron. If the potential well at the site of defect is deep enough, positron can form localized state with lower energy than that of delocalized one.

The positron binding energy E_B to defect is defined as difference between the energy eigenvalues for these two states. Binding energies of positrons trapped in monovacancies are typically in the order of a few eV [5, 6, 7, 8]. Positrons trapped in open-volume defects have longer lifetime than delocalized ones due to lower local electron density in such defects.

2.5 Positron lifetime spectroscopy

The positron annihilation rate is proportional to the overlap of the electron and positron density as shown in equations (2.10) and (2.11). Hence, all positrons annihilate with the same annihilation rate in homogeneous defect free sample because overlap of the electron and positron densities is the same for all of them.

Let $n(t)$ denote the probability that a positron at time t is still present in the sample and has not been annihilated yet. At the moment of implantation $t = 0$ the probability has value $n(0) = 1$. The $n(t)$ for a defect-free material will then decrease with increasing time t according to the equation

$$\frac{dn(t)}{dt} = -\lambda_B n(t), \tag{2.15}$$

where λ_B is the annihilation rate of a delocalized positron in the studied material. The probability $n(t)$ is therefore

$$n(t) = e^{-\lambda_B t}. \tag{2.16}$$

However, the probability $n(t)$ is not directly accessible in experiment. Instead, a positron lifetime spectrometer measures the time interval between emission and annihilation of positrons. Since the annihilation events are related to decrease of $n(t)$, the spectrometer measures negative time derivative of $n(t)$. An ideal positron lifetime spectrum S_{id} measured by a positron lifetime spectrometer with perfect time resolution has form

$$S_{id}(t) = -\frac{dn(t)}{dt} = \lambda_B e^{-\lambda_B t}. \tag{2.17}$$

Expected value of this distribution is the positron lifetime $\tau_B = 1/\lambda_B$.

Real positron lifetime spectrometers exhibit finite time resolution and recorded spectra contain background B from random coincidences. Hence, the real lifetime spectrum can be described by the equation

$$S(t) = S_{id}(t) * R(t) + B, \tag{2.18}$$

where $*$ denotes convolution and $R(t)$ is the resolution function of the spectrometer which describes the response of the spectrometer to a prompt coincidence. The resolution function is in practice usually expressed by sum of two or three Gaussians.

The situation is more complicated in case of materials containing defects. Let's consider a material with one type of defects which can trap positrons. We will denote $n_B(t)$ the probability that a positron is at time t delocalized in the material and $n_D(t)$ the probability that a positron is at time t trapped in defect. Therefore, the probability that positron has not annihilated yet is $n(t) = n_B(t) + n_D(t)$.

A thermalized positron can annihilate either from the delocalized state or from the trapped state at defect with the annihilation rates λ_B and λ_D, respectively. The transition rate from the delocalized state to the trapped state is given by the trapping rate K_D.

A positron must undergo two distinct processes before it forms a localized state at defect: (i) positron diffusion to the vicinity of defect, (ii) quantum transition from the delocalized to the localized state. Therefore, there are two limit cases:

1. Transition-limited regime: the mean distance between defects is smaller than the mean positron diffusion length L_+. Hence, the diffusion time from the place of thermalization to the location of defect can be neglected and the positron trapping rate is determined by the transition rate from the delocalized to the localized state. Trapping at monovacancies with sufficiently high concentration represents a typical example of this regime.

2. Diffusion-limited regime: the positron trapping rate is limited by diffusion of positrons to the vicinity of defects when the mean distance between defects is substantially larger than L_+. This case typically occurs when positrons are trapped at grain boundaries or in larger precipitates.

In general case neither diffusion nor transition time can be neglected and both positron diffusion and transition rate must be taken into account.

A simple trapping model (STM) was developed to describe the positron kinetics in the transition-limited regime [9, 10, 11]. This model is based on the following assumptions:

1. only thermalized positrons can be trapped
2. detrapping does not occur
3. space distribution of defects in material is uniform

Under these assumptions we obtain the following kinetic equations governing the time evolution of $n_B(t)$ and $n_D(t)$

$$\begin{aligned} \frac{dn_B(t)}{dt} &= -\lambda_B n_B(t) - K_D n_B(t) \\ \frac{dn_D(t)}{dt} &= -\lambda_D n_D(t) + K_D n_B(t). \end{aligned} \tag{2.19}$$

The assumption that only thermalized positrons can be trapped means that all positrons are in the delocalized state after thermalization and the initial conditions have the form

$$n_B(0) = 1, \qquad n_D(0) = 0. \tag{2.20}$$

The solution of the system of differential equations (2.19) with corresponding initial conditions (2.20) can be written as

$$\begin{aligned} n_B(t) &= e^{-(\lambda_B+K_D)t} \\ n_D(t) &= \frac{K_D}{\lambda_B + K_D - \lambda_D}(e^{-\lambda_D t} - e^{-(\lambda_B+K_D)t}). \end{aligned} \tag{2.21}$$

The ideal positron lifetime spectrum has two components in this case

$$S_{id}(t) = -\frac{d(n_B(t) + n_D(t))}{dt} = I_1\lambda_1 e^{-\lambda_1 t} + I_2\lambda_2 e^{-\lambda_2 t}, \tag{2.22}$$

where the positron lifetimes τ and the relative intensities I of each component are

$$\begin{aligned} \tau_1 &= \frac{1}{\lambda_1} = \frac{1}{\lambda_B + K_D} \\ \tau_2 &= \frac{1}{\lambda_2} = \frac{1}{\lambda_D} \\ I_1 &= 1 - I_2 \\ I_2 &= \frac{K_D}{\lambda_B + K_D - \lambda_D}. \end{aligned} \tag{2.23}$$

The concentration of defects in the sample can be calculated from measured trapping rate K_D according to the equation

$$c_D = \frac{K_D}{\nu_D}, \tag{2.24}$$

where the constant ν_D is the specific trapping rate which is characteristic for each type of defect.

The first component in the equation (2.22) corresponds to annihilation of free delocalized positrons. The apparent annihilation rate λ_1 is higher than λ_B because free positrons are not only annihilated but also trapped at defects with the trapping rate K_D. Therefore, the lifetime τ_1 and the intensity I_1 corresponding to the free positron component decrease with increasing concentration of defects.

The second component comes from annihilation of positrons trapped at defects. Its lifetime τ_2 is the same as the lifetime of positrons trapped at defects. In contrast to τ_1, the lifetime of the second component τ_2 does not depend on the concentration of defects. The intensity of the second component I_2 increases with increasing concentration of defects.

In a material with very high concentration of defects, the trapping rate K_D becomes significantly larger than λ_B. In this case practically every positron is trapped just after thermalization and so called saturated positron trapping occurs. The lifetime τ_1 and the intensity I_1 of the first component become essentially zero and the spectrum exhibits single component with lifetime τ_D. Furthermore, it is not possible to determine the concentration of defects only to estimate a lower limit of defect concentration from the lowest intensity I_1 which is detectable by a particular positron lifetime spectrometer.

The applicability of STM can be simply validated by testing the following relation

$$\tau_B^{-1} = \lambda_B = I_1\lambda_1 + I_2\lambda_2. \tag{2.25}$$

If it does not hold then STM cannot be used because some of its assumptions are violated.

2.6 Coincidence Doppler broadening of positron annihilation radiation

The energy and the momentum conservation implies that at least two annihilation photons must be created during annihilation of the electron-positron pair. For two photon annihilation, two anti-parallel photons are emitted. As the probability of emission of three or more photons is much smaller than that of two photon annihilation [12], these cases will be not discussed further.

Thermalized free positrons in condensed matter have negligible kinetic energies compared to surrounding electrons. Hence, the momentum of annihilating electron-positron pair is determined by the electron which annihilates the positron. Non-zero momentum of the electron-positron pair in the laboratory frame leads to a Doppler shift ΔE of the measured energy of annihilation photons

$$\Delta E = \frac{1}{2}cp_L, \tag{2.26}$$

where p_L is the momentum component of the electron-positron pair in the direction of emitted photons.

Therefore, the annihilation peak located at the energy of 511 keV is broadened by Doppler shift and its shape is defined by the one-dimensional projection of electron momentum distribution into the axis connecting the sample and the detector. The highest Doppler shifts are caused by annihilation with core electrons which posses high momentum. The momentum distribution of core electrons is unique for each chemical element. Therefore Doppler broadening of positron annihilation radiation carries information about chemical composition around positron annihilation sites.

In the conventional Doppler broadening spectroscopy energy of only single annihilation photon is measured. This simplifies the experimental setup but also limits achievable peak-to-background ratio. On the other hand, in the coincidence Doppler broadening spectroscopy (CDB) two detectors are used and energy of both annihilation photons are recorded. In CDB spectrometer only events where annihilation photons were simultaneously detected in both detectors are recorded. This so-called coincidence measurement leads to drastic reduction of background (typically by three orders of magnitude) which enables observation of rare annihilations by high momentum core electrons.

Annihilations with low momentum conduction electrons contribute to central region of the annihilation peak. High momenta of core electrons lead to a significant Doppler shift and annihilations with them create tails of the annihilation peak. Open-volume defects exhibit generally lower electron density than defect-free bulk material.

However, the decrease of the core electron density is larger than that of conduction electrons because core electrons are localized near nuclei while conduction electrons can move more freely. Therefore, the annihilation peak becomes narrower as the fraction of positrons trapped in defects increases.

A simple analysis of shape of the annihilation peak can be performed using the line shape parameters S and W. The sharpness of the peak is described by S parameter which is defined as relative area of the central part of the peak. Wings of the peak are represented by the W parameter which is defined as relative area of the peak tails. The S parameter represents a measure of the fraction of positrons annihilating with conduction electrons while the W parameter is a measure of the fraction of positrons annihilating with core electrons.

There are no exact rules for choosing the boundaries of regions used for calculation of S and W parameters. Instead the boundaries are usually chosen to maximize the observed variations of the parameters between measured samples. The area corresponding to the S parameter is typically set to one half of total peak area. The area for calculation of the W parameter is on the other hand selected to contain mainly annihilations of core electrons. Usual values of W parameter are in the order of percents of total area.

Absolute values of the S and W parameters do not have physical meaning because they are dependent on the choice of the area boundaries. Only their relative changes are meaningful. The S parameter generally increases while the W parameter decreases with increasing concentration of defects in material.

The changes in shape of the annihilation peak can be more precisely studied by using the ratio curves. These curves are constructed by dividing the annihilation peak of the measured material point by point by that of a well defined reference material. The ratio curve is even function so only one half corresponding to the positive Doppler shifts is usually shown. The advantage of using ratio curves over the S and W parameters is that one can clearly see in what momentum region the annihilation peak shapes differ.

3. Introduction to quasicrystals and Mg-Zn-Y system

3.1 Quasicrystals

Ordered crystal lattices are usually associated with translation symmetry which imposes certain constraints on symmetry axes in crystals. Namely space can be filled without gaps or overlaps with units exhibiting 2,3,4 and 6-fold rotational symmetries while preserving the translation symmetry. However, X-ray diffractograms with icosahedral five-fold symmetry axis were observed in 1984 by Shechtman et al. in a rapidly cooled Al-Mn alloy [13].

Five-fold and higher than six-fold rotational symmetries are forbidden in crystals because they fail to transform lattice into itself [14]. However, space can be tiled in these 'forbidden' symmetries by aperiodical tiling of multiple elementary units. Famous example of such tiling is the Penrose tiling of two-dimensional plane by two rhombic units with different vertex angle shown in figure 3.1. Thick rhombi have vertex angle of 72° and thin ones 36°.

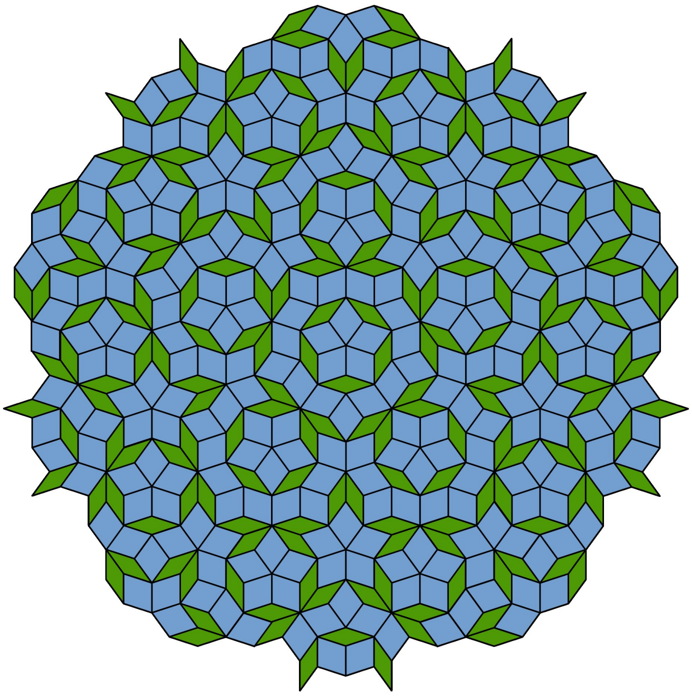

Figure 3.1: Penrose tiling [22].

The Penrose tiling exhibits reflection symmetry and five-fold rotational symmetry but lacks any translational symmetry. Hence, it is impossible to define a finite unit cell for the Penrose tiling. This can be also seen from the irrational ratio of the number of thick to thin rhombi which is equal to the golden ratio $\varphi = \frac{1+\sqrt{5}}{2}$. Therefore, no finite unit cell with this ratio of rombi can be constructed.

Analogically, three dimensional tiling with icosahedral symmetry can be constructed using five units shown in figure 3.2 [15].

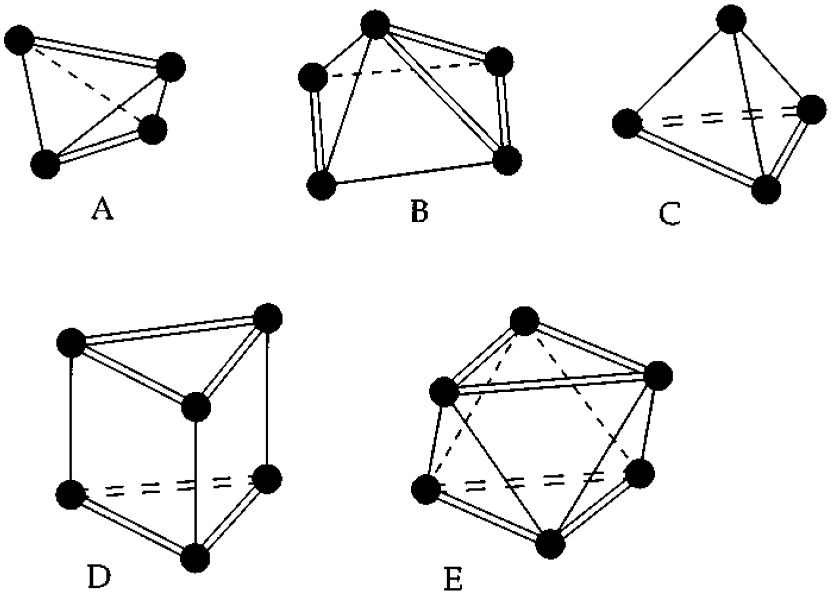

Figure 3.2: Canonical units of 3D icosahedral tiling [15].

Alternatively, quasicrystalline structure can be described by the projection method [16]. As an example, we will demonstrate this method on one-dimensional quasicrystal. Let's consider a square lattice and two two-dimensional Cartesian coordinate systems with axes X_1, X_2 and $X_\parallel$, $X_\perp$. A lattice with the lattice parameter a lies in the X_1, X_2 coordinate system which is rotated by the angle θ with respect the second coordinate system $X_\parallel$ and $X_\perp$, see figure 3.3.

The axis $X_\parallel$ is called physical or parallel space and represents the physical dimension of our one-dimensional quasicrystal. The second axis $X_\perp$ is called additional or perpendicular space. To determine the positions of quasicrystal lattice sites, square lattice sites inside so-called projection tube are projected onto the physical axis $X_\parallel$. The projection tube forms a strip of width $l = a(\cos\theta + \sin\theta)$ parallel to the axis $X_\parallel$.

On the physical axis, the sequence of long distances $L = a\cos\theta$ and short distances $S = a\sin\theta$ between the lattice sites is created. The sequence of the long and short distances forms the infinite Fibonacci word, sometimes called rabbit sequence (sequence A005614 in On-Line Encyclopedia of Integer Sequences [17]).

The projection technique can be extended to higher dimensions, N dimensional quasicrystals can be described by using N physical and N additional dimensions. Therefore, three-dimensional quasicrystal can be interpreted as projection of a six-dimensional periodical lattice into the three-dimensional space.

The projection technique can be also used for description of excitations of the quasicrystal lattice[16]. The density of quasicrystal can be expressed as

$$\rho(\mathbf{r}_\parallel) = \int \rho(\mathbf{r}) n(\mathbf{r}_\perp) d^3\mathbf{r}_\perp, \tag{3.1}$$

where $\rho(\mathbf{r})$ is the density of a six dimensional hypercrystal and $n(\mathbf{r}_\perp)$ represents the projection tube. The density of quasicrystal in the physical space can be expanded into the Fourier series

$$\rho(\mathbf{r}_{\|}) = \sum_{Q} \rho_Q \exp(i\mathbf{Q}\mathbf{r}), \tag{3.2}$$

where $\mathbf{Q}$ are vectors of the reciprocal lattice of a six-dimensional hypercrystal.

Distortions of $\rho(\mathbf{r})$ lead to appearance of additional phases $F_Q(\mathbf{r})$ in equation (3.2) which can be decomposed into parallel and perpendicular directions

$$F_Q(\mathbf{r}) = \mathbf{Q}_{\|}\mathbf{u}(\mathbf{r}) + \mathbf{Q}_{\perp}\mathbf{w}(\mathbf{r}), \tag{3.3}$$

where vectors fields $\mathbf{u}(\mathbf{r})$ and $\mathbf{w}(\mathbf{r})$ describe phonons and phasons respectively.

Phonons cause elastic deformations of the quasicrystalline lattice. On the other hand, phasons change local configurations in physical space to such which are forbidden in defect-free quasicrystals. These configurations are physically realized by atomic displacements which may involve numerous jumps of individual atoms. Existence of phasons is a consequence of additional degrees of freedom introduced in the projection formalism.

Since plastic deformation of crystalline material proceeds by dislocation mechanism, it is dependent on the motion of dislocations. However, Burgers dislocation vectors in quasicrystals always contain a phason component. Hence, reordering of atoms is needed for dislocation movement and mobility of dislocations in quasicrystals is very limited at temperatures below 600 °C. At higher temperatures, diffusion of the atoms in quasicrystal becomes significant and enables efficient movement of dislocations.

Clean surfaces of quasicrystals maintain aperiodic structure and exhibit low surface energy, only $\sim 25\%$ higher than that of teflon, due to presence of pseudogap in the electron density of states [16].

The majority of quasicrystalls was discovered in the form of single phase materials [18, 19, 20]. Recently, quasicrystalline icosahedral precipitates were observed in Mg-Zn-RE alloys [21]. Unique structure of these precipitates attracts attention because it could improve mechanical properties of magnesium alloys.

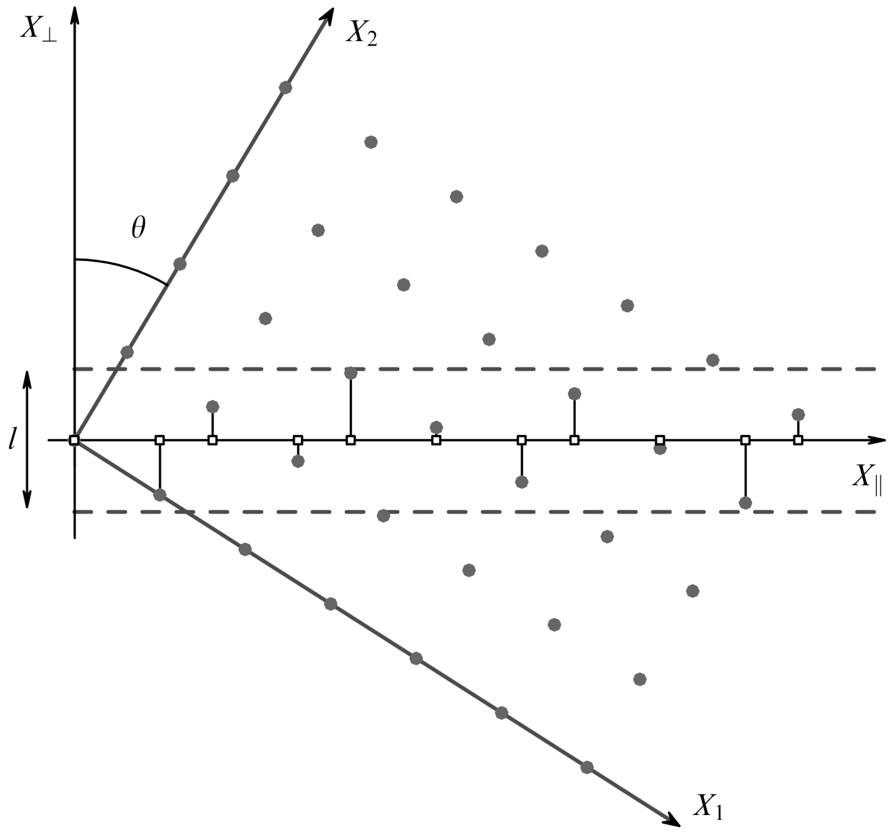

Figure 3.3: Construction of one-dimensional quasicrystal by the projection method. θ - angle between two coordinate systems $X_\parallel$, $X_\perp$ and X_1, X_1; l - width of the projection tube [16].

3.2 Mg-Zn-Y system

The Mg-Zn-Y system attracts attention due to recent discovery of a stable quasicrystalline phase $Mg_3Zn_6Y_1$ which exhibits icosahedral symmetry [23, 24, 25]. Icosahedral phase formed in this system is a thermodynamically stable phase which is in thermodynamic equilibrium with the Mg matrix [23, 24].

Two limiting cases of the ternary Mg-Zn-Y system relevant for Mg alloys are the binary systems Mg-Zn and Mg-Y. Their phase diagrams are plotted in figures 3.4 and 3.5. One can see that the solubilities of Zn and Y in Mg are limited. The maximal solubilities in Mg, which are reached at the eutectic temperature, are 2.4at.% and 3.75at.% for Zn and Y, respectively.

In addition to the icosahedral phase $Mg_3Zn_6Y_1$, large number of crystalline intermetallic phases was experimentally observed in the ternary Mg-Zn-Y system [26, 27], see table 3.1.

Two of these phases are closely related to the icosahedral phase. The Mg_7Zn_3 phase (sometimes referred as $Mg_{51}Zn_{20}$ [28]) can be considered as a 1/1 approximant of the icosahedral phase [29]. The Z-phase $Mg_{28}Y_7Zn_{65}$ was related to the icosahedral phase as well since it can be described as interpenetrating icosahedral clusters [30].

It was found out that the decisive factor governing the phase composition in Mg-Zn-Y system is the ratio of Zn to Y (Zn/Y) content [31]. High Zn/Y ratios (∼10 in wt.%) result in a situation close to the binary Mg-Zn system and favor the formation of binary Mg_7Zn_3 phase. At intermediate Zn/Y ratios (5-7 in wt.%) the icosahedral phase $Mg_3Zn_6Y_1$ is formed and the W-phase forms at low Zn/Y ratios (below 1.5-2.5 in wt.%).

The upper limit for the temperature stability of the binary Mg-Zn phases in the Mg-rich corner of the Mg-Zn-Y system can be estimated from the phase diagram of binary Mg-Zn system. Since the eutectic temperature in Mg-Zn system is 340°C, see figure 3.4, no binary Mg-Zn phases should be present in Mg-Zn-Y-based alloys above this temperature. Investigations by differential thermal analysis reported in literature suggest that icosahedral phase melts at $\sim$ 450°C [32] and the melting of W-phase occurs at $\sim$ 510°C [33].

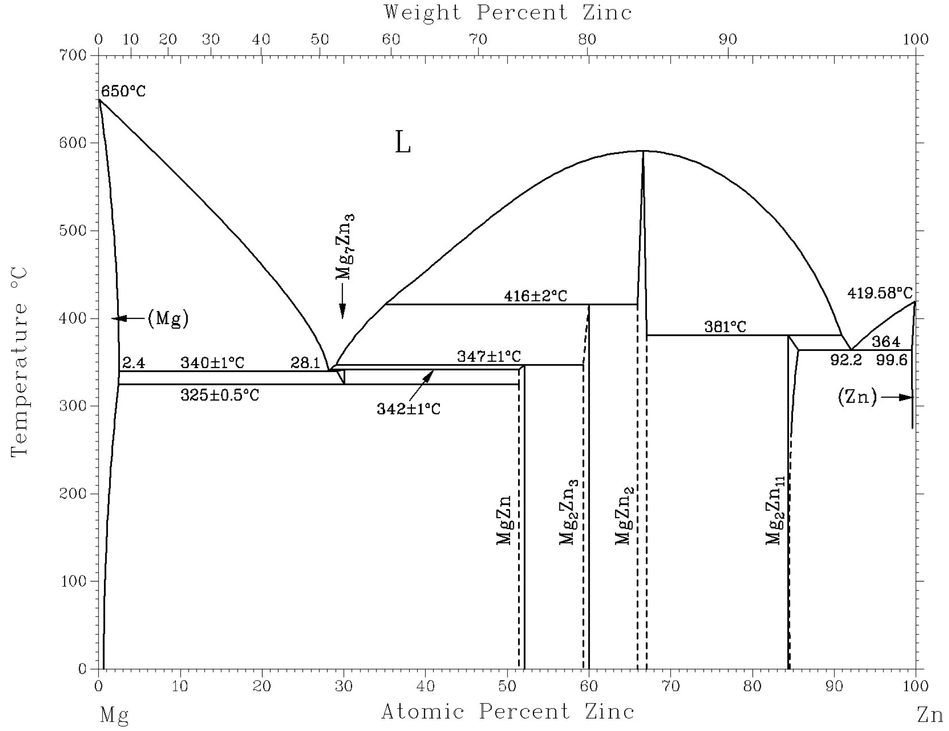

Figure 3.4: Equilibrium phase diagram of the Mg-Zn system [34, 35, 36, 37].

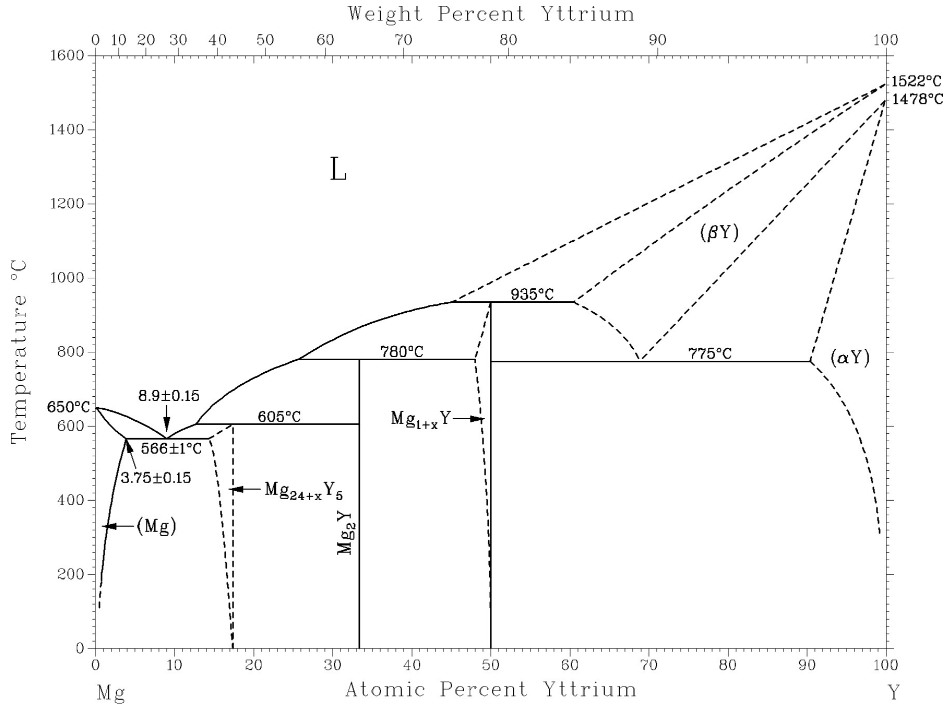

Figure 3.5: Equilibrium phase diagram of the Mg-Y system [38, 39, 40, 41, 42].

Phase	Pearson symbol, space group, structure type	Lattice parameters			
		a (nm)	b (nm)	c (nm)	γ (°)
$Mg_{24}Y_5$ (ε)	$cI58$, $I\bar{4}3m$	1.1257			
Mg_2Y	$hP12$, $P6_3/mmc$	0.6037		0.9752	120
MgY	$cP2$, $Im\bar{3}m$, $B2$	0.3796			
YZn	$cP2$, $Im\bar{3}m$, $B2$	0.3578			
αYZn_2	$oI12$, $Imma$	0.4504	0.7143	0.7664	
βYZn_2	?				
YZn_3	$oP16$, $Pnma$	0.6690	0.4405	1.0111	
Y_3Zn_{11}	$oI28$, $Immm$	0.4388	1.2929	0.8871	
$Y_{13}Zn_{58}$ (Y_2Zn_9)	$hP146$, $P6_3/mmc$	1.428		1.40	120
YZn_5	$hP36$, $P6_3/mmc$	0.8885		0.9201	120
Y_2Zn_{17}	$hP38$, $P6_3/mmc$	0.8911		0.8764	120
YZn_{12}	$tI26$, $I4/mmm$	0.8875		0.5192	
Mg_7Zn_3 ($Mg_{51}Zn_{20}$)	$oI158$, $Immm$	1.408	1.449	1.403	
MgZn	?				
Mg_2Zn_3	$mC110$, $B2/m$	2.596	1.428	0.524	102.5
$MgZn_2$	$hP12$, $P6_3/mmm$, $C14$	0.5253		0.8568	120
Mg_2Zn_{11}	$cP39$, $Pm\bar{3}$, $D8_c$	0.855			
W_$Mg_3Y_2Zn_3$	$cF16$, $Fm3m$	0.683			
Z_$Mg_{28}Y_7Zn_{65}$	$P6_3/mmc$	1.458	0.868		120
I_Mg_3YZn_6	$Fm53$	$a_R = 0.519$			
H_$Mg_{15}Y_{15}Zn_{70}$	Hexagonal	0.776		0.92	120
X_$Mg_{12}YZn$	?				

Table 3.1: Structure of binary and ternary phases present in Mg-Zn-Y system [23, 25, 43, 30, 44, 29]. Adapted from [26].

4. Experimental techniques

4.1 Hardness measurements

The knowledge of mechanical properties is crucial for applications of structural materials. Mechanical tests provide information about solid-solution and precipitation hardening in a studied material. The Vickers indentation hardness test provides smaller amount of information than the tensile or compression tests but offers several advantages. It does not require specific sample shape and it is virtually nondestructive method.

This allows us to repeatedly measure the hardness of a sample subjected to heat treatment, e.g. after each step of isochronal annealing. Some other hardness tests, such as Brinell test, produce large indentations and are not suitable for this purpose.

High flexibility of Vickers test allows its use for both soft and hard materials including practically every metal. Results of Vickers hardness test are reported in unit known as Vickers Pyramid number (HV). Measurement is performed by pressing a pyramid diamond indenter with square base and angle of opposing faces of 136° into polished sample by the force F. Imprint of the diamond tip with length of diagonals d_1 and d_2 is left on the surface after the test.

The hardness number HV is calculated by dividing the force F applied to the indenter in kilogram-force (kgf) by area the A of the resulting indentation imprint in mm^2

$$HV = \frac{F}{A}. \tag{4.1}$$

The area A is determined from optical measurement of the length of imprint diagonals

$$A = \frac{d^2}{2\sin(136°/2)}, \tag{4.2}$$

where d is the arithmetic mean of the diagonals d_1 and d_2. Hence,

$$HV = \frac{2F\sin(136°/2)}{d^2} \approx \frac{1.8544F}{d^2}, \tag{4.3}$$

where F is given in kgf and d in mm. To convert HV value to SI units, force must be converted from kilogram-force to newtons by multiplying it by the standard gravity $g_0 = 9.80665$ ms^{-2}, i.e. 1 kfg = 9.80665 N.

The yield strength of a non-work-hardening material can be estimated from HV value expressed in SI units [45]

$$\sigma_y = \frac{HV}{3}. \tag{4.4}$$

Vickers hardness numbers are usually written in form xHVl/t, where x is the hardness number, HV denotes Vickers hardness scale, l indicates the load used in kgf and t is the loading time. Abbreviated form xHVl, where loading time t is not explicitly stated, is commonly used when the loading time ranges from 10 to 15 s.To obtain correct results, surface of the sample has to be flat and polished. The indentations should have spacing of at least 2.5 times of the indentation diameter to avoid testing in the work-hardened region around neighboring indentation.

A microhardness tester Struers Duramin 300 was used for measurement of the Vickers hardness in the present work. At least ten indentations were made into each sample to improve the accuracy of measurement and to estimate the variance of measured hardness.

4.2 Scanning electron microscopy

Scanning electron microscopy (SEM) was used to characterize the microstructure of studied alloys. SEM images were taken by a FEI Phenom microscope which has a detector of back-scattered electrons and by a Tescan SEM Mira I equipped with a detectors of secondary and back-scattered electrons and a detector of characteristic X-rays which was employed for local chemical analysis of studied samples by energy-dispersive X-ray (EDX) spectroscopy.

Back-scattered electrons are produced by elastic backward scattering of primary electron beam. Elements with higher atomic number scatter the primary electron beam more than lighter elements. Therefore, SEM images captured by a detector of back-scattered electrons exhibit so called Z-contrast where locations containing heavier elements are represented by lighter color.

Example SEM image of Mg-Zn alloy showing Z-contrast is shown in figure 4.1. Since zinc has higher atomic number (30) than magnesium (12), zinc rich areas are lighter than zinc poor regions. Yttrium has even high atomic number (39) than zinc. Hence regions enriched by yttrium appear even brighter.

High contrast between Mg matrix and secondary phases rich in alloying elements allows us to estimate their volume fraction. Firstly, gray-scale images were converted to binary black-and-white scale. Careful adjustment of the conversion threshold level is necessary to produce accurate results. Finally, the volume fractions of zinc and yttrium-rich phases are calculated from relative fractions of white pixels in the black-and-white image. Multiple images of the same alloy were processed to average the volume fraction over larger area of sample. This procedure not only improves accuracy of measurement but also allows us to estimate the variance of the volume fraction value.

Figure 4.1: SEM image of as-cast Mg4Y26Zn alloy.

4.3 X-ray diffraction

X-ray diffraction is well-established experimental technique used to identify phases present in studied samples and to determine their lattice parameters. The positions of peaks in X-ray diffractogram can be calculated from interplanar distances d_{hkl} of crystallographic planes with Miller indices (hkl) according to the Bragg's law

$$n\lambda = 2d_{hkl}\sin\theta, \tag{4.5}$$

where λ is the wavelength of used X-ray radiation and n is the order of diffraction which is assumed $n = 1$ for X-ray diffraction. Hence, interplanar distance d_{hkl} can be determined from peak position using the expression

$$d_{hkl} = \frac{\lambda}{2\sin\theta}. \tag{4.6}$$

The X-ray diffraction spectra were measured on Panalytical X'Pert PRO MRD diffractometer fitted with copper anode in the symmetrical Bragg-Brentano geometry. A pseudo-Voigt profile function was used to fit the peak positions θ in the spectra measured using this laboratory machine.

In situ measurements of X-ray diffraction of synchrotron radiation were performed at the beamline P07 at DESY, Hamburg. Samples of as-cast alloys in shape of cylinder with a diameter of 3 mm were placed in a graphite crucible with steel cap. The vertically-oriented graphite crucible was heated by radio frequency induction heating.

The temperature of the sample was measured by a type S thermocouple which was attached to the steel cap by resistive spot welding. High energy of primary X-ray beam 87.1 keV (λ = 0.142 Å) enabled measurement of XRD in the transmission geometry. The diffraction pattern was recorded using 2D Mar555 flatpanel detector from Marresearch.

The modified dilatometer Bähr DIL 805 A/D was used for the *in situ* XRD investigations of ECAP-processed samples and for the compression tests. The setup was very similar to one used for the *in situ* studies of the as-cast samples, just the graphite crucible was placed in a horizontal orientation inside the dilatometer. X-ray synchrotron radiation with an energy of 100 keV (λ = 0.124 Å) was used for these studies and 2D diffraction patterns were recorded by Perkin Elmer XRD 1621 detector.

4.4 Positron lifetime spectroscopy

A $^{22}Na_2CO_3$ positron source with activity of 1.5 MBq deposited on a 2μm Mylar foil was used for positron lifetime spectroscopy. A digital positron lifetime (LT) spectrometer with excellent time resolution of 155 ps, expressed as FWHM of the resolution function, was used for all measurements. A scheme of the LT spectrometer is shown in figure 4.2 and detailed description of its operation is given in references [46, 47].

The digital LT spectrometer employs two detectors consisting of a BaF_2 scintillator crystal attached to a Hamatsu H3378 photomultiplier (PMT). Anode signal from PMTs is passively split. The main part of the signal is directly digitized by a pair of fast 8-bit digitizers Acqiris DC211 with the sampling rate of 4 GHz. The second part is used to ensure that measurement proceeds in coincidence.

Signal in coincidence circuit is firstly amplified by a fast amplifier HP MSA-0204 and then inverted by an inverting transformer (IT) Ortec IT 100. The inverted signal is connected to a constant fraction differential discriminator (CFDD) Ortec 583 which produces logic pulse when a pulse from the detector arrives.

To provide the timing information independent of the pulse height, threshold level is dynamically adjusted to given fraction of the pulse height for each pulse on the input of the discriminator. Hence, the logic pulse is emitted by CFDD when the input signal reaches e predefined fraction of its own height.

Passively summed output of both CFDDs is connected to external trigger input of the master digitizer. To ensure that only events where gamma photons were detected in both detectors in coincidence are digitized, the trigger level is set to such value that only sum of logic pulses from both CFDDs can fire the trigger.

During the measurement, the waveforms are digitized and stored on external hard-drive. The LT spectra are calculated offline from acquired data after the measurement by a dedicated software routine [48]. Decomposition of LT spectra into exponential components was performed by a least square fitting procedure, see figure 4.3.

A real LT spectrum contains not only components originating from positron annihilations inside the measured sample but also of several additional components. These additional components come from inevitable positron annihilations in the source and were determined by measurement of a reference well-annealed sample of pure Mg.

The reference lifetime spectrum is composed of a single sample component with a lifetime of 225 ps and two source components. Shorter component with lifetime of 368 ps and intensity of $\sim 8\%$ represents a contribution of positrons annhilated in the $^{22}\mathrm{Na_2CO_3}$ source spot. The longer component with lifetime 1.8 ns and intensity $\sim 1\%$ is a result of ortho-positronium formation in the covering Mylar foils.

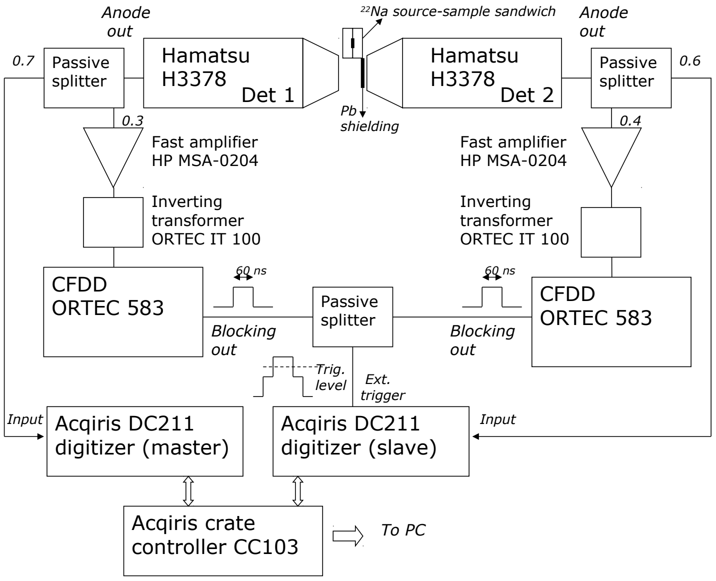

Figure 4.2: A scheme of a digital positron lifetime spectrometer.

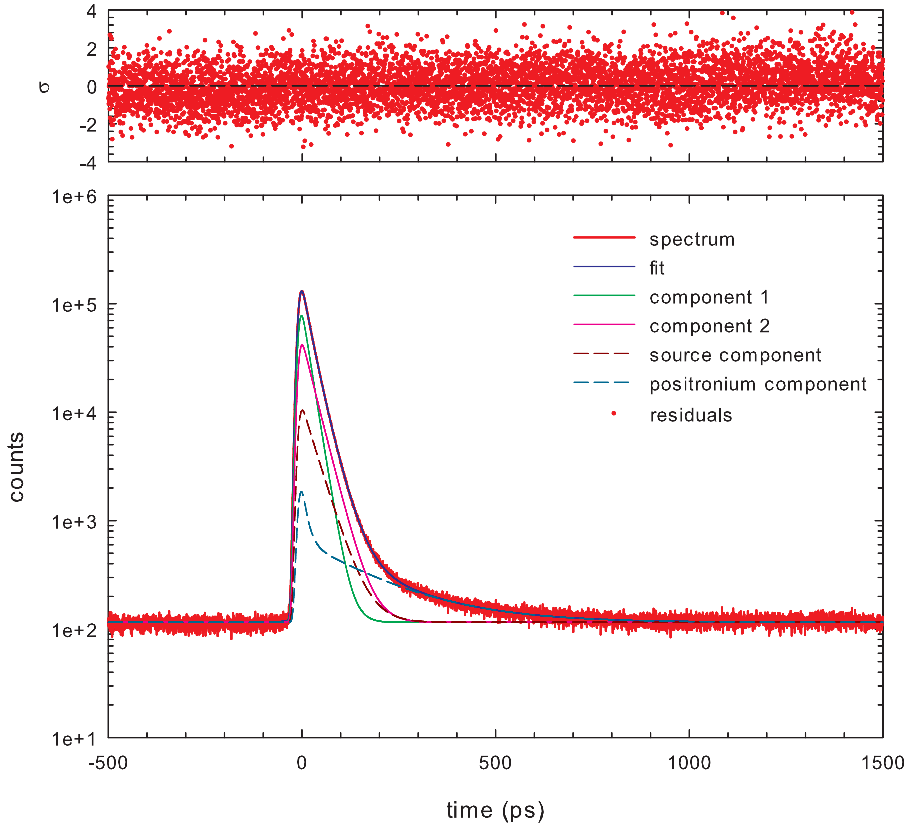

Figure 4.3: Fitted LT spectrum of WE43 alloy modified by addition of 26 wt.% of Zn (WE43+26Zn).

4.5 Coincidence Doppler-broadening spectroscopy

An analog spectrometer with the resolution of 1.0 keV (FWHM at 511 keV) was used for the coincidence measurement of Doppler broadening of annihilation radiation. Its scheme is shown in figure 4.4. Since achieving outstanding energy resolution is critical for CDB spectrometer, it contains two high-purity germanium (HPGe) detectors, Ortec GEM35190 and GEM35P. Height of the signal generated on the output of the HPGe detector is proportional to the energy of detected photon.

Pulses from HPGe detectors have short leading edges but long exponentially decaying tails. Spectroscopic amplifiers (SA) are used to amplify the signal and shape it into a pseudo-gaussian shape. The time constant of shaping was set to 4 μs. The amplitudes of shaped pulses are digitized by analog-to-digital converters (ADC) Canberra 8713 and resulting values are stored in a computer.

The measurement in coincidence, i.e. recording only events when photons are detected in both detectors simultaneously, is ensured by a coincidence circuit which consists of constant fraction discriminators (CFD) and time-amplitude converter (TAC) combined with single channel analyzer (SCA). The outputs of HPGe detectors are connected to CFDs which provide timing information independent on the pulse heights and produce logic pulses on the output. The start input of TAC is directly connected to one CFD while logic signal of the second CFD is passed through ~250 ns delay and led to the stop input of TAC.

TAC produces output signal with amplitude directly proportional to the time difference between the start and stop signals on its inputs. The signal from TAC is lead into the built-in SCA which serves for precise setting of the coincidence condition. SCA emits logical pulse only if the signal from TAC falls into predetermined time-window. SCA is connected to the gate inputs of ADCs which regulate which signals are digitized and sent to the computer. Only those events where a logical pulse is present at the gate input are recorded.

CDB spectrometer measures the energies E_1 and E_2 of both annihilation photons. Two-dimensional (2D) CDB spectrum can be constructed by plotting the sum of these energies versus their difference. As an example, 2D CDB spectrum of a well-annealed magnesium is shown in figure 4.5.

The energies E_1 and E_2 of the annihilation photons can be expressed as

$$\begin{aligned} E_1 &= m_e c^2 - \frac{E_B}{2} + \Delta E \\ E_2 &= m_e c^2 - \frac{E_B}{2} - \Delta E, \end{aligned} \tag{4.7}$$

where m_e is electron rest mass, c is speed of light, E_B is the binding energy of annihilated electron and ΔE is the Doppler shift from equation (2.26).

The sum of energies E_1 and E_2 is constant

$$E_1 + E_2 - 2m_e c^2 = -E_B. \tag{4.8}$$

Hence, in the ideal case, this sum should produce the delta function at the energy $-E_B$. However, finite resolution of the spectrometer leads to smearing of the delta function and the resolution function of the spectrometer can be observed in a real spectrum.

The subtraction of E_2 from E_1 allows us to extract the Doppler shift ΔE and cancel other terms in equation (4.7)

$$E_1 - E_2 = 2\Delta E. \tag{4.9}$$

It has to be noted, that only longitudinal component of the momentum in the direction of emitted photons contributes to the measured Doppler shift.

Therefore, the cut of 2D CDB spectrum along the line $E_1 + E_2 - 2m_e c^2 = 0$ gives us Doppler broadened profile of the annihilation peak while resolution function of the spectrometer can be determined from the cut along the line $E_1 - E_2 = 0$. Both cuts generated from the 2D CDB spectrum in figure 4.5 are shown in figure 4.6.

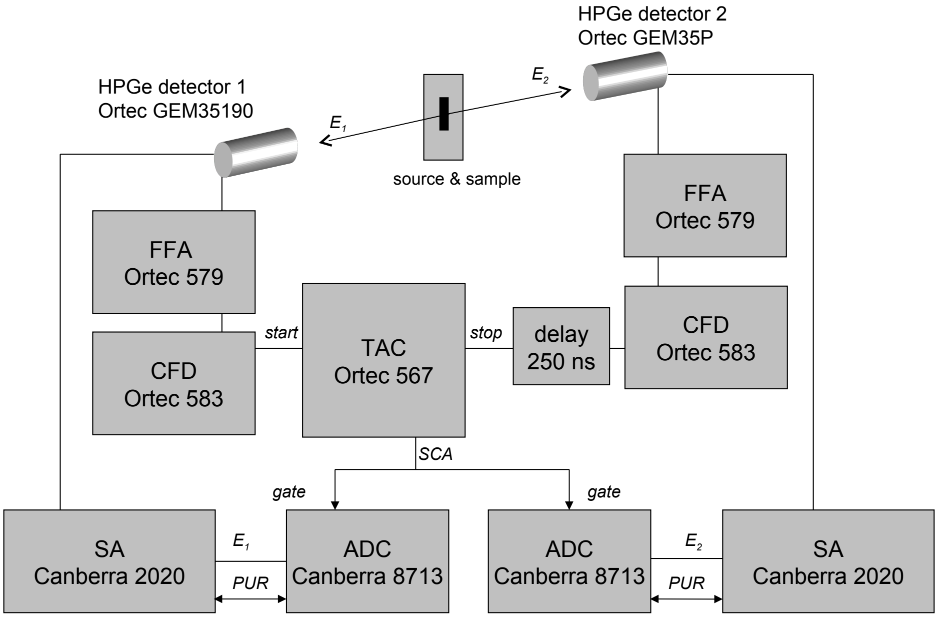

Figure 4.4: A scheme of CDB spectrometer.

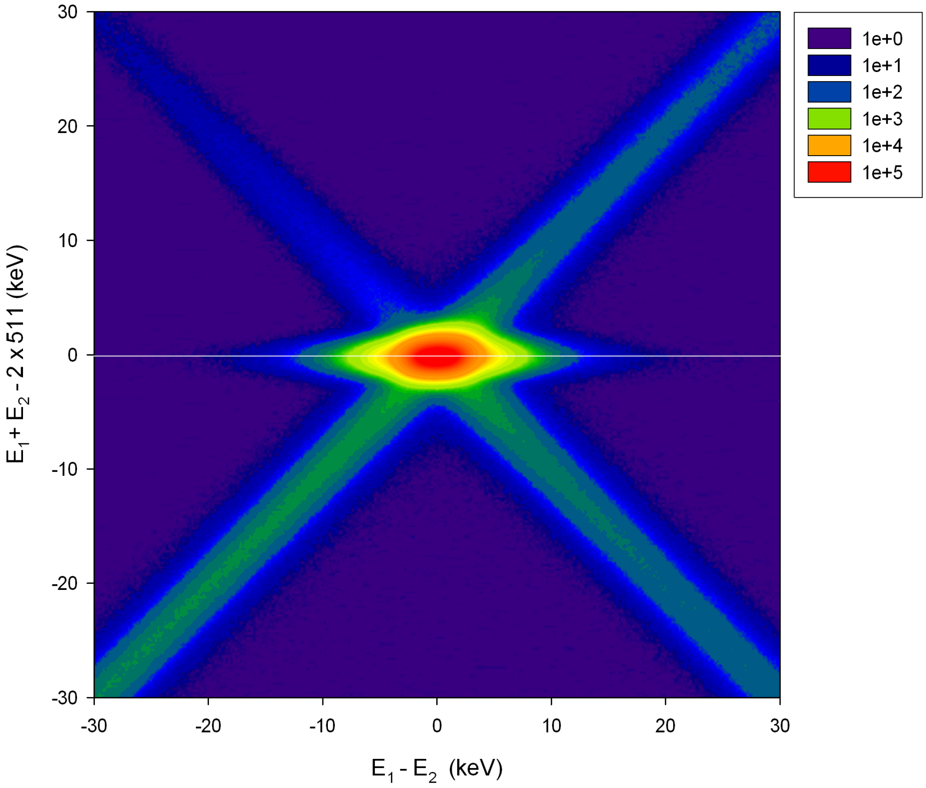

Figure 4.5: 2D CDB spectrum of a well annealed magnesium, the total statistics in the spectrum is 91 millions events.

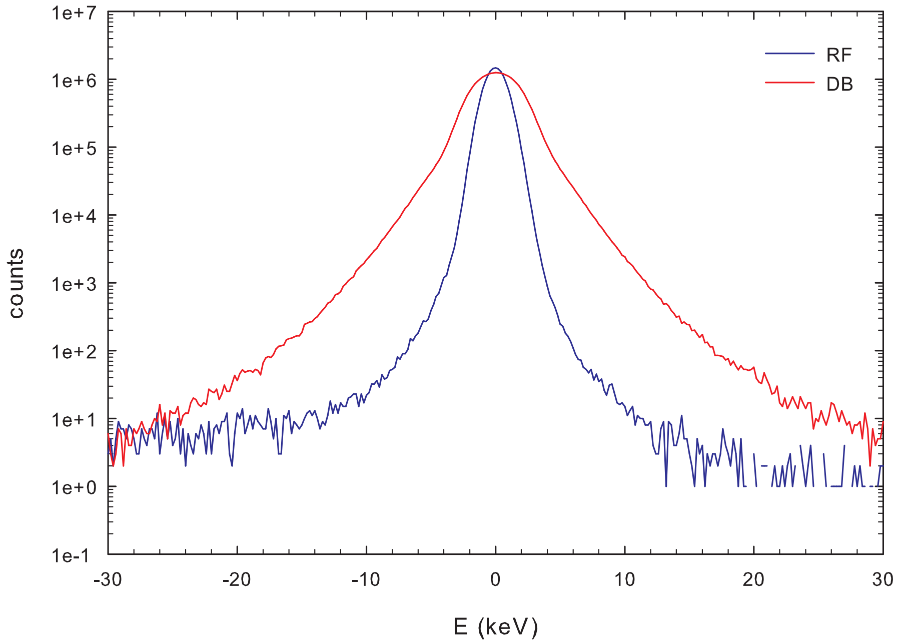

Figure 4.6: Cuts of 2D CDB spectrum of a well annealed magnesium: RF - resolution function, DB - Doppler broadened annihilation profile

5. Results

5.1 As cast alloys

5.1.1 Samples

Ingots of WE43 (Mg-Y-Nd-Zr based alloy), WE43 alloy modified by addition of 11 wt.% (WE43+11Zn), 14 wt.% (WE43+14Zn) and 26 wt.% (WE43+26Zn) of Zn and three ternary Mg-Zn-Y alloys (Mg3Y6Zn, Mg4Y23Zn and Mg4Y26Zn) were prepared by squeeze casting. Composition of studied alloys determined by chemical analysis is shown in in table 5.1 in wt.% and in table 5.2 in at.%.

	Zn	Y	Nd	Zr	Gd	Mg
WE43	-	2.95	2.48	0.30	0.15	balance
WE43+11Zn	10.90	1.80	0.73	0.28	0.12	balance
WE43+14Zn	13.80	3.06	1.04	0.29	0.10	balance
WE43+26Zn	25.82	3.02	1.16	0.27	0.17	balance
Mg3Y6Zn	5.81	3.19	-	-	-	balance
Mg4Y23Zn	23.1	3.59	-	-	-	balance
Mg4Y26Zn	26.0	3.87	-	-	-	balance

Table 5.1: Chemical composition of studied alloys in wt.%.

	Zn	Y	Nd	Zr	Gd	Mg
WE43	-	0.84	0.44	0.08	0.02	balance
WE43+11Zn	4.46	0.54	0.14	0.08	0.02	balance
WE43+14Zn	5.83	0.95	0.20	0.09	0.02	balance
WE43+26Zn	11.95	1.03	0.24	0.09	0.03	balance
Mg3Y6Zn	2.30	0.93	-	-	-	balance
Mg4Y23Zn	10.4	1.18	-	-	-	balance
Mg4Y26Zn	12.0	1.31	-	-	-	balance

Table 5.2: Chemical composition of studied alloys in at.%.

5.1.2 Mechanical properties and phase composition

Microstructure of studied samples was examined by SEM. Obtained images are shown in figures 5.2 to 5.11. Phases enriched by Zn and Y are preferentially formed at grain boundaries in all studied alloys alloys. SEM images were used to determine volume fraction of the grain boundary phase (GBP) in each alloy, results are shown in table 5.3.

As-cast WE43 alloy exhibits the lowest volume fraction of GBP and has diffuse areas with higher concentration of alloying elements along grain boundaries. Lamellar GBP, which can be clearly seen in figure 5.5, is formed in WE43+14Zn and WE43+26Zn alloys. The Mg3Y6Zn alloy has the second lowest volume fraction of GBP out of studied alloys. The GBP has lamellar structure and in addition, small rod-shaped particles are dispersed in the Mg matrix, see figure 5.7.

The GBP of Mg4Y23Zn and Mg4Y26Zn alloys is composed of two distinct phases: bright phase with lamellar structure and solid gray phase. According to results presented in table 5.3, the volume fraction of GBP significantly increases by the addition of Zn.

The mechanical properties of the studied samples were characterized by Vickers hardness test. The measured values are shown in table 5.4. Alloys with higher volume fraction of GBP exhibit also higher hardness. Hence, the studied alloys are hardened by GBP. Indentations of HV0.1 test, with a load of 0.1 kgf, are large enough to cover matrix and GBP at the same time. On the other hand, when the load is decreased to 25 gf corresponding to HV0.025 test, it is possible to measure the hardness of matrix and GBP practically separately.

Optical micrographs of the indentations shown in figure 5.1 demonstrate the smaller indentation size of the HV0.025 test (figure 5.1B) when compared to the HV0.1 test (figure 5.1A). Hence, HV0.025 measurements revealed that GBP is substantially harder than the Mg matrix, see table 5.5.

	vol. frac. of GBP (%)
WE43	1.8 ± 0.1
WE43+14Zn	9.8 ± 0.7
WE43+26Zn	25.1 ± 0.8
Mg3Y6Zn	4.5 ± 0.3
Mg4Y23Zn	25.7 ± 1.6
Mg4Y26Zn	38.9 ± 0.6

Table 5.3: The volume fraction of GBP in the studied alloys

	HV0.1
WE43	87 ± 2
WE43+14Zn	94 ± 2
WE43+26Zn	125 ± 4
Mg3Y6Zn	67 ± 1
Mg4Y23Zn	99 ± 1
Mg4Y26Zn	142 ± 4

Table 5.4: The hardness of studied alloys in the as-cast state

	WE43	WE43+14Zn	WE43+26Zn
HV0.025 - Matrix	-	101 ± 5	120 ± 2
HV0.025 - GBP	-	157 ± 6	195 ± 10

Table 5.5: Comparison of hardness of the matrix and GBP

Laboratory XRD measurement was used to determine the phase composition of WE43-based alloys. Obtained diffractograms are shown in figures 5.12 and 5.13. Following phases except the Mg matrix were identified: tetragonal phase $Mg_{41}Nd_5$; face-centered cubic (FCC) Mg_7Zn_3 phase; FCC $Mg_3Zn_3Y_2$ W-phase; FCC $Mg_5Nd_{0.4}Y_{0.6}$ β_1-phase and icosahedral phase $Mg_3Zn_6Y_1$. The icosahedral phase is present in WE43+14Zn and WE43+26Zn alloys but not in the plain WE43 alloy without addition of Zn.

The peak positions in the diffractograms were determined by fitting by pseudo-Voigt functions. The lattice parameters of the phases calculated from fitted positions of peaks are shown in table 5.6. Since the icosahedral phase $Mg_3Zn_6Y_1$ cannot be simply characterized by a lattice parameter, only interplanar distances were calculated. Comparison of the obtained results with the interplanar distances measured by selected-area electron diffraction (SAED) [49] is shown in table 5.7. The values of the interplanar distances obtained by XRD and SAED are in good agreement.

The phase composition of ternary Mg-Zn-Y alloys was examined by synchrotron X-ray diffraction. The details are discussed in section 5.2.3. It was found that in addition to the Mg matrix the Mg3Y6Zn alloy contains only the FCC W-phase ($Mg_3Zn_3Y_2$) phase while the Mg4Y23Zn and Mg4Y26Zn alloys contain the icosahedral phase $Mg_3Zn_6Y_1$ as well as the FCC Mg_7Zn_3 phase. The phase composition of studied alloys is in good agreement with the expectations based on their Zn/Y ratios, see section 3.2.

	WE43	WE43+14Zn	WE43+26Zn
Zn/Y ratio	0	4.5	8.5
Mg_7Zn_3 - fcc	-	-	a = 14.107(9) Å
$Mg_3Zn_3Y_2$ - fcc	-	a = 6.854(5) Å	-
$Mg_5Nd_{0.4}Y_{0.6}$ - fcc	a = 7.487(5) Å	-	-
$Mg_{41}Nd_5$ - tetragonal	a = 14.87(3) Å	-	-
	c = 10.14(2) Å	-	-

Table 5.6: The lattice parameters of the identified phases and the Zn/Y ratios of WE43-based alloys.

	WE43+14Zn XRD (Å)	WE43+14Zn SAED (Å)	WE43+26Zn XRD (Å)	WE43+26Zn SAED (Å)
i1a	6.495(8)	-	6.49(2)	-
i1b	6.14(2)	6.18(9)	6.063(9)	6.1(2)
??	-	3.82(3)	-	3.74(7)
i2a	3.389(2)		3.384(2)	-
i2b	3.272(5)	3.30(8)	3.277(5)	3.20(6)
i3a	2.34848(3)	2.36(2)	2.3556(4)	-
i3b	-	-	2.34160(5)	2.32(2)
i4	2.2780(3)	-	2.2899(4)	-
i5	2.1503(8)	-	2.1501(4)	-
i6a	2.06911(3)	2.03(2)	2.0769(3)	-
i6b	-	-	2.0640(5)	-
i7a	1.9986(3)	1.91(3)	2.01(5)	-
i7b	-	-	1.9863(7)	1.96(3)
i8a	1.7956(3)	-	1.8134(7)	-
i8b	1.7735(7)	-	1.7740(8)	-
i9a	1.45115(4)	1.48(1)	1.45045(8)	-
i9b	-	-	1.4457(7)	1.43(1)
i10	-	-	1.415(1)	-
i11	1.2793(3)	1.26(1)	1.2762(3)	-
i12	1.10(1)	-	1.1028(1)	-
i13	0.9398(1)	-	0.94005(7)	-

Table 5.7: A comparison of the interplanar distances measured by XRD and SAED in the icosahedral phase $Mg_3Zn_6Y_1$ in WE43-based alloys.

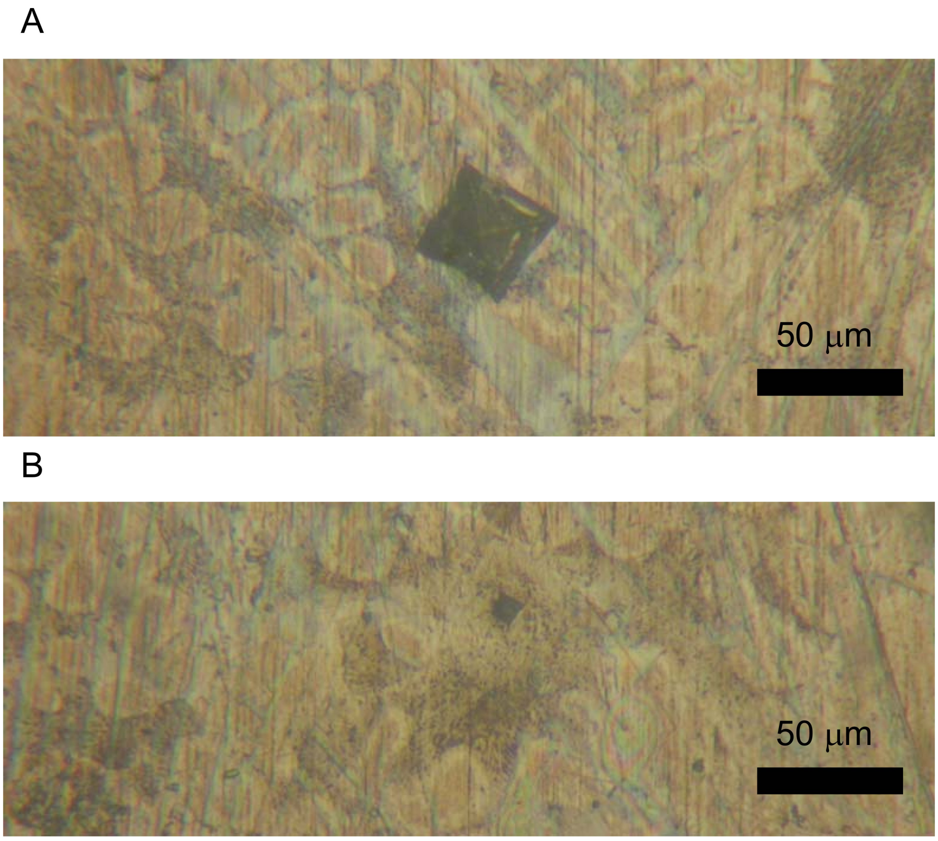

Figure 5.1: A comparison of the indentations after hardness test of WE43+26Zn alloy: A - matrix (HV0.1), B - GBP (HV0.025).

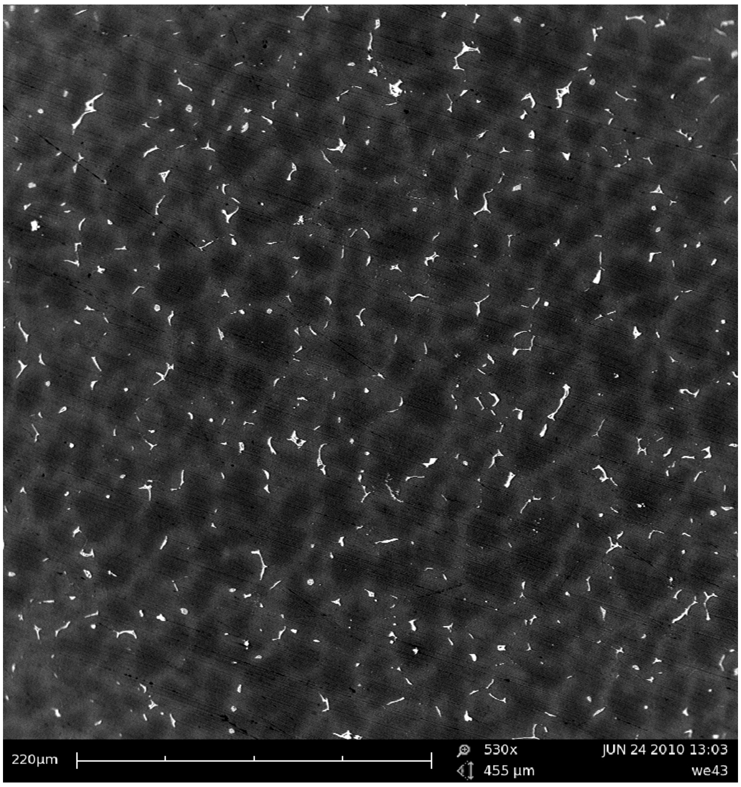

Figure 5.2: SEM image of as-cast WE43 alloy.

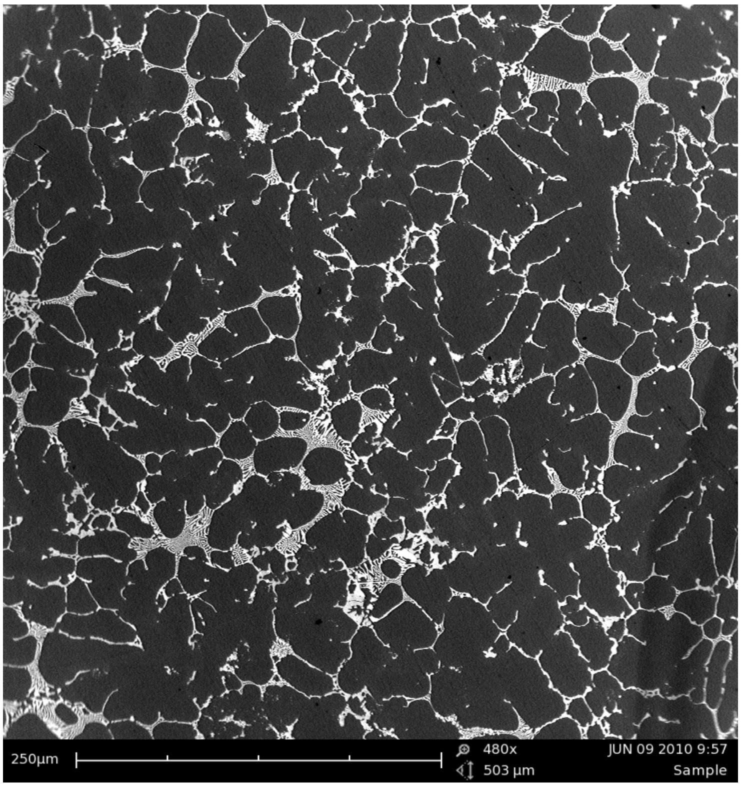

Figure 5.3: SEM image of as-cast WE43+14Zn alloy.

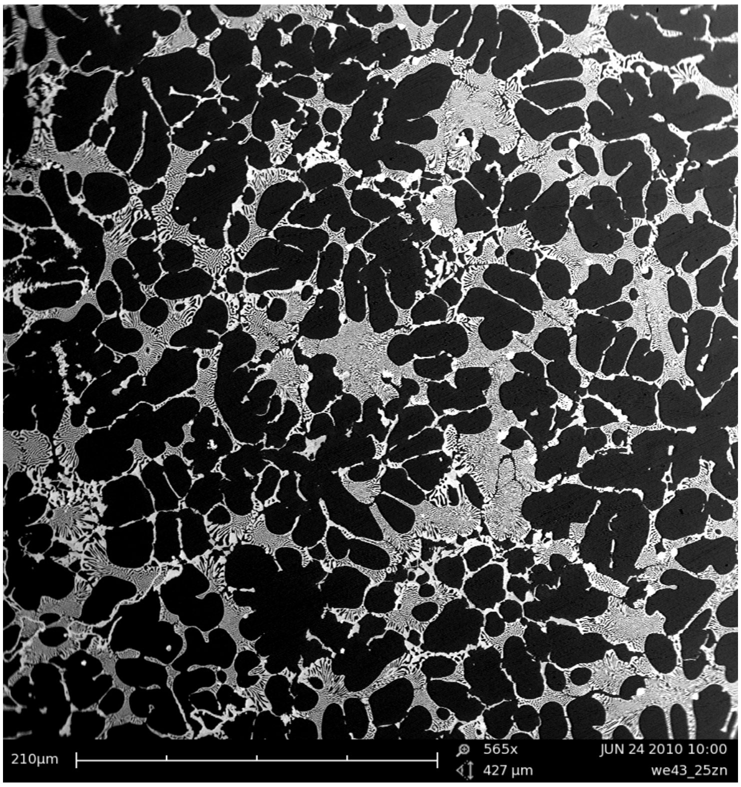

Figure 5.4: SEM image of as-cast WE43+26Zn alloy.

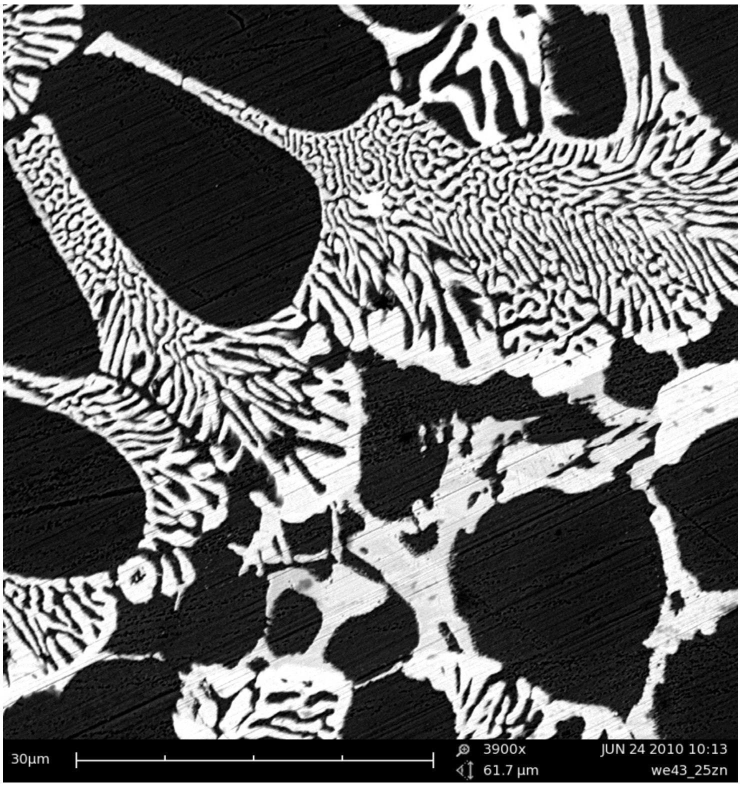

Figure 5.5: SEM image of as-cast WE43+26Zn alloy, detail of GBP.

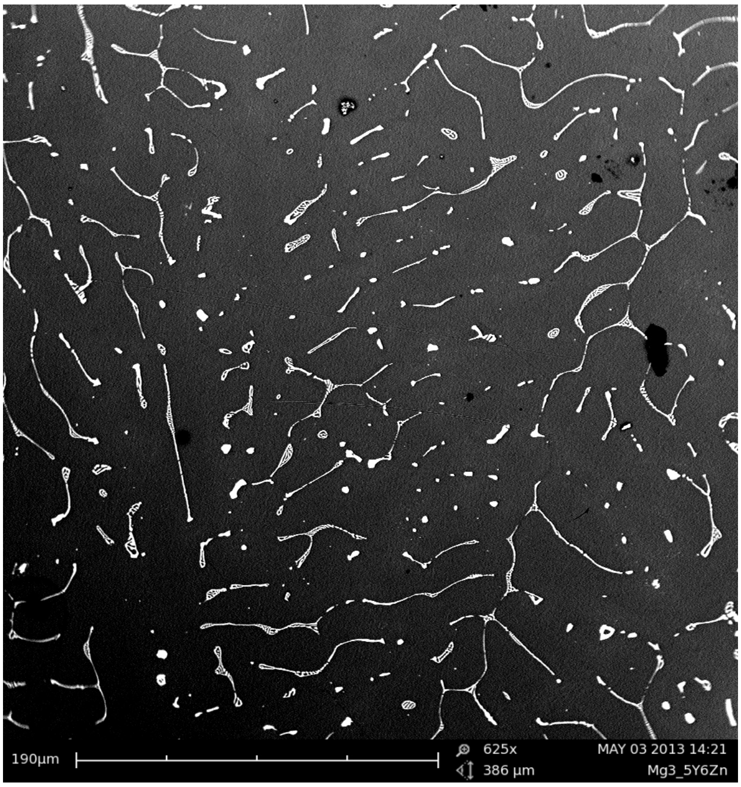

Figure 5.6: SEM image of as-cast Mg3Y6Zn alloy.

Figure 5.7: SEM image of as-cast Mg3Y6Zn alloy, detail.

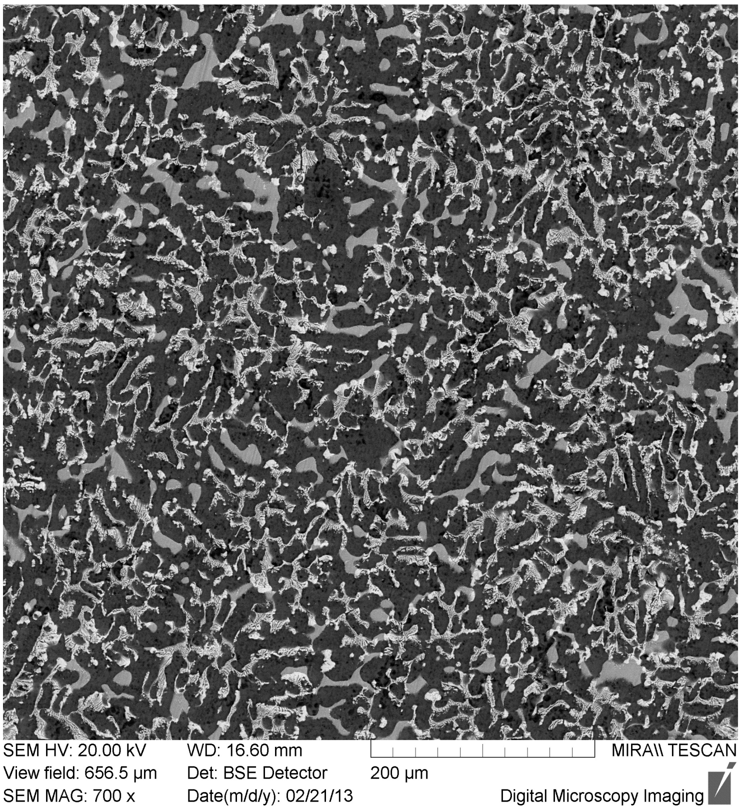

Figure 5.8: SEM image of as-cast Mg4Y23Zn alloy.

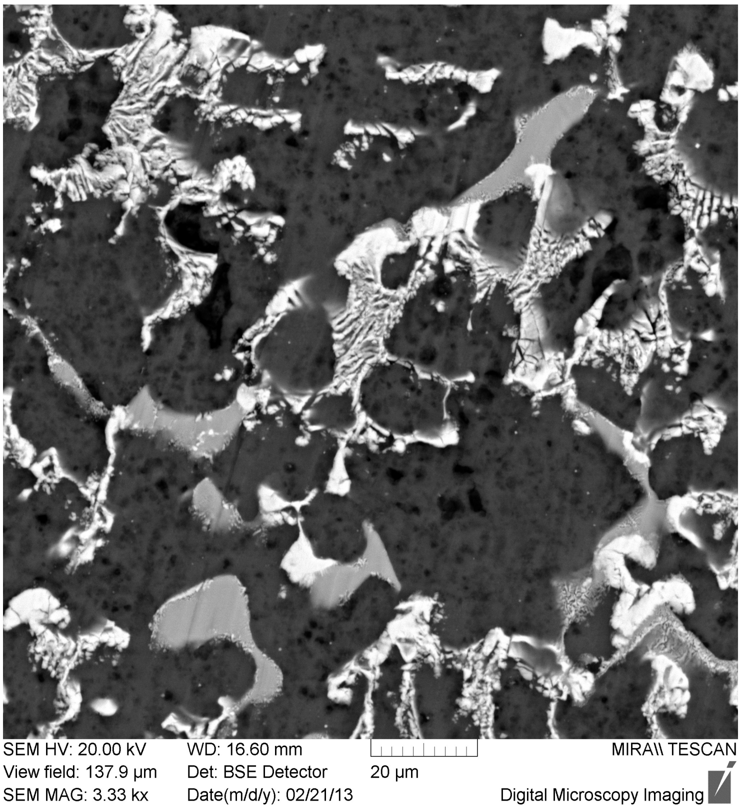

Figure 5.9: SEM image of as-cast Mg4Y23Zn alloy, detail.

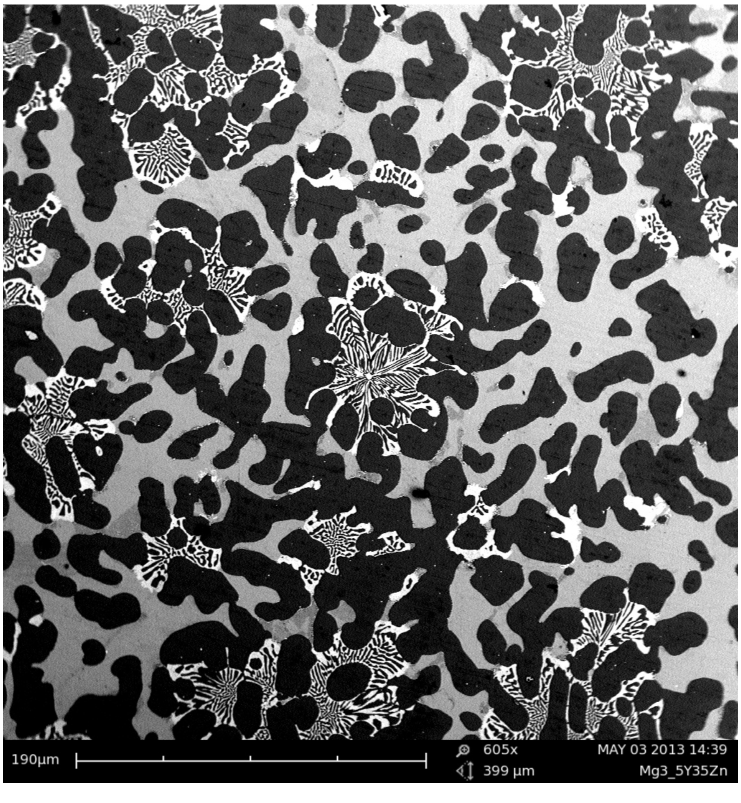

Figure 5.10: SEM image of as-cast Mg4Y26Zn alloy.

Figure 5.11: SEM image of as-cast Mg4Y26Zn alloy, detail.

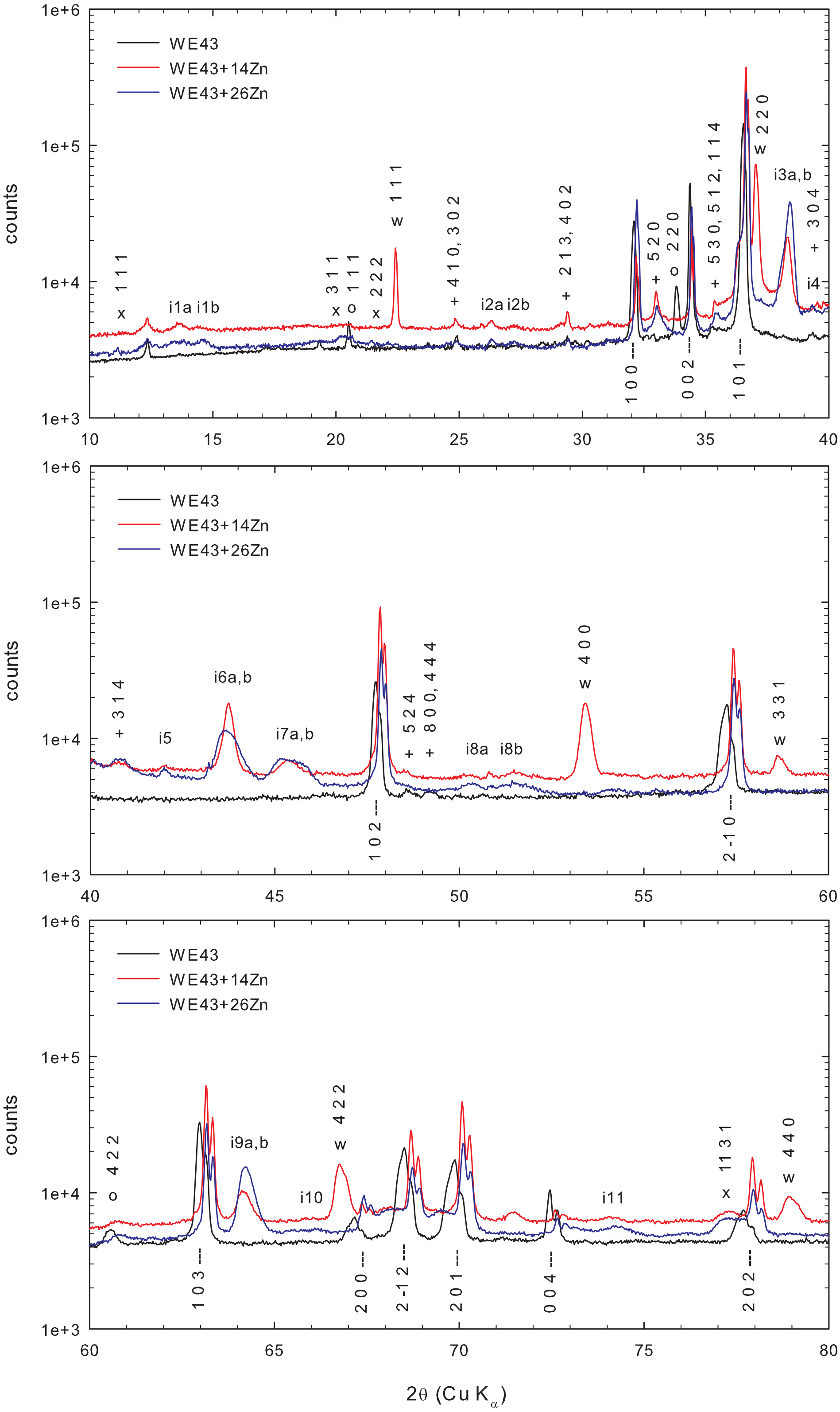

Figure 5.12: X-ray diffractograms of WE43-based alloys, $2\theta = 10 - 80°$. | - Mg matrix; + - $Mg_{41}Nd_5$ tetragonal phase; o - $Mg_5Nd_{0.4}Y_{0.6}$ fcc phase; x - Mg_7Zn_3 fcc phase; w - $Mg_3Zn_3Y_2$ fcc W-phase; i - $Mg_3Zn_6Y_1$ icosahedral phase.

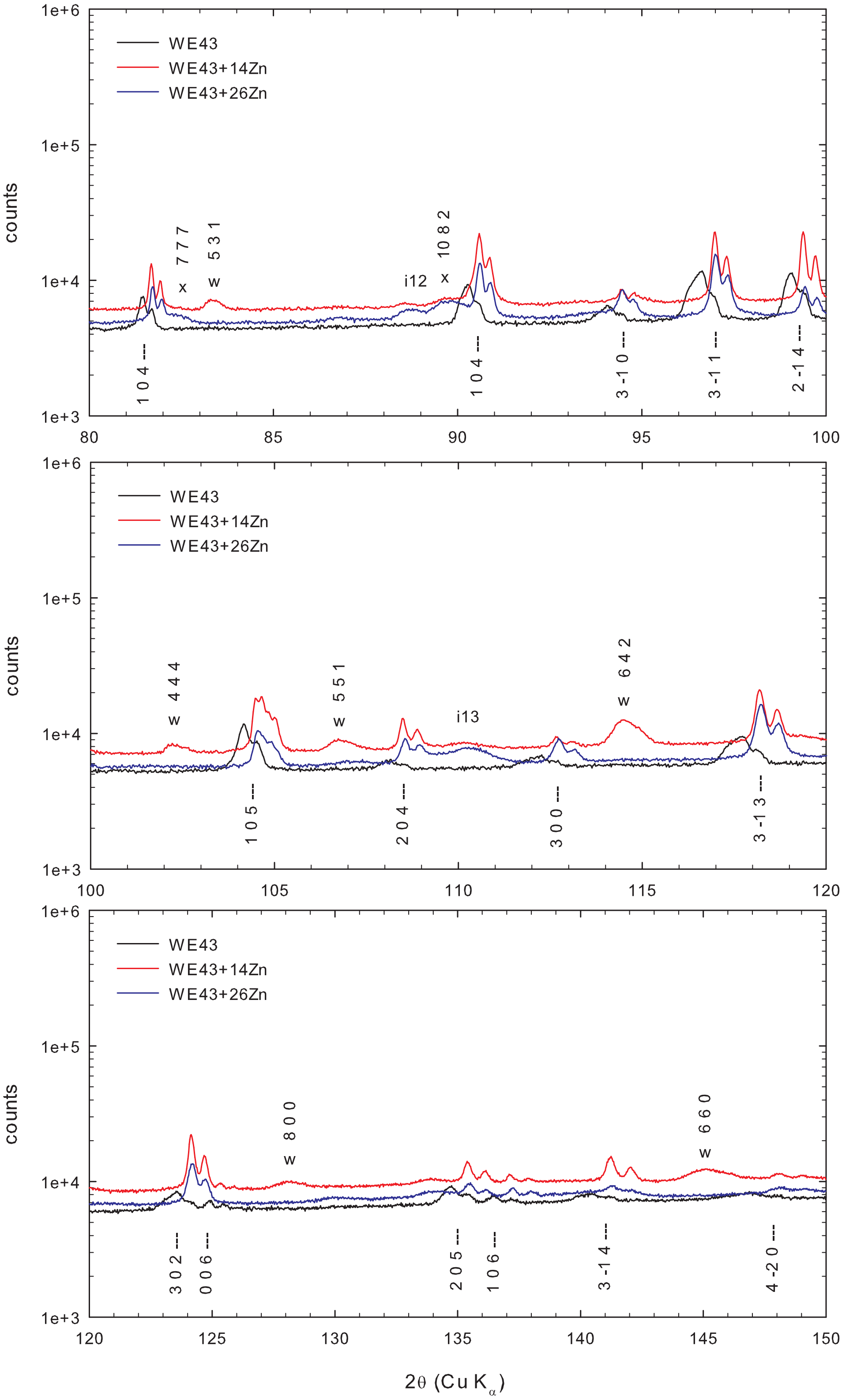

Figure 5.13: X-ray diffractograms of WE43-based alloys, 2θ = 80 - 150°. | - Mg matrix; + - $Mg_{41}Nd_5$ tetragonal phase; o - $Mg_5Nd_{0.4}Y_{0.6}$ fcc phase; x - Mg_7Zn_3 fcc phase; w - $Mg_3Zn_3Y_2$ fcc W-phase; i - $Mg_3Zn_6Y_1$ icosahedral phase.

5.1.3 Defect studies

Results of LT investigations performed on studied as-cast alloys are shown in table 5.8. Plain WE43 as well as Mg3Y6Zn alloy exhibit a single component LT spectrum with lifetime τ_1 which agrees well with the bulk positron lifetime of magnesium $\tau_B \sim 225$ ps [50]. Hence, the as-cast WE43 and Mg3Y6Zn alloys have lower concentration of defects than the detection threshold of positron lifetime spectroscopy.

On the other hand, WE43-based alloys with addition of zinc together with Mg4Y23Zn and Mg4Y26Zn alloys exhibit two component LT spectra. First component comes from annihilation of free positrons and its lifetime is shortened when compared to the bulk lifetime according to equation (2.23) by positron trapping. Lifetime of the second component $\tau_2 \sim 300$ ps corresponds to annihilation of positrons trapped at vacancy-like defects.

Since the defect component with lifetime $\tau_2 \sim 300$ ps is present only in alloys containing icosahedral phase it can be attributed to vacancy-like misfit defects associated with the quasicrystalline particles of icosahedral phase. It should be mentioned that the lifetimes of the positrons trapped at the open volume misfit defects at interfaces between semicoherent or incoherent crystalline precipitates and a-Mg matrix typically fall in the range 250–260 ps [50, 51].

However, the lifetime τ_2 corresponding to positrons trapped at vacancy-like defects associated with the interface between the I-phase and the α-Mg matrix is remarkably higher, which testifies to the specific structure of the low-energy interfaces between the quasicrystalline particles and the α-Mg matrix.

The existence of vacancy-like defects associated with the interface between the quasicrystalline phase and the α-Mg matrix is also supported by high-resolution transmission electron microscopy (HRTEM) observations [52], which revealed that, in order to retain the coherency between the I-phase and the α-Mg matrix, steps or ledges are introduced periodically along the interface. Vacancy-like defects are probably located at these steps along the interface

Applicability of STM for analysis of obtained results was checked by calculating the bulk lifetime τ_B according to the equation (2.25). Calculated values of τ_B match the bulk positron lifetime of magnesium ~ 225 ps. Therefore, the assumptions of STM are fulfilled here and it can be used to estimate the concentration of defects in the as-cast WE43-based alloys modified by addition of zinc.

The trapping rate K_D calculated according to equation (2.23) is proportional to density of defects in studied material, see equation (2.24). Knowledge of specific trapping rate ν_D is needed for calculation of actual concentration of defects. The value of ν_D for misfit defects is not known. However, the value of positron specific trapping rate of vacancies, which usually in metals falls into the range $\nu_D = 10^{14}$–10^{15} s^{-1} [53], can be used as its estimate. The value $\nu_D = 10^{14} s^{-1}$ at the lower limit of this range was used to estimate the concentration of misfit defects in Mg6Zn alloy. There are two reason to choose such value:

(i) the open volume of misfit defects is slightly lower than the open volume of a monovacancy in magnesium matrix. This is also testified by shorter lifetime of positron trapped at misfit defects. The reduced volume of the misfit defects decreases the cross section for positron trapping when compared to the monovacancy.

(ii) relatively low density of valence electrons in the interatomic regions leads to a lower positron binding energy to vacancy than in dense metals with higher electron density in the lattice. Hence, the specific positron trapping rate can be expected to be in the lower part of the range of specific trapping rates for vacancies in metals.

Resulting concentrations of misfit defects are presented in table 5.8.

	τ_1 (ps)	I_1 (%)	τ_2 (ps)	I_2 (%)	τ_B (ps)	c_D (10^{-6})
WE43	223.9(3)	100	-	-	-	-
WE43+11Zn	201(2)	67(3)	296(5)	33(3)	225(3)	5.3(3)
WE43+14Zn	187(2)	58(2)	302(3)	42(2)	223(3)	8.5(2)
WE43+26Zn	192(4)	56(3)	302(4)	44(3)	229(4)	8.9(3)
Mg3Y6Zn	225.1(2)	100	-	-	-	-
Mg4Y23Zn	217.5(6)	95.0(6)	300(5)	5.0(6)	220.5(7)	0.6(2)
Mg4Y26Zn	212.9(5)	91.7(5)	298(4)	8.3(5)	218.1(6)	1.0(5)

Table 5.8: Results of LT measurements of WE43-based and Mg-Zn-Y alloys.

CDB ratio curves of studied as-cast alloys are shown in figures 5.14 and 5.15. Since the contribution of valence electrons which form chemical bond is negligible in the high momentum region, the measured ratio curve ρ related to a well-annealed Mg can be expressed as a linear combination

$$\begin{aligned} \rho = (1-F_D)(\xi_{Mg,B} + \xi_{Zn,B}\rho_{Zn,B} + \xi_{Y,B}\rho_{Y,B} + \xi_{Nd,B}\rho_{Nd,B}) + \\ + F_D\ (\xi_{Mg,D}\rho_{Mg,D} + \xi_{Zn,D}\rho_{Zn,D} + \xi_{Y,D}\rho_{Y,D} + \xi_{Nd,D}\rho_{Nd,D} + \\ + \ \xi_{Zr,D}\rho_{Zr,D} + \xi_{Gd,D}\rho_{Gd,D}). \end{aligned} \tag{5.1}$$

The symbol F_D denotes the fraction of positrons trapped at the defects. The symbol $\rho_{X,Y}$ represents the ratio curve (with respect to a well annealed Mg) of element X and Y stands for annihilation of free positrons (B) or for annihilation of positrons trapped at defects (D). The coefficient $\xi_{X,Y}$ represents the weight for corresponding ratio curve. These coefficients fulfill the normalization conditions

$$\begin{aligned} \xi_{Mg,B} + \xi_{Zn,B} + \xi_{Y,B} + \xi_{Nd,B} = 1 \\ \xi_{Mg,D} + \xi_{Zn,D} + \xi_{Y,D} + \xi_{Nd,D} + \xi_{Zr,D} + \xi_{Gd,D} = 1. \end{aligned} \tag{5.2}$$

Since the Zr and Gd content of WE43-based alloys is very low, the contribution of Zr and Gd electrons to annihilation of free positrons will be negligible. Hence, the ratio curves $\rho_{Zr,B}$ and $\rho_{Gd,B}$ were omitted from the equation (5.1) ro reduce the number of free parameters.

The reference ratio curves of Mg, Zn, Y and Nd are shown in figures 5.16, 5.17, 5.18 and 5.19, respectively. Measurements of well-annealed and cold-rolled Mg, Zn, Y and Nd samples were used to obtain reference ratio curves for each element. The reference ratio curves determined from measurements of cold-rolled Zr and Gd samples are plotted in figure 5.20. While the ratio curves $\rho_{Mg,B}$, $\rho_{Zn,B}$, $\rho_{Y,B}$ and $\rho_{Nd,B}$ can be measured directly on the well-annealed samples, the ratio curves $\rho_{Mg,D}$, $\rho_{Zn,D}$, $\rho_{Y,D}$, $\rho_{Nd,D}$, $\rho_{Zr,D}$ and $\rho_{Gd,D}$ need to be extracted from a measurement of cold-rolled samples.

The ratio curve for annihilation of free positrons in Mg $\rho_{Mg,B}$ related to well annealed magnesium is $\rho_{Mg,B} = 1$. Therefore, the ratio curve of cold-rolled magnesium related to well annealed magnesium can be expressed as

$$\rho = (1 - F_D) + F_D \rho_{Mg,D}. \tag{5.3}$$

where F_D is the fraction of positrons annihilated at defects which was determined by LT measurement of the cold-rolled Mg sample. The ratio curve ρ of cold-rolled Zn related to well-annealed Mg can be written as

$$\rho = (1 - F_D)\rho_{Zn,B} + F_D \rho_{Zn,D}. \tag{5.4}$$

where F_D is the fraction of positrons annihilated at defects which was determined by LT measurement of the cold-rolled Zn sample. The reference ratio curves $\rho_{Y,D}$, $\rho_{Nd,D}$, $\rho_{Zr,D}$ and $\rho_{Gd,D}$ can be determined from the ratio curve of cold rolled Y, Nd, Zr and Gd analogically.

Measured CDB ratio curves of studied alloys were fitted by a model expressed by equation (5.1). The fitted fractions of positrons trapped at defects F_D and coefficients ξ obtained from fitting are shown in table 5.9. As an example, fitted ratio curve of WE43+14Zn alloy, including all components of the fit, is shown in figure 5.21. Plain WE43 alloy does not contain any zinc. Therefore, the coefficients $\xi_{Zn,B}$ and $\xi_{Zn,D}$ were fixed at zero value in the fit of the ratio curves of WE43 alloy.

In the WE43 alloys modified by addition of zinc, certain amount of zinc is dissolved in the Mg matrix. Presence of Zn in solid-solution is testified by a shift of Mg reflections in X-ray diffractograms shown in figures 5.12 and 5.13. The shift with respect to the plain WE43 alloy is the same for WE43+14Zn and WE43+26Zn alloys. It suggests that the saturated solid solution of Zn in Mg matrix was formed. Hence, the parameter $\xi_{Zn,B}$ was fixed at the value of 2.3% which corresponds to the maximum solubility of Zn in Mg, i.e. 2.3 at.%, to reduce the number of free fitting parameters.

A sharp peak in the ratio curves located at 8×10^{-3} m_0c corresponds to the annihilation of positrons by electrons of Y and Nd, cf. figures 5.18 and 5.19. On the other hand, a broad peak centered at 18×10^{-3} m_0c represents the annihilation of positrons by 3d electrons of Zn, cf. figure 5.17.

The fraction of positrons annihilated by Nd and Gd in the plain WE43 alloy obtained from fitting is significantly higher than the average concentration of Nd and Gd in the WE43 sample. Hence, certain fraction of positrons must annihilate from localized state at Nd and Gd-rich particles. Most likely candidates are finely dispersed precipitates of $Mg_{41}Nd_5$ phase which were identified in WE43 alloy by XRD, see table 5.6. Since no Gd-rich phases were detected by XRD the plain WE43 alloy, a substantial fraction of Nd atoms in the $Mg_{41}Nd_5$ phase has to be substituted by Gd in these precipitates.

However, the LT spectrum of WE43 alloy contains only single component with lifetime $\sim$ 225 ps. Therefore, there are most likely no open-volume defects related to $Mg_{41}Nd_5$ but positron localization occurs inside $Mg_{41}Nd_5$ precipitates beause they have higher absolute value of positron affinity than Mg matrix. Since the measured lifetime is very close to the bulk lifetime of defect-free Mg of $\sim$ 225 ps, the lifetime of positrons trapped at $Mg_{41}Nd_5$ particles is likely close to the lifetime of defect-free Mg. Hence, the positron trapping in WE43 alloy can be only detected by CDB measurements which revealed enhanced contribution of positron annihilations with Nd electrons.

According to the results of the fit presented in table 5.9, WE43-based alloys modified by addition of Zn show notably enhanced concentration of Zn and Y in the vicinity of defects. This further supports the hypothesis that vacancy-like defects are associated with Zn and Y-rich icosahedral phase $\mathrm{Mg_3Zn_6Y_1}$.

CDB ratio curves of ternary Mg-Zn-Y alloys have similar shape as ratio curves of WE43-based alloys modified by addition of Zn. The intensity of broad peak centered around 18×10^{-3} $\mathrm{m_0c}$ which represents the annihilations by 3d electrons of Zn increases with increasing Zn content in ternary alloys. This is expected as the volume fraction of Zn-rich eutectic significantly increases with increasing Zn content of Mg-Zn-Y alloys, see table 5.3.

Narrow peak located at 8×10^{-3} $\mathrm{m_0c}$ is most pronounced in Mg4Y23Zn alloy, which out of studied ternary alloys has the ratio of Zn/Y content closest to the optimum for creation of icosahedral phase (5-7 in wt.%) [31]. However, the contribution of annihilations with electrons of Y is also enhanced in Mg3Y6Zn alloy. This suggest, that the positron trapping occurs also in the particles of W-phase due to its higher positron affinity in absolute value when compared to the Mg matrix. Since, the Mg3Y6Zn alloy exhibits single component LT spectrum with lifetime which agrees well with the bulk lifetime of Mg, open-volume misfit defects are not created at the interface of W-phase $\mathrm{Mg_3Zn_3Y_2}$ with Mg matrix.

	$\xi_{Zn,B}$	$\xi_{Y,B}$	$\xi_{Nd,B}$	$\xi_{Zn,D}$	$\xi_{Y,D}$	$\xi_{Nd,D}$	$\xi_{Zr,D}$	$\xi_{Gd,D}$	F_D
WE43	-	0.8(5)	0.4(1)	-	0(2)	30(2)	10(2)	60(2)	14(1)
WE43+14Zn	2.3 Fix	1.0(5)	0.2(1)	19(3)	30(3)	-	-	-	16(1)
WE43+26Zn	2.3 Fix	1.0(5)	0.2(1)	54(4)	46(4)	-	-	-	16(1)

Table 5.9: Results of CDB measurements of WE43-based alloys. Values are shown in %. Adapted from appendix A.

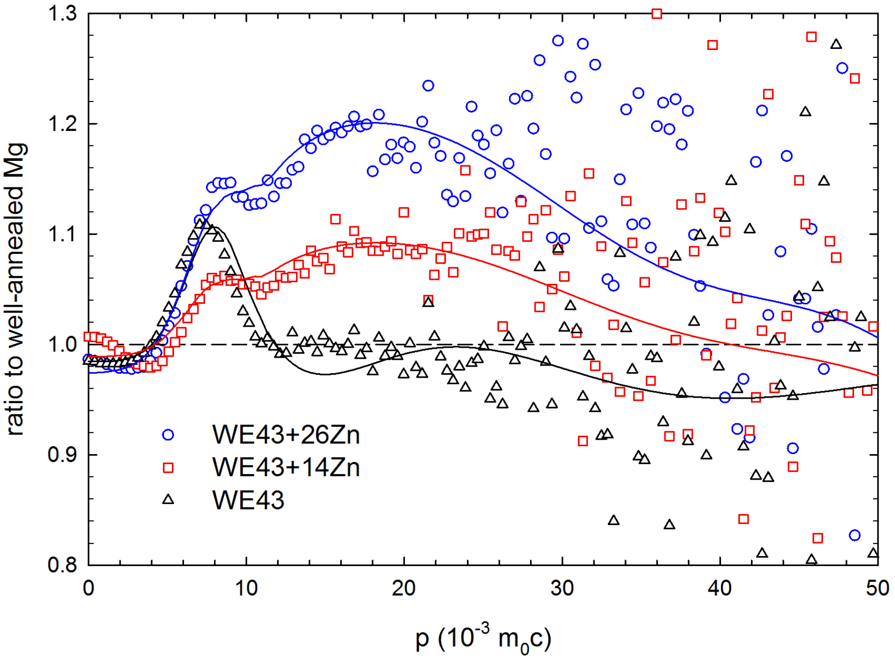

Figure 5.14: CDB ratio curves (related to well-annealed Mg) of WE43-based alloys. Open circles - measured data; lines - fit. Adapted from appendix A.

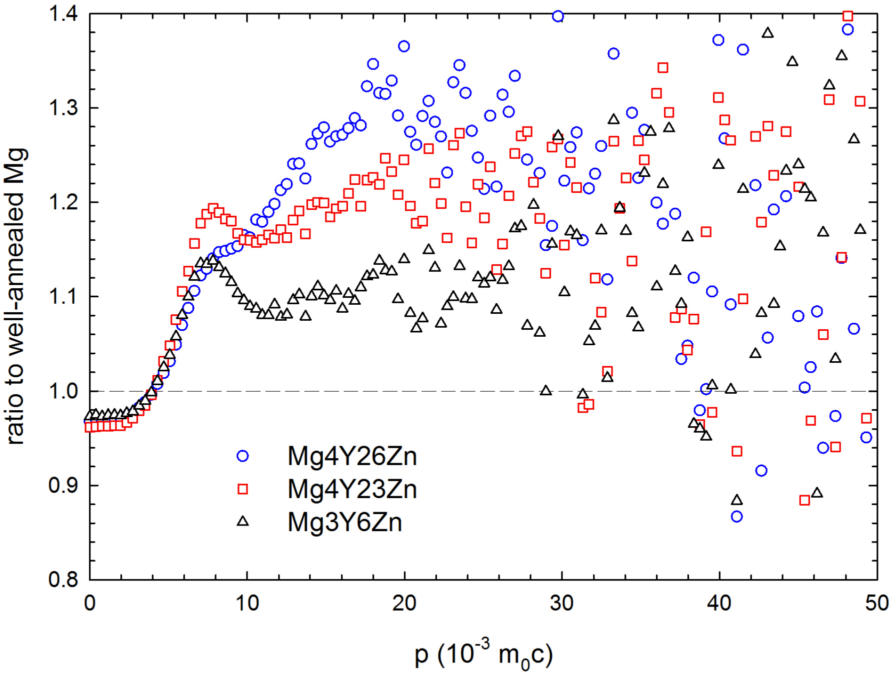

Figure 5.15: CDB ratio curves (related to well-annealed Mg) of Mg-Zn-Y alloys.

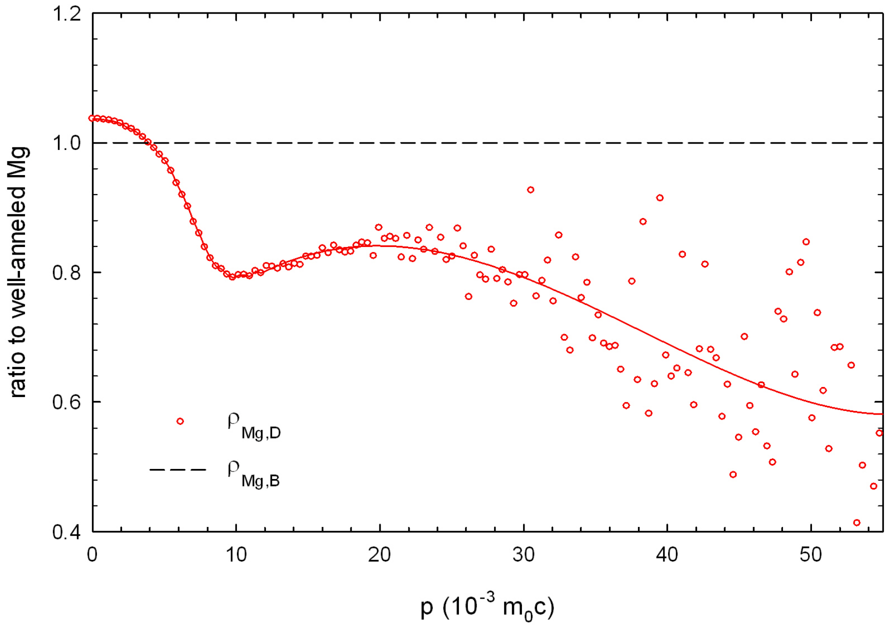

Figure 5.16: Reference ratio curves (related to well-annealed Mg) for ratio curves of free positrons annihilated by Mg electrons $\rho_{Mg,B}$ and positrons trapped at defects and annihilated by Mg electrons $\rho_{Mg,D}$.

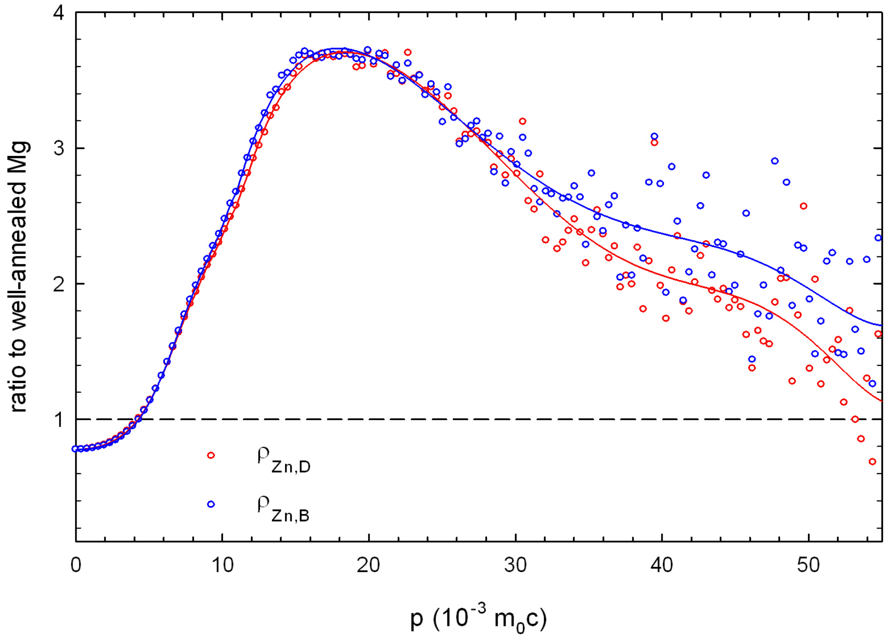

Figure 5.17: Reference ratio curves (related to well-annealed Mg) for ratio curves of free positrons annihilated by Zn electrons $\rho_{Zn,B}$ and positrons trapped at defects and annihilated by Zn electrons $\rho_{Zn,D}$.

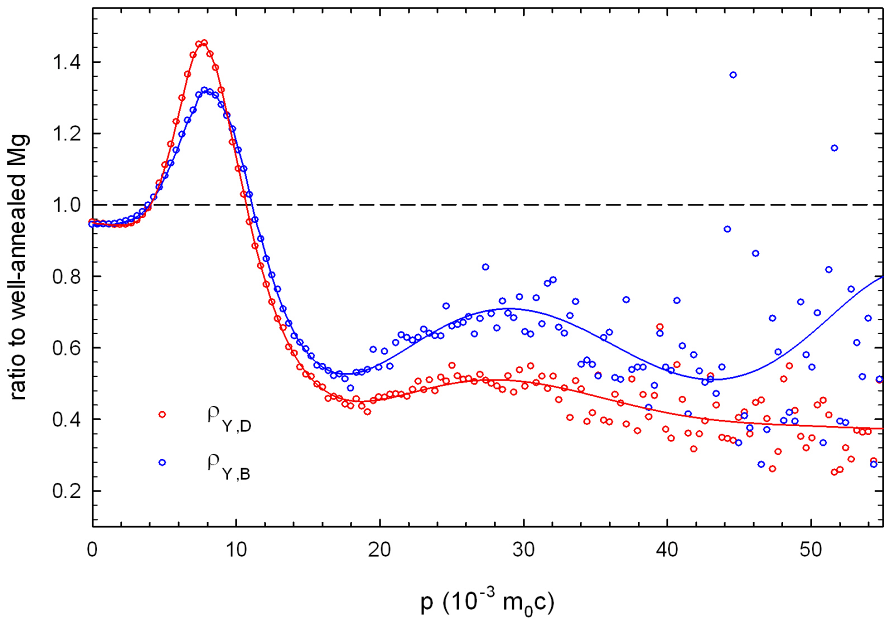

Figure 5.18: Reference ratio curves (related to well-annealed Mg) for ratio curves of free positrons annihilated by Y electrons $\rho_{Y,B}$ and positrons trapped at defects and annihilated by Y electrons $\rho_{Y,D}$.

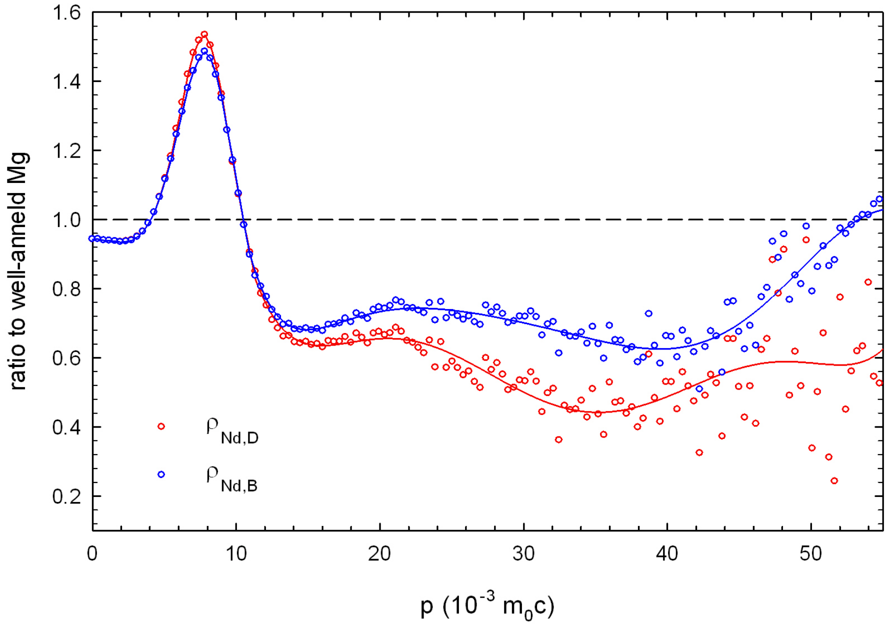

Figure 5.19: Reference ratio curves (related to well-annealed Mg) for ratio curves of free positrons annihilated by Nd electrons $\rho_{Nd,B}$ and positrons trapped at defects and annihilated by Nd electrons $\rho_{Nd,D}$.

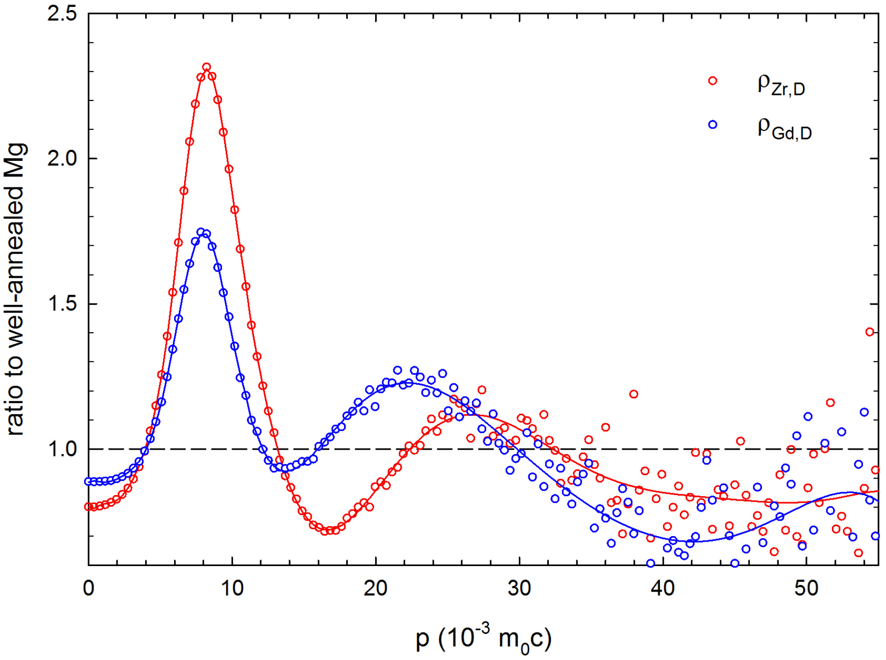

Figure 5.20: Reference ratio curves (related to well-annealed Mg) for ratio curves of positrons trapped at defects and annihilated by Zr electrons $\rho_{Zr,D}$ and by Gd electrons $\rho_{Gd,D}$.

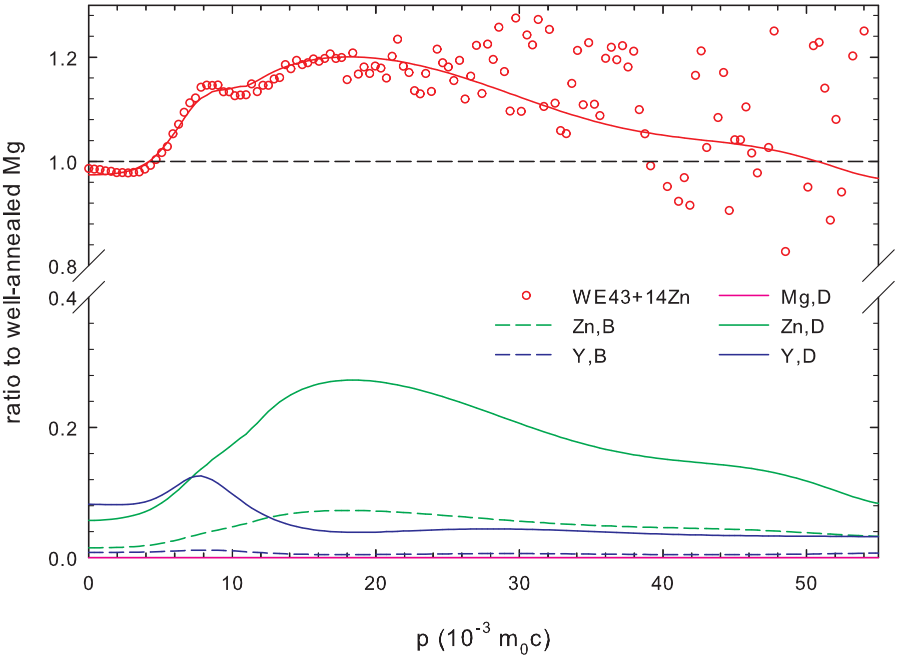

Figure 5.21: Fitted CDB ratio curve (related to well-annealed Mg) of WE43+14Zn alloy. Open circles - measured data; lines - components of the fit.

5.2 Heat treated alloys

5.2.1 Microstructure and mechanical properties

The effect of different cooling rates was investigated on isothermally annealed WE43+11Zn and Mg4Y26Zn alloys. Two samples of each alloys were annealed at 500°C for 1 hour, one was quenched into water of room temperature (Q) while the second one was slowly cooled down within the furnace (SC). SEM images of the annealed samples are shown in figures 5.22 to 5.29.

The grain boundary phase (GBP) melts during isothermal annealing at 500°C. Samples at this temperature are in a semi-solid state where solid grains of Mg matrix are surrounded by liquid melt with high Zn and Y content. The cooling rate has a crucial role in the development of the microstructure of the annealed samples. A high cooling rate during quenching results in GBP with finely spaced lamellas. On the other hand, a slow cooling generally produces GBP with much coarser structure.

5.2.1.1 WE43+11Zn alloy

The SEM images of WE43+11Zn alloys were analyzed to study the changes in the microstructure after isothermal annealing at 500°C. The mean grain size D, spacing of lamellas in GBP λ and the net fraction of GBPs f_{GBP} and the relative portion of icosahedral phase $f_{I-phase}$ in GBP were determined.

The results are shown in table 5.10. The grain size of the WE43+11Zn alloy increases from ~ 44 µm to approximately ~ 100 µm during the annealing. Although the grain size is practically the same in the quenched and slowly cooled samples, the morphology of GBP is markedly different. GBP in the quenched sample of WE43+11Zn alloy forms almost contiguous network along grain boundaries and has very fine lamellar structure, see figures 5.22 and 5.23.

On the other hand, thick lamellas develop during slow cooling of WE43+11Zn alloy. Furthermore, massive precipitation of secondary phases occurs inside the Mg matrix, see figure 5.25. As a result of isothermal annealing at 500°C, f_{GBP} slightly decreases in both quenched and slowly cooled samples. However, the fraction of icosahedral phase $Mg_3Zn_6Y_1$ substantially increases at the expense of W-phase $Mg_3Zn_3Y_2$.

State	D (µm)	λ (µm)	f_{GBP} (%)	$f_{I-phase}$ (%)
as-cast	44(5)	1-2	12.6(2)	33(5)
500°C/1 h Q	98(5)	0.2-0.4	8.5(5)	96(3)
500°C/1 h SC	102(5)	5-10	9.7(5)	81(4)

Table 5.10: Results of SEM measurements of WE43+11Zn samples annealed at 500°C: D - mean grain size, λ - spacing of lamellas in GBP, f_{GBP} - the net fraction of GBP, $f_{I-phase}$ - the relative fraction of icosahedral phase in GBP.

5.2.1.2 Mg4Y26Zn alloy

The Microstructure of Mg4Y26Zn alloy after isothermal annealing of at 500°C for 1 hour was examined by SEM. The quenched sample exhibits finely structured lamellar GBP with occasional bright particles, see figures 5.26 and 5.27. On the other hand, GBP in the slowly cooled sample of Mg4Y26Zn alloy is composed of thick bright lamellas and a compact gray phase, see 5.28. Closer examination reveals that the gray phase is not solid but has extremely fine lamellar structure and in some places there are coarser gray particles, see figure 5.29.

The chemical composition of phases present in the slowly cooled and quenched samples of Mg4Y26Zn alloy was examined by EDX. The results are shown in tables 5.11 and 5.12. The regions which were analyzed by EDX are marked by letters in figures 5.27 and 5.29. The measured EDX spectra are plotted in figures 5.30 to 5.37.

Region	State	Description	Zn (wt.%)	Y (wt.%)	Mg (wt.%)
A	500°C/1 h Q	Mg matrix	8.1	-	balance
B	500°C/1 h Q	Dense eutectic	47.1	-	balance
C	500°C/1 h Q	Coarse eutectic	44.8	5.6	balance
D	500°C/1 h Q	Flower-shaped particle	58.9	11.0	balance
E	500°C/1 h SC	Mg matrix	8.1	-	balance
F	500°C/1 h SC	Bright lamella	65.1	13.7	balance
G	500°C/1 h SC	Gray phase	50.1	-	balance
H	500°C/1 h SC	Gray particles	43.0	-	balance

Table 5.11: Results of EDX measurements of Mg4Y26Zn alloys annealed at 500°C. The concentrations are given in wt.%. The analyzed regions denoted by letters A–H are shown in figures 5.27 and 5.29.

Region	State	Description	Zn (at.%)	Y (at.%)	Mg (at.%)
A	500°C/1 h Q	Mg matrix	3.2	-	balance
B	500°C/1 h Q	Dense eutectic	24.9	-	balance
C	500°C/1 h Q	Coarse eutectic	24.5	2.3	balance
D	500°C/1 h Q	Flower-shaped particle	39.7	5.5	balance
E	500°C/1 h SC	Mg matrix	3.2	-	balance
F	500°C/1 h SC	Bright lamella	49.3	7.7	balance
G	500°C/1 h SC	Gray phase	27.5	-	balance
H	500°C/1 h SC	Gray particles	21.6	-	balance

Table 5.12: Results of EDX measurements of Mg4Y26Zn alloys annealed at 500°C. The concentrations are given in at.%. The analyzed regions denoted by letters A–H are shown in figures 5.27 and 5.29.

The Mg matrix of quenched Mg4Y26Zn alloy (region A) contains Zn but the Y concentration is below the detection limit of EDX. The measured concentration of Zn in Mg matrix is higher than the maximum solubility of Zn in Mg (2.4 at.%, see figure 3.4). Hence, some small precipitates of binary Mg-Zn phases must be present in the Mg matrix. These precipitates are however too small to be visible in figure 5.27. GBP with denser structure (region B) is free of Y and rich in Zn. According to the EDX analysis, we can conclude that it is composed of binary Mg-Zn phase.

On the other hand, GBP with slightly coarser structure (region C) contains Y. Therefore, in this part of GBP also the icosahedral phase $Mg_3Zn_6Y_1$ is present.

The highest concentration of Y in the quenched Mg4Y26Zn alloy was identified in the flower-shaped particle (region D). However, the measured concentration of Y in this particle is significantly lower than the Y concentration of 10at.% corresponding to the pure icosahedral phase $Mg_3Zn_6Y_1$. Hence, the particle is most likely not composed of pure icosahedral phase but contains also some fraction of binary Mg-Zn phases.

The concentration of Zn in the Mg matrix of the slowly cooled Mg4Y26Zn alloy (region E) is also higher than the solubility of Zn in Mg. However, contrary to the quenched alloy, the precipitates of the Mg-Zn binary phases are large enough to be visible in the SEM micrograph, see figure 5.29.

Bright lamellas of GBP (region F) enriched by Zn are the solely phase in slowly cooled Mg4Y26Zn which also contains Y according to EDX analysis. These lamellas can be identified as icosahedral phase since their composition is close to the nominal composition of the icosahedral phase $Mg_3Zn_6Y_1$. The composition of the gray phase (region G) matches the Mg_7Zn_3 phase. Coarser gray particles are most likely also composed of Mg_7Zn_3 phase but the presence of Mg matrix in their vicinity slightly lowers measured concentration of Zn.

5.2.1.3 Isochronnal annealing of WE43-based alloys

WE43-based alloys were isochronally annealed in steps 20 K/20 min to investigate the development of the mechanical properties with increasing annealing temperature. The results are presented in figure 5.38.

In general, hardness gradually decreases with increasing annealing temperature due to coarsening and dissolution of precipitates which leads to softening of studied alloys. However, there are two notable hardening peaks at $\sim$ 160°C and $\sim$ 440°C. The origin of the peak at $\sim$ 160°C which is most prominent in the WE43+26Zn alloy is most likely precipitation of some binary Mg-Zn phase. Similar peak, albeit at higher temperature ($\sim$ 220°C), was observed in binary Mg6wt.%Zn alloy [54].

An increase of hardness after annealing at temperatures higher than 400°C is caused by changes in the morphology of GBP. At these temperatures, GBP present along grain boundaries in WE43-based alloys modified by addition of Zn starts to melt.

The temperature and melted volume depend on the concentration of Zn in the alloy. Higher concentration of Zn leads to lower melting point and increases the volume fraction of the melt. Indeed, one can see in figure 5.38 that the hardening occurs at lower temperature in WE43+26Zn alloy and is shifted to higher temperatures in WE43+14Zn and WE43+11Zn alloys.

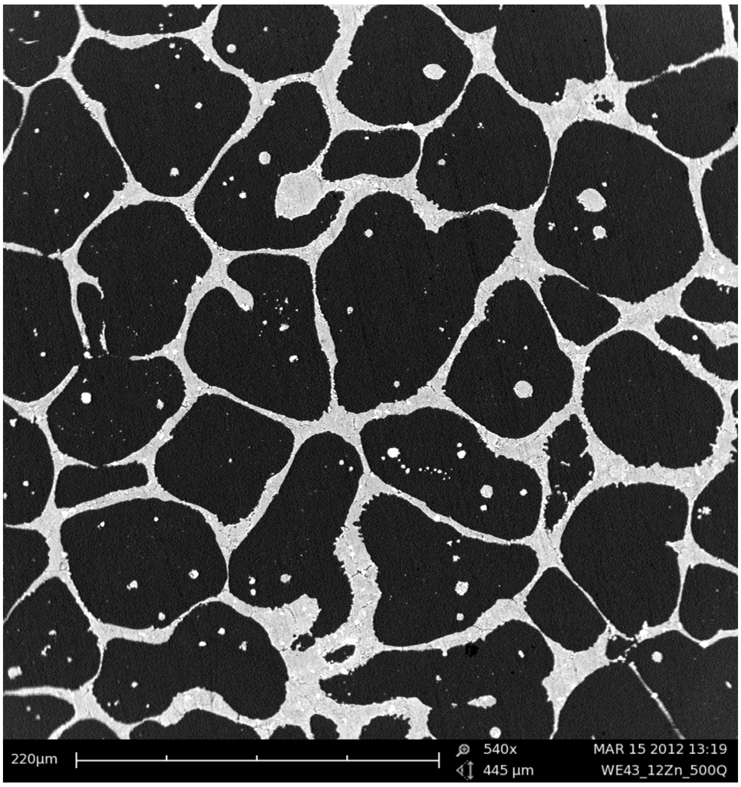

Figure 5.22: SEM image of WE43+11Zn alloy annealed at 500°C for 1 h and quenched.

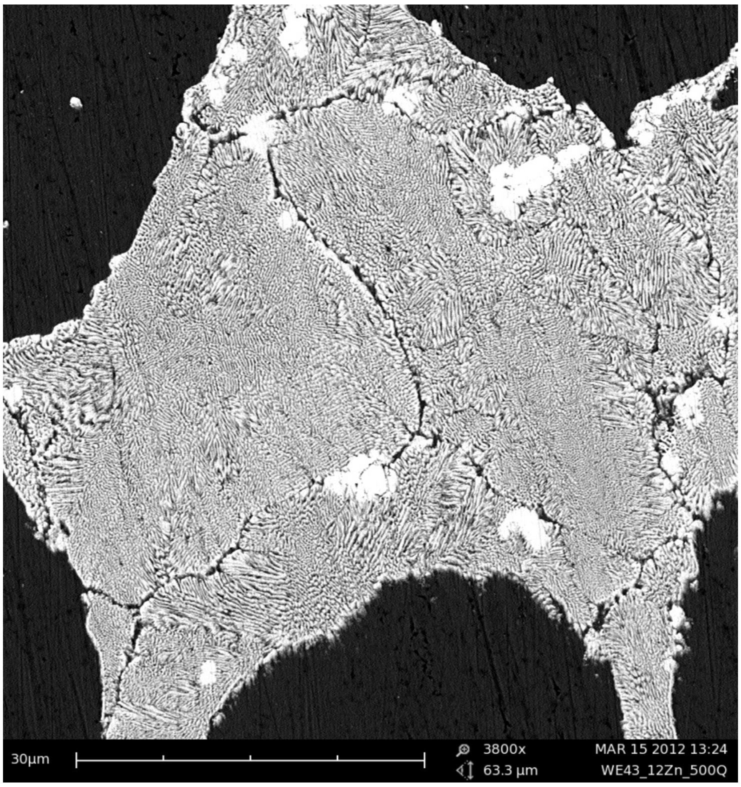

Figure 5.23: SEM image of WE43+11Zn alloy annealed at 500°C for 1 h and quenched, higher magnification.

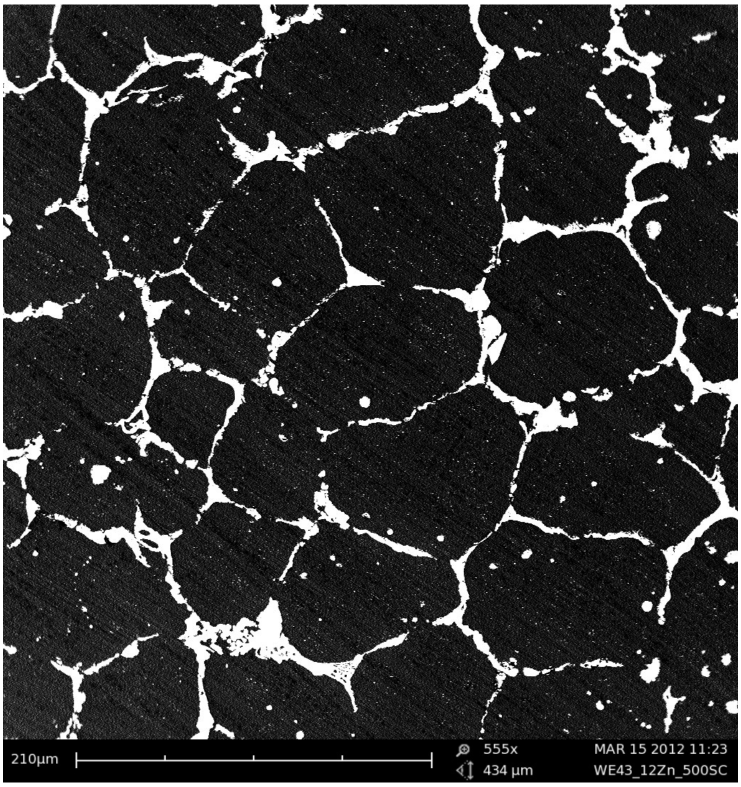

Figure 5.24: SEM image of WE43+11Zn alloy annealed at 500°C for 1 h and slowly cooled.

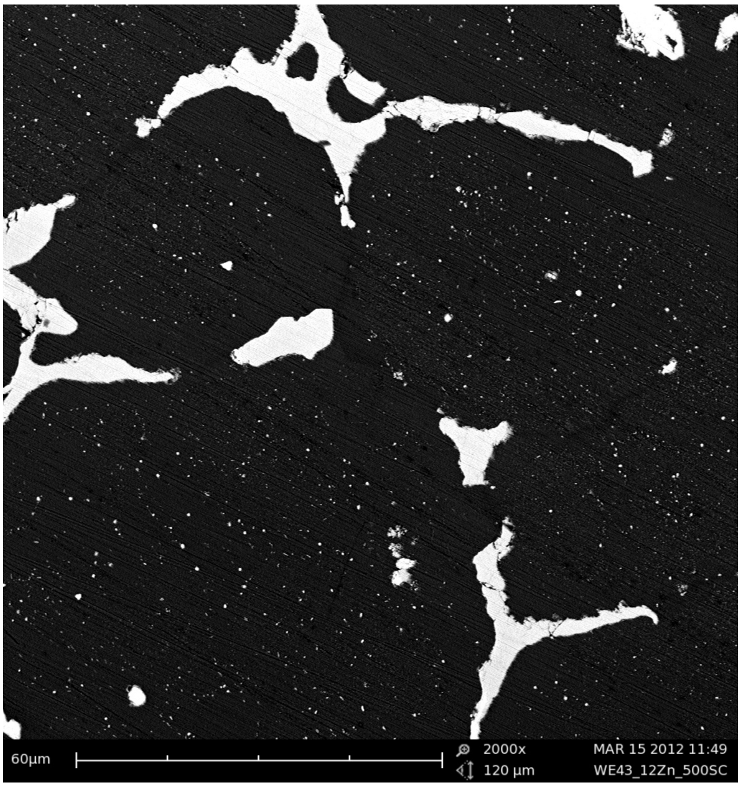

Figure 5.25: SEM image of WE43+11Zn alloy annealed at 500°C for 1 h and slowly cooled, higher magnification.

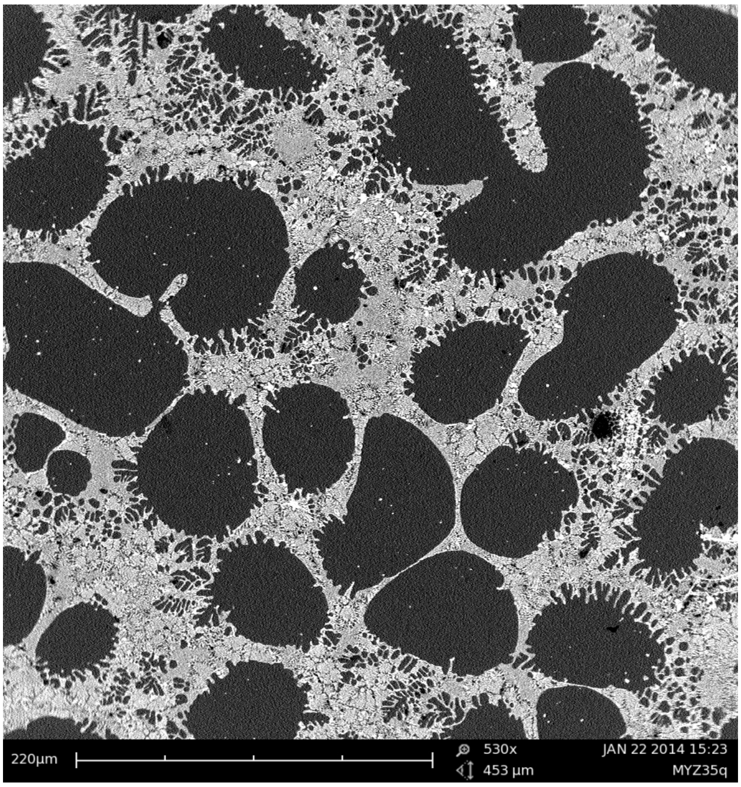

Figure 5.26: SEM image of Mg4Y26Zn alloy annealed at 500°C for 1 h and quenched.

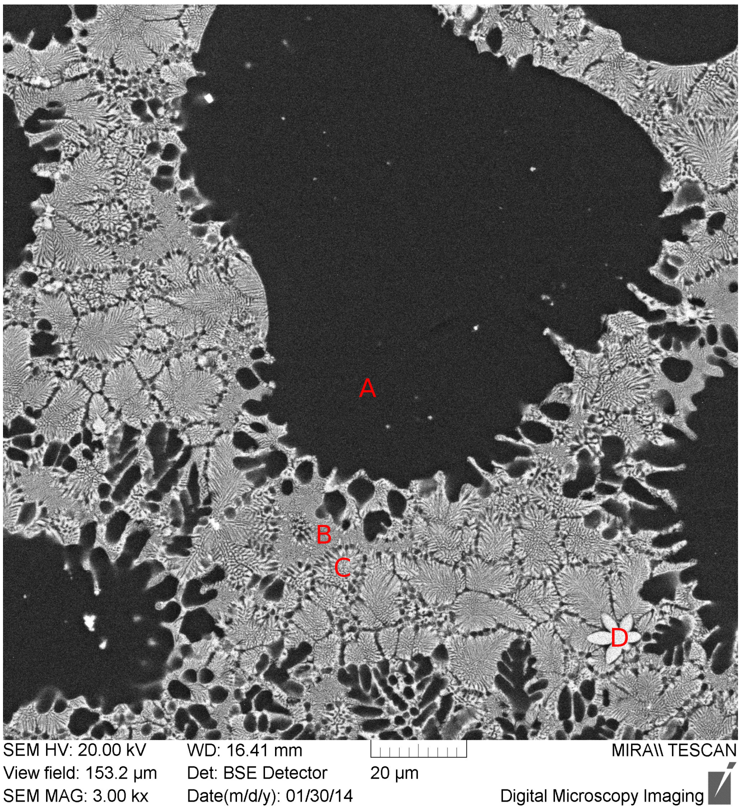

Figure 5.27: SEM image of Mg4Y26Zn alloy annealed at 500°C for 1 h and quenched, higher magnification. Letters denote regions analyzed by EDX.

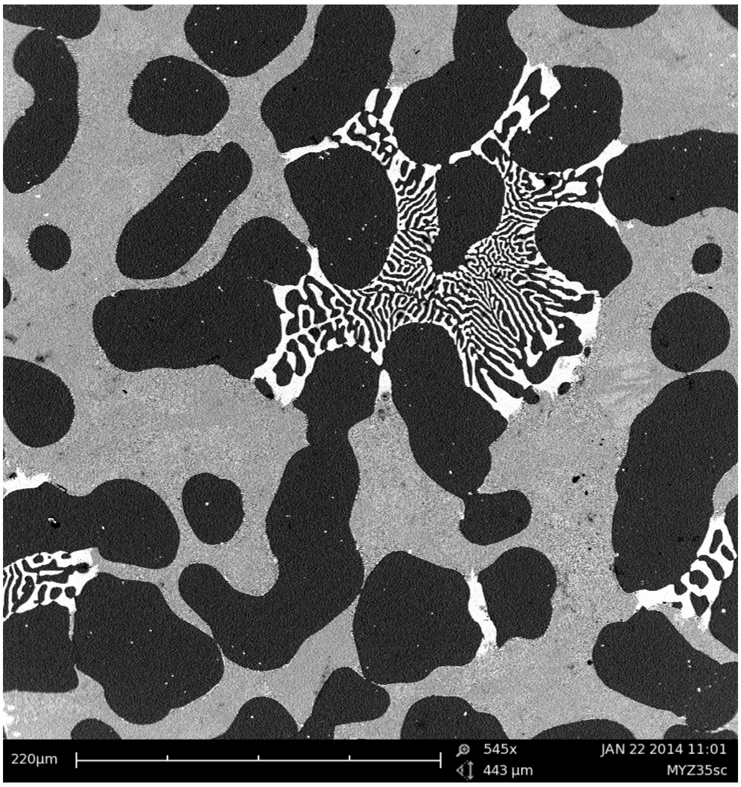

Figure 5.28: SEM image of Mg4Y26Zn alloy annealed at 500°C for 1 h and slowly cooledl.

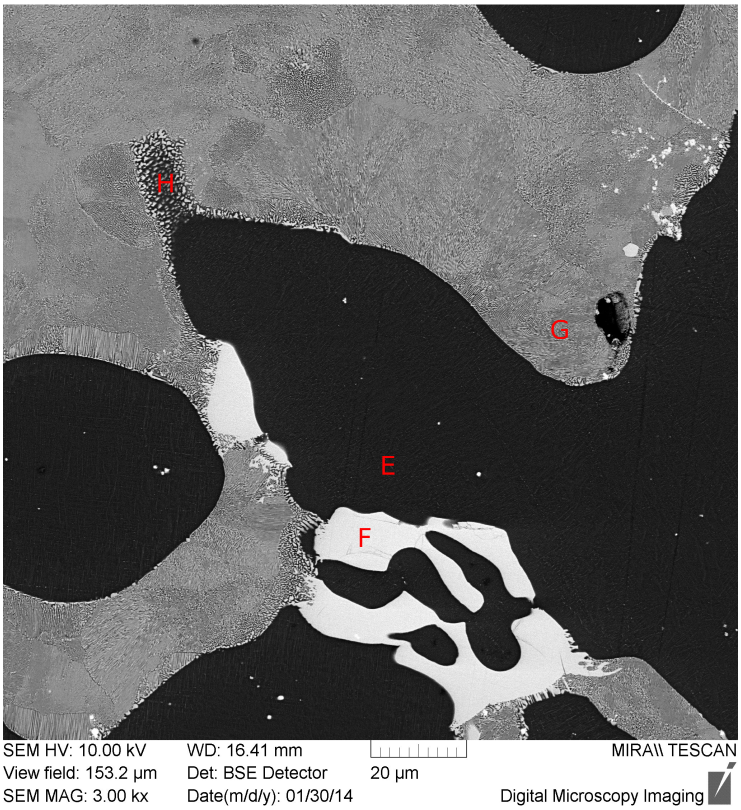

Figure 5.29: SEM image of Mg4Y26Zn alloy annealed at 500°C for 1 h and slowly cooled, higher magnification. Letters denote regions analyzed by EDX.

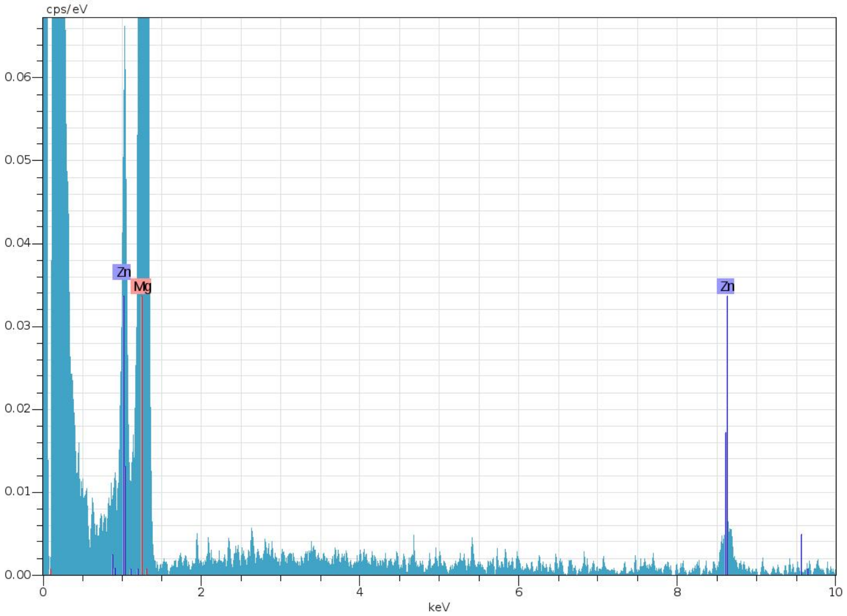

Figure 5.30: EDX spectrum of the region A in 5.27. Mg4Y26Zn alloy annealed at 500°C for 1 h and quenched.

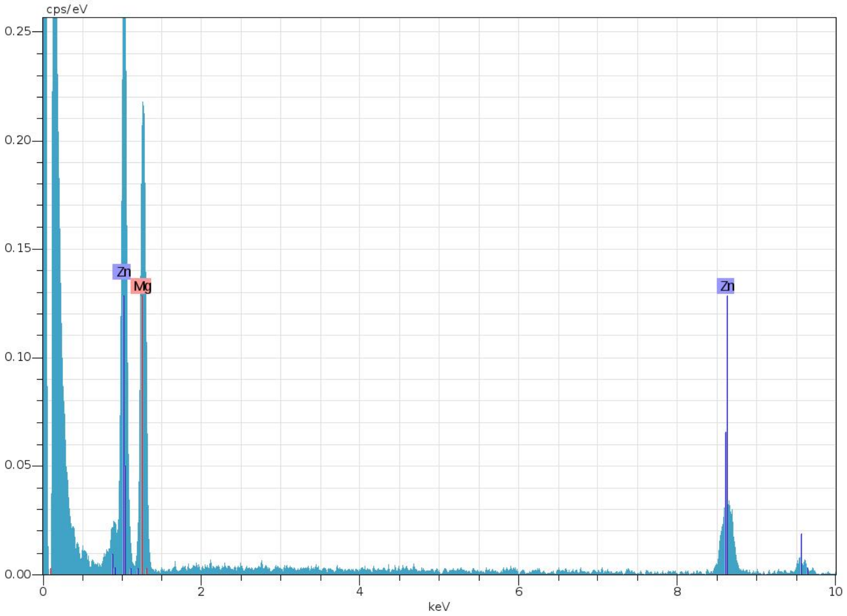

Figure 5.31: EDX spectrum of the region B in 5.27. Mg4Y26Zn alloy annealed at 500°C for 1 h and quenched.

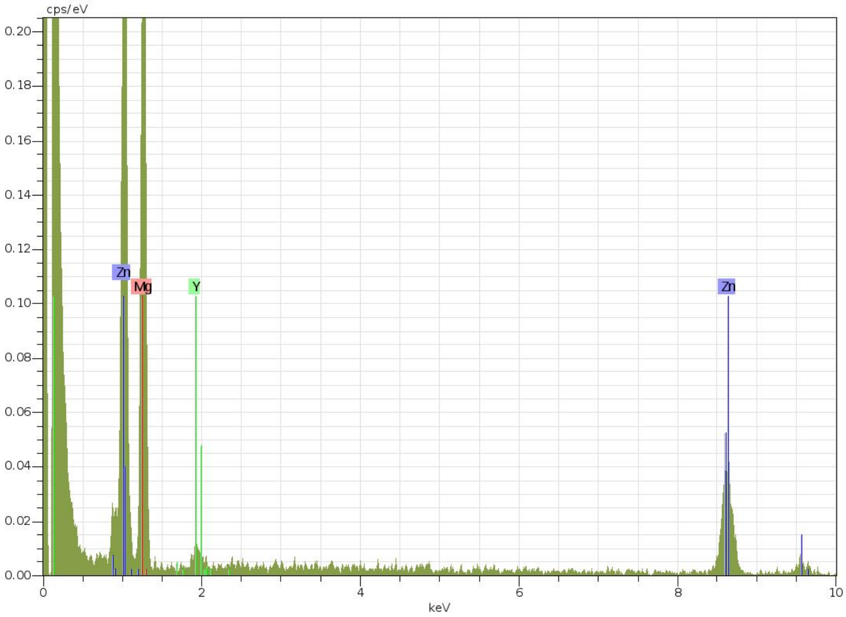

Figure 5.32: EDX spectrum of the region C in 5.27. Mg4Y26Zn alloy annealed at 500°C for 1 h and quenched.

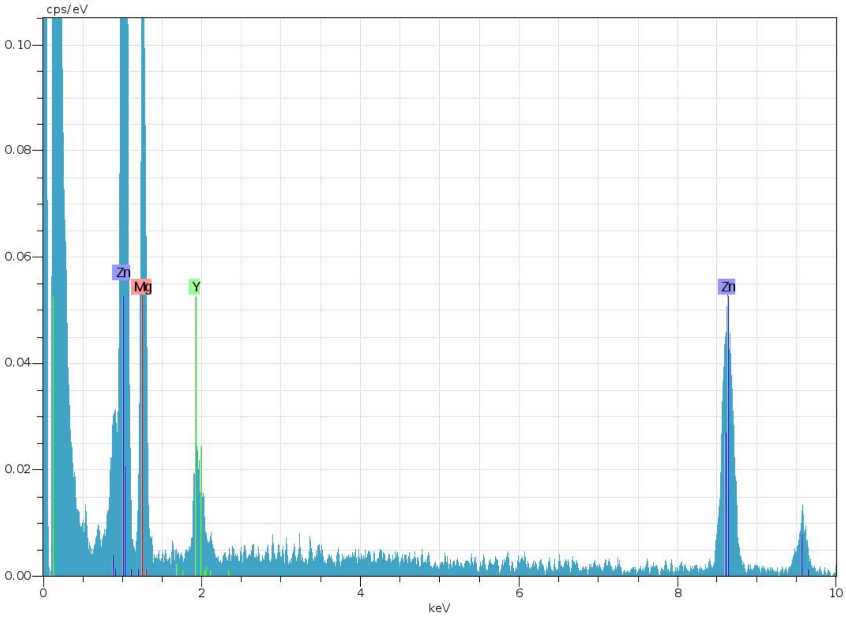

Figure 5.33: EDX spectrum of the region D in 5.27. Mg4Y26Zn alloy annealed at 500°C for 1 h and quenched.

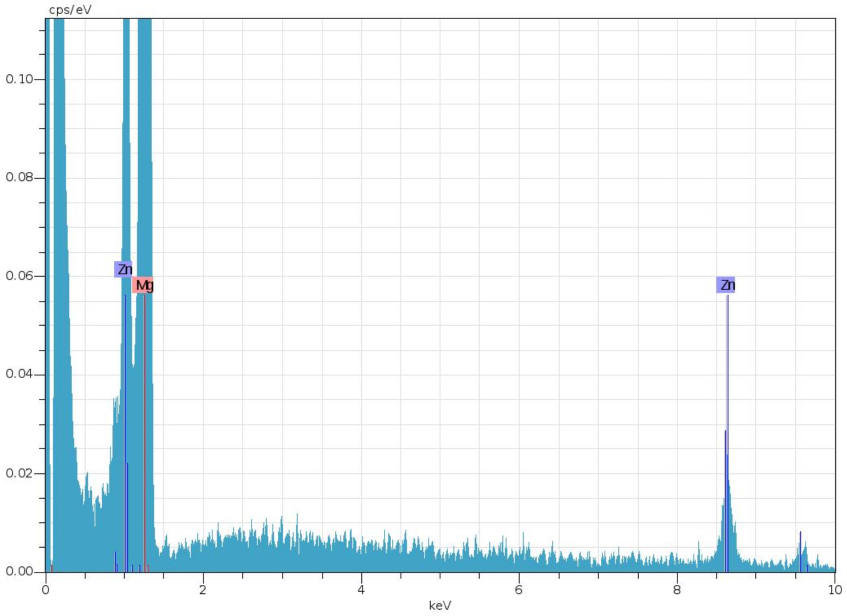

Figure 5.34: EDX spectrum of the region E in 5.29. Mg4Y26Zn alloy annealed at 500°C for 1 h and slowly cooled.

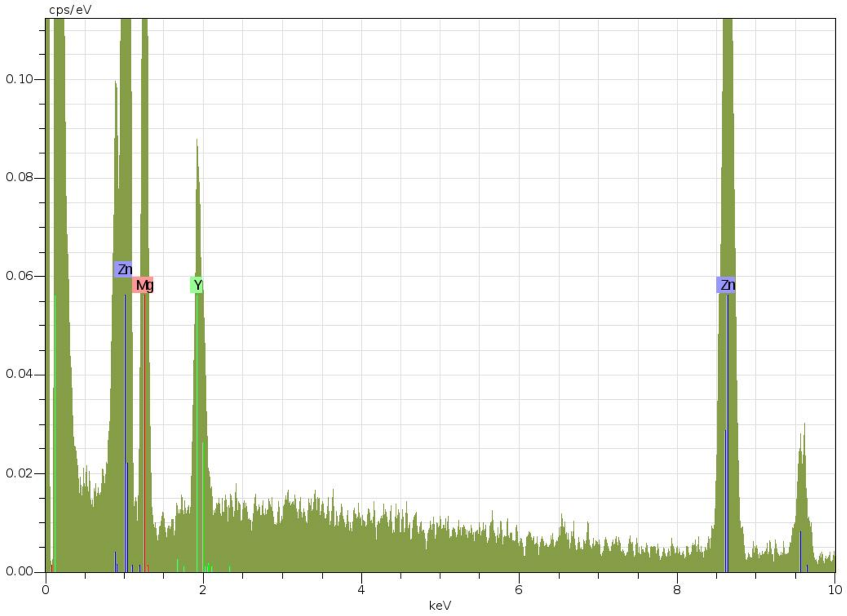

Figure 5.35: EDX spectrum of the region F in 5.29. Mg4Y26Zn alloy annealed at 500°C for 1 h and slowly cooled.

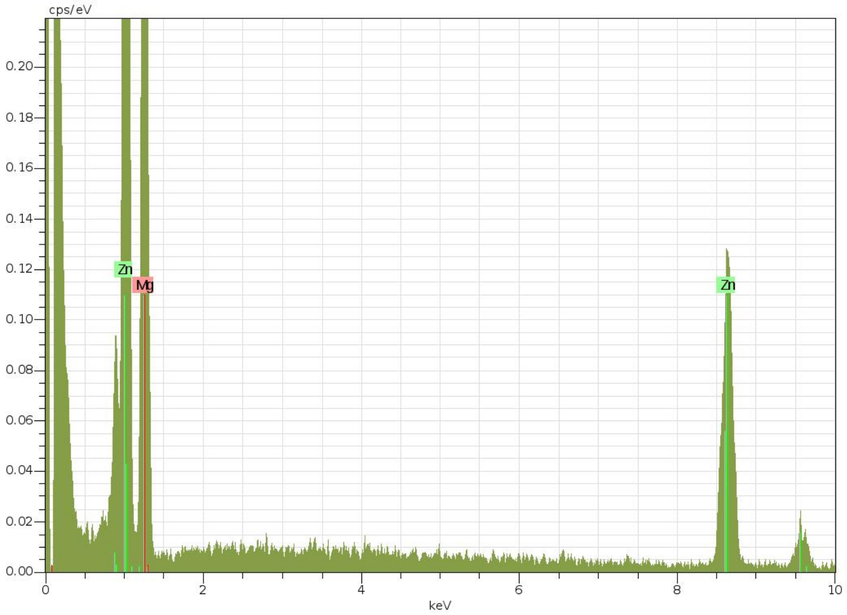

Figure 5.36: EDX spectrum of the region G in 5.29. Mg4Y26Zn alloy annealed at 500°C for 1 h and slowly cooled.

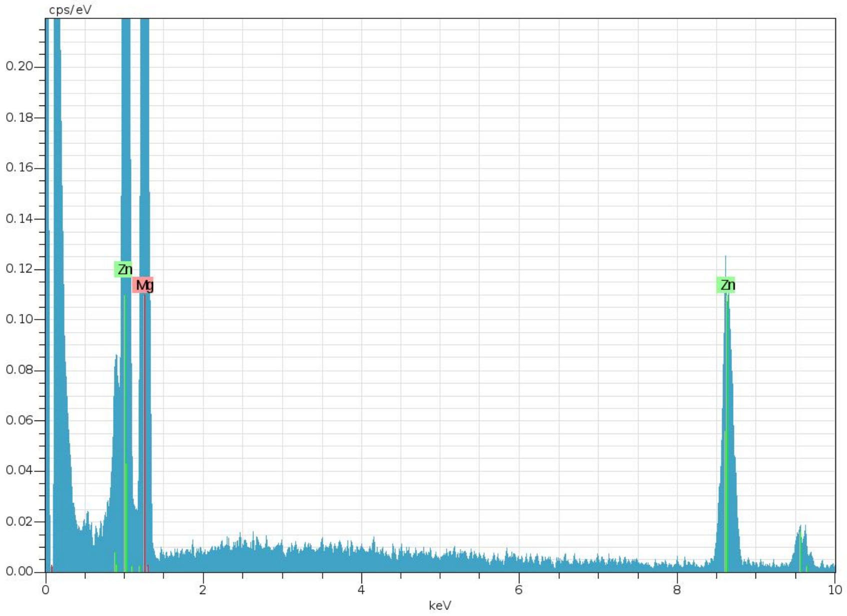

Figure 5.37: EDX spectrum of the region H in 5.29. Mg4Y26Zn alloy annealed at 500°C for 1 h and slowly cooled.

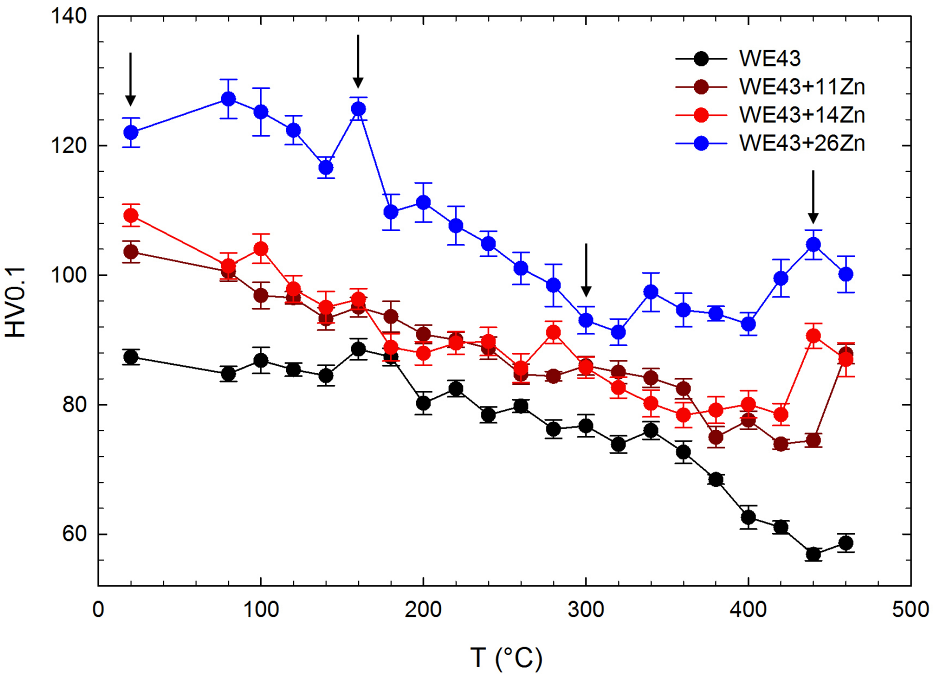

Figure 5.38: The development of hardness of WE43-based alloys subjected to isochronal annealing. The arrows denote states measured by positron lifetime spectroscopy. Adapted from appendix B.

5.2.2 Defect studies

The LT investigation were performed on the isothermally annealed WE43+11Zn and Mg4Y26Zn alloys to study the the influence of heat treatment on vacancy-like defects. The results are shown in table 5.13.

The Mg4Y26Zn alloy annealed at 500°C for 1 hour and slowly cooled exhibits a single component LT spectrum. Its lifetime τ_1 is in good agreement with the bulk positron lifetime for Mg $\sim$ 225 ps [50]. Therefore, the slowly cooled Mg4Y26Zn alloy can be considered as a defect-free material within the sensitivity of positron lifetime spectroscopy.

All other studied samples exhibit two component LT spectra. The lifetime of the first component τ_1 corresponding to annihilation of free positrons is shortened due to positron trapping at defects according to equation (2.23). The second component with the lifetime $\tau_2 \sim 300$ ps corresponds to annihilation of positrons trapped at vacancy-like defects.

The bulk lifetime τ_B was calculated according to the equation (2.25) to check the applicability of STM to the measured data. The calculated values of τ_B for all studied samples agree well with the bulk positron lifetime for Mg $\sim$ 225 ps [50]. Hence, the assumptions of STM are fulfilled here and it can be used to calculate the trapping rate K_D according to equation (2.23) and to estimate concentration of defects according to equation (2.24).

The resulting values are presented in table 5.13. The specific positron trapping rate $\nu_D = 10^{14}$ s^{-1} was used to calculate the concentration of vacancy-like defects. This value lies at the lower limit of 10^{14}–10^{15} s^{-1} range for a specific positron trapping rates to monovacancies in metals [53]. Reasons leading to selection of this value are discussed in section 5.1.3.

	τ_1 (ps)	I_1 (%)	τ_2 (ps)	I_2 (%)	τ_B (ps)	c_D (10^{-6})
WE43+11Zn AC	201(2)	67(3)	296(5)	33(3)	225(3)	5.3(3)
WE43+11Zn Q	212(5)	73(9)	280(10)	27(9)	227(7)	3.2(4)
WE43+11Zn SC	218(2)	89(1)	290(10)	11(1)	224(2)	1.2(2)
Mg4Y26Zn AC	212.9(5)	91.7(5)	298(4)	8.3(5)	218.1(6)	1.0(5)
Mg4Y26Zn Q	219.7(8)	81.0(7)	300(1)	19.0(7)	231(1)	2.6(4)
Mg4Y26Zn SC	225.7(5)	100	-	-	-	-

Table 5.13: Results of positron lifetime measurements of WE43+11Zn and Mg4Y26Zn alloys in as-cast state (AC) and after annealing at 500°C for 1 h finished by quenching (Q) or by slow cooling (SC).

The concentration of vacancy-like defects in WE43+11Zn alloy decreases after annealing although the heat treatment at 500°C increased the portion of icosahedral phase in GBP, see section 5.2.1. This is caused by the fact that most of finely dispersed precipitates of icosahedral phase present in the Mg matrix of the as-cast WE43+11Zn alloy dissolved during annealing.

The volume fraction of GBP in WE43+11Zn, where the portion of icosahedral phase significantly increased, is not high enough to compensate for the reduction of positron trapping at vacancy-like defects associated with the finely dispersed precipitates inside the Mg matrix. Hence, the total fraction of trapped positrons decreases in samples of WE43+11Zn alloy annealed at 500°C for 1 hour. This decrease is more pronounced in the slowly cooled sample where the thick lamellar structure of GBP further reduces interface area of icosahedral phase and Mg matrix.

The quenched Mg4Y26Zn alloy exhibits substantially larger concentration of vacancy-like defects than the as-cast sample. Although the precipitates of icosahedral phase in the Mg matrix dissolve during the annealing at 500°C like in the WE43+11Zn alloy, the high volume fraction of grain boundary phase and its fine lamellar structure causes an increase in the concentration of vacancy-like defects.

On the other hand, no positron trapping at defects was detected in slowly cooled Mg4Y26Zn alloy. Thick lamellas of icosahedral phase clearly do not provide enough surface area for measurable trapping of positrons at vacancy-like defects. Furthermore, we can conclude that binary the Mg-Zn phases present in Mg4Y26Zn alloys do not have misfit defects at their interface with Mg matrix.

The CDB measurements of heat treated samples of Mg4Y26Zn alloy are shown in figure 5.39. The narrow peak in the ratio curves located at the momentum $p \sim 8\times10^{-3}$ m_0c and broad peak centered at $p \sim 18\times10^{-3}$ m_0c corresponds to the annihilation of positrons by electrons belonging to Y and Zn, respectively, cf. figures 5.18 and 5.17.

The contribution of Zn decreases after annealing at 500°C for 1 hour to similar level for both quenched and slowly cooled samples. This is most likely due to coarsening and decrease of the numerical density of Zn-rich precipitates inside Mg matrix during the heat treatment at 500°C.

The sharp peak corresponding to annihilation by Y electrons is more prominent in the quenched alloy. Enhanced contribution of Y in the quenched Mg4Y26Zn alloy is caused by trapping of positrons at the vacancy-like defects associated with Y contained in the icosahedral phase $\mathrm{Mg_3Zn_6Y_1}$. The peak at $p \sim 8{\times}10^{-3}$ $\mathrm{m_0c}$ is significantly less pronounced in the slowly cooled Mg4Y26Zn alloy since no positron trapping occurs in this sample.

The results of positron lifetime measurements performed on isochronally annealed WE43+11Zn alloy are shown in table 5.14. The positron lifetime investigations were performed on selected states indicated in figure 5.38 by arrows. Applicability of STM was checked by calculating τ_B according to the equation (2.25) which was found to be in good agreement with the bulk positron lifetime of magnesium $\sim$ 225 ps [50].

The sample annealed at 160°C exhibits a two component LT spectrum. The lifetime of the second component $\tau_2 = 278(9)$ ps is shorter by approximately 20 ps than the lifetime corresponding to the vacancy-like defects associated with icosahedral phase. It has to be noted that positron trapping at open-volume misfit defects with lifetime $\sim$ 260 ps was observed in the binary Mg6wt.%Zn alloy after annealing at 220°C [54].

Furthermore, the intensity of the second component I_2 significantly increased. Hence, the measured lifetime is most likely an average of two components: the first one with lifetime of $\sim$ 300 ps comes from the vacancy-like defects associated with icosahedral phase while the second one with the lifetime of $\sim$ 260 ps is caused by positron trapping at misfit defects of newly formed precipitates. These two components cannot be separated due to limited resolution of the positron lifetime spectrometer and only one component with average lifetime $\tau_2 = 278(9)$ ps was observed.

Since the lifetime of the second component τ_2 is shorter than that for the vacancy-like defects associated with icosahedral phase, we can assume that the average specific positron trapping rate ν_D will be also slightly lower. As a rough approximation, specific positron trapping rate for the vacancy-like defects was rescaled by multiplying it by the ratio of the average lifetime 278 ps and the lifetime 300 ps of the vacancy-like defects. Thus, the specific positron rate $\nu_D = 0.93 \times 10^{14}$ $\mathrm{s^{-1}}$ was used to calculate the concentration of defects for WE43+11Zn alloy annealed at 160°C. One can see, that the concentration of defects, which is a sum of the concentrations of vacancy-like defects and misfit defects, is approximately two times higher than in the as-cast WE43+11Zn alloy.

The samples annealed at 300°C and 440°C exhibit two component positron lifetime spectra with lifetime of the second component $\tau_2 \sim 300$ ps which testifies to presence of vacancy-like defects.

The intensity I_2 of the defect component decreased to 25–30%, i.e. the value comparable to the as-cast sample. Hence annealing at 300°C caused coarsening and/or dissolution of Mg-Zn precipitates and thereby disappearance of the misfit defects associated with these precipitates. In the samples annealed at 300°C and 440°C positrons are trapped predominantly at vacancy-like defects associated with icosahedral phase.

The concentration of vacancy-like defects associated with icosahedral phase $\mathrm{Mg_3Zn_6Y_1}$ was estimated by application of STM. Values of specific positron trapping rate $\nu_D = 10^{14}$ $\mathrm{s^{-1}}$ was used for this calculation. Concentration of vacancy-like defects decreases after annealing at 300°C and 440°C. This decrease can be attributed to gradual coarsening and eventual dissolution of precipitates of icosahedral phase inside Mg matrix with increasing annealing temperature.

State	τ_1 (ps)	I_1 (%)	τ_2 (ps)	I_2 (%)	τ_B (ps)	c_D (10^{-6})
as-cast	201(2)	67(3)	296(5)	33(3)	225(3)	5.3(3)
160°C	180(10)	48(4)	278(9)	52(4)	220(8)	10(1)
300°C	203(9)	70(5)	298(7)	30(5)	224(8)	4.7(7)
440°C	210(10)	75(5)	300(10)	25(5)	227(9)	3.7(5)

Table 5.14: Results of positron lifetime measurements of isochronally annealed WE43+11Zn alloy.

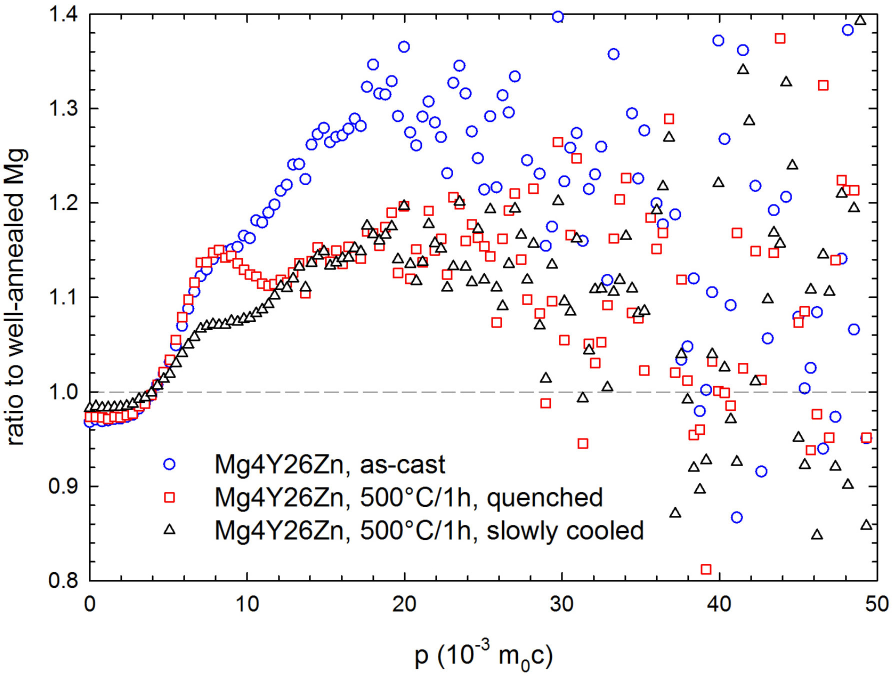

Figure 5.39: CDB ratio curves (related to well-annealed Mg) of heat treated Mg4Y26Zn alloy.

5.2.3 *In situ* XRD studies during heat treatment

In situ measurement of XRD during linear heating and cooling with the rate of change 5 K/min was used to study phase transformations in WE43+14Zn and ternary Mg-Zn-Y alloys. 2D XRD patterns of studied alloys in the as-cast conditions are shown in figures 5.40 to 5.43.

Separate reflection spots can be clearly observed due to relatively coarse grain of the as-cast alloys. Continuous ring present in all images which is approximately at the quarter of the distance from the center to the edge of the 2D image corresponds to the (0 0 2) peak of graphite originating from the graphite crucible.

2D XRD patterns were azimuthally integrated to obtain 1D diffractograms. The diffractograms of the samples in the as-cast condition are shown in figure 5.44. Following intermetallic phases were identified in the as-cast alloys. As cast Mg3Y6Zn alloy contains only W-phase while the as-cast WE43+14Zn alloy contains W-phase as well as icosahedral phase. Binary fcc Mg_7Zn_3 phase and icosahedral phase are present in the as-cast Mg4Y23Zn and Mg4Y26Zn alloys.

The results of *in situ* XRD investigations are presented in figures 5.45 to 5.48. In order to compress the information contained in several hundred diffractograms into one image, individual 1D XRD patterns are shown as horizontal lines and their intensity was converted to color. The evolution of XRD patterns during heat treatment is shown in the vertical direction.

The temperature stability of intermetallic phases was determined from the measured XRD data for each alloy. The results are summarized in table 5.15.

	State	W-phase	I-phase	Mg_7Zn_3	Z-phase	Mg_2Zn_3
WE43+14Zn	heating	435^a	390^a	-	-	-
	cooling	425^b	385^b	-	-	-
Mg3Y6Zn	heating	510^a	-	-	-	-
	cooling	510^b	-	-	-	-
Mg4Y23Zn	heating	-	425^a	230^c, 325^{ae}	230^d, 325^e	-
	cooling	-	410^b	-	-	305^b
Mg4Y26Zn	heating	-	390^a	245^c, 305^{ae}	245^d, 305^e	-
	cooling	-	365^b	-	-	295^b

Table 5.15: Phase transformation temperatures of intermetallic phases in WE43+14Zn and Mg-Zn-Y alloys obtained from *in situ* XRD studies. Indices denote type of phase transformation: a - melting, b - solidification, c - dissolution, d - precipitation, e - transformation of Z-phase to Mg_7Zn_3 phase.

During the heat up of the WE43+14Zn sample, peaks corresponding to icosahedral phase disappear when temperature exceeds $\sim$ 390°C. At the same time, a diffuse bump in the background signifying presence of a liquid phase appears. W-phase remains present in the sample up to $\sim$ 435°C. During the cooling, W-phase and icosahedral phase form at $\sim$ 425°C and $\sim$ 385°C, respectively.

The only intermetallic phase present in the sample of Mg3Y6Zn alloy is W-phase which melts and solidifies at $\sim$ 510°C in this alloy.

Icosahedral phase and Mg_7Zn_3 phase are present in the as-cast Mg4Y23Zn alloy. While icosahedral phase is present up to $\sim$ 425°C during the heat up, behavior of binary Mg-Zn phases is more complicated. At first the Mg_7Zn_3 phase transform to Z-phase at $\sim$ 230°C. This phase stays in the sample up to $\sim$ 325°C where it transforms back to Mg_7Zn_3 which then melts practically immediately. During the cooling, icosahedral phase appears at $\sim$ 410°C and new binary Mg-Zn phase solidifies at $\sim$ 305°C. This phase is most likely the monoclinic Mg_2Zn_3 phase [26].

Behavior of Mg4Y26Zn alloy is similar to the sample of Mg4Y23Zn albeit the measured temperatures of phase transformations are slightly different, see table 5.15. Due to higher concentration of Zn, the peaks corresponding to binary Mg-Zn phases are much more pronounced than in Mg4Y23Zn alloy. Hence, the phase transformation from Mg_7Zn_3 to Z-phase and back can be clearly seen in figure 5.48.

A position shift of diffraction peaks to lower diffraction angles occurs during *in situ* heat treatment due to thermal expansion of crystal lattice. Heating and cooling cycle creates the characteristic “V” shape which can be observed in figures

5.45 to 5.48. The diffraction peaks corresponding to icosahedral phase exhibit different behavior than other peaks. While the other peaks show almost linear dependence of their position on temperature, the expansion of icosahedral phase shows significant nonlinearity. This can be seen in the form of bent curves in figures 5.45, 5.47 and 5.48.

To obtain a quantitative measurement of this nonlinearity, positions of selected diffraction peaks were fitted by pseudo-Voigt function. The relative expansion of the Mg matrix, icosahedral phase and graphite crucible with respect to the room temperature calculated from fitted positions is shown in figure 5.49.

Thermal expansions of the Mg matrix and graphite crucible are approximately linear with temperature. However, the icosahedral phase exhibits a strong nonlinearity in the thermal expansion around 310°C where the coefficient of thermal expansion substantially increases.

Since the thermocouple used for temperature measurement in *in situ* XRD experiments was placed on the steel cap of the crucible, the temperature was not measured directly at the place where the primary beam penetrated into the studied samples. Therefore, the thermal expansion of graphite was used to determine the actual temperature of the crucible.

Comparison of temperature measured by thermocouple and the temperature calculated from thermal expansion of graphite (0 0 2) peak during the *in situ* XRD measurement of WE43+14Zn alloy is shown in figure 5.50. One can see that the temperature calculated from thermal expansion of graphite is in very good agreement with temperature measured by the thermocouple.

In addition to the *in situ* XRD investigations, differential scanning calorimetry (DSC) measurements of as-cast WE43-based alloys with addition of Zn and ternary Mg-Zn-Y alloys were performed with the heating rate of 5 K/min. The DSC curves of of WE43+14Zn and WE43+26Zn alloys are shown in figure 5.51.

The DSC curve of WE43+14Zn alloy contains endothermic peaks at temperatures 330-360°C, $\sim$ 420°C, $\sim$ 445°C and $\sim$ 505°C. First three endothermic peaks are also present in the DSC curve of WE43+26Zn alloy but the peak at $\sim$ 505°C was not observed in WE43+26Zn alloy. According to the results of differential thermal analysis measurements reported in literature, icosahedral phase melts at $\sim$ 450°C [32] and W-phase at $\sim$ 510°C [33].

These temperatures are in good agreement with positions of last two endothermic peaks in WE43-based alloys with addition of Zn. Since as-cast WE43+26Zn alloy does not contain W-phase, the peak at $\sim$ 505°C should not be present in WE43+26Zn alloy. The endothermic peak at $\sim$ 420°C coincides with melting point of Zn (419.53°C) and it most probably comes from remnants of Zn which were not dissolved or which segregated during casting. The group of peaks in the 330-360°C range likely comes from dissolution of Mg-Zn binary phases [55]. However, according to this interpretation, melting of icosahedral phase and W-phase occurs at significantly higher temperature than those which were measured by *in situ* XRD, see table 5.15.

The DSC measurement of Mg3Y6Zn alloy up to 500°C did not reveal any endothermic peak. This is in accordance with the results of *in situ* XRD measurements where melting of W-phase occurred at $\sim$ 510°C.

DSC curves of Mg4Y23Zn and Mg4Y26Zn alloys exhibit two endothermic peaks. The first one is located at $\sim$ 345°C in both alloys. The second peak occurs at ~ 430°C in Mg4Y26Zn alloy and at slightly higher temperature of ~ 450°C in Mg4Y23Zn alloy. In addition, a small and broad exothermic peak at ~ 275°C was observed in Mg4Y26Zn alloy. Only two processes which could correspond to endothermic peaks were identified by *in situ* XRD investigations in Mg4Y23Zn and Mg4Y26Zn alloys: melting of Mg_7Zn_3 phase and melting of icosahedral phase.

Since the melting of Mg_7Zn_3 phase occurs at lower temperature, it can by assigned to the endothermic peak at ~ 345°C and the peaks at temperature over 400°C are then associated with melting of icosahedral phase. The doublet structure of DSC peak at ~ 345°C reflects the transformation of Z-phase back to Mg_7Zn_3 phase and subsequent melting of Mg_7Zn_3 phase which was observed by *in situ* XRD. The broad peak exothermic peak at ~ 275°C likely originates in the transformation of Mg_7Zn_3 phase to Z-phase.

As was the case for WE43+14Zn alloy, the temperatures of phase transitions Mg4Y23Zn and Mg4Y26Zn alloys determined by DSC do not agree with ones obtained by *in situ* XRD studies shown in table 5.15. The phase transformation temperatures determined by *in situ* XRD are systematically lower than those measured by DSC. The precise temperature calibration of the DSC machine makes systematic errors in temperature measurements of this degree very unlikely. Hence, we can assume that the temperatures determined by DSC are correct and the temperatures measured during *in situ* XRD investigations are too low.

Since it was confirmed that the temperature of graphite crucible matches the temperature measured by thermocouple at the steel cap, see figure 5.50, the only plausible explanation is that the sample placed into the crucible is heated to higher temperature than the crucible. Since sample heating during the *in situ* XRD measurements was realized by induction heating it is likely that the sample was heated to higher temperature than the crucible.

Cylindrical samples used here fitted only loosely to the graphite crucible. Therefore, good thermal contact of the sample and the crucible was not guaranteed. Variations in thermal contact could also explain the scatter in phase transformation temperatures determined by *in situ* XRD for different alloys.

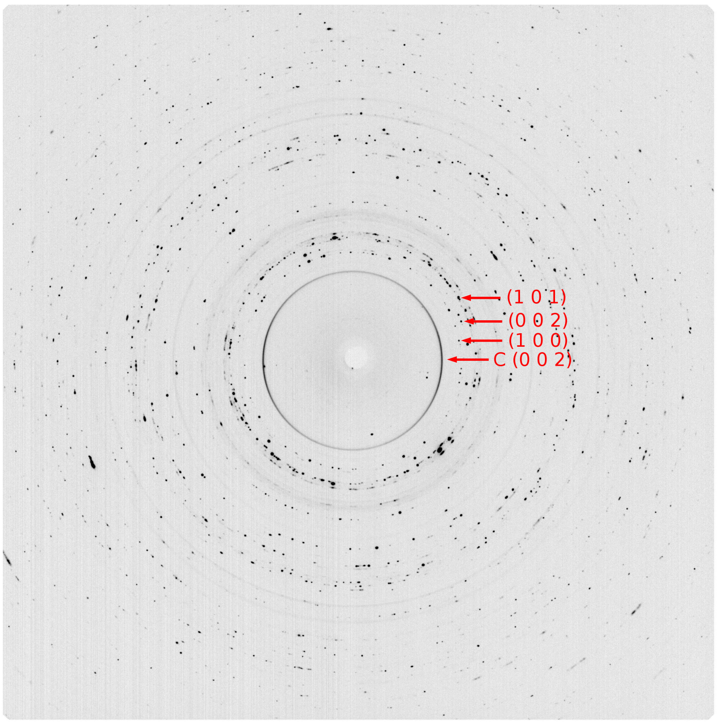

Figure 5.40: 2D diffractogram of as-cast WE43+14Zn alloy. First three reflections of the Mg matrix and the (0 0 2) reflection of graphite (C) are marked by the arrows.

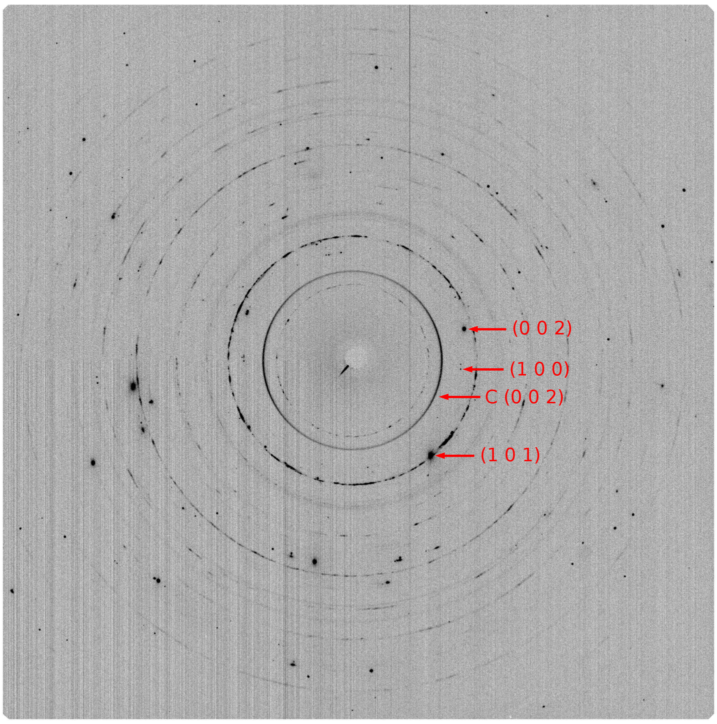

Figure 5.41: 2D diffractogram of as-cast Mg3Y6Zn alloy. First three reflections of the Mg matrix and the (0 0 2) reflection of graphite (C) are marked by the arrows.

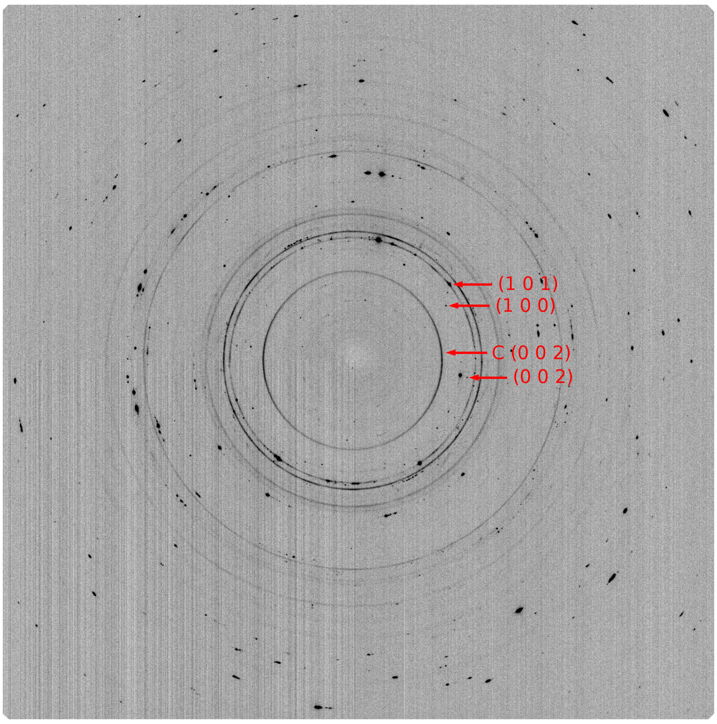

Figure 5.42: 2D diffractogram of as-cast Mg4Y23Zn alloy. First three reflections of the Mg matrix and the (0 0 2) reflection of graphite (C) are marked by the arrows.

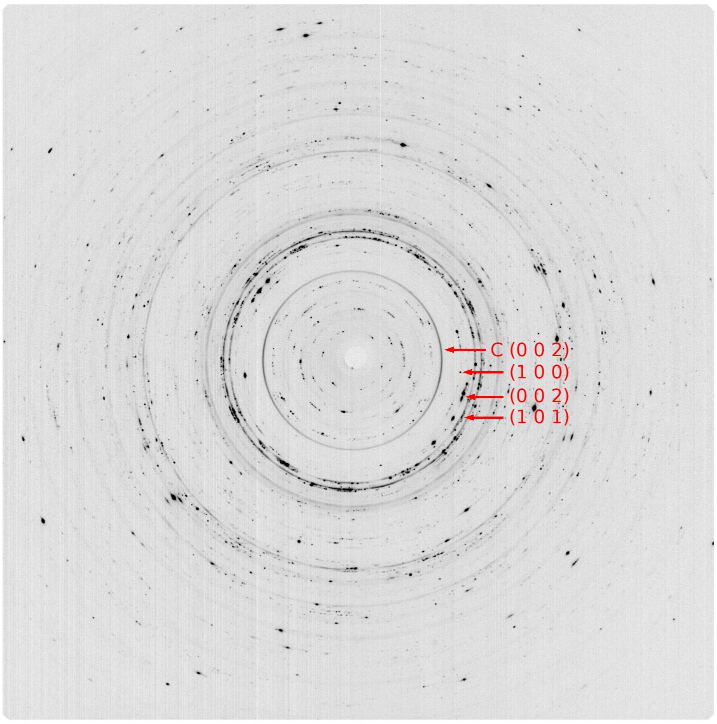

Figure 5.43: 2D diffractogram of as-cast Mg4Y26Zn alloy. First three reflections of the Mg matrix and the (0 0 2) reflection of graphite (C) are marked by the arrows.

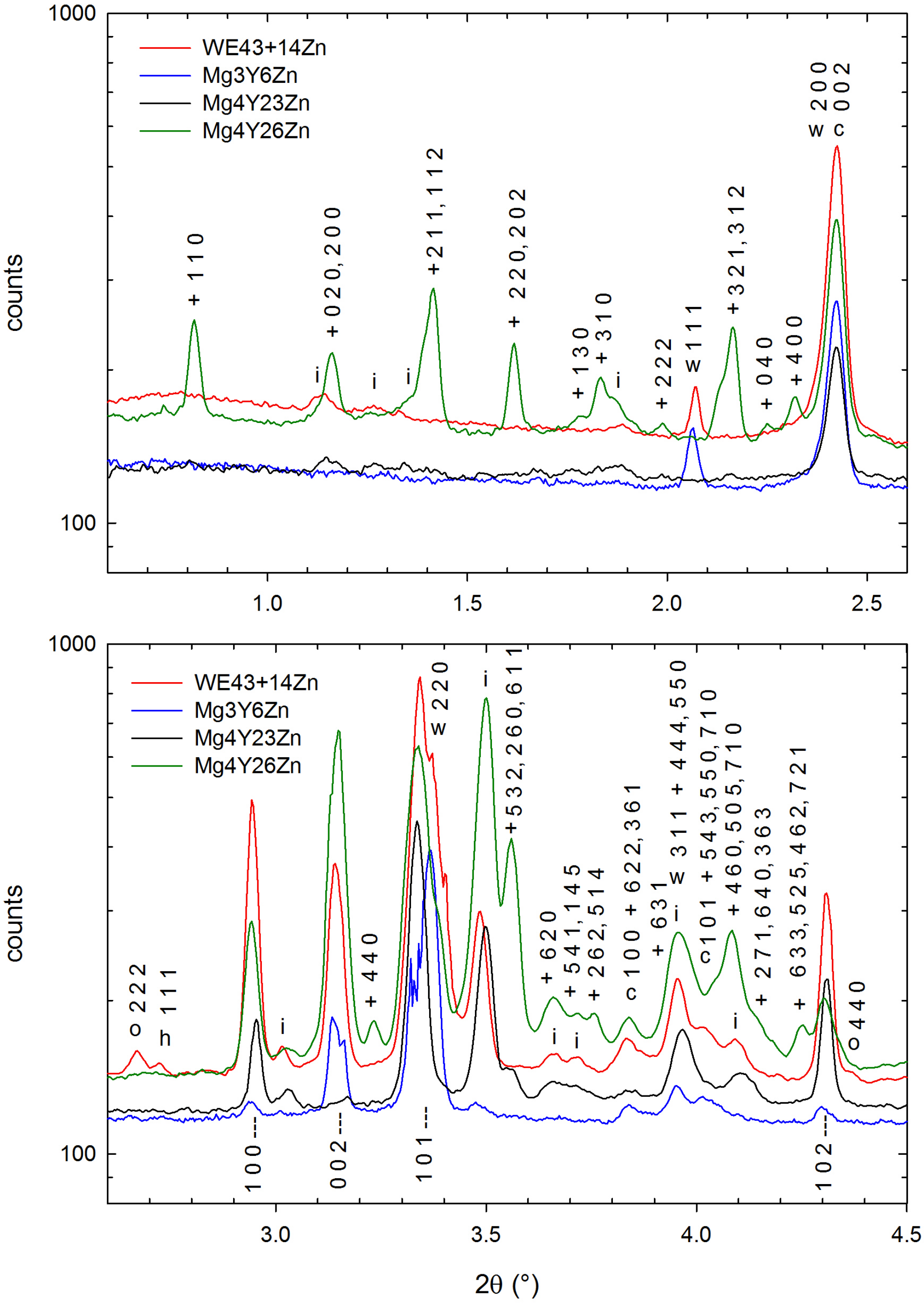

Figure 5.44: 1D diffractograms of as-cast alloys studied by *in situ* XRD ($\lambda = 0.142$ Å). | - Mg matrix; i - icosahedral phase ($Mg_3Zn_6Y_1$); w - W-phase ($Mg_3Zn_3Y_2$); + - Mg_7Zn_3; c - graphite; o - Y_2O_3; h - YH_2.

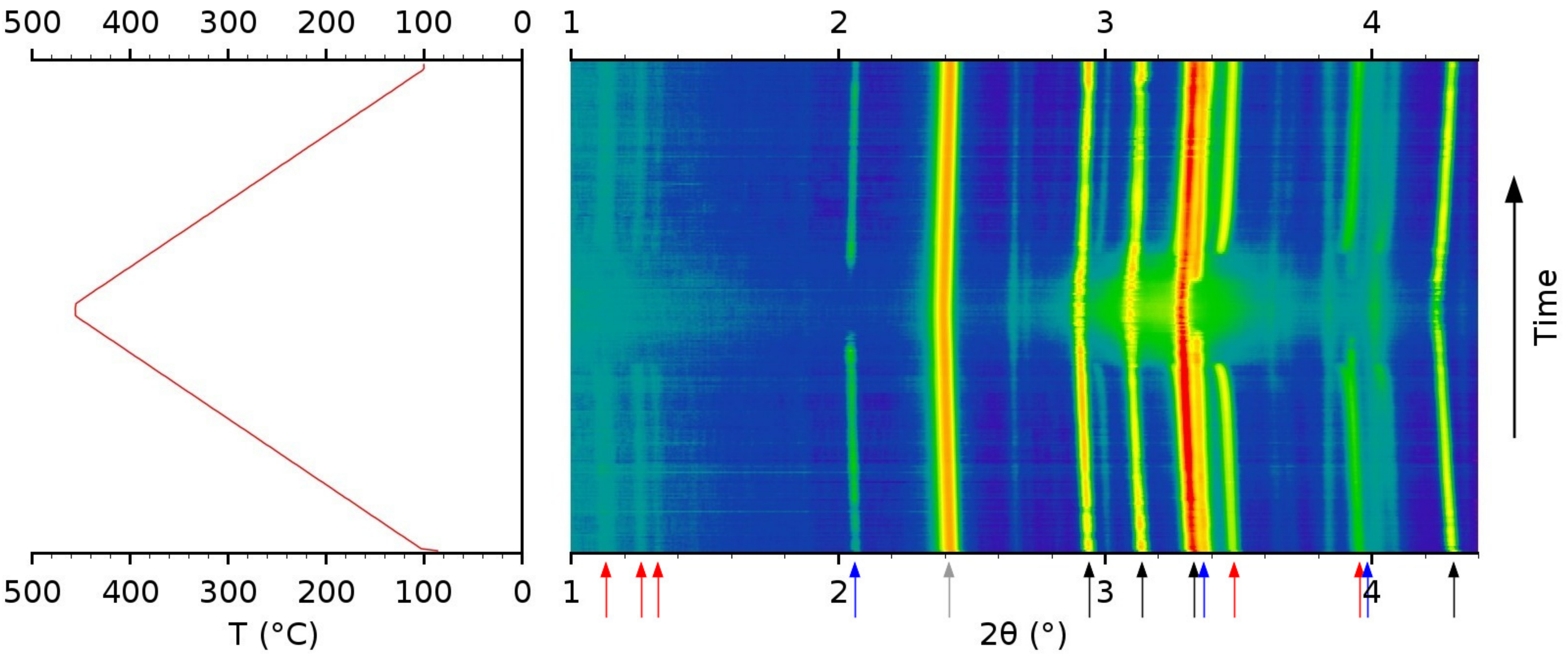

Figure 5.45: The evolution of XRD pattern of WE43+14Zn alloy during linear heat up and cool down from the room temperature to 455°C (λ = 0.142 Å). Each horizontal line in the right section of the figure represents a 1D diffraction pattern at some temperature. Intensity was converted to the color scale and increases from black through violet, blue, green, yellow and orange to red. Temperatures at which were the diffractograms recorded are plotted in the left part of the figure. Most pronounced peaks of Mg matrix (black), icosahedral phase (red), W-phase (blue) and graphite crucible (gray) are marked by colored arrows.

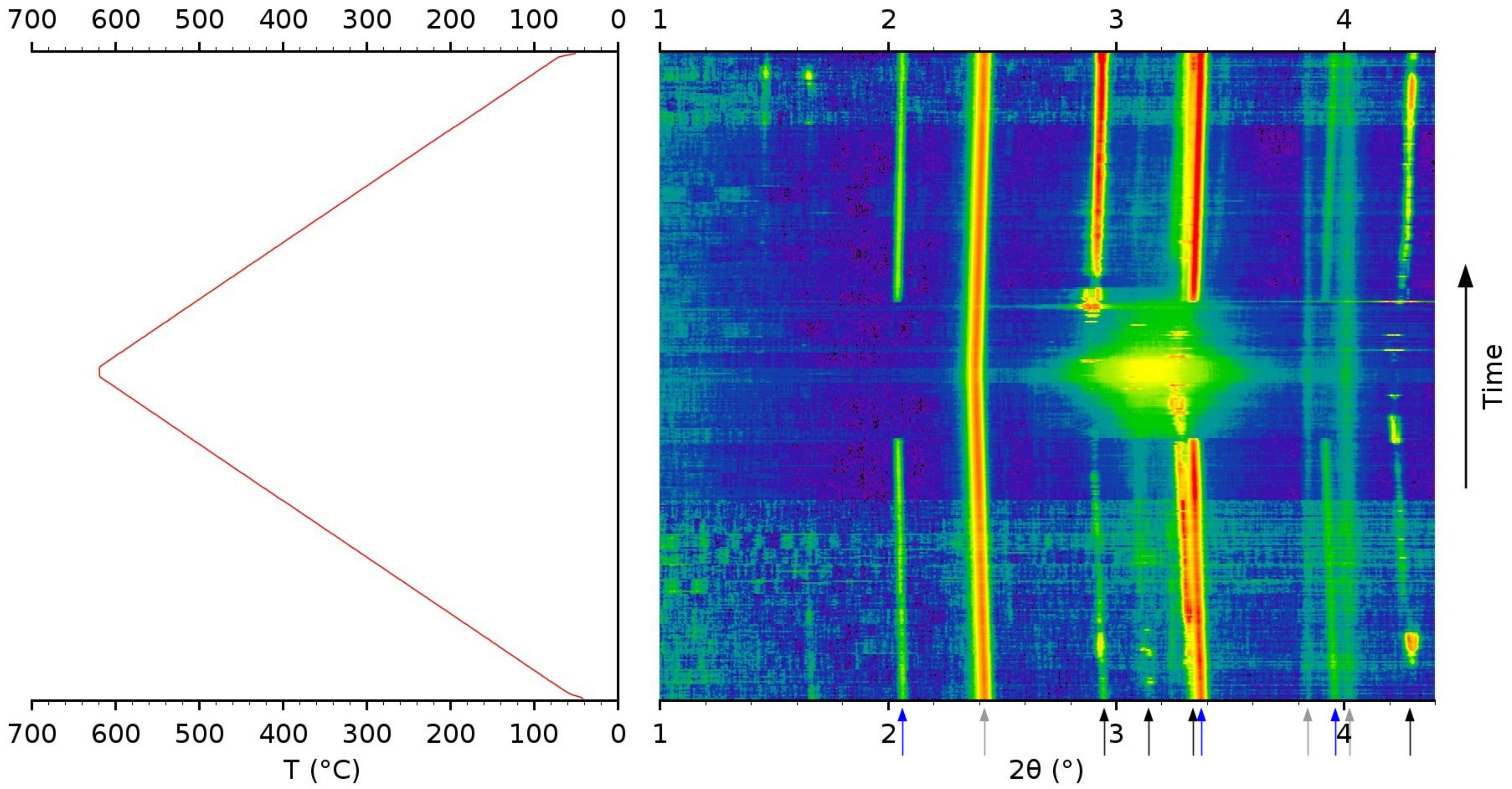

Figure 5.46: The evolution of XRD pattern of Mg3Y6Zn alloy during linear heat up and cool down from the room temperature to 620°C ($\lambda = 0.142$ Å). Each horizontal line in the right section of the figure represents 1D diffraction pattern at some temperature. Intensity was converted to the color scale and increases from black through violet, blue, green, yellow and orange to red. Temperatures at which were the diffractograms recorded are plotted in the left part of the figure. Most pronounced peaks of Mg matrix (black), W-phase (blue) and graphite crucible (gray) are marked by colored arrows.

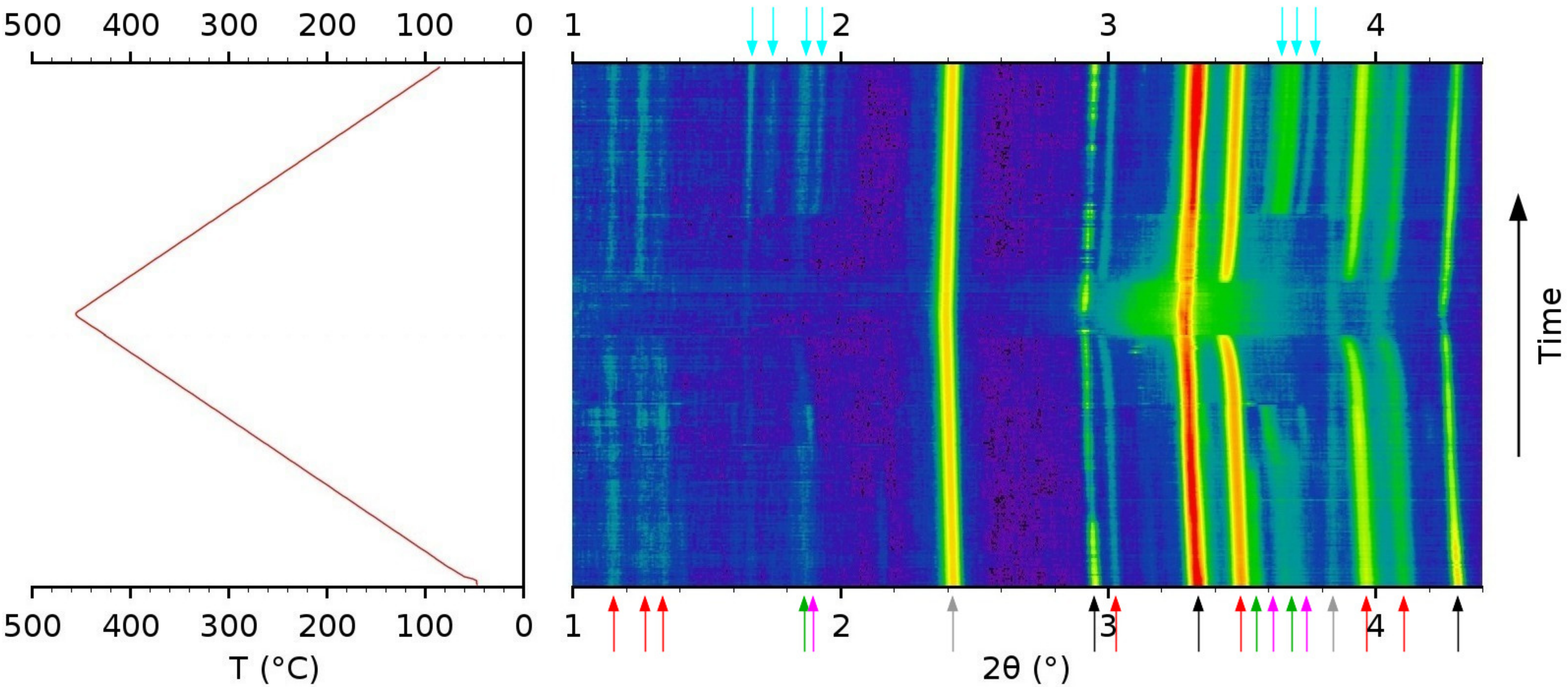

Figure 5.47: The evolution of XRD pattern of Mg4Y23Zn alloy during linear heat up and cool down from the room temperature to 455°C ($\lambda = 0.142$ Å). Each horizontal line in the right section of the figure represents 1D diffraction pattern at some temperature. Intensity was converted to the color scale and increases from black through violet, blue, green, yellow and orange to red. Temperatures at which were the diffractograms recorded are plotted in the left part of the figure. Most pronounced peaks of Mg matrix (black), icosahedral phase (red), Mg_7Zn_3 (green), Z-phase (magenta), Mg_2Zn_3 (cyan) and graphite crucible (gray) are marked by colored arrows.

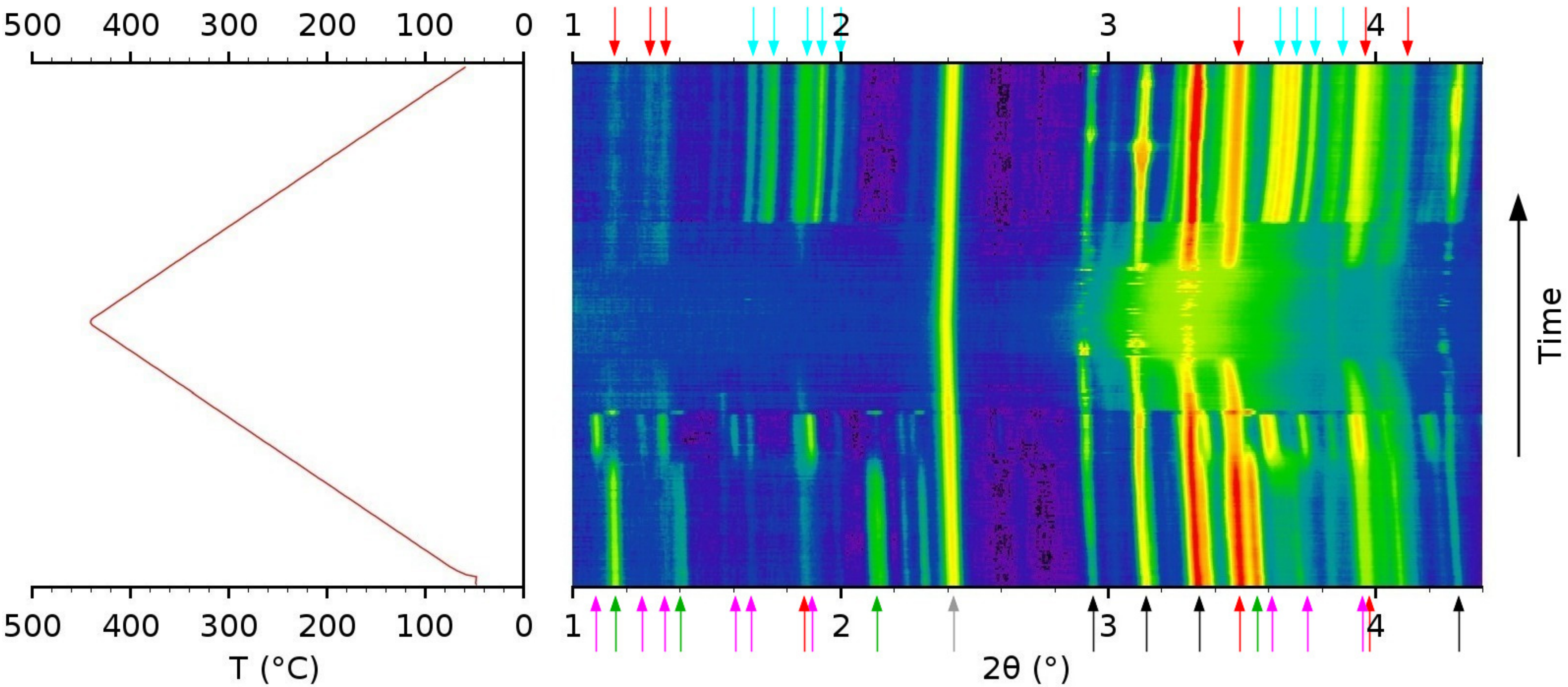

Figure 5.48: The evolution of XRD pattern of Mg4Y26Zn alloy during linear heat up and cool down from the room temperature to 440°C ($\lambda = 0.142$ Å). Each horizontal line in the right section of the figure represents 1D diffraction pattern at some temperature. Intensity was converted to the color scale and increases from black through violet, blue, green, yellow and orange to red. Temperatures at which were the diffractograms recorded are plotted in the left part of the figure. Most pronounced peaks of Mg matrix (black), icosahedral phase (red), Mg_7Zn_3 (green), Z-phase (magenta), Mg_2Zn_3 (cyan) and graphite crucible (gray) are marked by colored arrows.

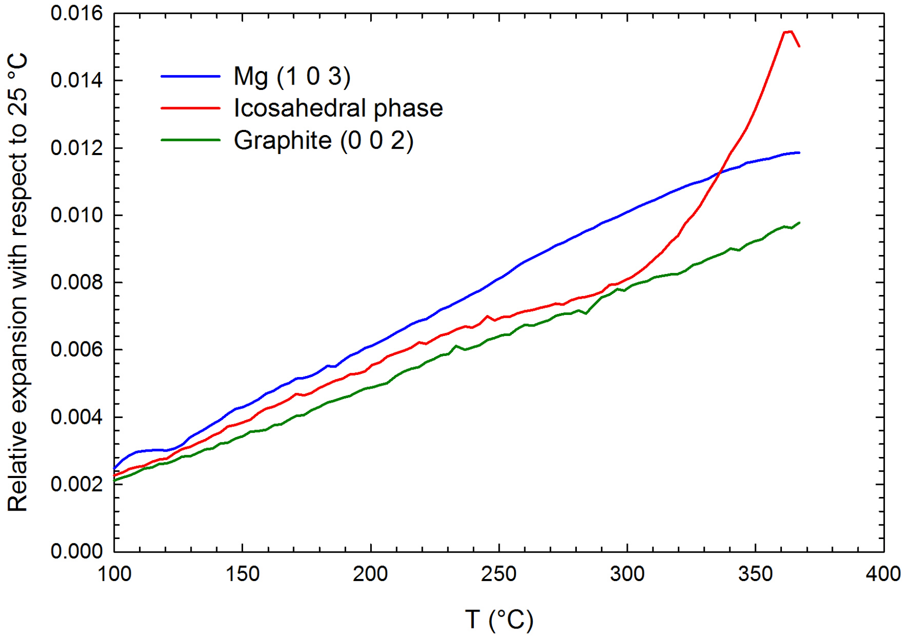

Figure 5.49: Relative thermal expansion of WE43+14Zn alloy with respect to the 25°C calculated from *in situ* XRD data. Adapted from appendix B.

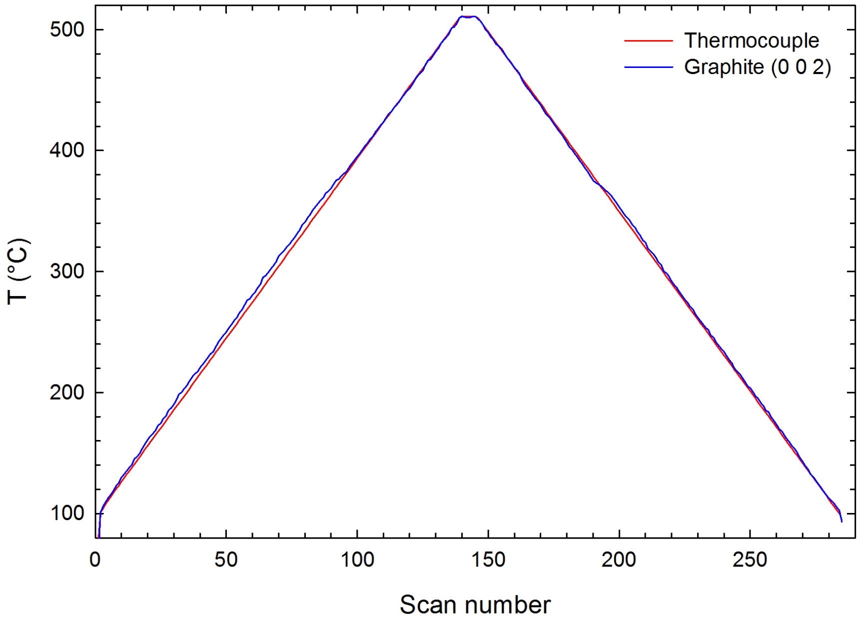

Figure 5.50: The temperature of WE43+14Zn sample during heating and cooling cycle used in *in situ* XRD measurement. The temperature measured by thermocouple is compared with temperature calculated from the shift of the peaks of graphite crucible. Considering the thermal expansion coefficient of graphite α_c labeled “New calculation” in [56].

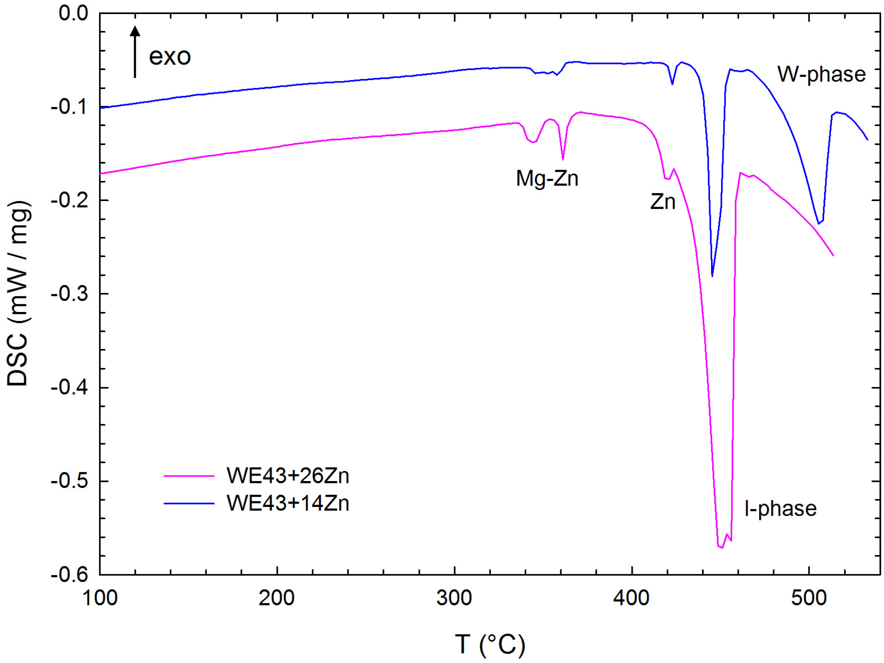

Figure 5.51: DSC curves of the as-cast WE43-based alloys modified by addition of Zn. Labels show phases which are associated with observed peaks in measured curves.

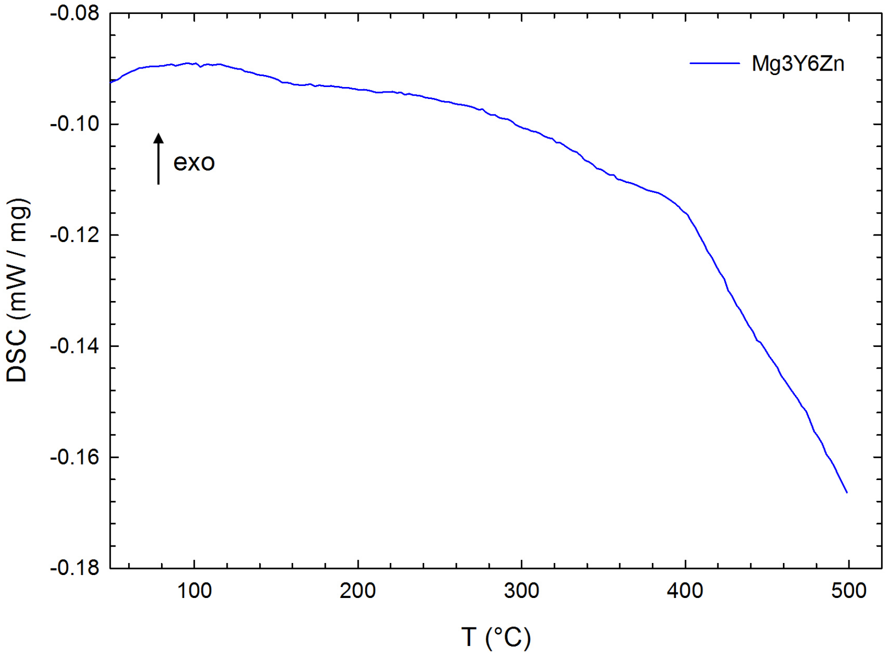

Figure 5.52: DSC curve of the as-cast Mg3Y6Zn alloy.

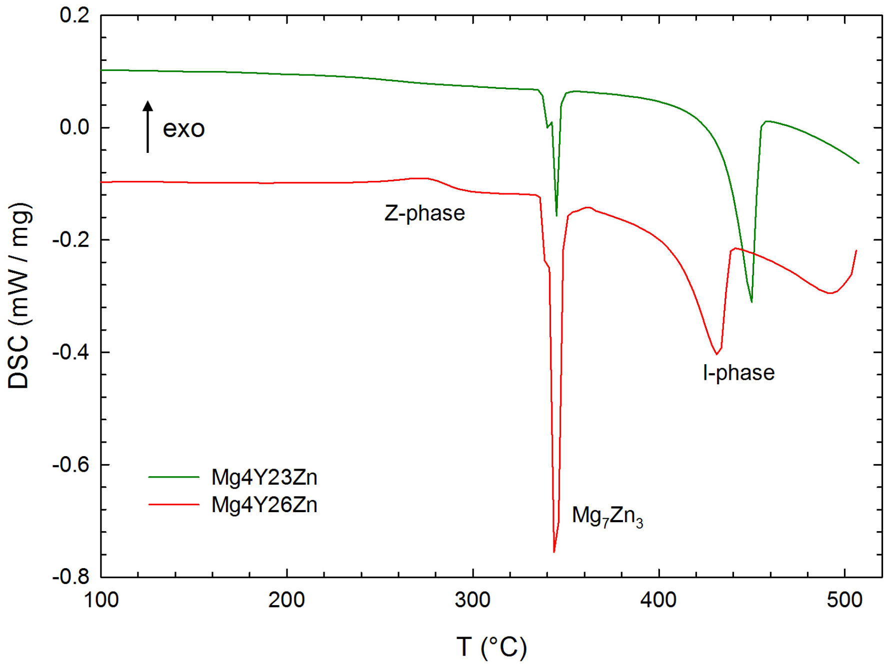

Figure 5.53: DSC curves of the as-cast Mg4Y23Zn and Mg4Y26Zn alloys. Labels show phases which are associated with observed peaks in measured curves.

5.3 Alloys processed by ECAP

5.3.1 Samples

The microstructure of WE43+14Zn, Mg3Y6Zn and Mg4Y26Zn alloys was refined by severe plastic deformation using equal channel angular pressing (ECAP) [57]. The samples in the form of rods with dimensions $10 \times 10 \times 50$ mm^3 were repeatedly pressed through a die consisting of two perpendicular channels, see figure 5.54.

The angle between the entrance and exit channels of ECAP die was 90° and no outer curvature of the channel was used. A back-pressure (BP) plunger was applied during ECAP process to increase the hydrostatic pressure in order to avoid fracturing of the sample. After each pass the billet was rotated by 90° prior to next pass (so-called route B_c) [58]. The ECAP die was preheated to temperature $T = 140$ or 200°C. The parameters of ECAP processing are summarized in table 5.16.

Alloy	Notation	T (°C)	Route	Nbr. of passes	BP (MPa)
WE43+14Zn	WE43+14ZnE200	200	B_c	1, 2, 4	500
Mg3Y6Zn	Mg3Y6ZnE200	200	B_c	1, 4	500
Mg4Y23Zn	Mg4Y23ZnE200	200	B_c	4	500
Mg4Y26Zn	Mg4Y26ZnE140	140	B_c	4	500
Mg4Y26Zn	Mg4Y26ZnE200	200	B_c	4	500

Table 5.16: Parameters of ECAP processing of studied samples.

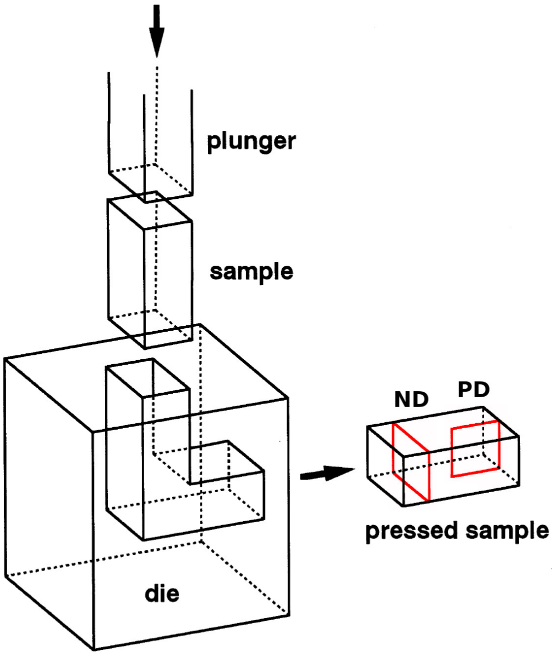

Figure 5.54: Schematic illustration of ECAP facility. Labels show the directions used for a preparation of SEM samples: ND - normal direction, PD - parallel direction. Adapted from [59].

5.3.2 Microstructure and mechanical properties

The microstructures of the samples processed by ECAP were examined by SEM. Images of WE43+14ZnE200 sample after 1 pass are shown in figures 5.55 to 5.58. The microstructure of ECAP-deformed samples was examined in the normal direction, i.e. in cuts perpendicular to the pressing direction, and in the parallel direction, i.e. in cuts parallel with the pressing direction, see figure 5.54. One can clearly see that network of GBP is stretched in the direction of shear. This effect is more pronounced in micrographs obtained in the parallel direction, see figures 5.57 and 5.58.

Secondary phases are significantly more distorted in planes where localized shear deformation occurred, see figures 5.55 and 5.56. Hence, particles of secondary phases can serve as a tracers of deformation during ECAP. Icosahedral phase is broken into smaller pieces during ECAP due to its high brittleness, see figure 5.58.

Micrographs of Mg3Y6ZnE200 sample after 1 ECAP pass are shown in figures 5.59 to 5.60. The tracing effects of secondary phases is not very pronounced in this sample due to their low volume fraction. Nevertheless, the W-phase which is present in the Mg3Y6ZnE200 sample does not exhibit the brittleness of icosahedral phase. This is testified by figure 5.60 which shows bright particles of plastically deformed W-phase.

SEM micrographs of samples Mg4Y26ZnE140 and Mg4Y26ZnE200 both after 4 ECAP passes are shown in figures 5.61 to 5.64. The microstructure of both samples is very similar despite the fact that they were processed by ECAP at different temperatures. High strain imposed during ECAP processing leads to a significant distortion of GBP in these samples.

Gray areas which correspond to binary Mg-Zn phases have crumpled appearance. The Mg-Zn phases are ductile and can be significantly deformed without cracking, this is best seen in figure 5.64 which shows stretched regions of the Mg-Zn phase. On the other hand, the brittle particles of icosahedral phase are broken into many pieces and their morphology resembles broken bones, see figure 5.62.

The temperature stability of mechanical properties of the WE43+14ZnE200 sample after 1, 2 and 4 ECAP passes was studied by microhardness measurement during isochronal annealing performed in steps 20 K/20 min. The results are presented in figure 5.65. The hardness of the WE43+14ZnE200 sample after the first pass is significantly higher than the hardness of the as cast WE43+14Zn alloy, cf. table 5.4. After second pass, the hardness of the WE43+14ZnE200 sample increases further but afterwards it saturates and the hardness after 4 passes is practically equal to that after 2 passes. The hardness of WE43+14ZnE200 samples remains virtually constant during annealing up to 200°C.

A significant drop of hardness which occurs between 260 and 300°C is caused by the recovery of dislocations and subsequent grain growth. One can see that after annealing at 280°C, the hardness of samples subjected to 1, 2 and 4 ECAP passes becomes approximately the same. Hence, we can conclude that annealing at this temperature is sufficient to eliminate the differences in microstructure which were produced by different numbers of ECAP passes.

Gradual decrease of hardness continues until a minimum is reached at 420°C. At 440°C, the GBP present in the WE43+14ZnE200 samples already melts. Upon solidification, the molten GBP forms a network along grain boundaries, cf. figures 5.22 and 5.23, which strengthens the materials and causes the observed increase in hardness. The volume fraction of melt increases with increasing annealing temperature and the maximum of hardness was reached after annealing at 520°C.

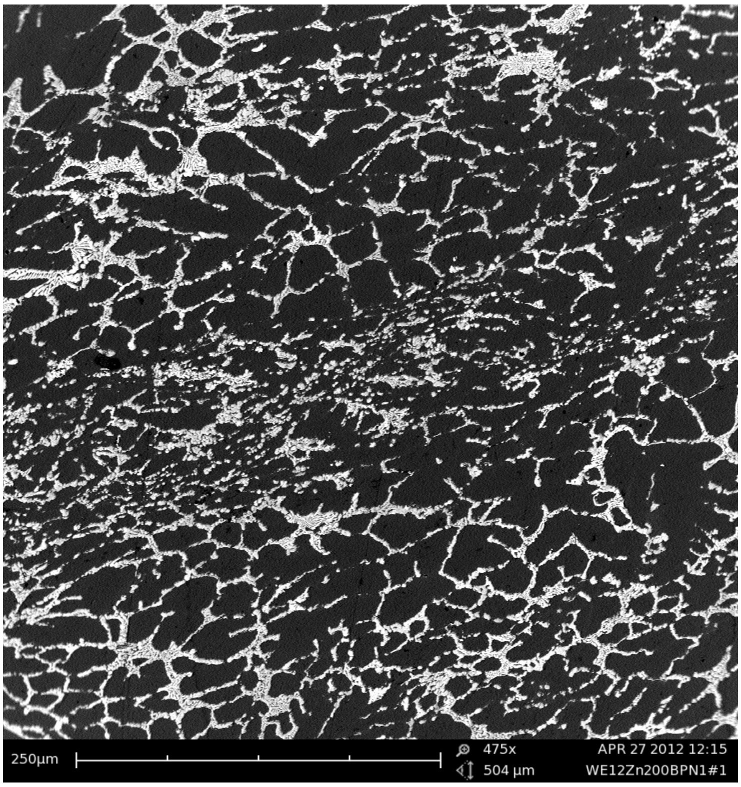

Figure 5.55: SEM image of WE43+14ZnE200 sample after 1 pass, the normal direction.

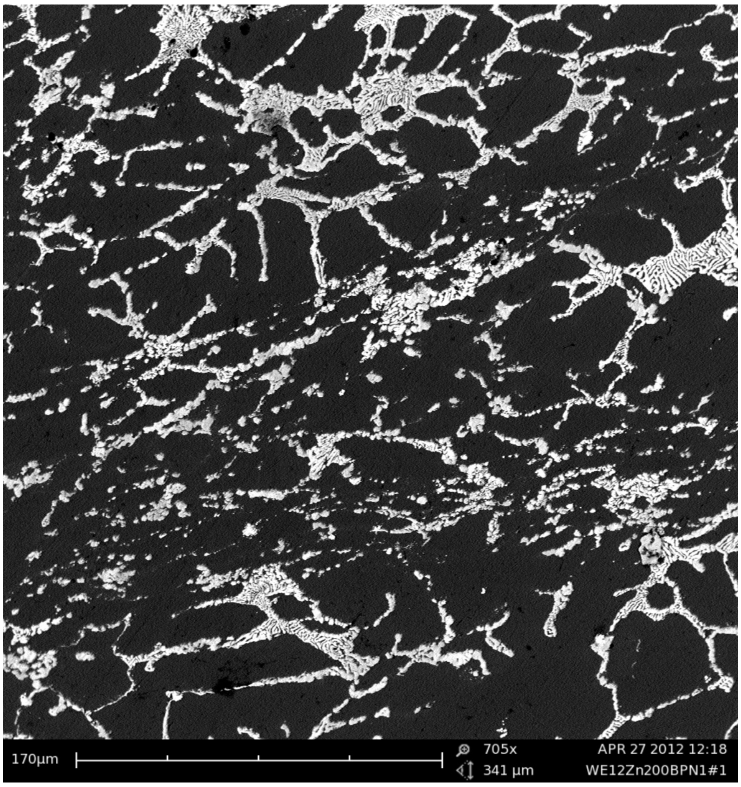

Figure 5.56: SEM image of WE43+14ZnE200 sample after 1 pass, the normal direction. The micrograph was taken with higher magnification than figure 5.55 and shows bands of localized deformation.

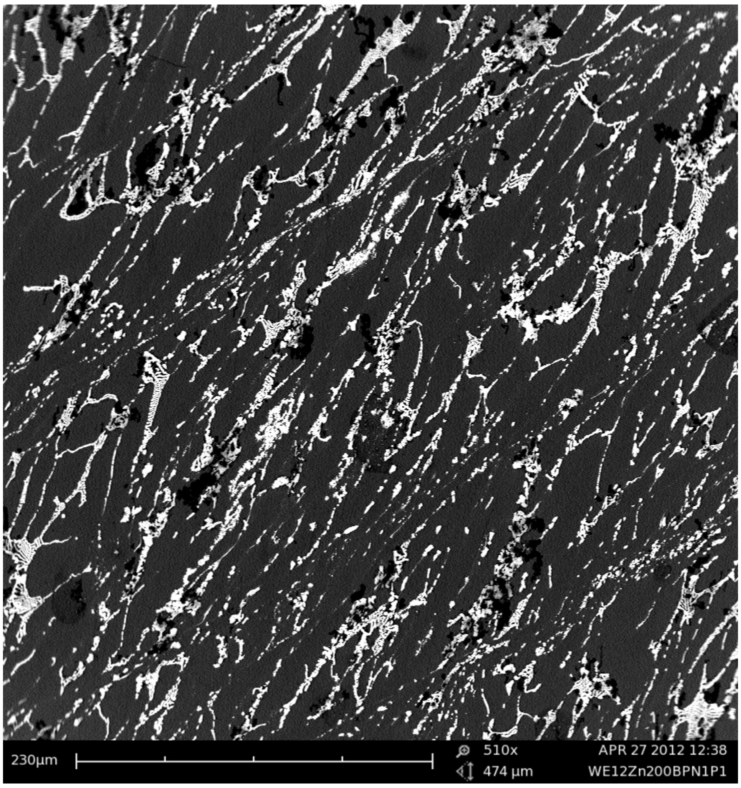

Figure 5.57: SEM image of WE43+14ZnE200 sample after 1 pass, the parallel direction.

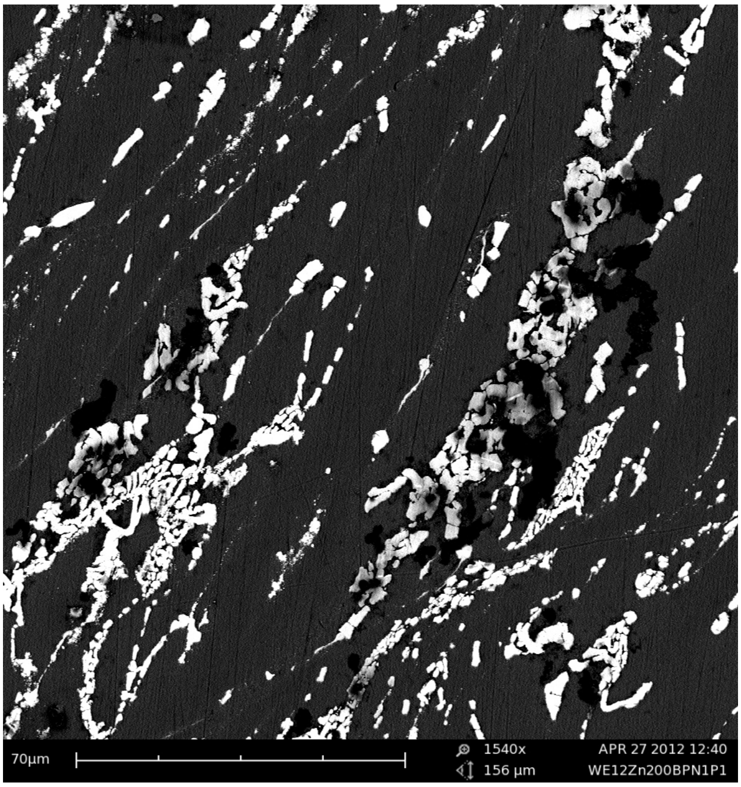

Figure 5.58: SEM image of WE43+14ZnE200 sample after 1 pass, the parallel direction. A detail of broken icosahedral phase.

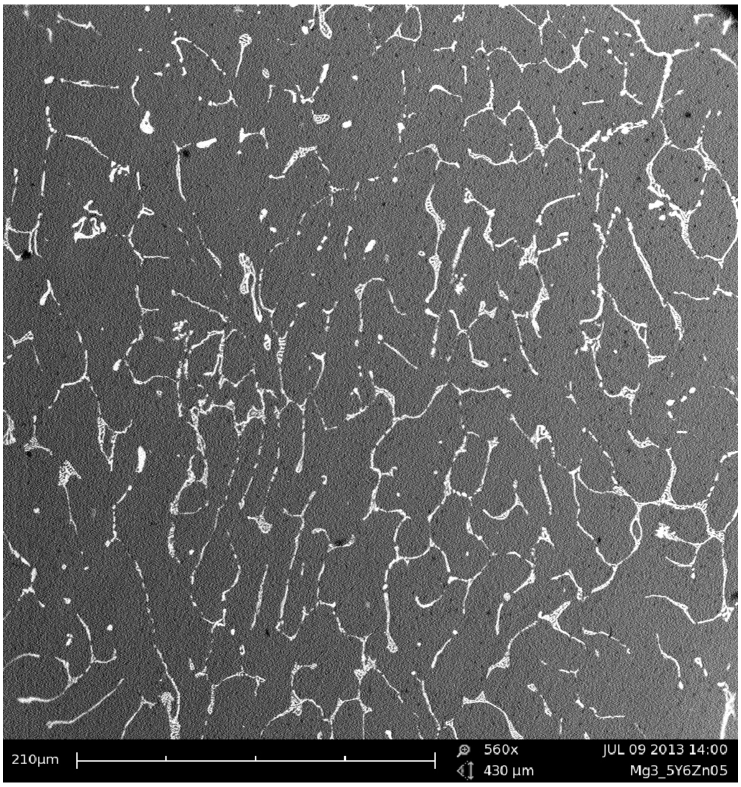

Figure 5.59: SEM image of Mg3Y6ZnE200 sample after 1 pass, the normal direction.

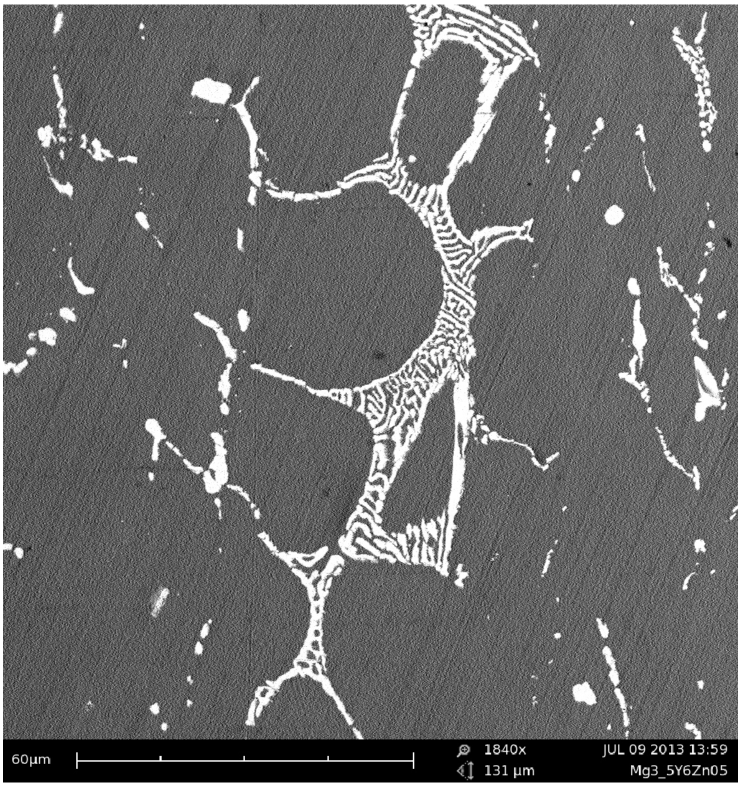

Figure 5.60: SEM image of Mg3Y6ZnE200 sample after 1 pass, the normal direction. A detail of deformed W-phase.

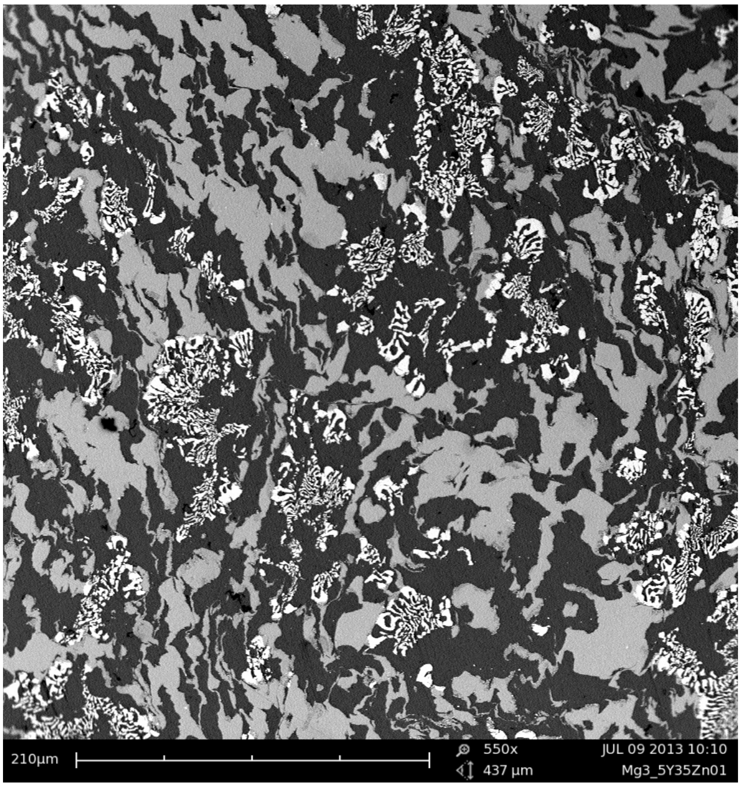

Figure 5.61: SEM image of Mg4Y26ZnE140 sample after 4 passes, the normal direction.

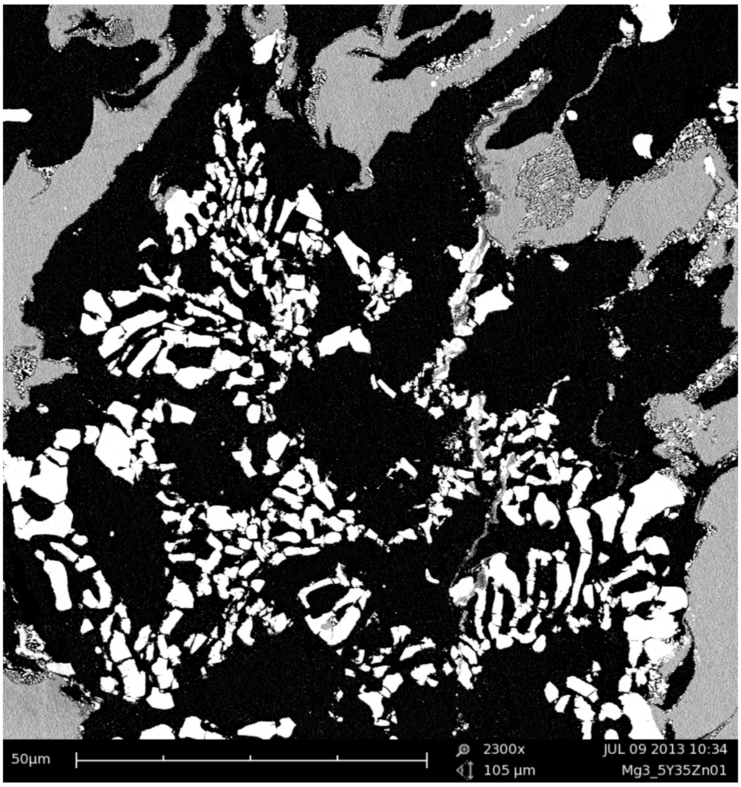

Figure 5.62: SEM image of Mg4Y26ZnE140 sample after 4 passes, the normal direction. A detail of broken icosahedral phase.

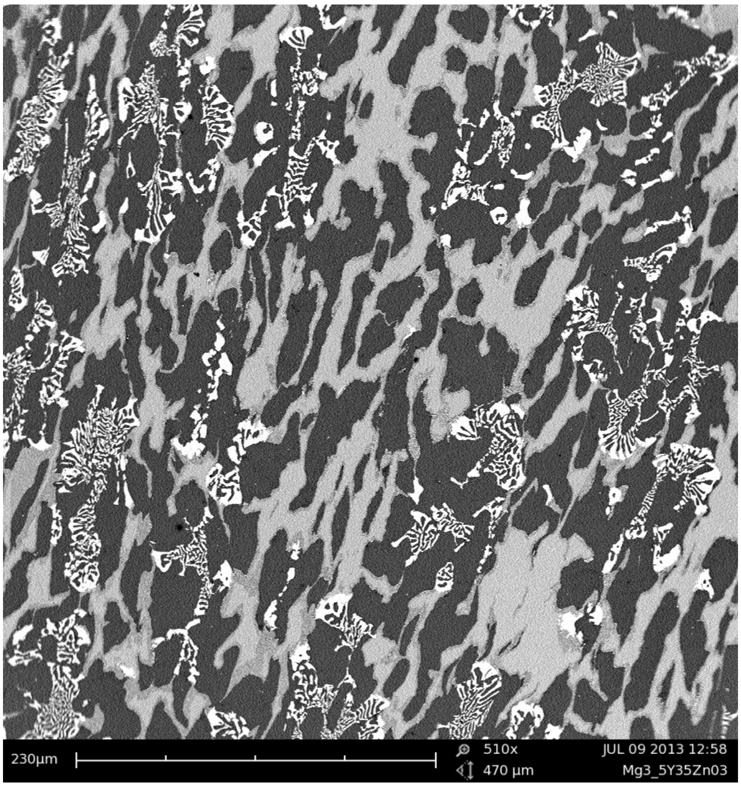

Figure 5.63: SEM image of Mg4Y26ZnE200 sample after 4 passes, the normal direction.

Figure 5.64: SEM image of Mg4Y26ZnE200 sample after 4 passes, the normal direction. A detail showing ductility of Mg-Zn phases in the zone of localized deformation.

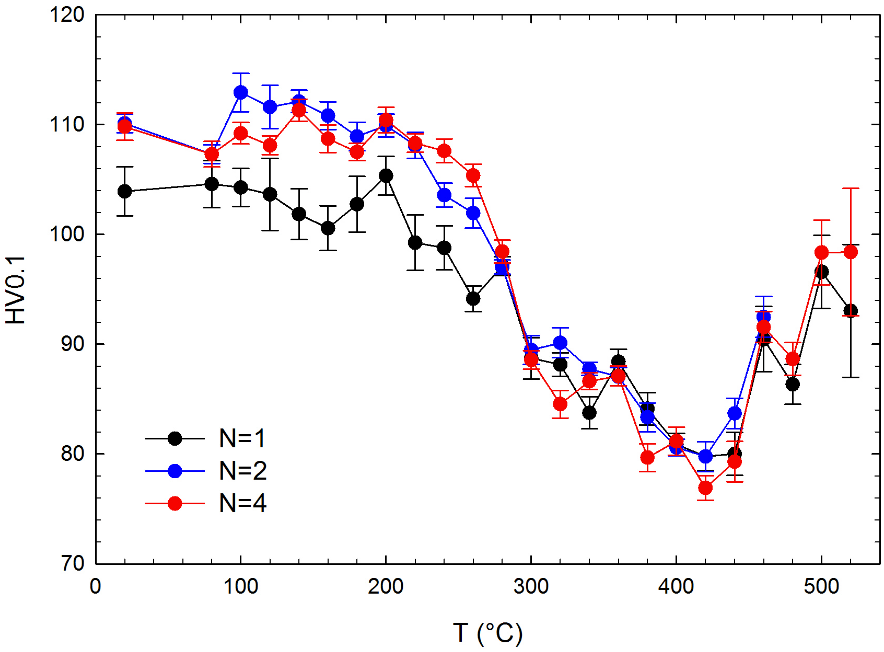

Figure 5.65: The evolution of hardness of WE43+14ZnE200 samples after 1, 2 and 4 ECAP passes during isochronal annealing.

5.3.3 *In situ* XRD during compression test

A compression tests of the as-cast Mg4Y26Zn alloy and ECAP-processed Mg4Y26ZnE140 sample after 4 ECAP passes were performed in order to elucidate the influence of ECAP on mechanical properties of Mg4Y26Zn alloy. Cylindrical samples with diameter of 5.4 mm and length of 10 mm were deformed at 140°C, which is the temperature used for production of Mg4Y26ZnE140 sample by ECAP. The compression was performed under a constant true strain rate $\dot{\epsilon}_t = 0.001$ s^{-1}.

Resulting engineering stress-strain curves are plotted in figure 5.66. Periodic spikes in the stress-strain curves are an experimental artifact caused by the hydraulic pump. Surprisingly, the as-cast Mg4Y26Zn alloy shows higher yield stress ($\sigma_{0.2} \sim 175$ MPa) than the ECAP-processed Mg4Y26ZnE140 sample ($\sigma_{0.2} \sim 114$ MPa).

On the other hand, the ECAP-processed Mg4Y26ZnE140 sample exhibits significantly higher ductility and rupture was not reached up to the engineering strain $\epsilon = 0.54$ where the compression test was terminated. Slight decrease in stress σ around $\epsilon = 0.45$ was most probably caused by a flow of the sample out of dilatometer jaws. Lower strength of the ECAP-processed sample leads us to the conclusion that grain boundary sliding occurs during compression of the Mg4Y26ZnE140 sample. It causes the decrease of the yield stress when compared to the as-cast Mg4Y26Zn alloy as well as very high ductility of the ECAP-processed sample.

2D diffractograms of the as-cast Mg4Y26Zn alloy recorded during the compression test are shown in figures 5.67 to 5.69. The force during the compression test was applied in the horizontal direction with respect to the diffractograms. In the undeformed Mg4Y26Zn alloy, distinct diffraction spots can be observed due to coarse-grained structure, see figure 5.67. During the deformation they gradually blend together (see figure 5.68) until almost continuous rings are formed at $\epsilon = 0.30$, see figure 5.69.

The ECAP-processed Mg4Y26ZnE140 sample before deformation exhibits continuous diffraction rings which testify to the small grain size achieved by ECAP. The evolution of the diffraction pattern during the compression test is much more subtle in this case. The intensity of (0 0 2) ring increases at the 3 o'clock and 9 o'clock positions while it decreases 6 o'clock and 12 o'clock positions. Hence, a preferential orientation of basal planes perpendicular to the applied force develops in the Mg4Y26ZnE140 sample during the compressive deformation.

After the compression test, the microstructure of deformed samples was examined by SEM. Micrographs of as-cast Mg4Y26Zn alloy after the compression test are shown in figures 5.72 and 5.73. Large amount of cracks was formed during the compressive deformation of Mg4Y26Zn alloy as a consequence of its low ductility. These cracks are formed in the icosahedral phase (white) as well as in the Mg_7Zn_3 phase (gray). On the other hand, the SEM micrographs of ECAP-processed Mg4Y26ZnE140 sample after the compression test in figures 5.74 to 5.76 testify that no cracks were created in the samples during the compressive deformation.

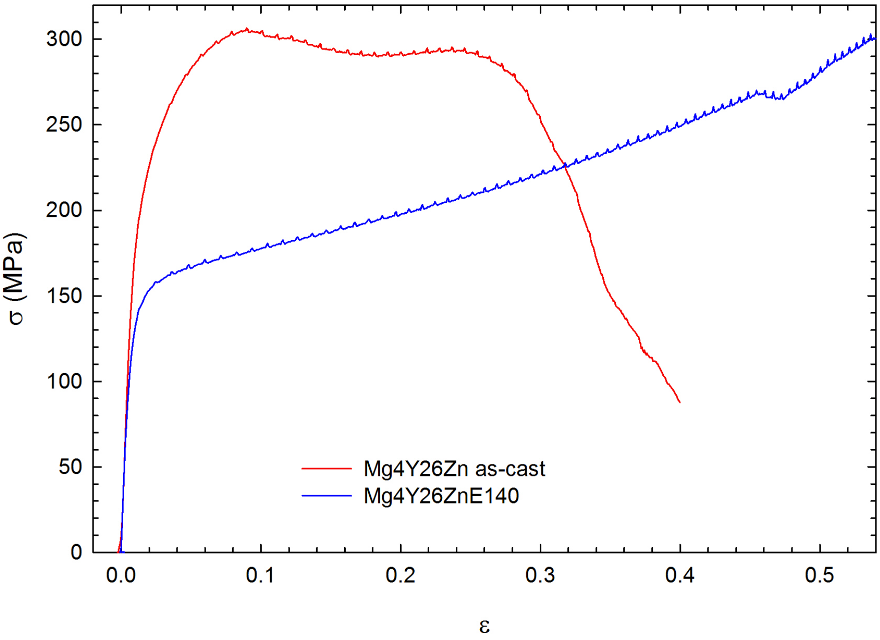

Figure 5.66: Engineering stress-strain curves for a compression test of the as-cast Mg4Y26Zn alloy and the ECAP-processed Mg4Y26ZnE140 sample at 140°C.

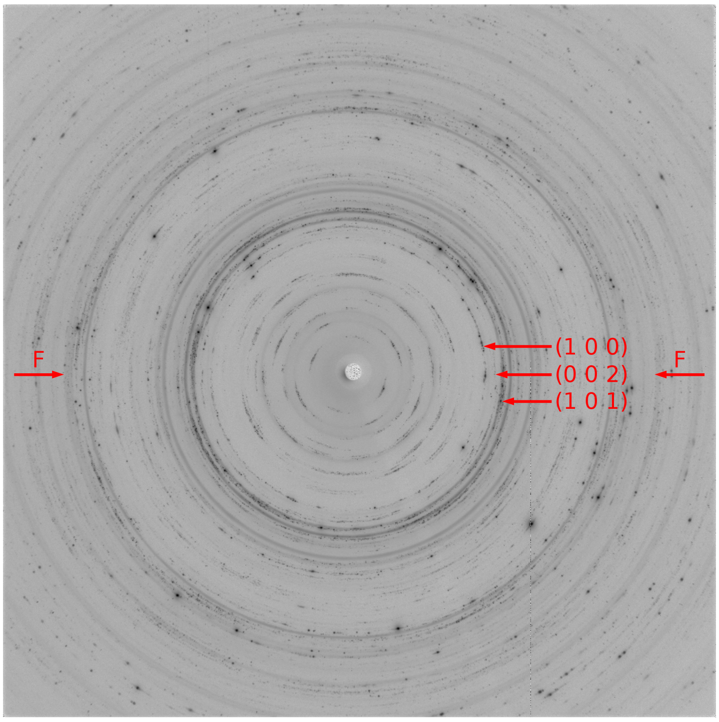

Figure 5.67: 2D diffraction pattern of the as-cast Mg4Y26Zn alloy before the compression test. First three reflections of the Mg matrix are marked by the arrows. Label *F* denotes the direction of applied force.

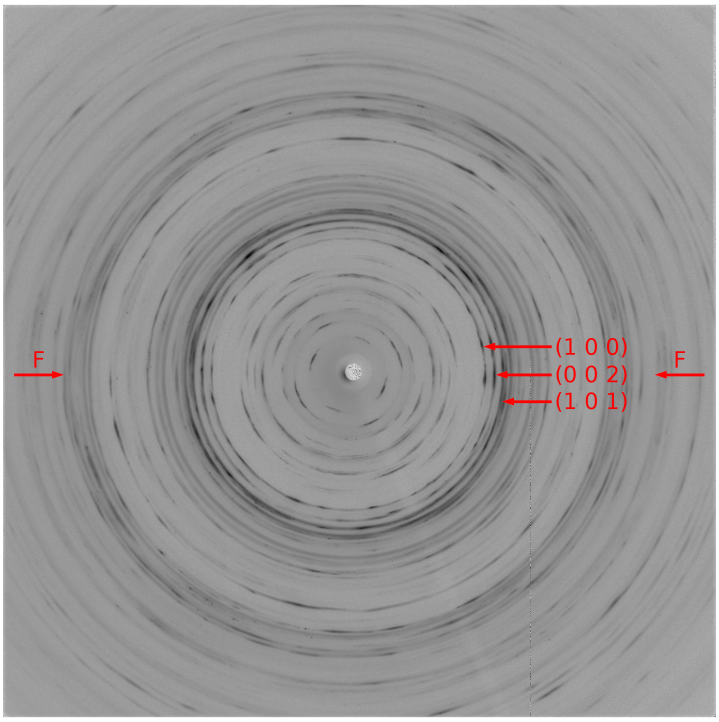

Figure 5.68: 2D diffraction pattern of the as-cast Mg4Y26Zn alloy during the compression test at 140°C. The sample was deformed up to the strain $\epsilon = 0.09$. First three reflections of the Mg matrix are marked by the arrows. Label F denotes the direction of applied force.

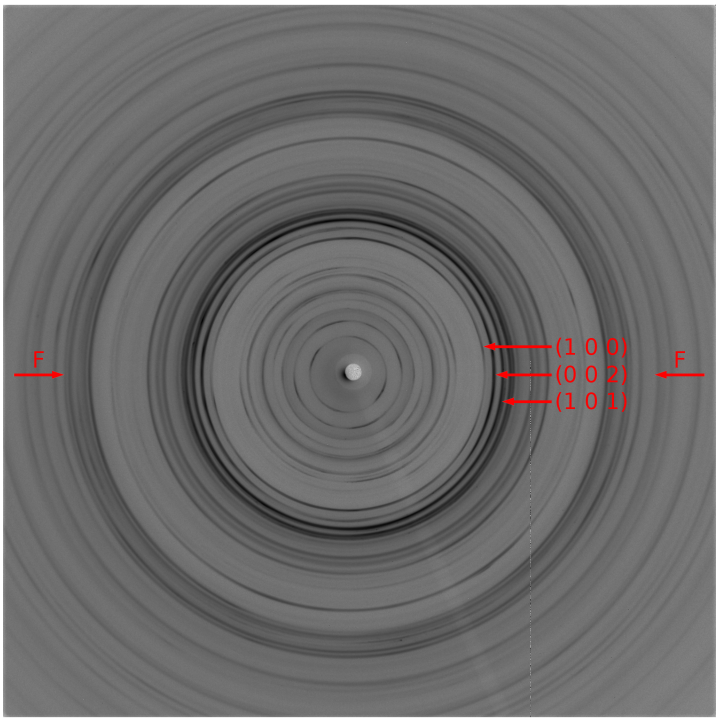

Figure 5.69: 2D diffraction pattern of the as-cast Mg4Y26Zn alloy during the compression test at 140°C. The sample was deformed up to the strain $\epsilon = 0.30$. First three reflections of the Mg matrix are marked by the arrows. Label F denotes the direction of applied force.

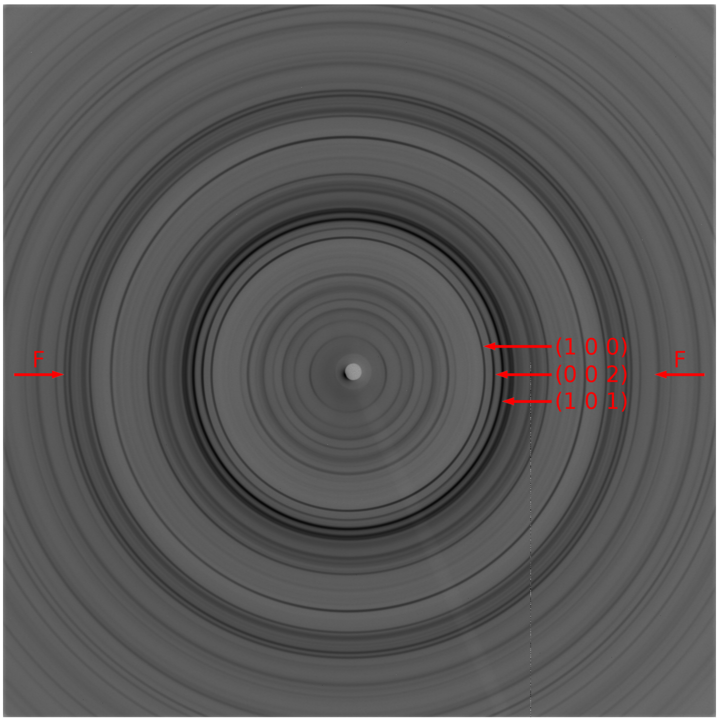

Figure 5.70: 2D diffraction pattern of Mg4Y26ZnE140 sample before the compression test. First three reflections of the Mg matrix are marked by the arrows. Label *F* denotes the direction of applied force.

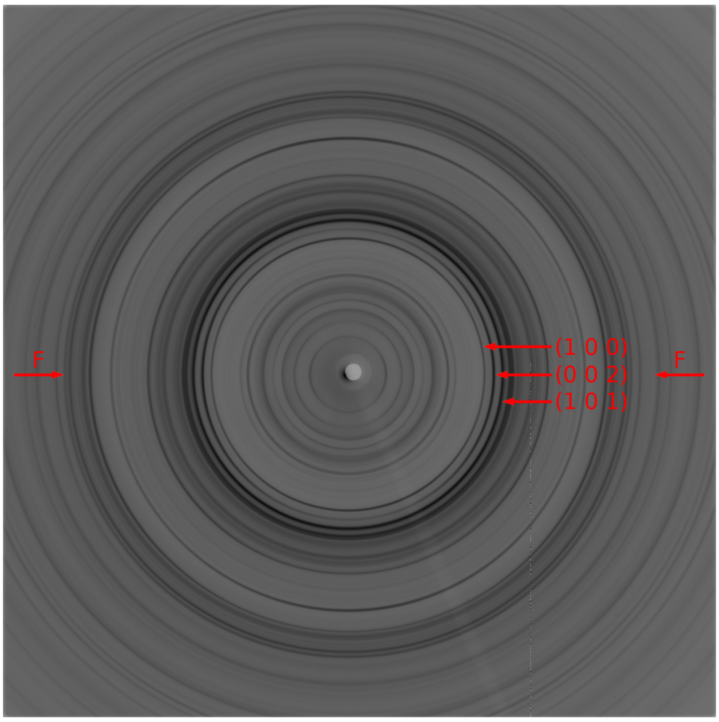

Figure 5.71: 2D diffraction pattern of Mg4Y26ZnE140 sample during compression test at 140°C. The sample was deformed up to the strain $\epsilon = 0.48$. First three reflections of the Mg matrix are marked by the arrows. Label *F* denotes the direction of applied force.

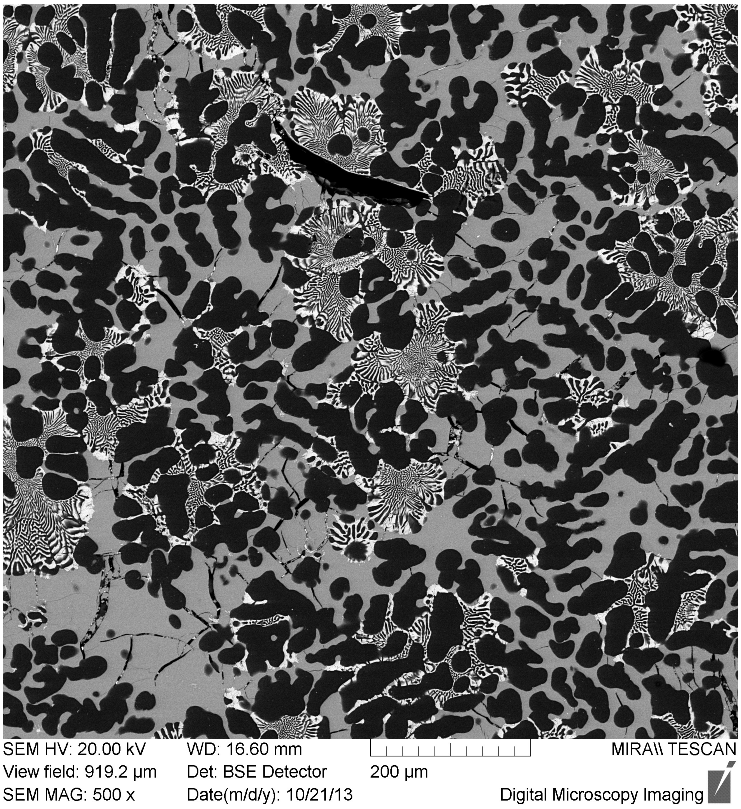

Figure 5.72: SEM image of the as-cast Mg4Y26Zn alloy after the compression test at 140°C.

Figure 5.73: SEM image of the as-cast Mg4Y26Zn alloy after the compression test at 140°C. A detail of cracks formed during the deformation.

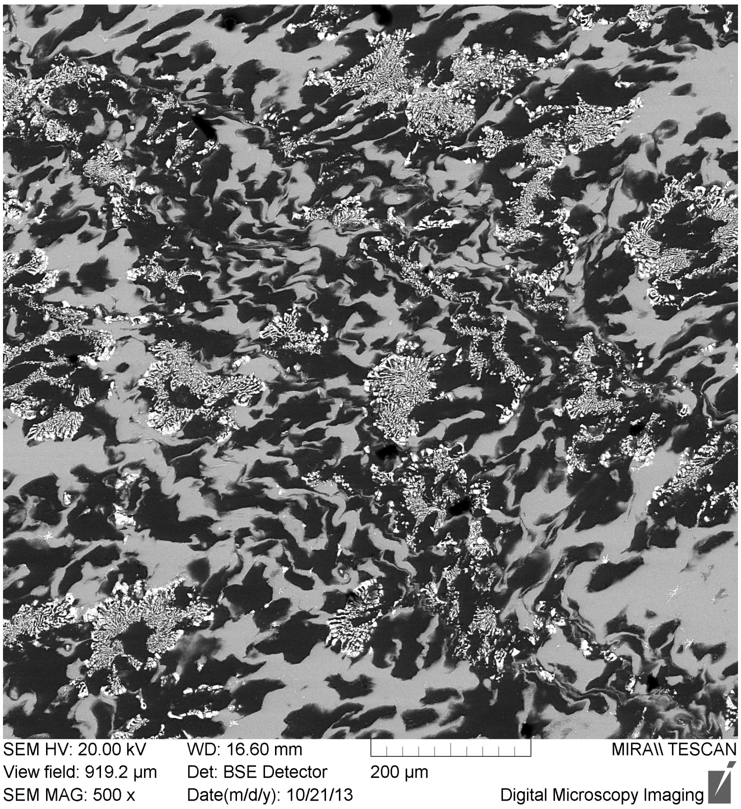

Figure 5.74: SEM image of the ECAP-processed Mg4Y26ZnE140 sample after the compression test at 140°C.

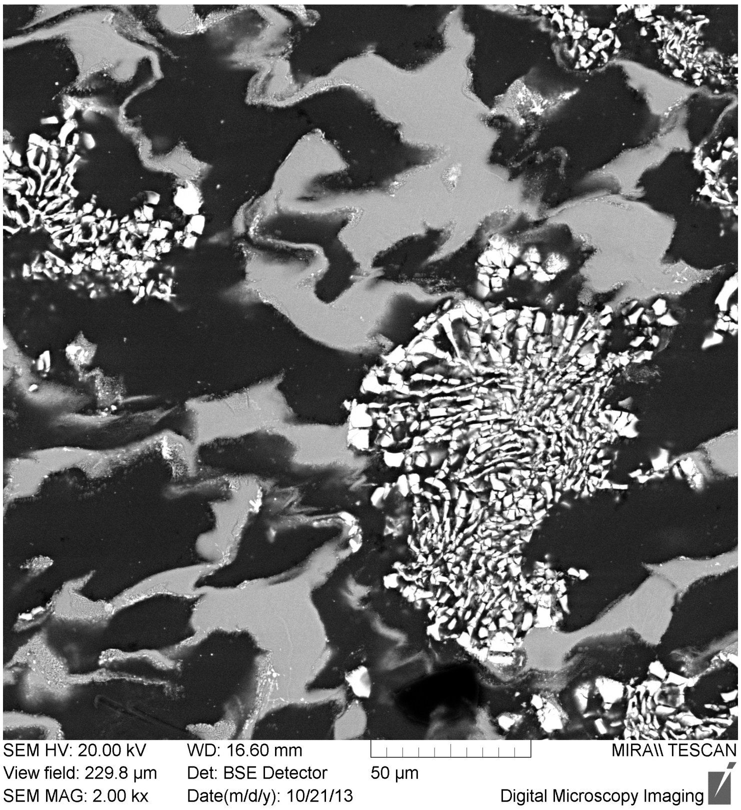

Figure 5.75: SEM image of the ECAP-processed Mg4Y26ZnE140 sample after the compression test at 140°C. A detail showing deformed Mg-Zn particles.

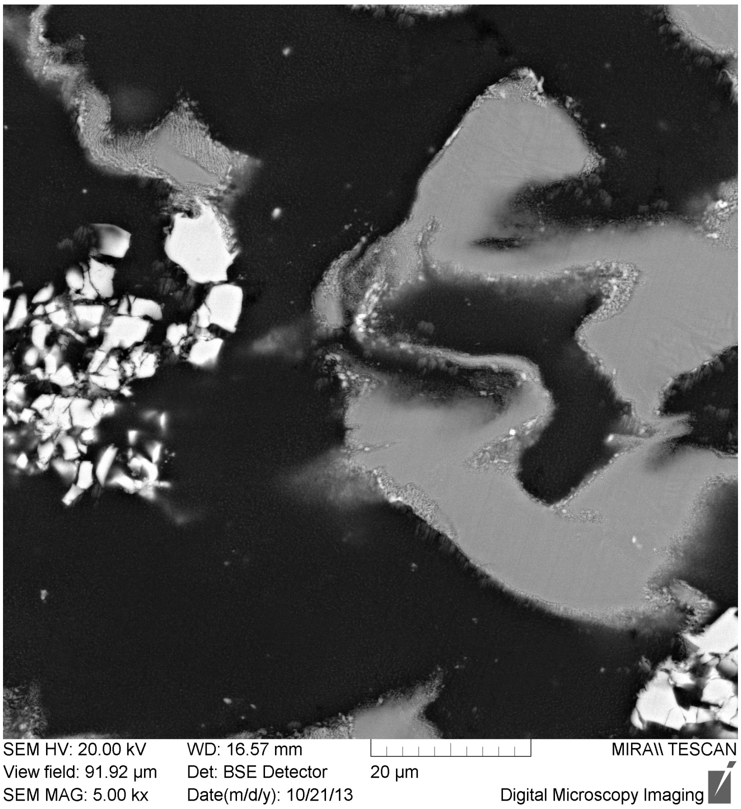

Figure 5.76: SEM image of the ECAP-processed Mg4Y26ZnE140 sample after the compression test at 140°C. A detail of broken icosahedral phase and deformed Mg-Zn particles.

5.3.4 Defect studies

Positron LT measurements were performed on the Mg4Y23ZnE200 sample deformed by 4 ECAP passes. The sample was subjected to isochronal annealing performed in steps 20 K/20 min up to 300°C. The results are shown in figures 5.77 and 5.78. As one can see in figure 5.77, all measured LT spectra of the Mg4Y23ZnE200 sample exhibit two components.

The first component originates in the annihilation of free positrons and its lifetime τ_1 is shorter than the bulk positron lifetime of Mg ($\sim$ 225 ps [50]) due to positron trapping at defects. The second component comes from annihilation of positrons trapped at defects. Lifetime of the second component $\tau_2 \sim 254$ ps is in good agreement with the lifetime of positrons trapped at dislocations in Mg [51, 60, 61].

Dislocations and vacancies were introduced into the sample by severe plastic deformation during ECAP. Vacancies are highly mobile in Mg at room temperature and quickly disappear by diffusion to sinks at grain boundaries and at the surface. However, some vacancies are anchored at the compressive elastic field of dislocations.

Dislocation lines are shallow positron traps incapable of positron confinement. However, vacancies bound to dislocations are deep positron traps. Hence, a positron pre-trapped at dislocation diffuses along the dislocation line until it finds a vacancy attached to dislocation is finally trapped and annihilated there [62].

Since the open-volume of vacancies anchored in the elastic compressive field of dislocations is slightly compressed, the lifetime of positrons trapped at dislocations ($\sim$ 256 ps) is slightly shorter than the lifetime associated with monovacancies in Mg ($\sim$ 300 ps).

The intensity of the second component I_2 slightly decreases during annealing up to 160°C. Above 180°C, there is sharp drop in the I_2 and it further decreases with increasing annealing temperature until a plateau is reached at 260°C. The lifetime of the first component τ_1 increases with decreasing intensity I_2 according to the equation (2.23).

The applicability of STM for analysis of measured LT spectra was verified by calculation of the bulk lifetime τ_B according to equation (2.25). All calculated values of τ_B were in good agreement with the bulk positron lifetime of Mg ($\sim$ 225 ps [50]). The dislocation density ρ_D was calculated from the LT results according to equation (2.24) using the specific trapping rate $\nu_D = 10^{-5} m^2 s^{-1}$ [63]. The result are plotted in figure 5.79.

Except of a drop after annealing at 180°C, the calculated dislocation density of the Mg4Y23ZnE200 sample decreases slowly with increasing annealing temperature. A non-zero dislocation density was detected even after annealing at 300°C. However, it would be expected that recovery of dislocation structure should be completed at this temperature, cf. results obtained on the Mg4Y26ZnE140 and Mg4Y26ZnE200 samples which are discussed in the next part of this this section.

The most likely explanation is that the second component in the LT spectra of the Mg4Y23ZnE200 sample comprises not only positron annihilation at dislocations but also trapping at some other type of defects with comparable open volume.

These defects are likely misfit defects associated with binary Mg-Zn phases. Note that misfit defects characterized by similar lifetime of $\sim$ 260 ps were observed in binary Mg6wt.%Zn alloy [54]. Since the lifetimes of positrons trapped at dislocations and at misfit defects are similar, their contributions in LT spectra cannot be separated.

Nevertheless, we can conclude that positron trapping at misfit defects dominates at 260–300°C where the plateau in the defect concentration was observed. If we would assume that the specific trapping for the misfit defects is $\nu_D = 10^{14} s^{-1}$, i.e. similar value as for monovacancy in Mg, then the concentration of misfit defects in Mg4Y23ZnE200 sample after annealing at 300°C can be estimated as $c_D \sim 2.4 \times 10^{-6}$.

The result of LT measurements for the Mg4Y26ZnE140 and Mg4Y26ZnE200 samples deformed by 4 ECAP passes are shown in figures 5.80 and 5.81. Isochronal annealing of these samples was performed again in steps 20 K/20 min, i.e. with the effective heating rate 1 K/min, but only selected states were examined by the LT spectroscopy.

One can clearly see that the results for the Mg4Y26ZnE140 and Mg4Y26ZnE200 samples are practically identical when the statistical errors of the measurement are taken into account. Therefore, the difference in temperatures used for ECAP processing of these two samples does not play crucial role in the development of defects. The samples annealed up to 260°C exhibit two components in their

LT spectra while only a single component is present in the samples annealed at 300°C.

The first component with the lifetime τ_1 comes again from annihilation of free positrons. The second component with the lifetime $\tau_2 \sim 260$ ps represents a contribution of positrons trapped at dislocations.

The bulk positron lifetime τ_B calculated according to equation (2.25) was found to be in a good agreement with the bulk positron lifetime of Mg ~ 225 ps [50]. Hence, the assumptions of STM are fulfilled and it can be used to estimate the dislocation density in the samples.

The dislocation density in Mg4Y26ZnE140 and Mg4Y26ZnE200 samples determined from the LT data is plotted in figure 5.82. One can see in the figure that only very slight decrease of dislocation density occurred during annealing up to 200°C. A significant decrease in dislocation density was observed after annealing at 260°C and after annealing at 300°C the concentration of dislocations fell below the detection threshold of LT spectroscopy.

Thus, we can conclude that the annealing at temperatures lower than 200°C has marginal impact on the dislocation density and a complete recovery of the dislocation structure starts above 200°C and is finished at 300°C. This behavior also explains the practically identical dislocation densities of the ECAP-processed Mg4Y26ZnE140 and Mg4Y26ZnE200 samples in the as-deformed state.

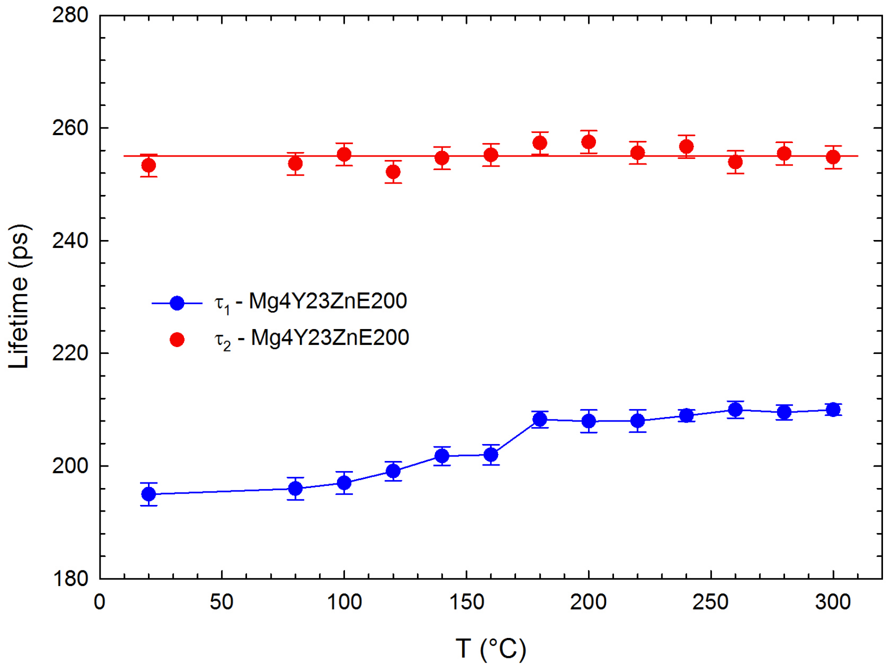

Figure 5.77: The evolution of positron lifetimes during isochronal annealing of the Mg4Y23ZnE200 sample.

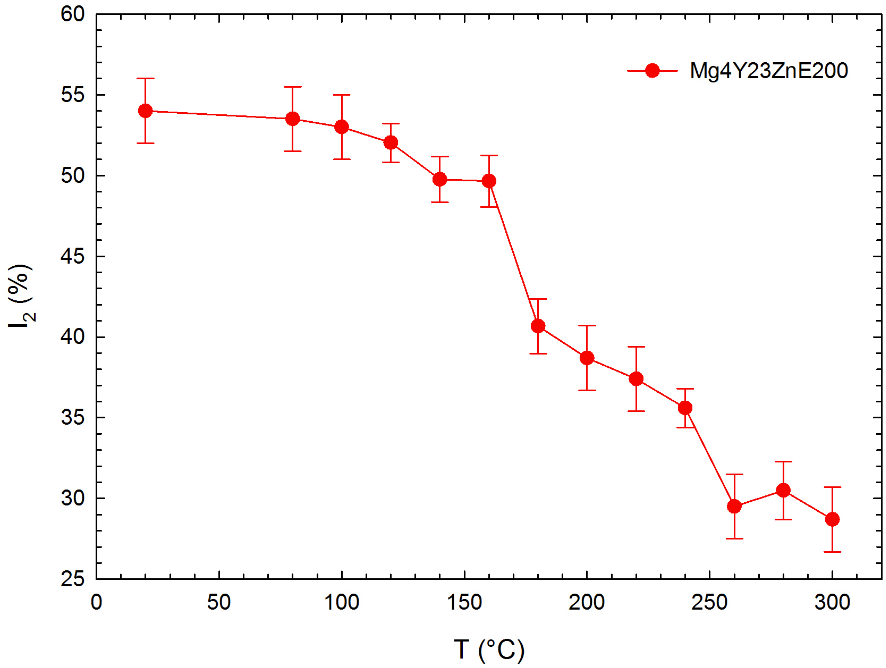

Figure 5.78: Thermal development of the intensity I_2 of the second component in LT spectra corresponding to trapped positrons in the Mg4Y23ZnE200 sample.

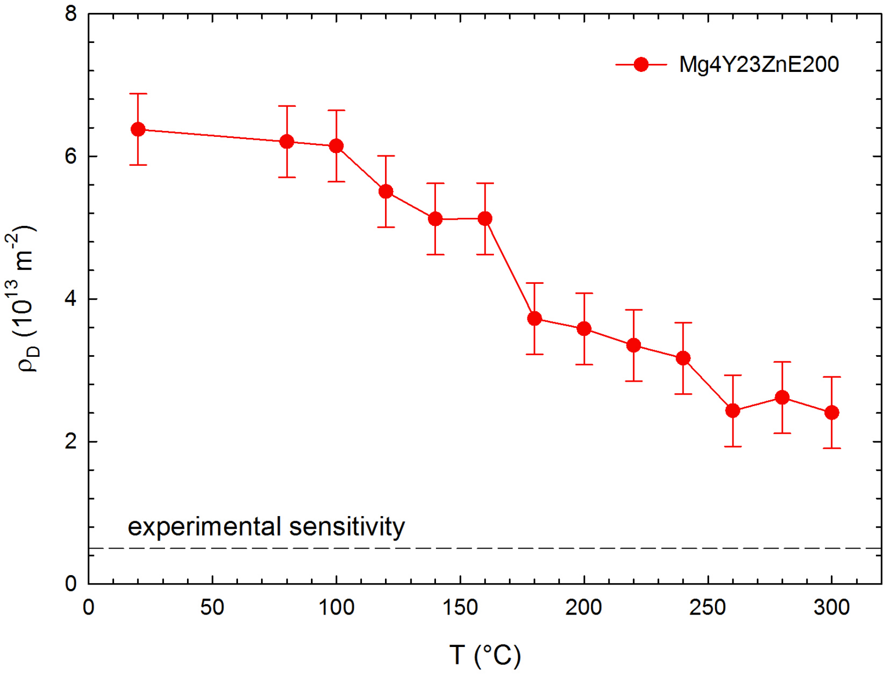

Figure 5.79: The evolution of the dislocation density in Mg4Y23ZnE200 sample during isochronal annealing.

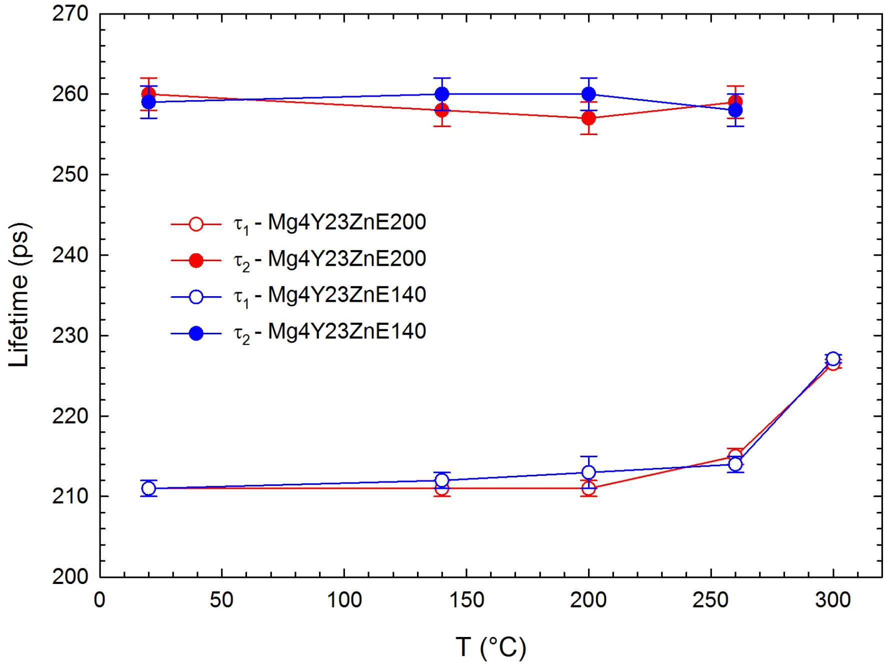

Figure 5.80: The evolution of positron lifetimes during isochronal annealing of the Mg4Y26ZnE140 and Mg4Y26ZnE200 samples.

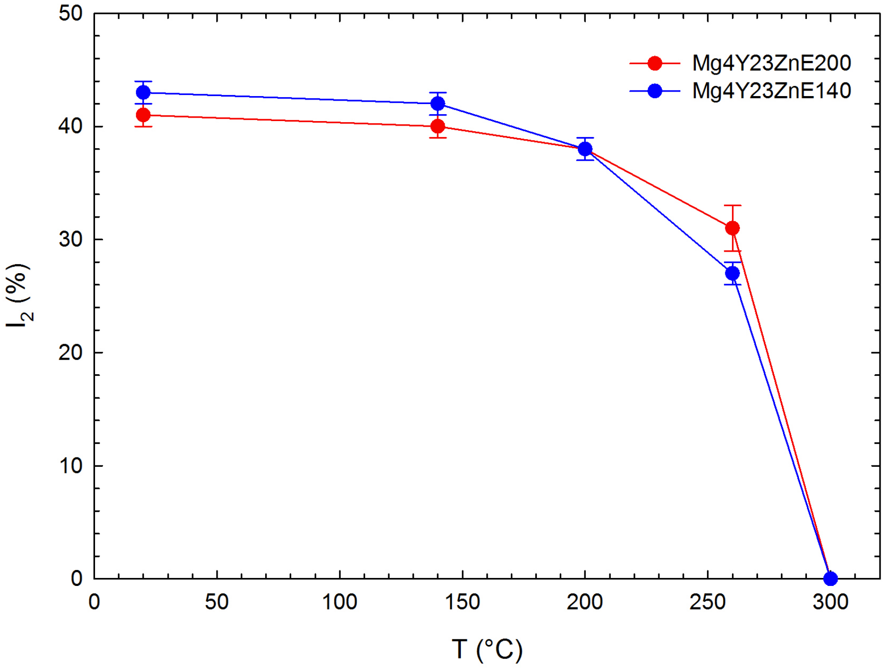

Figure 5.81: The evolution of the intensity I_2 of the second component in LT spectra corresponding to trapped positrons during isochronal annealing of the Mg4Y26ZnE140 and Mg4Y26ZnE200 samples.

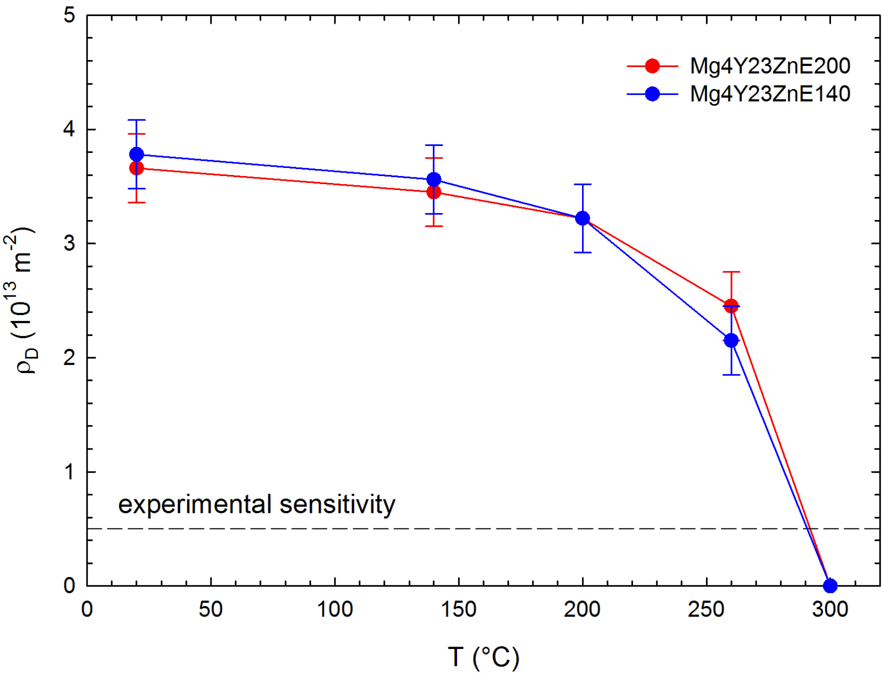

Figure 5.82: The evolution of the dislocation density in the Mg4Y26ZnE140 and Mg4Y26ZnE200 samples during isochronal annealing.

5.3.5 *In situ* XRD during heat treatment of the samples deformed by ECAP

Phase transformations in the ECAP-processed samples WE43+14ZnE200, Mg3Y6ZnE200 and Mg4Y26ZnE140 subjected to 4 passes were studied by *in situ* XRD measurements performed during linear heating and cooling with the rate of temperature change 5 K/min. Two heating and cooling cycles were performed to compare the influence of the ultra-fine-grained structure on the phase transformations in the studied alloys.

The initial 2D diffraction patterns of the studied samples taken in the beginning of *in situ* XRD measurements are shown in figures 5.83 to 5.85. The diffractograms of all ECAP-processed samples consist of continuous rings which testifies their small grain size.

For comparison, a 2D diffraction pattern of WE43+14ZnE200 sample remelted after first heating and cooling cycle is shown in figure 5.86. Coarse grains developed during solidification and distinct diffraction spots can be observed in the latter diffractogram. Since the ultra-fine-grained structure produced by ECAP is destroyed during the first heating cycle, the behavior during cool down and second heating cycle should be identical to the as-cast alloys.

1D diffractograms were obtained from the measured 2D diffractograms by an azimuthal integration. Initial 1D diffractograms of samples in as-deformed state, i.e. at the beginning of the *in situ* measurement, are shown in figure 5.87. The following intermetallic phases were identified in these samples. The WE43+14ZnE200 sample contains W-phase as well as icosahedral phase while only the W-phase is present in the Mg3Y6ZnE200 sample. In the Mg4Y26ZnE140 sample, binary fcc Mg_7Zn_3 phase and icosahedral phase are present.

2D images showing the evolution of the XRD patterns are presented in figures 5.88 to 5.90. Since it is not possible to include several thousand measured diffractograms separately, individual 1D XRD patterns are shown as horizontal lines and their intensity was converted to color. The evolution of the XRD patterns during the heat treatment is shown in the vertical direction.

The temperature ranges of the occurrence of various phases were determined from the measured XRD data. The results are presented in table 5.17.

	State	W-phase	I-phase	Mg_7Zn_3	Z-phase
WE43+14ZnE200	1st heating	470^a	430^a	-	-
	cooling	460^b	415^b	-	-
	2nd heating	490^a	430^a	-	-
Mg3Y6ZnE200	1st heating	490^a	-	-	-
	cooling	510^b	-	-	-
	2nd heating	520^a	-	-	-
Mg4Y26ZnE140	1st heating	-	425^a	245^c, 340^{ae}	245^d, 340^e
	cooling	-	405^b	330^b	-
	2nd heating	-	430^a	250^c, 340^{ae}	215^d, 340^e

Table 5.17: Phase transformation temperatures of intermetallic phases in the ECAP-processed samples obtained from *in situ* XRD studies. Indices denote type of phase transformation: a - melting, b - solidification, c - dissolution, d - precipitation, e - transformation of Z-phase to Mg_7Zn_3 phase.

During the first heating cycle of WE43+14ZnE200 sample, the icosahedral phase melts at temperature ~ 430°C. Presence of the liquid phase is testified by appearance of a diffuse bump in the background. Peaks corresponding to the W-phase remain visible up to ~ 470°C. During the cooling, W-phase and icosahedral phase form from melt at ~ 460°C and ~ 415°C, respectively. The melting temperatures of W-phase and icosahedral phase during the second heating cycle were ~ 490°C and ~ 430°C, respectively.

The W-phase, which is the only intermetallic phase presnent in Mg3Y6ZnE200, melted at ~ 490°C during the first heating cycle and at ~ 520°C during the second heating cycle. The temperature of solidification of W-phase during the cooling cycle was determined as ~ 510°C.

The as-prepared Mg4Y26ZnE140 sample contains the Mg_7Zn_3 phase and the icosahedral phase. The icosahedral phase exhibits higher temperature stability than the Mg_7Zn_3 phase and it remains present up to ~ 425°C during the first heating cycle and up to ~ 430°C during the second one. The solidification of icosahedral phase during the cooling cycle was observed at ~ 405°C.

Binary Mg-Zn phases exhibit more complex behavior in the Mg4Y26ZnE140 sample. During the first heating cycle, the Mg_7Zn_3 phase transforms to the Z-phase at ~ 245°C which remains present up to ~ 340°C. At this temperature, the Z-phase transforms back to the Mg_7Zn_3 phase which melts just after this transformation. During cooling the Mg_7Zn_3 phase solidifies at ~ 330°C and then stays in the sample during the whole cooling cycle.

Similar transformation sequence of binary Mg-Zn phases occurs during the second heating cycle. The only difference is that the Mg_7Zn_3 phase and the Z-phase coexist in the temperature range 215–250°C. The peaks corresponding to the Mg_7Zn_3 gradually disappears while the intensity of Z-phase peaks increases in this temperature region. Above ~ 250°C only the Z-phase is present in the sample. The transformation of the Z-phase back to the Mg_7Zn_3 phase and subsequent melting of the Mg_7Zn_3 phase occurs at ~ 340°C like in the first heating cycle.

The diffraction peaks shift to lower diffraction angles with increasing temperature due to thermal expansion of the crystal lattice. Like in the section 5.2.3, one can notice that diffraction peaks corresponding to icosahedral phase form bent curves which indicate a nonlinearity in the thermal expansion of icosahedral phase. This behavior can be clearly seen in the 2D image shown in figure 5.88 which corresponds to the WE43+14ZnE200 sample. Peaks of the binary Mg-Zn phases present in the Mg4Y26ZnE140 sample overlap with the peaks of icosahedral phase and make the observation of this effect in figure 5.48 more difficult.

The positions of selected diffraction peaks were fitted by pseudo-Voigt function to quantify the thermal expansion of the Mg matrix, icosahedral phase, W-phase and the graphite crucible during the first heating cycle of the WE43+14ZnE200 sample. The positions obtained from fitting were used to calculate the relative lattice expansion with respect to the room temperature which is plotted figure 5.91.

The expansion of the Mg matrix exhibits an abrupt change at ~ 430°C at which the icosahedral phase melts. This is caused by the fact, that in addition to the thermal expansion, the lattice parameter of Mg matrix also depends on the concentration of dissolved alloying elements. Addition of Zn causes a decrease of the lattice parameter, see discussion of CDB results in section 5.1.3. The solubility of Zn in Mg reaches maximum at the eutectic temperature, see figure 3.4.

Hence, the decrease of the lattice parameter of the Mg matrix caused by dissolved Zn will be largest at the eutectic temperature. In the WE43+14ZnE200 sample, this temperature coincides with the the melting point of icosahedral phase. The concentration of dissolved Zn in Mg matrix decreases above this temperature and the observed lattice expansion is the sum of thermal expansion and the expansion caused by decrease of the Zn content in the Mg matrix.

The W-phase exhibits a linear expansion up to ~ 430°C where the expansion slightly decreases and stays constant until the melting of this phase. The change of behavior at this temperature is most likely caused by the fact that some fraction of icosahedral phase transforms to W-phase at ~ 430°C instead of melting. This is testified by the increase of intensities of XRD peaks corresponding to the W-phase at ~ 430°C, see figure 5.88. Newly formed W-phase might not exhibit the exact stoichiometric composition which significantly influences its lattice parameter.

The remarkable nonlinearity is present in the thermal expansion of the icosahedral phase. The coefficient of its thermal expansion at first slightly decreases around ~ 220°C and then the thermal expansion accelerates around ~ 300°C. This behavior leads us to the conclusion that structural changes, e.g. generation of large amount of defects leading to a gradual change of thermal expansion, most likely occur in the icosahedral phase at elevated temperatures. However, the exact nature of this process cannot be determined from the results presented in this work.

Since the temperature measured by the thermocouple was not measured directly at the place of the primary beam, the thermal expansion of the (0 0 2) peak of graphite was used to calculate the temperature of the graphite crucible in which the samples were placed. A comparison of the temperature calculated from the thermal expansion of graphite and the temperature measured by the thermocouple welded to the steel cap of the crucible during the heating and cooling cycles of the Mg3Y6ZnE200 sample is shown in figure 5.92. Both temperatures are in an excellent agreement.

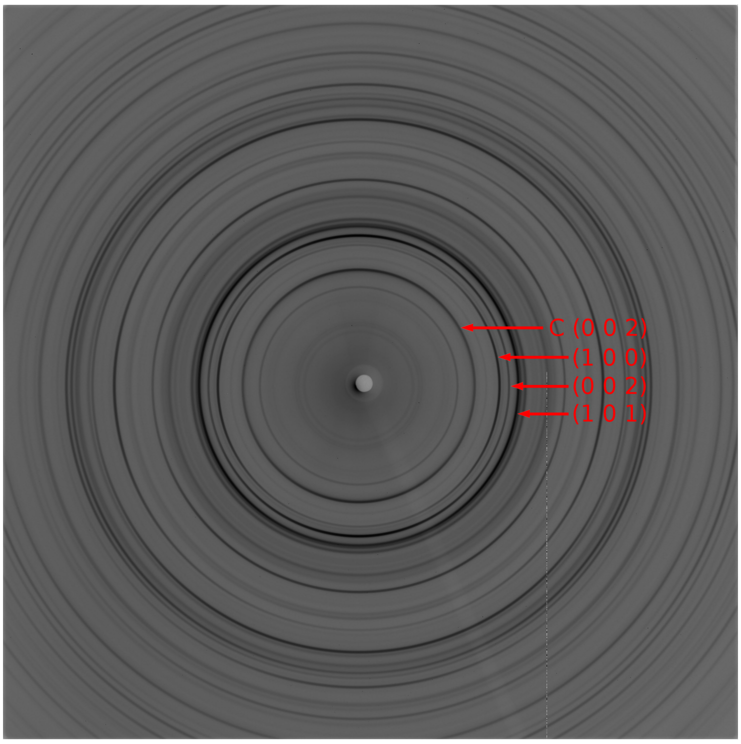

Figure 5.83: 2D diffraction pattern of the ECAP-processed WE43+14ZnE200 sample in the as-deformed state. First three reflections of the Mg matrix and the (0 0 2) reflection of graphite (C) are marked by the arrows.

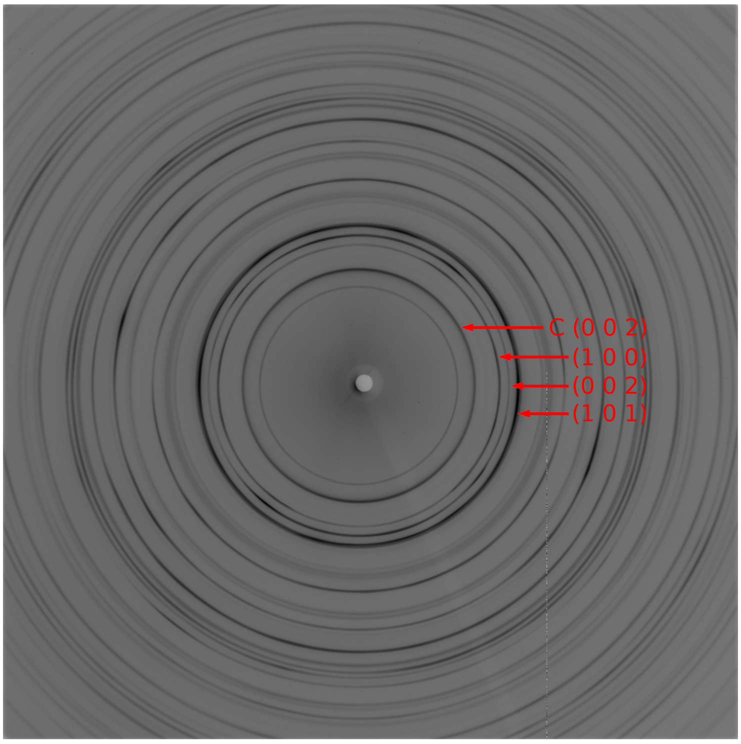

Figure 5.84: 2D diffraction pattern of the ECAP-processed Mg3Y6ZnE200 sample in the as-deformed state. First three reflections of the Mg matrix and the (0 0 2) reflection of graphite (C) are marked by the arrows.

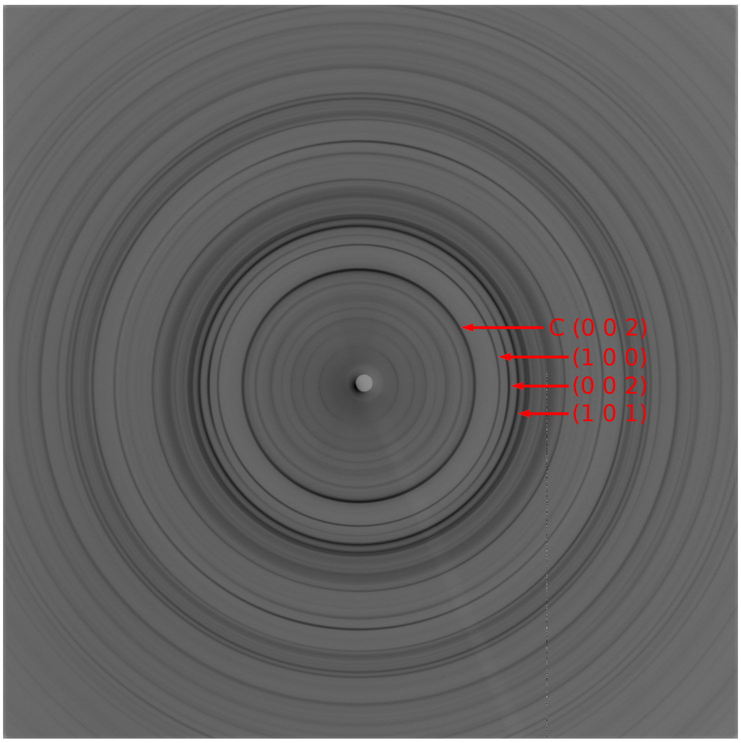

Figure 5.85: 2D diffraction pattern of the ECAP-processed Mg4Y26ZnE140 sample in the as-deformed state. First three reflections of the Mg matrix and the (0 0 2) reflection of graphite (C) are marked by the arrows.

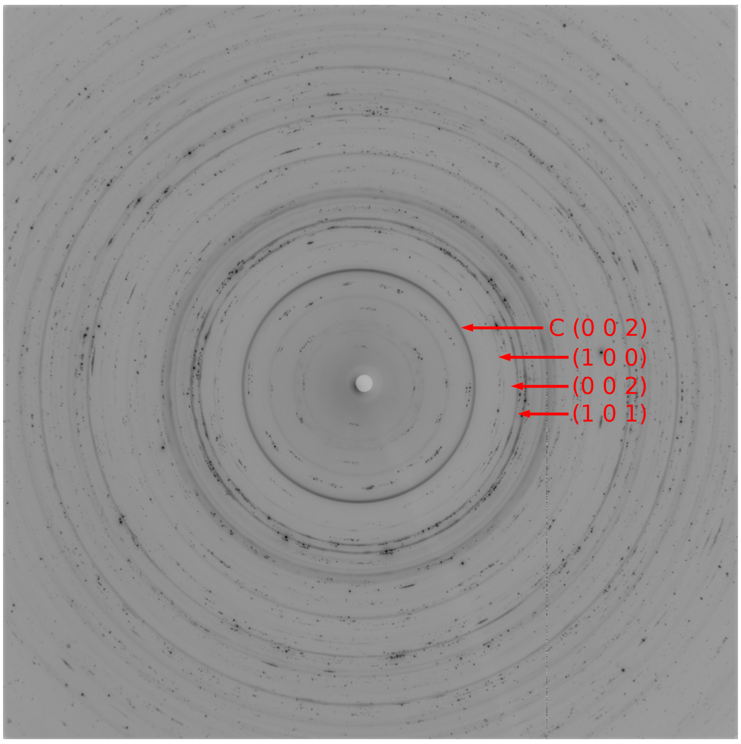

Figure 5.86: 2D diffraction pattern of the Mg4Y26ZnE140 sample heated up to 470°C and subsequently cooled down to 80°C.

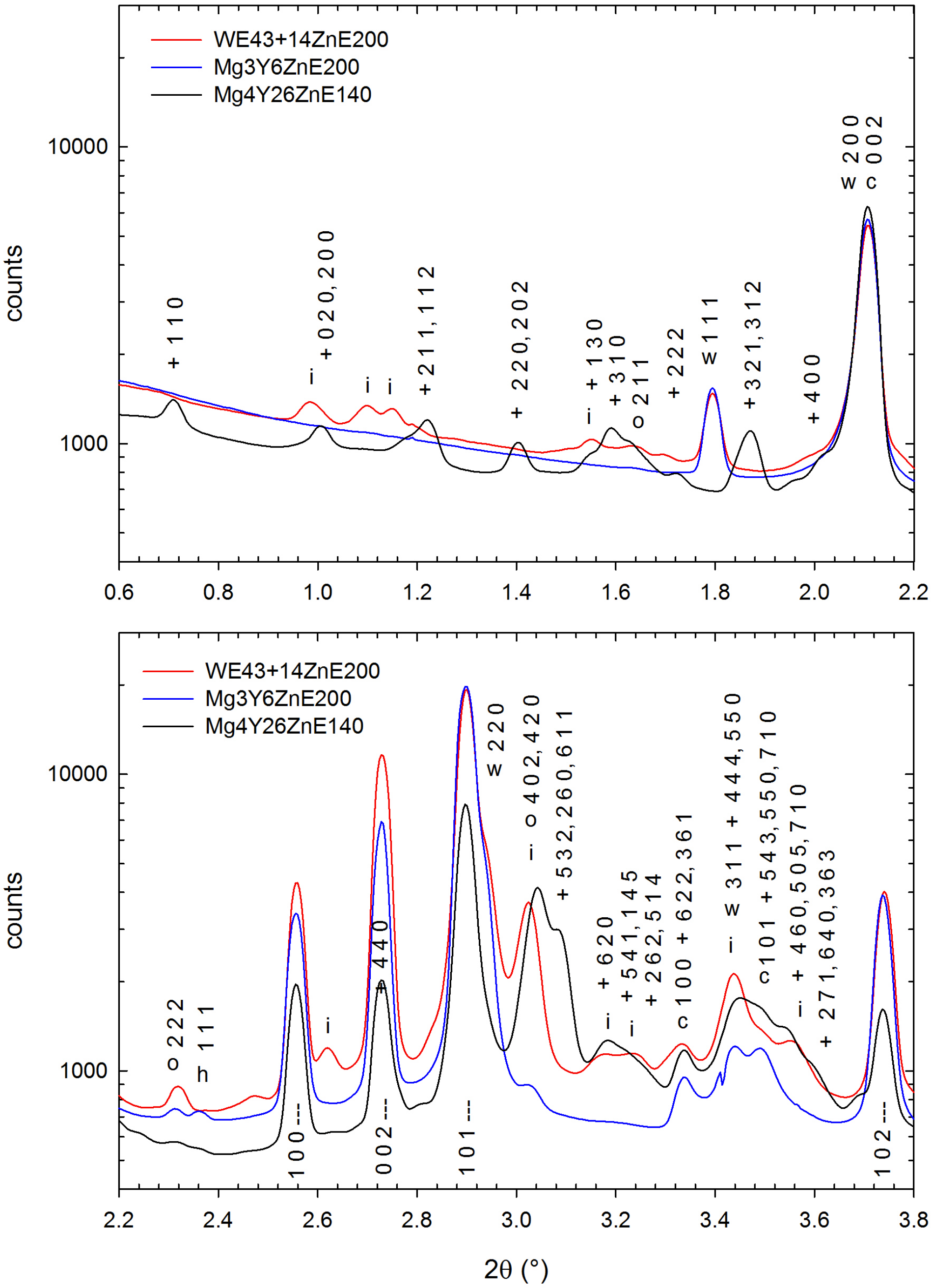

Figure 5.87: 1D diffractograms of the ECAP-processed samples in the as-deformed state ($\lambda = 0.124$ Å). | - Mg matrix; i - icosahedral phase ($Mg_3Zn_6Y_1$); w - W-phase ($Mg_3Zn_3Y_2$); + - Mg_7Zn_3; c - graphite; o - Y_2O_3; h - YH_2.

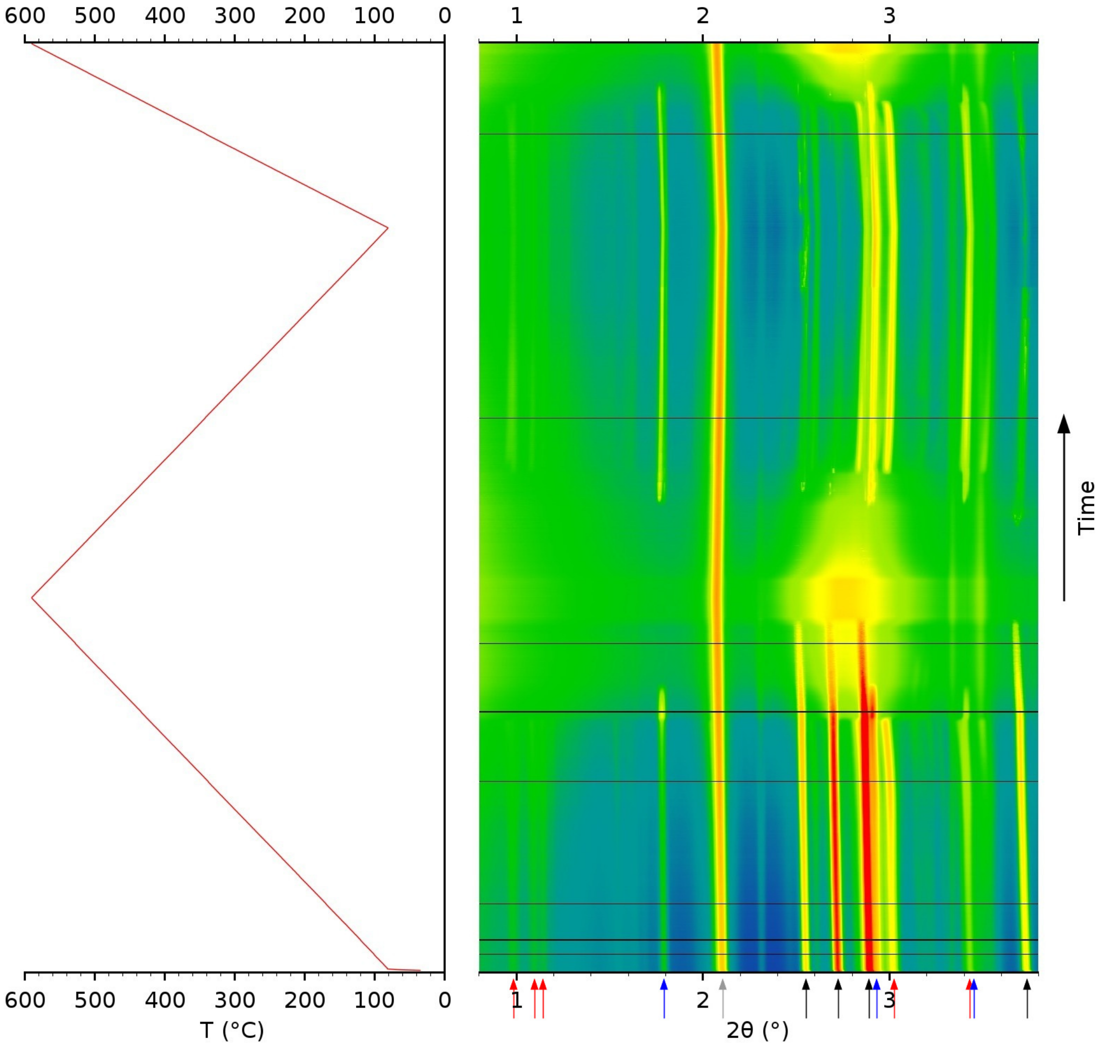

Figure 5.88: The evolution of the XRD patterns of the WE43+14ZnE200 sample during linear heating and cooling between room temperature and 590°C ($\lambda = 0.124$ Å). Each horizontal line in the right section of the figure represents a 1D diffraction pattern at some temperature. The intensity was converted to the color scale and increases from black through violet, blue, green, yellow and orange to red. The temperatures at which the diffractograms were recorded are plotted in the left part of the figure. The most pronounced peaks of Mg matrix (black), I-phase (red), W-phase (blue) and graphite crucible (gray) are marked by colored arrows.

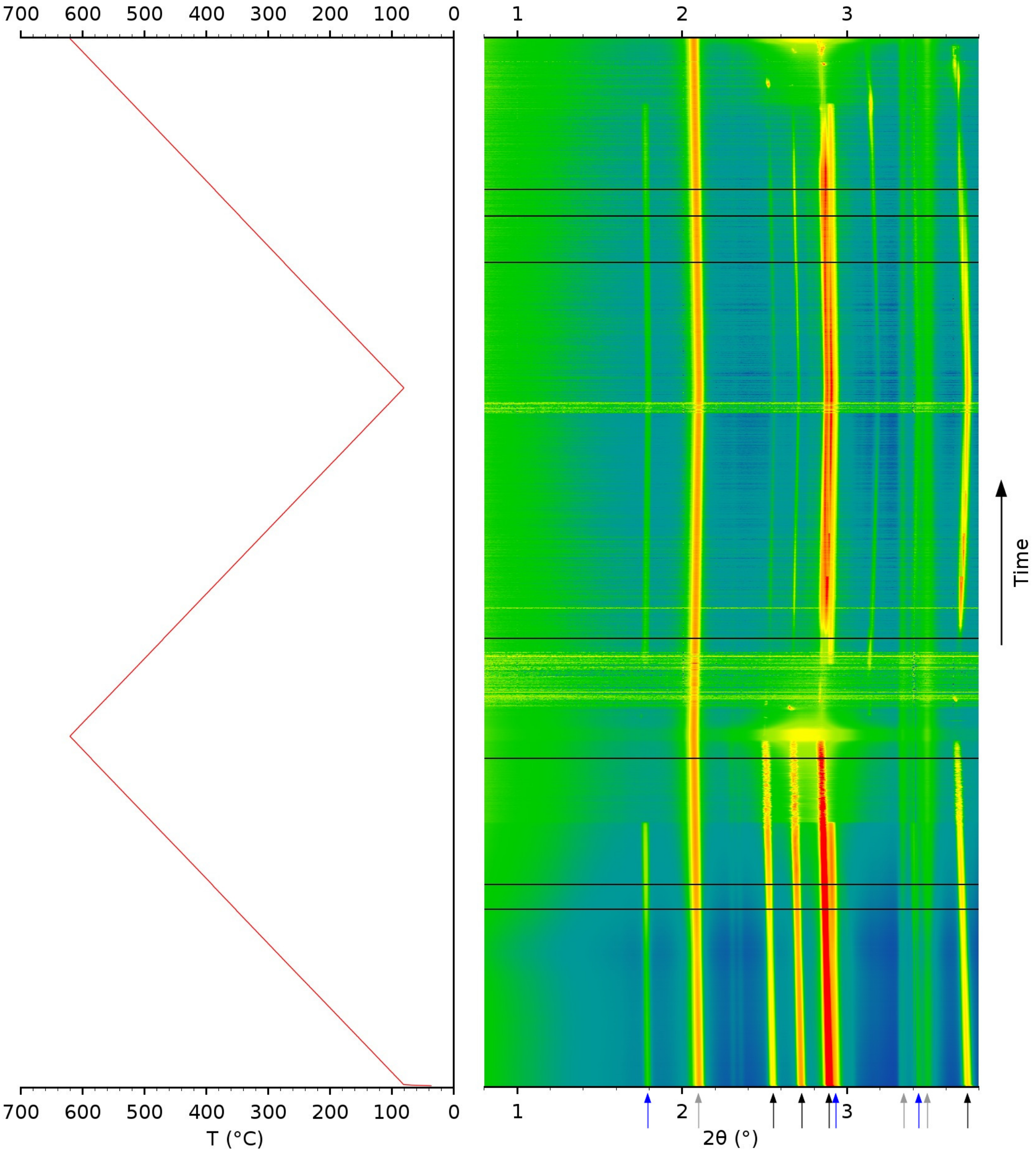

Figure 5.89: The evolution of the XRD patterns of the Mg3Y6ZnE200 sample during linear heating and cooling between room temperature and 620°C ($\lambda = 0.124$ Å). Each horizontal line in the right section of the figure represents a 1D diffraction pattern at some temperature. The intensity was converted to the color scale and increases from black through violet, blue, green, yellow and orange to red. The temperatures at which the diffractograms were recorded are plotted in the left part of the figure. The most pronounced peaks of Mg matrix (black),W-phase (blue) and graphite crucible (gray) are marked by colored arrows.

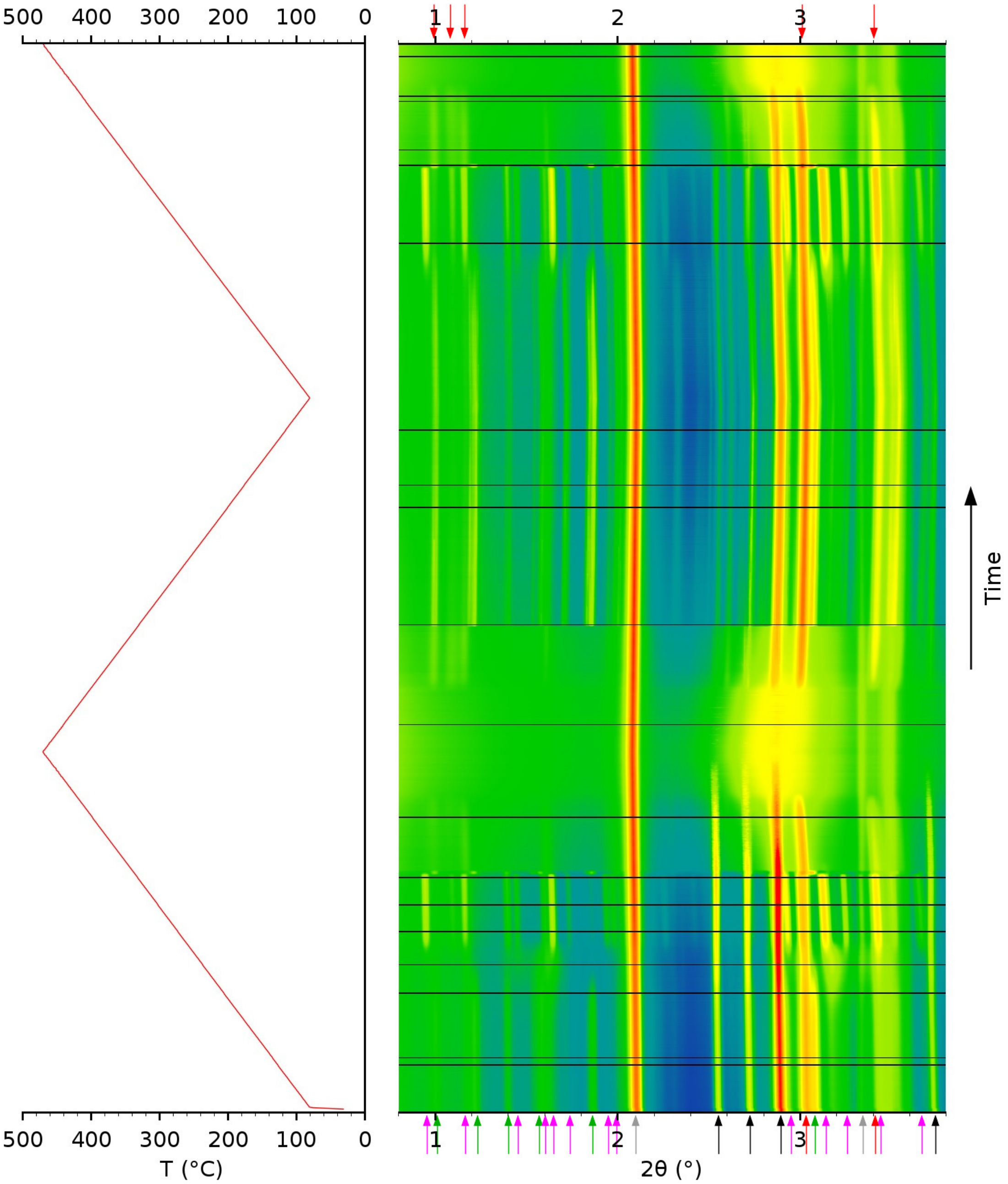

Figure 5.90: The evolution of the XRD patterns of the Mg4Y26ZnE140 sample during linear heating and cooling between room temperature and 470°C ($\lambda = 0.124$ Å). Each horizontal line in the right section of the figure represents a 1D diffraction pattern at some temperature. The intensity was converted to the color scale and increases from black through violet, blue, green, yellow and orange to red. The temperatures at which the diffractograms were recorded are plotted in the left part of the figure. The most pronounced peaks of Mg matrix (black), icosahedral phase (red), Mg_7Zn_3 (green), Z-phase (magenta) and graphite crucible (gray) are marked by colored arrows.

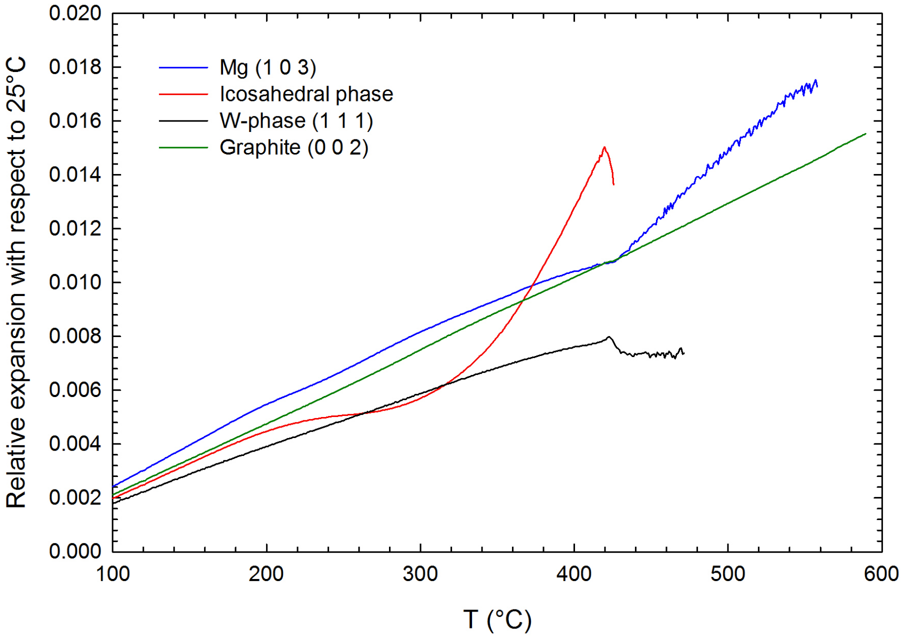

Figure 5.91: The relative thermal expansions of various phases present in the WE43+14ZnE200 sample with respect to 25°C. The thermal expansions were calculated from *in situ* XRD data obtained during the first heating cycle.

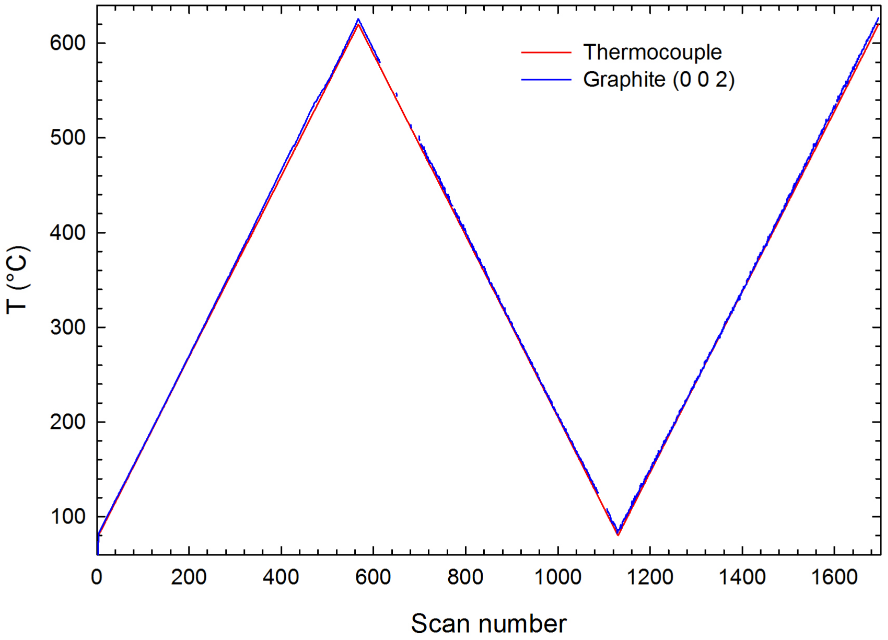

Figure 5.92: Comparison of the temperature measured by the thermocouple and the temperature calculated from thermal expansion of graphite crucible during *in situ* measurement of Mg3Y6ZnE200 sample.

6. Discussion

6.1 As-cast and heat treated samples

The measurements of microhardness and analysis of SEM images revealed that the hardness and the volume fraction of GBP in studied as-cast alloys increases with increasing Zn content, see tables 5.4 and 5.3. To visualize this relationship, the dependencies of the hardness and the volume fraction of GBP on the Zn content are shown in figures 6.1 and 6.2. It is clear that the Zn content is a crucial factor which determines the mechanical properties of studied alloys as well as their microstructure.

The correlation of the microhardness and the volume fraction of GBP plotted in figure 6.3 shows that the microhardness is approximately linear function of the volume fraction of GBP. Since the GBP is much harder than the Mg matrix (see table 5.5), it strengthens the alloys. The linear dependence of the hardness on the volume fraction of GBP suggests that a composite hardening mechanism plays major role in the mechanical properties of the studied alloys. This is further supported by the fact, that majority of cracks which were observed in the as-cast Mg4Y26Zn alloy after the compression test were located in GBP, see figure 5.73.

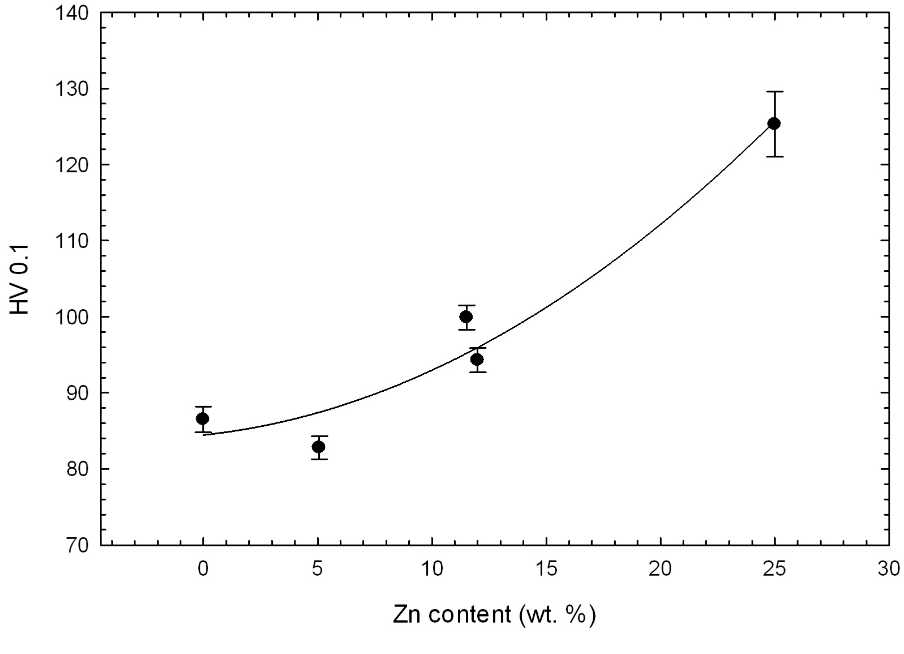

Figure 6.1: The dependence of the Vickers hardness of WE43-based and MgZnAl-based alloys on the Zn content.

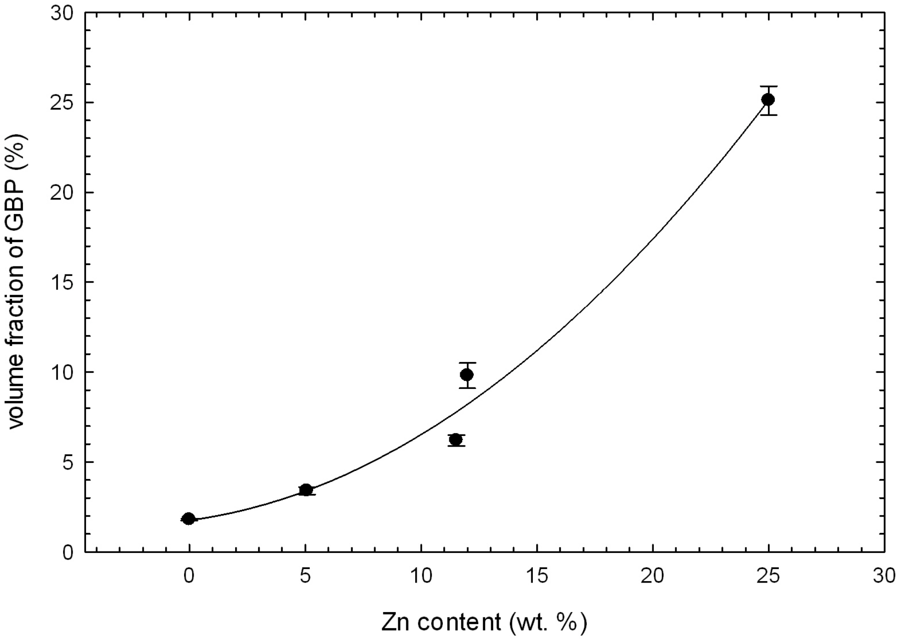

Figure 6.2: The dependence of the volume fraction of GBP in WE43-based and MgZnAl-based alloys on the Zn content.

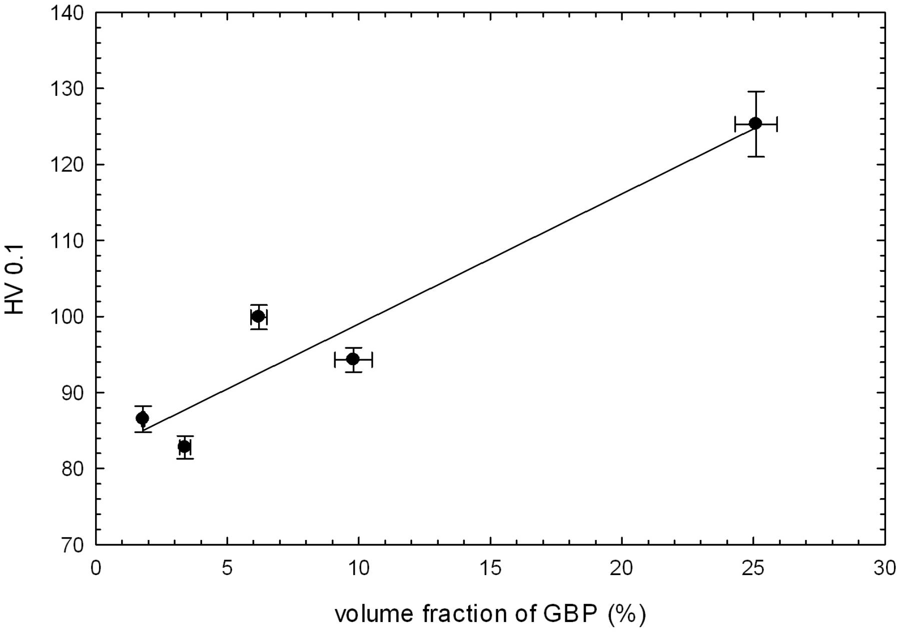

Figure 6.3: The correlation of the Vickers hardness with the volume fraction of GBP.

Defects studies performed by LT showed that positron trapping at vacancy-like defects occurs in all as-cast alloys containing icosahedral phase, see table 5.8. These defects exhibit characteristic lifetime of ~ 300 ps, which was also observed in MgZnAl-based alloys containing quasicrystalline phase $Mg_{44}Zn_{41}Al_{15}$

with icosahedral structure, see appendix B. The positron lifetime corresponding to the vacancy-like defects associated with icosahedral phase is longer than the lifetime of positrons trapped at misfit defects observed in binary Mg6wt.%Zn alloy [54] or in the MgTbNd alloy (see appendix D) which is around 260 ps. Therefore, the vacancy-like defects created at the interface of the icosahedral phase and the Mg matrix are larger than the misfit defects at the interfaces between crystalline precipitates and the Mg matrix.

The comparison of vacancy-like defects with the size of monovacancy is complicated by the fact that there is a discrepancy between experimentally measured ($\sim$ 255 ps [64]) and theoretically calculated ($\sim$ 300 ps [65]) lifetimes of positron trapped at monovacancy in Mg. This issue is thoroughly discussed in appendix C. Hence, the theoretical results suggest that the open volume of the vacancy-like defects associated with icosahedral phase is approximately the same as that for a monovacancy. On the other, the interpretation based on the experimentally measured lifetime of monovacancy in Mg would lead us to a conclusion that the vacancy-like defects associated with icosahedral phase are roughly 2–3 times larger than a monovacancy in Mg, see calculation of the positron lifetime for vacancy clusters in appendix C.

The CDB measurements indicate enhanced concentration of Y and Zn at the vicinity of positron annihilation sites, see figure 5.14. This supports the picture that positrons are trapped at the interface of the Y and Zn-rich icosahedral phase and the Mg matrix.

Heat treatment above melting points of GBP has significant impact on the microstructure of the samples. Key factors influencing the microstructure after such heat treatment are the annealing temperature and the cooling rate. The volume fraction of the melt increases with increasing temperature. On the other hand, the cooling rate controls the morphology of GBP after solidification. Fast quenching results in finely-structured GBP while slow-cooling produces GBP with coarse structure, see figures 5.26 and 5.28.

Since the vacancy-like defects are located at the surface of icosahedral phase, the changes in the morphology of GBP and the size of precipitates of icosahedral phase in Mg matrix may lead to dramatic changes in the concentration of vacancy-like defects even at fixed volume fraction of icosahedral phase. For example, the heat treatment of the WE43+11Zn alloy at 500°C for 1 hour leads to an increase of the volume fraction of the icosahedral phase but at the same time the concentration of vacancy-like defects decreased, see tables 5.10 and 5.13.

6.2 ECAP-processed samples

Processing of samples by ECAP has a significant influence on the microstructure of GBP in the studied alloys. The network of GBP which is present in the as-cast samples is stretched in the direction of shear, see figure 5.57. While the W-phase and the Mg_7Zn_3 phase are ductile and undergo plastical deformation during ECAP, the brittle icosahedral phase brakes into smaller pieces, see figures 5.60 and 5.62.

According to expectations, the LT measurements of as-prepared Mg4Y26ZnE140 and Mg4Y26ZnE200 samples shown in figures 5.80 to 5.82 revealed a high dislocation density which was introduced into the samples by ECAP. Both samples exhibit virtually the same dislocation density although they were processed by ECAP at different temperatures. However, this is consistent with the fact, that the dislocation density in these samples is almost constant during the isochronal annealing up to 200°C. The decrease of dislocation density was observed after annealing at higher temperatures and finally the dislocation density decreased under the detection limit of LT measurement after annealing at 300°C. Hence, we can conclude that dislocations induced by ECAP into Mg4Y26ZnE140 and Mg4Y26ZnE200 samples were annealed out at 300°C.

Similar temperature stability of dislocation structure was determined by the microhardness measurements of WE43+14ZnE200 samples after 1,2 and 4 ECAP passes. Isochronal annealing up to 200°C had little effect on the microhardness of these samples, see figure 5.65. However, a sharp drop of hardness was observed after annealing at 280 and 300°C. In addition, the hardness values of all three samples converged and become identical after annealing at 280°C. These results indicate that isochronal annealing up to 300°C results in the recovery of the dislocation structure in WE43+14ZnE200 samples after 1, 2 and 4 ECAP passes.

On the other hand, the LT results obtained on the Mg4Y23ZnE200 sample presented in figures 5.80 to 5.82 seem to indicate that there is a non-zero dislocation density in the Mg4Y23ZnE200 sample even after annealing at 300°C. Since there is a plateau in the calculated dislocation density after annealing at temperatures 260–300°C, the positron trapping at misfit defects most likely occurs in this temperature range.

Positrons trapped at the misfit defects in binary Mg6wt.%Zn alloy exhibit the positron lifetime practically identical with the lifetime of positrons trapped at dislocations [54]. Hence, these two components cannot be separated and the presence of misfit defects leads to apparent non-zero dislocation density after annealing at high temperatures while the dislocations are in fact annealed out and positrons are instead trapped at the misfit defects.

No trapping at vacancy-like defects was detected by LT investigations in the samples with microstructure refined by ECAP deformation. In the as-deformed state, the component corresponding to the trapping at vacancy-like defects associated with icosahedral phase may be masked by the much stronger component arising from positrons trapped at dislocations.

However, no positron trapping at the vacancy-like defects occurred in the Mg4Y26ZnE140 and Mg4Y26ZnE200 samples annealed at 300°C when the dislocations were annealed out. The recovery of the dislocation structure probably causes coarsening of the precipitates of the icosahedral phase located in the Mg matrix. Another possibility is that the ECAP-processing directly leads to a low numerical density of the icosahedral precipitates in the Mg matrix. Both cases would lead to a decrease of the concentration of the vacancy-like defects below the detection limit of the LT spectroscopy.

6.3 *In situ* XRD studies of phase transformations and compression test

Phase transformations of intermetallic phases in the as-cast and ECAP-processed samples were investigated by *in situ* XRD measurements during linear heating and cooling. The temperature stabilities of intermetallic phases determined from these measurements are presented in tables 5.15 and 5.17. DSC was employed as a complementary method to the *in situ* XRD studies for characterization of as-cast samples. Resulting DSC curves are plotted in figures 5.51. The phase transformation temperatures determined by *in situ* XRD studies of the as-cast alloys are substantially lower than the temperatures determined by DSC.

However, the *in situ* XRD studies of the ECAP-processed samples which were performed in a slightly different experimental configuration produced values which are in reasonable agreement with the DSC results. It was found out that ECAP processing has no influence on the types of intermetallic phases present in the studied samples since the same phases were observed both in the as-cast and ECAP-processed samples, see figures 5.44 and 5.87. Two heating cycles were performed to investigate the influence of the ultra-fine-grained structure on the phase transformations. The ultra-fine-grained structure is destroyed at the end of the first heating cycle by melting in the whole sample volume. Therefore, the second heating cycle should yield similar results as the *in situ* XRD studies of as-cast alloys. However, the phase transformations occurred at the same temperatures during both heating cycles.

Hence, there is a disagreement between the phase transformation temperatures determined by *in situ* XRD studies and DSC measurements of the as-cast alloys. On the other hand, the results obtained by *in situ* XRD investigations of ECAP-processed samples exhibit satisfactory agreement with the DSC curves.

The experimental setup used in the *in situ* XRD studies exhibits a certain limitation in the accuracy of the temperature measurement. Since the temperature of the sample cannot be measured directly, the accuracy of the temperature measurement depends on the quality of the thermal contact between the sample and the graphite crucible. If it is not satisfactory, the induction heating of the sample causes its overheating with respect to the temperature indicated by thermocouple placed on the steel cap of the crucible.

It seems that vertical orientation of the crucible which was used during the *in situ* XRD studies of as-cast alloys results in significantly worse thermal contact than the horizontal orientation of the crucible in the dilatometer which was employed for the *in situ* XRD studies of the ECAP-processed samples.

The W-phase and icosahedral phase melt at temperatures around 500°C and 430°C which are good agreement with the the available literature data [26, 43]. Scatter of values obtained for the different heating cycles of the same alloy can be attributed to differences in the thermal contact between the sample and the graphite crucible.

The binary Mg_7Zn_3 phase exhibit quite peculiar transformation sequence, since it at first transforms to the Z-phase at temperatures roughly about 240°C. At $\sim$ 340°C, the Z-phase transforms back to the Mg_7Zn_3 phase which melts just after this transformation. This temperature coincides with the eutectic temperature 340°C of the binary Mg-Zn system, see figure 3.4.

The engineering stress-strain curves for the as-cast Mg4Y26Zn alloy and the ECAP-processed Mg4Y26ZnE200 sample measured during the compression test at 140°C in a dilatometer are shown in figure 5.66.

The as-cast Mg4Y26Zn alloy exhibits higher yield stress ($\sigma_{0.2} \sim 175$ MPa) than the ECAP-processed Mg4Y26ZnE140 sample ($\sigma_{0.2} \sim 114$ MPa). Since the ECAP processing leads to refinement of the grain size, the increase of the yield stress would be expected according to the Hall-Patch relation. Instead, the yield stress of the ECAP-processed sample is lower than the yield stress of the as-cast alloy. In addition, the Mg4Y26ZnE140 sample showed outstanding ductility since it did not rupture up to $\epsilon = 0.54$ where the compression test was terminated.

In situ XRD studies revealed that the compressive deformation leads to the development of a crystallographic texture where the (0 0 1) basal planes of Mg matrix preferentially assume perpendicular orientation with respect to the applied force. This is manifested by an anisotropy in the 2D diffraction patterns shown in figures 5.69 and 5.71.

7. Conclusions

Samples of WE43 alloy, the WE43-based alloys modified by addition of 11wt.%, 14wt.% and 26wt.% of Zn and three ternary Mg-Zn-Y alloys Mg3wt.%Y6wt.%Zn, Mg4wt.%Y23wt.%Zn, Mg4wt.%Y26wt.%Zn were investigated. The Zn content of studied alloys has decisive influence on the volume fraction of the grain boundary phases (GBPs) and the mechanical properties since GBPs strengthen the studied alloys by the composite hardening mechanism.

The presence of icosahedral phase $Mg_3Zn_6Y_1$ in the as-cast WE43-based alloys modified by addition of Zn and the Mg4Y23Zn, Mg4Y26Zn ternary alloys was confirmed by X-ray diffraction. Positron annihilation spectroscopy revealed that the characteristic vacancy-like defects are formed at the interfaces of the icosahedral phase $Mg_3Zn_6Y_1$ and Mg matrix.

The microstructure of GBPs in Mg-Zn-Y-based alloys can be modified by annealing at temperatures above the melting point of GBPs. Final microstructure of GBPs after melting is determined by the cooling rate of heat treated samples.

Samples of WE43-based alloy modified by addition of 14wt.% Zn and ternary Mg-Zn-Y were processed by equal-channel angular pressing (ECAP). The ECAP introduces a high density of dislocations into the sample and also leads to deformation of GBPs. The thermal stability of the dislocation structure was investigated by microhardness and positron lifetime measurements during isochronal annealing. The recovery of the dislocations in studied samples occurred in the temperature range 260–300°C.

Phase transformations of the as-cast alloys and the samples deformed by ECAP were examined by *in situ* X-ray diffraction during linear heating and cooling. Obtained results were compared with the data obtained by differential scanning calorimetry and the thermal processes observed in differential scanning calorimetry curves were assigned to phase transformations detected by *in situ* X-ray diffraction.

A compression test of the as-cast Mg4wt.%Y26wt.%Zn alloy and a sample of the same alloy processed by ECAP was used to compare their mechanical properties. It was revealed that the sample with ultra-fine-grained structure created by ECAP deforms by grain boundary sliding which lowers the yield stress but also significantly improves the ductility of the Mg4wt.%Y26wt.%Zn alloy processed by ECAP compared to as-cast sample.

References

[1] W. Brandt, *Proceedings of the International School of Physics "Enrico Fermi"*. Varenna: North-Holland Publishing Company, 1983.

[2] W. Brandt and R. Paulin, "Positron implantation-profile effects in solids," *Physical Review B*, vol. 15, pp. 2511–2518, 1977.

[3] B. Bergersen, E. Pajanne, P. Kubica, M. J. Stott, and C. D. Hodges, "Positron diffusion in metals," *Solid State Communications*, vol. 15, pp. 1377–1380, 1974.

[4] M. J. Puska and R. M. Nieminen, "Theory of positrons in solids and on solid surfaces," *Reviews of Modern Physics*, vol. 66, pp. 841–897, 1994.

[5] C. H. Hodges, "Trapping of positrons at vacancies in metals," *Physical Review Letters*, vol. 25, pp. 284–287, 1970.

[6] M. Manninen, R. Nieminen, P. Hautojärvi, and J. Arponen, "Electrons and positrons in metal vacancies," *Physical Review B*, vol. 12, pp. 4012–4022, 1975.

[7] R. P. Gupta and R. W. Siegel, "Electron and positron densities and the temperature dependence of the positron lifetime in a vacancy in aluminum," *Physical Review Letters*, vol. 39, pp. 1212–1215, 1977.

[8] R. P. Gupta and R. W. Siegel, "Positron trapping and annihilation at vacancies in bcc refractory metals," *Journal of Physics F: Metal Physics*, vol. 10, no. 1, p. L7, 1980.

[9] W. Brandt, *Positron annihilation.* New York: Academic, 1967.

[10] D. Connors and R. West, "Positron annihilation and defects in metals," *Physics Letters A*, vol. 30, no. 1, pp. 24–25, 1969.

[11] B. Bergersen and M. Stott, "The effect of vacancy formation on the temperature dependence of the positron lifetime," *Solid State Communications*, vol. 7, no. 17, pp. 1203–1205, 1969.

[12] A. Ore and J. L. Powell, "Three-photon annihilation of an electron-positron pair," *Physical Review*, vol. 75, pp. 1696–1699, 1949.

[13] D. Shechtman, I. Blech, D. Gratias, and J. Cahn, "Metallic phase with long-range orientational order and no translational symmetry," *Physical Review Letters*, vol. 53, p. 1951, 1984.

[14] L. D. Landau and E. M. Lifshitz, *Statisticheskaya Fizika (Statistical Physics) Pt. 1.* Moscow: Nauka, 1976.

[15] M. Mihalkovič, W.-J. Zhu, C. L. Henley, and M. Oxborrow, "Icosahedral quasicrystal decoration models. I. geometrical principles," *Physical Review B*, vol. 53, p. 9002, 1996.

[16] Y. K. Vekilov and M. A. Chernikov, “Quasicrystals,” *Physics-Uspekhi*, vol. 53, p. 537, 2010.

[17] In On-Line Encyclopedia of Integer Sequences: *sequence A005614*, https://oeis.org/A005614.

[18] A. P. Tsai, A. Inoue, and T. Masumoto, “A stable quasicrystal in Al-Cu-Fe system,” *Japanese Journal of Applied Physics*, vol. 26, p. L1505, 1987.

[19] G. V. S. Sastry and P. Ramachandrarao, “A study of the icosahedral phase: $Mg_{32}(Al,Zn)_{49}$,” *Journal of Materials Research*, vol. 1, p. 247, 1986.

[20] W. Ohashi and F. Spaepen, “Stable Ga-Mg-Zn quasi-periodic crystals with pentagonal dodecahedral solidification morphology,” *Nature*, vol. 330, p. 555, 1987.

[21] S. Yi, E. S. Park, J. B. Ok, W. T. Kim, and D. H. Kim, “(Icosahedral phase + α-Mg) two phase microstructures in the Mg-Zn-Y ternary system,” *Materials Science and Engineering A*, vol. 300, pp. 312–315, 2001.

[22] In Wikipedia: *Penrose tiling*, http://en.wikipedia.org/wiki/Penrose_tiling, 2011.

[23] A.-P. Tsai, Y. Murakami, and A. Niikura, “The Zn-Mg-Y phase diagram involving quasicrystals,” *Philosophical Magazine A: Physics of Condensed Matter, Structure, Defects and Mechanical Properties*, vol. 80, no. 5, pp. 1043–1054, 2000.

[24] J. Ok, I. Kim, S. Yi, W. Kim, and D. Kim, “Solidification microstructure of as-cast Mg-Zn-Y alloys,” *Philosophical Magazine*, vol. 83, no. 20, pp. 2359–2369, 2003.

[25] E. Padezhnova, E. Mel’nik, R. Miliyevskiy, T. Dobatkina, and V. Kinzhibalo, “Investigation of the Mg-Zn-Y system,” *Russian Metallurgy*, vol. 4, no. 4, 1982.

[26] G. Shao, V. Varsani, and Z. Fan, “Thermodynamic modelling of the Y-Zn and Mg-Zn-Y systems,” *Calphad*, vol. 30, no. 3, pp. 286–295, 2006.

[27] J. Gröbner, A. Kozlov, X. Fang, J. Geng, J. Nie, and R. Schmid-Fetzer, “Phase equilibria and transformations in ternary Mg-rich Mg-Y-Zn alloys,” *Acta Materialia*, vol. 60, no. 17, pp. 5948–5962, 2012.

[28] R. Agarwal, S. G. Fries, H. L. Lukas, G. Petzow, F. Sommen, T. G. Chart, and G. Effenberg, “Assessment of the Mg-Zn system,” *Zeitschrift fuer Metallkunde/Materials Research and Advanced Techniques*, vol. 83, no. 4, pp. 216–223, 1992.

[29] Z. Luo, H. Sui, and S. Zhang, “On the stable Mg-Zn-Y quasicrystals,” *Metallurgical and Materials Transactions A*, vol. 27, no. 7, pp. 1779–1784, 1996.

[30] H. Takakura, A. Sato, A. Yamamoto, and A. Tsai, “Crystal structure of a hexagonal phase and its relation to a quasicrystalline phase in Zn-Mg-Y alloy,” *Philosophical Magazine Letters*, vol. 78, no. 3, pp. 263–270, 1998.

[31] J. Lee, D. Kim, H. Lim, and D. Kim, "Effects of Zn/Y ratio on microstructure and mechanical properties of Mg-Zn-Y alloys," *Materials Letters*, vol. 59, no. 29-30, pp. 3801–3805, 2005.

[32] D. Bae, S. Kim, D. Kim, and W. Kim, "Deformation behavior of Mg-Zn-Y alloys reinforced by icosahedral quasicrystalline particles," *Acta Materialia*, vol. 50, no. 9, pp. 2343–2356, 2002.

[33] Y. Zhang, X. Zeng, L. Liu, C. Lu, H. Zhou, Q. Li, and Y. Zhu, "Effects of yttrium on microstructure and mechanical properties of hot-extruded Mg-Zn-Y-Zr alloys," *Materials Science and Engineering: A*, vol. 373, no. 1–2, pp. 320–327, 2004.

[34] R. J. Chadwick, "The constitution of the alloys of magnesium and zinc," *Journal of the Institute of Metals*, vol. 39, pp. 285–299, 1928.

[35] W. Hume-Rothery and E. D. Rounswfell, "The system magnesium-zinc," *Journal of the Institute of Metals*, vol. 41, pp. 119–138, 1929.

[36] J. B. Clark and F. N. Rhines, "Central region of the magnesium-zinc phase diagram," *AIME*, vol. 209, pp. 425–430, 1957.

[37] J. J. Park and L. L. Wyman, "Phase relationships in magnesium alloys," *WADC Tech. Rept. 57-504, Astia Document No. AD142110*, pp. 1–27, 1957.

[38] E. D. Gibson and O. N. Carlson *Transactions of the American Society for Metals*, vol. 52, pp. 1084–1096, 1960.

[39] D. Mizer and J. B. Clark, "The magnesium-rich region of the magnesium-yttrium phase diagram," *Transactions of the Metallurgical Society of AIME*, vol. 221, pp. 207–208, 1961.

[40] J. Smith, D. Bailey, D. Novotny, and J. Davison, "Thermodynamics of formation of yttrium-magnesium intermediate phases," *Acta Metallurgica*, vol. 13, no. 8, pp. 889 – 895, 1965.

[41] D. Miannay, P. Grégoire, P. Azou, and P. Bastien, "Étude par l'analyse thermique différentielle de la réaction eutectique dans les alliages binaires magnésium-yttrium," *Comptes rendus hebdomadaires des séances de l'Académie des sciences. Série C, Sciences chimiques*, vol. 265, pp. 1107–1112, 1967.

[42] Z. Sviderskaya and E. Padezhnova, "Phase equilibria in the Mg-Y and Mg-Y-Mn systems," *Izvestiya Rossiiskoi Akademii Nauk, Metally*, vol. 6, pp. 183–190, 1968.

[43] H. Okamoto *Desk Handbook Phase Diagrams for Binary Alloys*, 2000.

[44] P. Villars and L. Calvert *Pearson's Handbook of Crystallographic Data for Intermetallic Phases*, 1991.

[45] M. A. Meyers and K. K. Chawla, *Mechanical Behavior of Materials (Second edition).* Cambridge: Cambridge University Press, 2009.

[46] F. Bečvář, Čížek J., I. Procházka, and J. Janotová, "The asset of ultrafast digitizers for positron-lifetime spectroscopy," *Nuclear Instruments and Methods in Physics Research A*, vol. 539, pp. 372–385, 2005.

[47] F. Bečvář, J. Čížek, and I. Procházka, "High-resolution positron lifetime measurement using ultra fast digitizers Acqiris DC211," *Applied Surface Science*, vol. 255, pp. 111–114, 2008.

[48] F. Bečvář, "Methodology of positron lifetime spectroscopy: Present status and perspectives," *Nuclear Instruments and Methods in Physics Research B*, vol. 261, pp. 871–874, 2007.

[49] B. Smola, *unpublished results*, 2011.

[50] J. Čížek, I. Procházka, B. Smola, I. Stulíková, and V. Očenášek, "Influence of deformation on precipitation process in Mg-15 wt.% Gd alloy," *Journal of Alloys and Compounds*, vol. 430, pp. 92–96, 2007.

[51] J. Čížek, I. Procházka, B. Smola, I. Stulíková, R. Kužel, Z. Matěj, and V. Cherkaska, "Thermal development of microstructure and precipitation effects in Mg-10wt%Gd alloy," *physica status solidi (a)*, vol. 203, no. 3, pp. 466–477, 2006.

[52] D. Bae, M. Lee, K. Kim, W. Kim, and D. Kim, "Application of quasicrystalline particles as a strengthening phase in Mg-Zn-Y alloys," *Journal of Alloys and Compounds*, vol. 342, no. 1–2, pp. 445–450, 2002. Proceedings from the 'Quasicrystals 2001' Conference.

[53] P. Hautojärvi and C. Corbel, *Proceedings of the International School of Physics "Enrico Fermi"*. Varenna: IOS Press, 1995.

[54] P. Hruška, J. Čížek, M. Vlček, O. Melikhova, and I. Procházka, "Precipitation effects in Mg-Zn alloys studied by positron annihilation and hardness testing," *Acta Physica Polonica A*, vol. 125, no. 3, pp. 718–721, 2014.

[55] S. Wasiur-Rahman and M. Medraj, "Critical assessment and thermodynamic modeling of the binary Mg-Zn, Ca-Zn and ternary Mg-Ca-Zn systems," *Intermetallics*, vol. 17, no. 10, pp. 847–864, 2009.

[56] D. Tsang, B. Marsden, S. Fok, and G. Hall, "Graphite thermal expansion relationship for different temperature ranges," *Carbon*, vol. 43, no. 14, pp. 2902–2906, 2005.

[57] R. Valiev, R. Islamgaliev, and I. Alexandrov, "Bulk nanostructured materials from severe plastic deformation," *Progress in Materials Science*, vol. 45, no. 2, pp. 103–189, 2000.

[58] M. Furukawa, Y. Iwahashi, Z. Horita, M. Nemoto, and T. G. Langdon, "The shearing characteristics associated with equal-channel angular pressing," *Materials Science and Engineering: A*, vol. 257, no. 2, pp. 328–332, 1998.

[59] K. Nakashima, Z. Horita, M. Nemoto, and T. G. Langdon, “Development of a multi-pass facility for equal-channel angular pressing to high total strains,” *Materials Science and Engineering: A*, vol. 281, no. 1–2, pp. 82–87, 2000.

[60] J. del Río, C. Gómez, and M. Ruano, “Positron trapping mechanism in plastically deformed magnesium,” *Philosophical Magazine*, vol. 92, p. 535, 2012.

[61] J. Dryzek and E. Dryzek, *Magnesium Alloys - Corrosion and Surface Treatments*, p. 289. Rijeka: InTech, 2011.

[62] L. C. Smedskjaer, M. Manninen, and M. J. Fluss, “An alternative interpretation of positron annihilation in dislocations,” *Journal of Physics F: Metal Physics*, vol. 10, 1980. 2237.

[63] M. Janeček, J. Čížek, J. Gubicza, and J. Vrátná, “Microstructure and dislocation density evolutions in MgAlZn alloy processed by severe plastic deformation,” *Journal of Materials Science*, vol. 47, no. 22, pp. 7860–7869, 2012.

[64] P. Hautojärvi, J. Johansson, A. Vehanen, and J. Yli-Kauppila, “Trapping of positrons at vacancies in magnesium,” *Applied Physics A*, vol. 27, p. 49, 1982.

[65] J. M. C. Robles, E. Ogando, and F. Plazaola, “Positron lifetime calculation for the elements of the periodic table,” *Journal of Physics: Condensed Matter*, vol. 19, p. 176222, 2007.

List of Tables

List of Abbreviations

2D - Two-dimensional
3D - Three-dimensional
ADC - Analog-to-digital converter
BCC - Body-centered cubic
CDB - Coincidence Doppler broadening
CFD - Constant fraction discriminator
CFDD - Constant fraction differential discriminator
DSC - Differential scanning calorimetry
ECAP - Equal channel angular pressing
EDX - Energy-dispersive X-ray spectroscopy
FCC - Face-centered cubic
FFA - Fast filtering amplifier
GBP - Grain boundary phase
HRTEM - High-resolution transmission electron microscopy
HV - Vickers pyramind number
IT - Inverting transformer
LT - Lifetime spectroscopy
PMT - Photomultiplier
SA - Spectroscopic amplifier
SAED - Selected area electron diffraction
SCA - Single channel analyzer
SEM - Scanning electron microscopy
STM - Simple trapping model
TAC - Time-amplitude converter
XRD - X-ray diffraction

Articles related to thesis

1. M. Vlček, J. Čížek, B. Smola, I. Stulíková, I. Procházka, R. Kužel, A. Jäger, P. Lejček, "Defects in Mg-Zn-Y-Nd alloys with icosahedral phase", *Physics Procedia* 35, 45 (2012).
2. J. Čížek, M. Vlček, B. Smola, I. Stulíková, I. Procházka, R. Kužel, A. Jäger, P. Lejček, "Vacancy-like defects associated with icosahedral phase in Mg-Y-Nd-Zr alloys modified by the addition of Zn", *Scripta Materialia* 66, 630 (2012).
3. M. Vlček, J. Čížek, O. Melikhova, P. Hruška, I. Procházka, "Investigation of Precipitation Effects in Mg-Tb and Mg-Tb-Nd Alloys", *Acta Physica Polonica A* 744–747 (2014).
4. M. Vlček, J. Čížek, O. Melikhova, P. Hruška, I. Procházka, M. Vlach, I. Stulíková, B. Smola, "Early stages of precipitation in Mg-RE alloys studied by positron annihilation spectroscopy", *Journal of Physics: Conference Series* (accepted).
5. M. Vlček, J. Čížek, F. Lukáč, O. Melikhova, I. Procházka, M. Vlach, I. Stulíková, B. Smola, A. Jäger, "Precipitation Effects in Mg-Zn-based Alloys Strengthened by Quasicrystalline Phase", *Journal of Physics: Conference Series* (accepted).

Other articles

1. J. Čížek, M. Vlček, I. Procházka: "Digital spectrometer for coincidence measurement of Doppler broadening of positron annihilation radiation", *Nuclear Instruments and Methods in Physics Research Section A* 623, 982–994 (2010).
2. J. Čížek, M. Vlček, I. Procházka, "Digital setup for Doppler broadening spectroscopy", *Journal of Physics: Conference Series* 262, 012014 (2011).
3. S. Wagner, H. Uchida, V. Burlaka, M. Vlach, M. Vlček, F. Lukáč, J. Čížek, C. Bähtz, A. Bell, A. Pundt, "Achieving coherent phase transition in palladium–hydrogen thin films", *Scripta Materialia* 64, 978 (2011).
4. F. Lukáč, J. Čížek, M. Vlček, I. Procházka, W. Anwand, G. Brauer, F. Träger, D. Rogalla, H-W. Becker, "Hydrogen-induced plastic deformation in ZnO", *Physics Procedia* 35, 128 (2012).
5. J. Čížek, F. Lukáč, M. Vlček, I. Procházka, F. Träger, D. Rogalla, H-W. Becker, "Diffusivity of Hydrogen in ZnO Single Crystal", *Defect and Diffusion Forum* 326–328, 459 (2012).
6. J. Čížek, M. Vlček, F. Lukáč, I. Procházka, W. Anwand, G. Brauer, W. Anwand, A. Mücklich, S. Wagner, H. Uchida, A. Pundt, "Structural studies of nanocrystalline thin Pd films electrochemically doped with hydrogen", *Defect and Diffusion Forum* 331, 137 (2012).
7. J. Čížek, M. Vlček, I. Procházka, "Investigation of positron annihilation-in-flight using a digital coincidence Doppler broadening spectrometer", *New Journal of Physics* 14, 035005 (2012).
8. J. Čížek, B. Smola, I. Stulíková, P. Hruška, M. Vlach, M. Vlček, O. Melikhova, I. Procházka, "Natural afing of Mg-Gd and Mg-Tb alloys", *Physica Status Solidi A* 209, 2135 (2012).
9. O. Melikhova, J. Čížek, P. Hruška, M. Vlček, I. Procházka, M. Vlach, I. Stulíková, B. Smola, N. Žaludová, R. K. Islamgaliev, "Influence of Deformation on Precipitation Kinetics in Mg-Tb Alloy", *Defect and Diffusion Forum* 332, 151 (2012).
10. F. Lukáč, J. Čížek, M. Vlček, I. Procházka, M. Vlach, W. Anwand, G. Brauer, F. Träger, D. Rogalla, H-W. Becker, S. Wagner, H. Uchida, C. Bähtz, "Hydrogen interaction with defects in ZnO", *Materials Science Forum* 733, 228 (2013).
11. M. Vlček, J. Čížek, I. Procházka, "Software for analysis of waveforms acquired by digital Doppler broadening spectrometer", *Journal of Physics: Conference Series* 443, 012087 (2013).
12. J. Čížek, F. Lukáč, M. Vlček, M. Vlach, I. Procházka, F. Traeger, D. Rogalla, H.-W. Becker, W. Anwand, G. Brauer, S. Wagner, H. Uchida, A. Pundt, C. Bähtz, "Anisotropy of Hydrogen Diffusivity in ZnO", *Defect and Diffusion Forum* 333 39–49 (2013).

13. J. Čížek, O. Melikhova, M. Vlček, F. Lukáč, M. Vlach, I. Procházka, W. Anwand, G. Brauer, A. Mücklich, S. Wagner, H. Uchida, A. Pundt, "Hydrogen-induced microstructural changes of Pd films", *International Journal of Hydrogen Energy* 38, 12115 (2013).
14. J. Čížek, , F. Lukáč, M. Vlček, O. Melikhova, F. Traeger, D. Rogalla, H.-W. Becker, "Hydrogen absorption and diffusivity in ZnO single crystals", *Journal of Alloys and Compounds* 580, S51 (2013).
15. O. Melikhova, J. Čížek, F. Lukáč, M. Vlček, M. Novotný, J. Bulíř, J. Lančok, W. Anwand, G. Brauer, J. Connolly, E. McCarthy, S. Krishnamurthy, J.-P. Mosnier, "Hydrogen absorption in thin ZnO films prepared by pulsed laser deposition", *Journal of Alloys and Compounds* 580, S40 (2013).
16. P. Hruška, J. Čížek, M. Vlček, O. Melikhova, I. Procházka, “Precipitation Effects in Mg-Zn Alloys Studied by Positron Annihilation and Hardness Testing”, *Acta Physica Polonica A* 125 718–721 (2014).
17. J. Čížek, M. Vlček, F. Lukáč, O. Melikhova, I. Procházka, W. Anwand, M. Butterling, R. Krause-Rehberg, “Positron annihilation in flight: experiment with slow and fast positrons”, *Journal of Physics: Conference Series* 505 012043 (2014).
18. M. Vlček, J. Čížek, I. Procházka, M. Novotný, J. Bulíř, J. Lančok, W. Anwand, G. Brauer, J. P. Mosnier, “Defect studies of thin ZnO films prepared by pulsed laser deposition”, *Journal of Physics: Conference Series* 505 012021 (2014).
19. O. Melikhova, J. Čížek, M. Vlček, F. Lukáč, I. Procházka, W. Anwand, G. Brauer, “Structural studies of thin Pd films loaded with hydrogen”, *Journal of Physics: Conference Series* 505 012015 (2014).
20. J. Čížek, O. Melikhova, M. Vlček, F. Lukáč, M. Vlach, P. Dobroň, I. Procházka, W. Anwand, G. Brauer, S. Wagner, H. Uchida, R. Gemma, A. Pundt, "Hydrogen Interaction with Defects in Nanocrystalline, Polycrystalline and Epitaxial Pd Films", *Journal of Nano Research* 26 123–133 (2014).
21. F. Lukáč, M. Vlček, M. Vlach, S. Wagner, H. Uchida, A. Pundt, A. Bell, J. Čížek, "Stress release during cyclic loading of 20 nm palladium films" *Journal of Alloys and Compounds*, In Press, Corrected Proof, Available online 30 December (2014).
22. M. Vlček, F. Lukáč, M. Vlach, S. Wagner, H. Uchida, C. Baehtz, A. Shalimov, A. Pundt, J. Čížek, "Influence of microstructure and mechanical stress on behavior of hydrogen in 500 nm Pd films" *Journal of Alloys and Compounds*, In Press, Corrected Proof, Available online 30 December (2014).
23. F. Lukáč, M. Vlček, I. Stulíková, B. Smola, H. Kudrnová, M. Vlach, T. Kekule, G. Szakács, N. Hort, K. Kainer, "Magnesium alloy containing silver for degradable biomedical implants", *METAL 2014 - 23rd International Conference on Metallurgy and Materials*, Conference Proceedings, 1086–1091 (2014)
24. M. Vlček, F. Lukáč, I. Stulíková, B. Smola, H. Kudrnová, M. Vlach, V. Kodetová, G. Szakács, N. Hort, K. Kainer, " Precipitation processes in Mg-Y-Nd-Ag alloys suitable for biodegradable implants", *METAL 2014 - 23rd International Conference on Metallurgy and Materials*, Conference Proceedings, 1103–1108 (2014).

25. J. Čížek, F. Lukáč, I. Procházka, M. Vlček, Y. Jirásková, P. Švec, D. Janičkovič, "Positive effect of hydrogen-induced vacancies on mechanical alloying of Fe and Al", *Journal of Alloys and Compounds* 629 22 (2015).
26. M. Vlček, F. Lukáč, I. Stulíková, B. Smola, H. Kudrnová, M. Vlach, V. Kodetová, G. Szakács, N. Hort, "Heat treatment of Mg-Y-based alloys with addition of Ca or Ag", *European Cells and Materials* (accepted).
27. I. Stulíková, B. Smola, J. Čížek, M. Vlček, F. Lukáč, "Properties of deformed Mg-Gd alloys", *European Cells and Materials* (accepted).
28. S. Galli, J.-U. Hammel, J. Herzen, G. Szakács, F. Lukáč, M. Vlček, I. Marco, A. Wennerberg, R. Willumeit-Römer, R. Jimbo, "Corrosion behaviour of 3 Mg-alloys in bone: a high-resolution investigation", *European Cells and Materials* (accepted).

A. Author's publication 1

Title	Defects in Mg-Zn-Y-Nd alloys with icosahedral phase
Authors	M. Vlček, J. Čížek, B. Smola, I. Stulíková, I. Procházka, R. Kužel, A. Jäger, P. Lejček
Journal	Physics Procedia
Volume	35
Year	2012
Pages	45–50

Available online at www.sciencedirect.com

SciVerse ScienceDirect

Physics Procedia 35 (2012) 45 – 50

Physics Procedia

Positron Studies of Defects 2011

Defects in Mg-Zn-Y-Nd alloys with icosahedral phase

M. Vlček[a*], J. Čížek[a], B. Smola[a], I. Stulíková[a], I. Procházka[a], R. Kužel[a], A. Jäger[b] and P. Lejček[b]

[a]*Charles University in Prague, Faculty of Mathematics and Physics, V Holešovičkách 2, 180 00 Praha 8, Czech Republic*
[b]*Institut of Physics, Academy of Sciences of the Czech Republic, Na Slovance 2, 182 21 Praha 8, Czech Republic*

Abstract

Recently it was reported that icosahedral phase (I-phase) with quasicrystalline structure is formed in some lightweight Mg alloys. It was found that Mg alloys containing I-phase exhibit improved mechanical properties which make them attractive for industrial applications. This work presents microstructure investigations and defect studies of squeeze cast Mg-Y-Nd-Zr (WE43) alloy with addition of 14 wt.% and 26 wt.% Zn. For comparison WE43 alloy without any Zn was investigated as well. Presence of the quasicrystalline I-phase was detected by electron diffraction and X-ray diffraction in both WE43 alloys modified by Zn addition. On the other hand, WE43 without Zn does not contain any I-phase. Mechanical properties of as-cast alloys were examined by Vickers microhardness (HV) testing. It was found that presence of I-phase leads to a significant hardening.

Defects in as-cast alloys were investigated by positron lifetime (LT) spectroscopy combined with coincidence Doppler broadening (CDB). Reference sample WE43 alloy without Zn exhibits a single-component LT spectrum with lifetime of ~ 224 ps which is close to the Mg bulk lifetime. On the other hand, vacancy-like defects characterized by positron lifetime of ~ 300 ps were found in WE43 alloys modified by Zn addition. CDB investigations revealed that chemical environment of these defects is enriched with Zn and Y. Hence, our results indicate the existence of vacancy-like defects connected with the I-phase. We suggest that these defects are located at the interfaces between the I-phase and the Mg-matrix.

© 2012 The Authors Published by Elsevier B.V. Selection and/or peer-review under responsibility of Organizing Committee. Open access under CC BY-NC-ND license.

Keywords: quasicrystals; Mg-alloys; positron annihilation spectroscopy

---

* *Corresponding author: marian.vlcek@gmail.com*

1875-3892 © 2012 The Authors Published by Elsevier B.V. Selection and/or peer-review under responsibility of Organizing Committee.
Open access under CC BY-NC-ND license. doi:10.1016/j.phpro.2012.06.009

1. Introduction

Quasicrystals exhibit unique structure without translation symmetry. Quasicrystalline materials exhibit attractive properties such as high hardness, high corrosion and wear resistance, low friction and surface energy. Quasicrystalline phases with icosahedral symmetry were recently observed in magnesium alloys with zinc and rare earth elements [1]. It was found that interfaces between the icosahedral phase (I-phase) and the α-Mg matrix are characterized by very low surface energy [2]. Mg-alloys strengthened with I-phase precipitates exhibit promising mechanical properties associated with the unique properties of the quasicrystalline phase.

2. Experimental

Samples of WE43 (Mg-Y-Nd-Zr based alloy) and WE43 modified by addition of 14 wt.% (WE43+14Zn) and 26 wt.% (WE43+26Zn) of Zn were prepared by squeeze casting. Composition of the studied alloys determined by chemical analysis is listed in Table 1. All investigations were performed on the as-cast alloys.

Table 1 Chemical composition (in wt.%) of alloys studied.

Sample	Zn	Y	Nd	Zr	Gd	Mg
WE43	-	2.95	2.48	0.30	0.15	balance
WE43+14Zn	13.80	3.06	1.04	0.29	0.10	balance
WE43+26Zn	25.82	3.02	1.16	0.27	0.17	balance

Scanning electron microscopy (SEM) was performed on the FEI Phenom microscope equipped with a detector of backscattered electrons. Since the cross-section of electron backscattering increases with the increasing atomic number, heavier elements are represented by the lighter areas in resulting SEM images (so called Z-contrast).

Positron lifetime (LT) measurements were performed using a digital positron lifetime spectrometer equipped with BaF_2 scintillators coupled to photomultipliers (PMT) Hamamatsu H3378. Anode signal from PMTs is digitized with sampling rate of 4 GHz by a pair of fast 8-bit digitizers Acqiris DC211. Sampled waveforms are stored in a personal computer and analyzed off-line by software employing the integral constant fraction algorithm [3]. Detailed description of the spectrometer is given in Refs. [4,5]. Resolution of the spectrometer expressed as full width at half maximum of resolution function is ~150 ps.

Coincidence Doppler broadening (CDB) spectroscopy of annihilation radiation was performed using a spectrometer equipped with two high purity germanium detectors. The spectrometer exhibits resolution of ~1.0 keV expressed as full width at half maximum of the resolution function at 511 keV.

3. Results and discussion

A representative SEM image of WE43 alloy is shown in Fig. 1(a). Lighter pattern observed along the grain boundaries testifies presence of heavier elements. Moreover, isolated prolonged particles of the eutectic are located at the grain boundaries. Two phases were identified in WE43 sample by XRD in addition to Mg matrix: (i) larger precipitates of β_1 face-centered cubic (fcc) $Mg_5Nd_{0.4}Y_{0.6}$ phase giving sharp reflections to XRD pattern and (ii) fine particles of tetragonal $Mg_{41}Nd_5$ phase resulting in broad and reflections with low intensity.

The SEM images of WE43 modified with Zn are shown in Fig. 1 (b-d). Both alloys modified with Zn exhibit typical pattern consisting of grains of the α-Mg phase separated by Zn enriched grain boundary eutectic (GBE). The GBE volume fraction f_E determined from the SEM images is given in Table 2. Obviously, the f_E increases with increasing Zn content. Fig. 1(d) shows the morphology of GBE in WE43+26Zn alloy in higher magnification. The eutectic exhibits lamellar structure with very high surface-to-volume ratio. This is in striking contrast with the morphology of the eutectic phase in WE43 alloy where the fine lamellar structure is absent; see Fig. 1(a).

The quasicrystalline I-phase with composition $Mg_3Zn_6Y_1$ was detected by XRD in both WE43 alloys modified by Zn addition. Moreover, the fcc W-phase ($Mg_3Zn_3Y_2$) was found in WE43+14Zn, while WE43+26Zn contains the fcc Mg_7Zn_3 phase. This is in agreement with Lee et al. [6] who found that presence of the W-phase is typical for Mg-Zn-Y alloys with low Zn/Y ratio, while in the alloys with higher Zn/Y ratio the Mg_7Zn_3 phase is formed.

Table 2 Results of LT investigations: lifetimes τ_i and relative intensities I_i of the exponential components resolved in LT spectra; the quantity τ_f calculated from Eq. (1) to check the consistency of decomposition with the two state simple trapping model, the concentration of vacancy-like defects c_D calculated from LT data using simple trapping model; Vickers hardness HV0.1; the volume fraction of eutectic f_E determined by SEM.

Sample	τ_1 (ps)	I_1 (%)	τ_2 (ps)	I_2 (%)	τ_f (ps)	c_D (ppm)	HV0.1	f_E (%)
WE43	223.9(3)	100	-	-	-	-	87 ± 2	1.8 ± 0.1
WE43+14Zn	187(2)	55(2)	302(3)	45(2)	226(4)	9.1(1)	94 ± 2	9.8 ± 0.7
WE43+26Zn	192(4)	56(3)	302(4)	44(3)	228(5)	8.3(2)	125 ± 4	25.1 ± 0.8

Results of LT measurements are shown in Table 2. WE43 alloy exhibits a single component spectrum with lifetime $\tau_1 \approx 224$ ps which agrees well with the Mg bulk positron lifetime of $\tau_B = 225$ ps [7]. Therefore, we can conclude that the concentration of positron traps in WE43 alloy is lower than detection threshold of positron lifetime spectroscopy. LT spectra of WE43 alloys modified by Zn addition consist of two components. The lifetime τ_1 of the first component is shortened below τ_B due to the positron trapping in defects. The lifetime of the second component $\tau_2 \approx 302$ ps agrees well with the lifetime of positrons trapped in Mg vacancy ($\tau_V = 299$ ps) calculated in Ref. [8]. Hence, the second component represents a contribution of the positrons trapped at vacancy-like defects. Interestingly, vacancy-like defects were detected only in WE43 alloy modified by Zn addition and not in the original WE43 (without Zn). This indicates that the vacancy-like defects are associated with quasicrystalline I-phase which is present in both WE43 alloys modified by Zn addition (WE+14Zn and WE43+26Zn) but is absent in the original WE43 alloy.

Results of LT investigations were analyzed by application of simple trapping model. Consistency of the decomposition of LT spectra with the two state trapping model can be checked using the quantity [9]

$$\tau_f = \left(\frac{I_1}{\tau_1} + \frac{I_2}{\tau_2} \right)^{-1} . \tag{1}$$

If assumptions of the two state simple trapping model, i.e. a single type of homogeneously distributed positron traps, no detrapping and no trapping of non-thermalized positrons, are fulfilled, then the quantity τ_f obtained from Eq. (1) equals to the bulk positron lifetime τ_B. One can see in Table 2 that in both WE43 alloys modified by Zn addition τ_f indeed agrees well with the Mg bulk lifetime testifying that the simple trapping model assumptions are fulfilled and the concentration of vacancy-like defects can be calculated using the equation [9]

$$c_D = \frac{1}{\nu_D} \frac{I_2}{I_1} \left(\frac{1}{\tau_B} - \frac{1}{\tau_2} \right), \tag{2}$$

where ν_D is the specific positron trapping rate. For vacancies in metals ν_D falls into the range 10^{14} - 10^{15} s^{-1} [9]. Here we used $\nu_D \approx 10^{14}$ s^{-1} since Mg exhibits low electron density in interatomic regions which makes the positron binding energy to vacancy lower than in dense metals and, thereby, ν_D is expected to be close to the lower limit of the aforementioned interval. The concentration of vacancy-like defects obtained from Eq. (2) is listed in Table 2. Obviously, both WE43 alloys modified by Zn addition exhibit comparable concentration of vacancy-like defects, despite the fact that GBE volume fraction in the WE43+26Zn alloy is significantly higher than in the WE43+14Zn sample. Furthermore, the lifetime $\tau_2 \approx$ 302 ps is substantially longer than lifetimes reported for positrons trapped at defects in single-phase quasicrystals (~210 ps) reported by Sato et. al. [10]. These results suggest that vacancy-like defects are most probably located not inside of the I-phase but at the interface between the I-phase and Mg matrix.

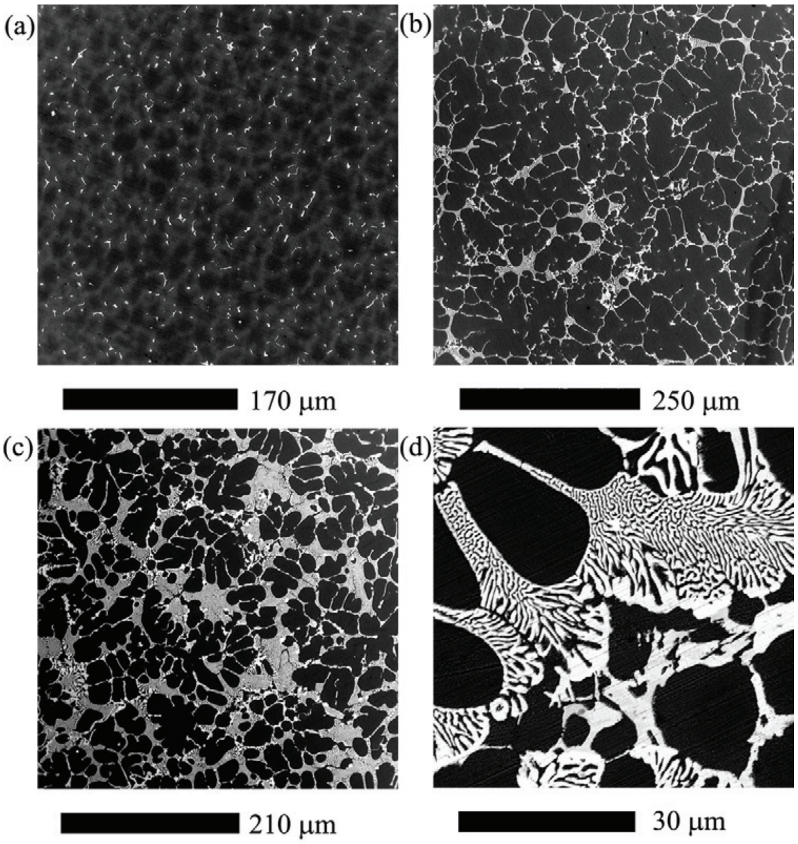

Figure 1 SEM images of: (a) WE43 alloy; (b) WE43+14Zn; (c) WE43+26Zn alloy; (d) WE43+26Zn alloy (detail in higher magnification).

Measured CDB ratio curves (related to well-annealed Mg) are shown in Fig. 2. All studied samples exhibit a peak in the ratio curves at 8×10^3 m_0c which represents a contribution of positrons annihilated by electrons belonging to rare Earth elements, i.e., Y, Nd and Gd. In addition WE43 alloys modified by Zn addition exhibit also a broad peak centered at 18×10^3 m_0c which comes from positrons annihilated by *3d* Zn electrons. In the high momentum region, where the contribution of positrons annihilated by core electrons dominates, the ratio curve ρ related to well-annealed Mg can be expressed as linear combination

$$\begin{aligned}\rho = (1-F_V)\big(&\xi_{Mg,B} + \xi_{Zn,B}\rho_{Zn,B} + \xi_{Y,B}\rho_{Y,B} + \xi_{Nd,B}\rho_{Nd,B} + \xi_{Zr,B}\rho_{Zr,B} + \xi_{Gd,B}\rho_{Gd,B}\big) \\ &+ F_V\big(\xi_{Mg,V}\rho_{Mg,V} + \xi_{Zn,V}\rho_{Zn,V} + \xi_{Y,V}\rho_{Y,V} + \xi_{Nd,V}\rho_{Nd,V} + \xi_{Zr,V}\rho_{Zr,V} + \xi_{Gd,V}\rho_{Gd,V}\big),\end{aligned} \tag{3}$$

where $\rho_{Zn,B}$, $\rho_{Y,B}$, $\rho_{Nd,B}$, $\rho_{Zr,B}$ and $\rho_{Gd,B}$ are the ratio curves of free positrons annihilated by Zn, Y, Nd, Zr and Gd electrons, respectively. These curves were obtained by the measurement of the well-annealed reference sample of corresponding pure metals. The symbols $\rho_{Mg,V}$, $\rho_{Zn,V}$, $\rho_{Y,V}$, $\rho_{Nd,V}$, $\rho_{Zr,V}$ and $\rho_{Gd,V}$ denote the ratio curves for positrons trapped at vacancy-like defects and annihilated by Mg, Zn, Y, Nd, Zr and Gd electrons, respectively. These curves were obtained by the measurement of cold rolled reference samples of corresponding pure metals which exhibit saturated positron trapping at defects. The fraction F_V of positrons trapped at the vacancy-like defects was calculated from LT data using the two state simple trapping model [9]

$$F_V = I_2 \frac{\tau_2 - \tau_1}{\tau_2}. \tag{4}$$

The coefficients $\xi_{Mg,B}$, $\xi_{Zn,B}$, $\xi_{Y,B}$, $\xi_{Nd,B}$, $\xi_{Zr,B}$ and $\xi_{Gd,B}$ represent the fraction of free positrons annihilated by Mg, Zn, Y, Nd, Zr and Gd electrons, respectively, and always fulfill the normalization condition $\xi_{Mg,B} + \xi_{Zn,B} + \xi_{Y,B} + \xi_{Nd,B} + \xi_{Zr,B} + \xi_{Gd,B} = 1$. Similarly, the coefficients $\xi_{Mg,V}$, $\xi_{Zn,V}$, $\xi_{Y,V}$, $\xi_{Nd,V}$, ξ_{ZrVB} and $\xi_{Gd,V}$ represent the fraction of positrons trapped at vacancy-like defects and annihilated by Mg, Zn, Y, Nd, Zr and Gd electrons, respectively. These coefficients also fulfill the normalization condition $\xi_{Mg,V} + \xi_{Zn,V} + \xi_{Y,V} + \xi_{Nd,V} + \xi_{Zr,V} + \xi_{Gd,V} = 1$.

Table 3 Results of fitting of CDB curves using model function described by Eq. (3). The fraction $\xi_{\mathrm{Zn,B}}$ was fixed at 0.023 representing the maximum Zn solubility in Mg. Fraction F_V was calculated according to Eq. (4) for WE43 alloys modified by addition of zinc, in case of WE43 alloy it was obtained from fitting of CDB ratio curves by model function decribed by Eq. (3).

	$\xi_{Zn,B}$	$\xi_{Y,B}$	$\xi_{Nd,B}$	$\xi_{Zr,B}$	$\xi_{Gd,B}$	$\xi_{Zn,V}$	$\xi_{Y,V}$	$\xi_{Nd,V}$	$\xi_{Zr,V}$	$\xi_{Gd,V}$	F_V
WE43	-	0.008(2)	0.004(1)	0.00	0.00	0.00	0.00	0.30(2)	0.10(2)	0.60(2)	0.14(1)
WE43+14Zn	0.023	0.010(5)	0.002(1)	0.00	0.00	0.19(3)	0.30(3)	0.00	0.00	0.00	0.16(1)
WE43+26Zn	0.023	0.010(5)	0.002(1)	0.00	0.00	0.54(4)	0.46(4)	0.00	0.00	0.00	0.16(1)

The fractions ξ obtained from fitting of CDB ratio curves by the model curve described by Eq. (3) are listed in Table 3 and the model curves which gave the best fit with experimental data are plotted in Fig. 2 by solid lines. Table 3 shows that fraction of positrons annihilated by electrons of rare Earth elements is substantially higher than the concentration of Y, Nd and Gd in the samples obtained from chemical analysis. This testifies that positrons are annihilated in the rare Earth enriched phases.

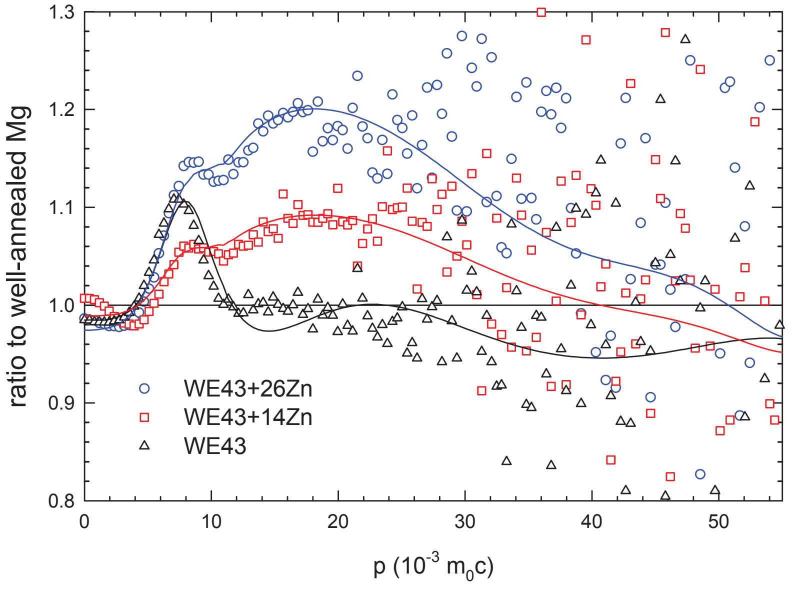

Figure 2 CDB ratio curves (relative to well-annealed Mg). Open circles - measured data; solid lines - fit.

CDB results indicate that in the WE43 alloy positrons annihilate predominantly in Mg matrix but certain fraction of positrons annihilate from localized state at Nd and Gd-rich precipitates. The Nd-rich particles are apparently finely dispersed particles of $Mg_{41}Nd_5$ phase identified in WE43 sample by XRD. A high fraction of positrons annihilated by Gd electrons indicate that substantial fraction of Nd atoms in $Mg_{41}Nd_5$ phase is substituted by Gd. Since only a single component with lifetime comparable with τ_B was found in LT spectrum of WE43 sample, there are probably no open-volume defects associated with Nd and Gd-rich precipitates but positrons are localized directly inside these particles due to higher absolute value of positron affinity compared to Mg matrix.

It is clear that chemical environment of vacancy like defects in WE43 alloy modified by Zn addition and characterized by lifetime of ≈ 300 ps contain substantially enhanced concentration of Zn and Y as seen from Table 3. This is most pronounced in the case of WE43+26Zn alloy where virtually all positrons trapped at vacancy-like defects are annihilated by Zn or Y electrons. This result supports the picture that vacancy-like defects in WE43 modified by Zn addition are associated with quasicrystalline I-phase $Mg_3Zn_6Y_1$ characterized by high Zn and Y content. Vacancy-like defects are probably situated at interfaces between the I-phase precipitates and the Mg matrix where misfit defects are necessary to accommodate the incommensurable atom spacing in these phases. However, further investigations are needed to support this hypothesis.

4. Conclusions

Samples of WE43 alloy and WE43 alloy modified by addition of 14 wt.% and 26 wt.% of zinc were investigated. Quasicrystalline icosahedral phase $Mg_3Zn_6Y_1$ was identified in the samples of WE43 alloy modified by Zn addition. It was found that the samples containing icosahedral phase contain vacancy-like defects located most probably at the interface between the icosahedral phase and Mg matrix.

Acknowledgements

This work was supported by the Czech Science Foundation (project P108/10/0648), the Academy of Science of Czech Republic (project KAN300100801, the Ministry of Schools, Youths and Sports of the Czech Republic (project MS 0021620834) and project SVV-2010-261303.

References

[1] S. Yi., E.S. Park, J.B. Ok, W.T. Kim, D.H. Kim, Mater. Sci. Eng. A 300 (2001) 312.

[2] J.M. Dubois, P. Plaindoux, E. Belin-Ferre, N. Tamura, D.J. Sordelet, in: Proceedings of the 6th International Conference on Quasicrystals, World Scientific, Singapore (1997), p. 733.

[3] F. Bečvář, Nucl. Instrum. Methods B 261 (2007) 871.

[4] F. Bečvář, J. Čížek, I. Procházka, J. Janotová, J. Nucl Instrum Methods A 539 (2005) 372.

[5] F. Bečvář, J. Čížek, I. Procházka , Appl. Surf. Sci. 255 (2008) 111.

[6] J.Y. Lee, D.H.. Kim, H.K. Lim, D.H. Kim, Materials Letters 59 (2005) 3801.

[7] J. Čížek, I. Procházka, B. Smola, I. Stulíková, V. Očenášek, J. Alloys Comp. 430 (2007) 92.

[8] J. Čížek, I. Procházka, B. Smola, I. Stulíková, R. Kužel, Z. Matěj, V. Cherkaska, Phys. Stat. Sol. A 203 (2006) 466.

[9] P. Hautojärvi, C. Corbel in: Proceedings of the International School of Physics "Enrico Fermi", Course CXXV, Ed. A. Dupasquier, A. P. Mills, IOS Press, Varenna (1995), p. 491.

[10] K. Sato, H. Murakami, I. Kanazawa, Y. Kobayashi, Phys. Stat. Sol. C 4 (2007) 3455.

B. Author's publication 2

Title	Precipitation Effects in Mg-Zn-based Alloys Strengthened by Quasicrystalline Phase
Authors	M. Vlček, J. Čížek, F. Lukáč, O. Melikhova, I. Procházka, M. Vlach, I. Stulíková, B. Smola, A. Jäger
Journal	Journal of Physics: Conference Series (accepted)
Volume	-
Year	-
Pages	-

Precipitation Effects in Mg-Zn-based Alloys Strengthened by Quasicrystalline Phase

M Vlček[1], J Čížek[1], F Lukáč[1], O Melikhova[1], I Procházka[1], M Vlach[1], I. Stulíková[1], B Smola[1], A Jäger[2]

[1]Charles University in Prague, Faculty of Mathematics and Physics, V Holešovičkách 2, 18000 Praha 8, Czech Republic

[2]Institute of Physics, Academy of Sciences of the Czech Republic, Na Slovance 2, 18221 Praha 8, Czech Republic

E-mail: `marian.vlcek@gmail.com`

Abstract. Mg-based alloys are promising lightweight structural materials for automotive, aerospace and biomedical applications. Recently Mg-Zn-Y system attracted a great attention due to a stable icosahedral phase (I-phase) with quasicrystalline structure which is formed in these alloys. Positron lifetime spectroscopy and *in situ* synchrotron X-ray diffraction were used to study thermal stability of I-phase and precipitation effects in Mg-Zn-Y and Mg-Zn-Al alloys. All alloys containing quasicrystalline I-phase exhibit misfit defects characterized by positron lifetime of $\sim$ 300 ps. These defects are associated with the interfaces between I-phase particles and Mg matrix. The quasicrystalline I-phase particles were found to be stable up to temperatures as high as $\sim 370^\circ$C. The W-phase is more stable and melts at $\sim 420^\circ$C. Concentration of defects associated with I-phase decreases after annealing at temperatures above $\sim 300^\circ$C.

1. Introduction

Mg-Zn-Y system attracts attention due to presence of icosahedral phase (I-phase) with quasicrystalline structure [1]. Quasicrystals exhibit structure with lack of translation symmetry and posses unique combination of physical properties: high hardness, high corrosion resistance and low surface energy [2]. Although they are not directly applicable for structural applications due to their brittleness, they could be used as strengthening agents in Mg alloys. Moreover, I-phase has strong interfacial bonding to the Mg matrix, low friction coefficient and low surface energy which is beneficial for ductility and deformability.

Positron annihilation spectroscopy revealed existence of misfit defects associated with the interfaces between I-phase particles and α-Mg matrix [3]. Thermal stability of I-phase and precipitation effects in Mg-Zn-Y and Mg-Zn-Al alloys were studied in this work using positron lifetime spectroscopy combined with *in situ* synchrotron X-ray diffraction (XRD). Development of mechanical properties was monitored by microhardness testing.

2. Experimental details

Three groups of alloys were studied in this work: (i) Mg-Y-Nd-Zr (WE43) alloy, (ii) WE43 alloy modified by addition of various amount of Zn, and (iii) Mg-Zn-Al alloys. Both WE43 modified by Zn and Mg-Zn-Al alloys contain quasicrystalline I-phase. The WE43 alloy without

Zn does not contain quasicryrstalline phase and was used as a reference material. All alloys were produced by squeeze casting under a protective atmosphere (Ar + 1% SF6). Chemical compositions of studied alloys are shown in tables 1 and 2.

Table 1. Compositions of Mg-Zn-Y-based alloys in wt.%.

	Zn	Y	Nd	Zr	Gd	Mg
WE43	-	2.95	2.48	0.30	0.15	balance
WE43+11Zn	10.90	1.80	0.73	0.28	0.12	balance
WE43+14Zn	13.80	3.06	1.04	0.29	0.10	balance
WE43+26Zn	25.82	3.02	1.16	0.27	0.17	balance

Table 2. Compositions of Mg-Zn-Al-based alloys in wt.%.

	Zn	Al	Ca	Mg
Mg5Zn3Al	5.3	3.2	0.1	balance
Mg12Zn3Al	11.9	3.1	-	balance

Digital positron lifetime spectrometer [4] with excellent time resolution of 145 ps was used for positron lifetime measurements. The resolution of the spectrometer was calculated as FWHM of resolution function obtained from fitting of positron lifetime spectrum of a well-annealed Mg reference sample. Each measured spectrum consisted of at least 10^7 annihilation events. The $^{22}Na_2CO_3$ positron source deposited on a 2 µm thick mylar foil exhibits source contribution consisting of two components with lifetimes 368 ps and 1.5 ns and relative intensities 7% and 1%, respectively, which was always subtracted from the spectra.

The measurements of Vickers microhardness (HV) were performed using a STRUERS Duramin 300 hardness tester with a load of 100 g applied for 10 s.

In-situ measurement of synchrotron X-ray diffraction during heat treatment was used to monitor evolution of phase composition at elevated temperatures. Sample of as-cast WE43+14Zn alloy was subjected to linear heating from room temperature to 425°C. Subsequently the sample was cooled down back to room temperature. Heating and cooling rates were 5 K/min, wavelength of X-ray radiation was set to $\lambda = 0.142$ Å.

3. Results

Results of positron lifetime measurements of as-cast alloys are shown in table 3. The WE43 alloy, which does not contain quasicrystalline I-phase, exhibits single component spectrum with lifetime $\tau_1 = 223.9 \pm 0.3$ ps which agrees well with the bulk positron lifetime in well-annealed Mg [5]. All other alloys, which contain quasicrystalline phase, exhibit two component spectra, see table 3. The first component comes from annihilation of free positrons while the second component can be attributed to annihilation of positrons trapped at defects. The lifetime of the second component $\tau_2 \approx 300$ ps provides characteristic signature of misfit defects associated with quasicrystalline phase [3].

The effect of different cooling rates after isothermal annealing was studied on WE43+11Zn alloy. Two samples were annealed at 500°C for 1 hour, one was quenched into the water (Q) while the second one was slowly cooled down with furnace (SC). Results of positron lifetime measurements presented in table 4 revealed that misfit defects remain present in the alloys after

Table 3. Results of positron lifetime measurements of as cast samples.

	State	τ_1 (ps)	I_1 (%)	τ_2 (ps)	I_2 (%)
WE43	as-cast	223.9(3)	100	-	-
WE43+26Zn	as-cast	192(4)	56(3)	302(4)	44(3)
WE43+14Zn	as-cast	187(2)	58(2)	302(3)	42(2)
WE43+11Zn	as-cast	201(2)	67(3)	296(5)	33(3)
Mg5Zn3Al	as-cast	219(1)	96(1)	290(10)	4(1)
Mg12Zn3Al	as-cast	217.3(5)	93.9(5)	300(10)	6.1(5)

annealing at 500°C. However, the fraction of positrons trapped at defects significantly decreases after annealing, especially in the slowly cooled sample.

Table 4. Results of positron lifetime measurements of WE43+11Zn samples annealed at 500°C.

	State	τ_1 (ps)	I_1 (%)	τ_2 (ps)	I_2 (%)
WE43+11Zn	as-cast	201(2)	67(3)	296(5)	33(3)
WE43+11Zn	500°C/1 h Q	212(5)	73(9)	280(10)	27(9)
WE43+11Zn	500°C/1 h SC	218(2)	89(1)	290(10)	11(1)

The Mg-Zn-Y-based alloys were isochronally annealed with step 20 K/20 min to monitor the development of physical properties with increasing annealing temperature. The evolution of microhardness during isochronal annealing is shown in figure 1. Hardness has generally decreasing trend but there are two notable hardening peaks at $\sim$ 160°C and $\sim$ 440°C. Based on the development of hardness, annealing temperatures of 160°C, 300°C and 440°C (indicated in figure 1 by arrows) were selected for positron lifetime spectroscopy measurements.

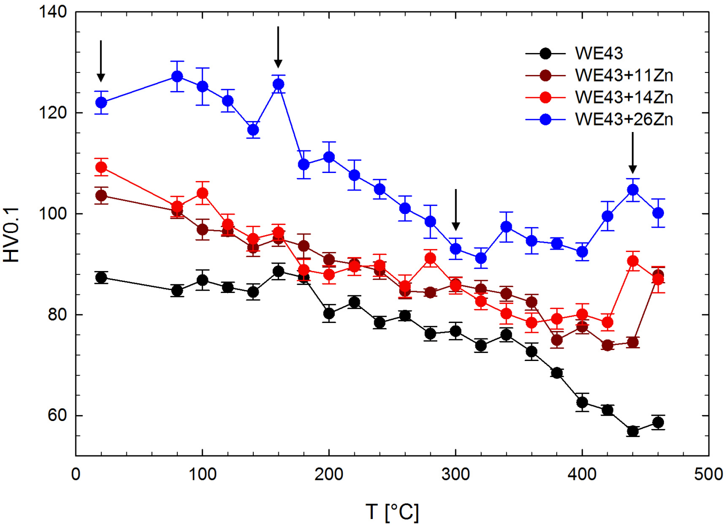

Figure 1. Evolution of microhardness during isochronal annealing.

Table 5. Results of positron lifetime measurements of isochronally annealed WE43+11Zn alloy.

	State	τ_1 (ps)	I_1 (%)	τ_2 (ps)	I_2 (%)
WE43+11Zn	as-cast	201(2)	67(3)	296(5)	33(3)
WE43+11Zn	160°C	180(10)	48(4)	278(9)	52(4)
WE43+11Zn	300°C	203(9)	70(5)	298(7)	30(5)
WE43+11Zn	440°C	210(10)	75(5)	300(10)	25(5)

The results of these measurements for WE43+11Zn alloy are summarized in table 5. After annealing at 160°C, the intensity of the second component increased and its lifetime decreased by roughly 20 ps. It has to be noted that positron lifetime of ~ 260 ps was observed in binary Mg-Zn alloy after annealing at 220°C [6]. This lifetime was attributed to positrons trapped at open-volume misfit defects at the interfaces between precipitates and Mg matrix. Therefore, most likely explanation of shortened lifetime τ_2 in WE43+11Zn alloy is that precipitation occurred after annealing at 160°C and components with lifetimes ~ 260 ps (misfit defect at precipitate-matrix interfaces) and ~ 300 ps (misfit defects associated with I-phase) cannot be separated due to limited experimental resolution. Instead, one component with a lifetime of $\tau_1 = 278 \pm 9$ ps was observed. Precipitates formed at 160°C dissolve at higher annealing temperatures and the lifetime τ_2 of the second component again has value of ~ 300 ps. However, intensity of the second component is slightly decreased compared to the as-cast state.

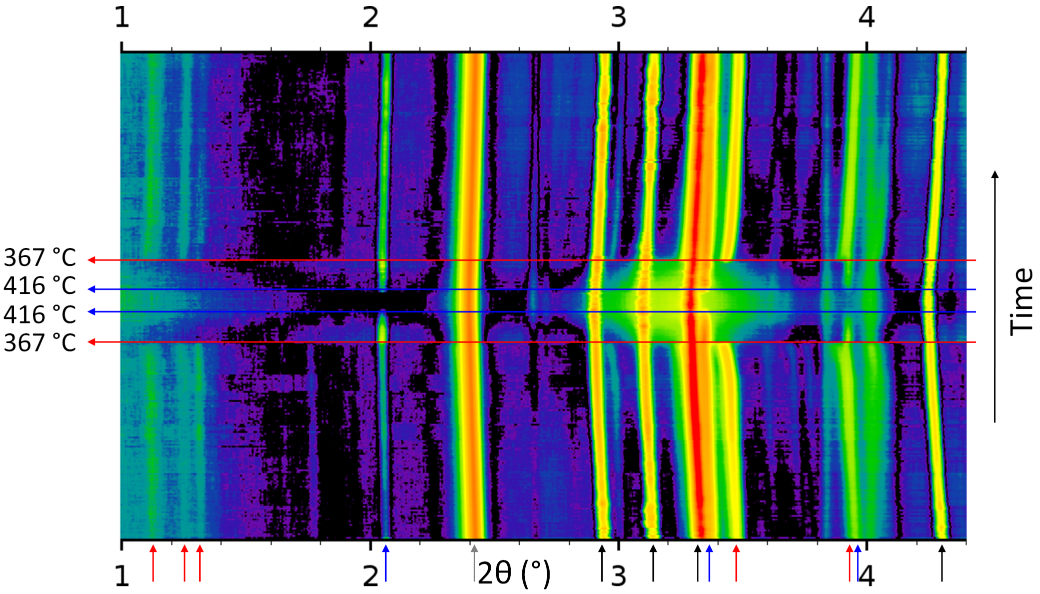

Figure 2. Results of *in situ* XRD measurement during linear heat up and cool down from room temperature to 425°C. Each horizontal line represents diffraction pattern at some temperature. Intensity was converted to the color scale and increases from black to red. Most pronounced peaks of Mg matrix (black), I-phase (red), W-phase (blue) and graphite crucible (gray) are marked by colored arrows.

Results of in-situ XRD studies of WE+14Zn alloy are presented in figure 2 as a 2D image in which individual XRD patterns for each temperature are shown as horizontal lines and intensity is converted to color. The vertical axis shows evolution of XRD patterns during heat treatment.

In the as-cast sample, peaks corresponding to Mg matrix, icosahedral I-phase (Mg_3Zn_6Y), cubic W-phase ($Mg_3Zn_3Y_2$) and graphite crucible in which the sample was placed were identified. Peaks corresponding to the I-phase disappeared when temperature exceeded $\sim 367°C$, indicated by the red horizontal arrow in the figure. Diffuse bump in the background, testifying presence of liquid phase, also appeared at this temperature. Peaks of W-phase remained visible up to $\sim$ 416°C, indicated by the blue horizontal arrow in the figure. During the cooling, peaks of W-phase and I-phase appeared at temperature $\sim$ 416°C and $\sim$ 367°C, respectively.

Because of lattice expansion the diffraction peaks shift to lower diffraction angles with increasing temperature their temperature evolution during heating and subsequent cooling in figure 2 forms typical "V" shape. The diffraction peaks corresponding to I-phase show different behavior than other peaks. Contrary to other phases the positions of the peaks corresponding to I-phase do not change linearly with temperature but exhibits nonlinear dependence which can be seen as slightly bent curves in figure 2. The relative lattice expansion with respect to room temperature was calculated from fitted positions of the diffraction peaks and is plotted in figure 3. Thermal expansion of Mg matrix and graphite is approximately linear with temperature. On the other hand, thermal expansion of I-phase exhibits a strong nonlinearity indicating that the coefficient of thermal expansion of I-phase remarkably changes around 310°C.

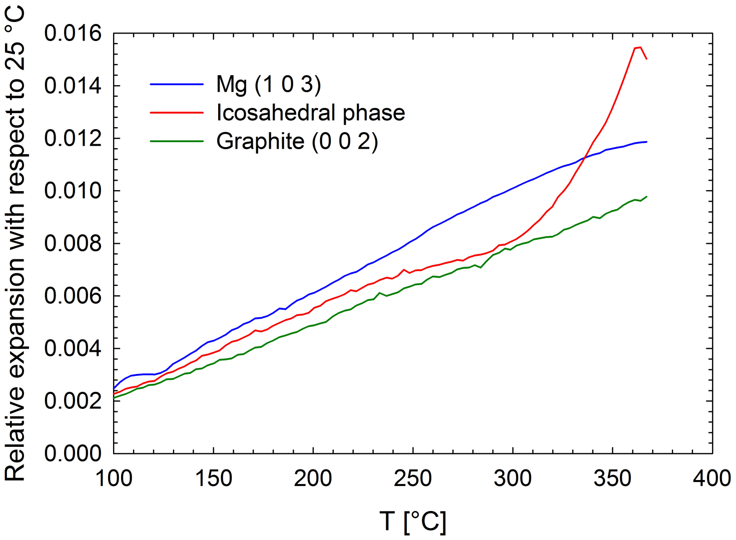

Figure 3. Relative thermal expansion with respect to 25°C calculated from XRD data.

4. Discussion

Results of positron lifetime measurements show that all studied alloys containing quasicrystalline phase exhibit two component spectrum with lifetime of the second component $\tau_2 \approx 300$ ps. This lifetime therefore characterizes misfit defects which are uniquely associated with quasicrystalline phase in Mg alloys. These defects are most likely situated at the interface of quasicrystalline phase and Mg matrix. Due to incommensurability of their lattices, misfit defects must be created at their interface. In order to partially retain the coherency between I-phase and α-Mg matrix steps or ledges are introduced periodically along the interface and misfit defects are located at these steps along the interface. Presence of these ledges was confirmed by high resolution transmission electron microscopy [7].

Size of the misfit defects can be estimated by comparison of the $\tau_2 \approx 300$ ps with the positron lifetime for a Mg monovacancy. Theoretically calculated lifetime for a Mg monovacancy is

≈ 300 ps [5]. This would suggest that misfit defects associated with I-phase are approximately of the same size as Mg monovacancy. On the other hand, the experimental positron lifetime reported for Mg monovacancy is ≈ 255 ps [8]. Hence, according to these experimental results, the misfit defects associated with I-phase are larger than Mg monovacancy. The discrepancy between experimental results and theoretical calculations of positron lifetime for Mg monovacancy is further discussed in reference [9].

Although annealing at 500°C increased the volume fraction of I-phase in grain boundary phase [10], the intensity of the second component in positron lifetime spectrum decreased after annealing. This is due to the fact, that finely dispersed precipitates of I-phase are present in the in Mg matrix of the as-cast alloy and most of these small precipitates are dissolved during annealing. Hence, the content of I-phase in grain boundary phase is enhanced by annealing at 500°C but its concentration in Mg grains is decreased due to dissolution of the fine I-phase precipitates. This leads to a reduction of the fraction of positrons trapped at misfit defects associated with I-phase. Decrease in the intensity of the second component in positron lifetime spectra after isochronal annealing at temperatures 300°C and 440°C is caused by the same reason.

In situ XRD investigations were performed to study phase transformations in WE43+14Zn alloy during linear heating. The temperatures of formation, i.e. $\sim$ 367°C for the I-phase and $\sim$ 416°C for the W-phase, determined by XRD differ significantly from the values obtained by differential thermal analysis, which are $\sim$ 450°C [7] and $\sim$ 510°C [11]. Our differential scanning calorimetry measurements of WE+14Zn alloy revealed presence of four endothermic peaks at temperatures 330-360°C, $\sim$ 420°C, $\sim$ 445°C and $\sim$ 505°C. First two peaks could be attributed to melting of I-phase and W-phase respectively. The most pronounced peak located at 445°C might be due to melting of whole grain boundary region. However, using this interpretation, the origin of the last peak located around 505°C remains unknown. Further investigations are clearly needed to definitively assign phase transitions observed by X-ray diffraction to peaks measured by differential scanning calorimetry.

Thermal lattice expansion of I-phase shows significant nonlinearity with increase of the thermal expansion around 310°C. This is most likely linked to some structural changes in I-phase occurring in this temperature range. Additional work is needed to elucidate the cause of this effect.

5. Conclusions

Misfit defects associated with interfaces between I-phase and Mg matrix were observed in Mg-Zn-Y and Mg-Zn-Al alloys. Density of defects decreases after annealing at 500°C due to decrease of density of precipitates in Mg matrix and grain growth.

Nonlinear thermal expansion of I-phase lattice was observed above 310°C, which indicates some structural change in the I-phase. Temperatures of phase transformations occurring in WE43+14Zn alloy were determined by in situ XRD during linear heating.

Acknowledgements

This work was supported by the Czech Science Foundation (project P108/10/0648), the grant agency of Charles University (project 566012) and by the grant SVV-2014-260091.

References

[1] Luo Z, Zhang S, Tang Y and Zhao D 1993 *Scripta Metall. Mater.* **28** 1513

[2] Vekilov Y K and Chernikov M A 2010 *Physics - Uspekhi* **53** 537

[3] Čížek J, Vlček M, Smola B, Stulíková I, Procházka I, Kužel R, Jäger A and Lejček P 2012 *Scripta Mater.* **66** 630

[4] Bečvář F, Čížek J, Procházka I and Janotová J 2005 *Nucl. Instrum. Meth. A* **539** 372

[5] Robles J M C, Ogando E and Plazaola F 2007 *J. Phys.: Condens. Matter* **19** 176222

[6] Hruška P, Čížek J, Vlček M, Melikhova O and Procházka I 2014 *Acta Phys. Pol. A* **125** 718
[7] Bae D, Kim S, Kim D and Kim W 2002 *Acta Mater.* **50** 2343
[8] Hautojärvi P, Johansson J, Vehanen A and Yli-Kauppila J 1982 *Appl. Phys. A* **27** 49
[9] Vlček M, Čížek J, Melikhova O, Hruška P, Procházka I, Vlach M, Stulíková I and Smola B *J. Phys. Conf. Ser.* Submitted
[10] Melikhova O, Čížek J, Vlček M, Lukáč F, Vlach M, Smola B, Stulíková I, Kužel R, Procházka I, Kudrnová H and Jäger A 2014 *Acta Phys. Pol. A* **125** 718
[11] Zhang Y, Zeng X, Liu L, Lu C, Zhou H, Li Q and Zhu Y 2004 *Mater. Sci. Eng. A* **373** 320

C. Author's publication 3

Title	Early stages of precipitation in Mg-RE alloys studied by positron annihilation spectroscopy
Authors	M. Vlček, J. Čížek, O. Melikhova, P. Hruška, I. Procházka, M. Vlach, I. Stulíková, B. Smola
Journal	Journal of Physics: Conference Series (accepted)
Volume	-
Year	-
Pages	-

Early stages of precipitation in Mg-RE alloys studied by positron annihilation spectroscopy

M Vlček[1], **J Čížek**[1], **O Melikhova**[1], **P Hruška**[1], **I Procházka**[1], **M Vlach**[1], **I Stulíková**[1], **B Smola**[1]

Charles University in Prague, Faculty of Mathematics and Physics, V Holešovičkách 2, 18000 Praha 8, Czech Republic

E-mail: `marian.vlcek@gmail.com`

Abstract. Magnesium alloys with rare earth (RE) elements are promising structural materials exhibiting favorable mechanical properties at elevated temperatures. However, the processes occurring during early stages of precipitation in these alloys are still not completely understood. In this work positron lifetime spectroscopy combined with coincidence Doppler broadening was employed for investigation of early stages of precipitation in Mg-RE alloys. Presence of quenched-in vacancy clusters was observed after solution treatment of studied alloys. These quenched-in vacancy clusters are bound to RE solutes and thereby stabilized at room temperature. During natural aging, RE clusters are formed by vacancy-assisted long-range diffusion. In addition, hardness of studied materials increases and quenched-in vacancy clusters are annealed out during the course of natural aging. Simple model was developed to describe hardening during natural aging.

1. Introduction

Mg-based alloys with rare earth (RE) alloying elements, e.g. Gd and Tb, represent promising light hardenable alloys with a high creep resistance at elevated temperatures [1]. Since the solubility limit of RE alloying elements in Mg strongly decreases at low temperatures, supersaturated solid solution of RE solutes in α-Mg matrix can be formed by fast quenching from elevated temperatures. During subsequent heating the supersaturated solid solution decomposes by formation of a sequence of metastable phases which may cause significant hardening of the alloy. For example the supersaturated solid solution of Gd in Mg decomposes in the sequence [2]:

$$\alpha' \text{ (hcp)} \rightarrow \beta'' \text{ (D0}_{19}\text{ clusters)} \rightarrow \beta' \text{ (c-bco)} \rightarrow \beta \text{ (fcc, Mg}_5\text{Gd type)}. \tag{1}$$

The β'' particles are coherent with the α-Mg matrix while for the β' and β precipitates the coherency with the α-Mg matrix is partially lost. Although the precipitation sequences are nowadays well documented for various Mg-RE systems, there is still a lack of information about very early stages of decomposition leading eventually to formation of coherent metastable particles usually with D0$_{19}$ structure.

Natural aging is a process where solute atoms and vacancies cluster at room temperature in materials quenched from high annealing temperature. It is well known effect and was thoroughly investigated in Al-based alloys [3, 4, 5, 6]. Significant strengthening occurs because solute clusters developed during natural aging hinder movement of dislocations. Contrary to Al-based alloys, natural aging of Mg-based alloys is not common. So far, natural aging was observed in Mg-Zn-based alloys [7] and, recently, in our work in Mg-Gd and Mg-Tb alloys [8]. In this work positron lifetime spectroscopy combined with coincidence Doppler broadening was employed for investigation of early stages of precipitation in Mg-RE alloys.

2. Experimental details

Binary Mg-Gd and Mg-Tb were produced by squeeze casting under a protective atmosphere (Ar + 1% SF_6). Chemical composition of studied alloys is shown in table 1.

Table 1. Composition of studied alloys.

	Gd		Tb		Mg
	wt. %	at. %	wt. %	at. %	
Mg4Gd	4.48	0.72	-	-	balance
Mg9Gd	9.24	1.55	-	-	balance
Mg15Gd	14.58	2.57	-	-	balance
Mg13Tb	-	-	13.39	2.31	balance

The as-cast Mg-Gd and Mg-Tb alloys were subjected to solution treatment at 500 and 530°C, respectively, for 6 hours finished by quenching into water at room temperature. Samples were subsequently naturally aged at ambient temperature.

Positron lifetime spectroscopy measurements were performed using a digital positron lifetime spectrometer [9] with excellent time resolution of 145 ps (FWHM of the resolution function obtained from fitting of positron lifetime spectrum of a well-annealed Mg reference sample). At least 10^7 annihilation events were accumulated in each spectrum. Source contribution consisting of two components with lifetimes 368 ps and 1.5 ns with relative intensities 8% and 1%, respectively, which originated from positrons annihilated in the $^{22}Na_2CO_3$ positron source deposited on a 2 μm thick mylar foil, was substracted from the spectra.

Coincidence Doppler broadening (CDB) measurements were carried out using a digital spectrometer [10] equipped with two HPGe detectors with the resolution of 0.9 keV at 511 keV (FWHM). The total statistics accumulated in each two-dimensional CDB spectrum was at least 10^8 positron annihilation events in each spectrum.

The Vickers microhardness (HV) testing was carried out using a STRUERS Duramin 300 hardness tester with a load of 100 g applied for 10 s.

3. Results

Time development of hardness of solution treated samples aged at ambient temperature is shown in figure 1a. Hardness of all studied alloys clearly increases with increasing aging time. The time dependence of microhardness plotted in the logarithmic time scale exhibits characteristic S-shaped curve typical for natural aging.

The hardness of alloy aged for time t can be expressed as:

$$HV(t) = HV_0 + \Delta HV(t), \tag{2}$$

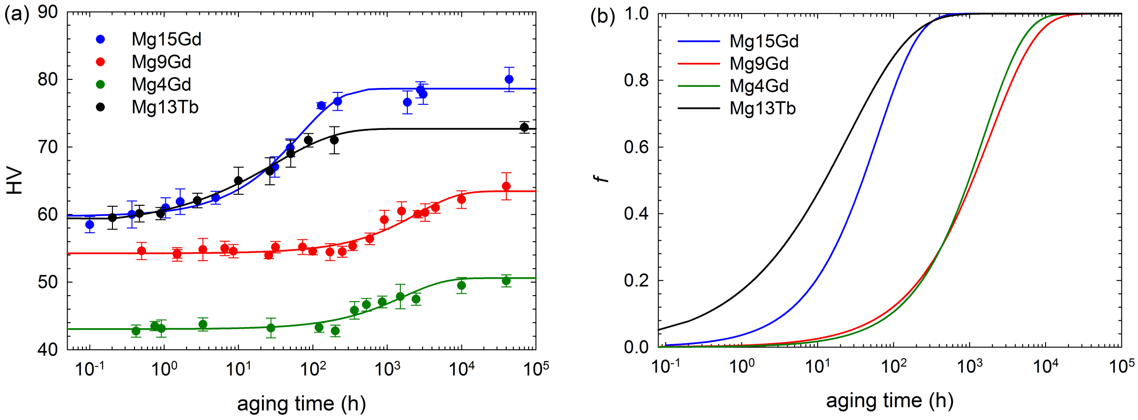

Figure 1. (a) Comparison of microhardness evolution during natural aging of studied alloys. (b) Time development of relative volume fraction of clusters obtained from fitting.

where $HV_0 = 30 \pm 2$ is the hardness of pure Mg matrix and $\Delta HV(t)$ denotes hardening caused by solute elements:

$$\Delta HV(t) = (HV_{ss}^2 + HV_{cl}^2)^{1/2}. \tag{3}$$

The symbols HV_{ss} and HV_{cl} denote contribution to the hardening caused by solid solution hardening and by clusters of alloying elements, respectively. Let f denote the relative fraction of solute atoms present in clusters. The hardening caused by clusters HV_{cl} is then proportional to $f^{1/2}$ while the solid solution hardening HV_{ss} is proportional to $(1-f)^{2/3}$ [3]. Hence, the evolution of the hardness during aging can be written as:

$$HV(t) = HV_0 + \left[\left(h_{ss} c^{2/3} (1-f)^{2/3} \right)^2 + \left(h_{cl} \left(\frac{c}{N_{cl}} \right)^{1/2} f^{1/2} \right)^2 \right]^{1/2}, \tag{4}$$

where c is the total concentration of alloying element (Gd or Tb) in at.%, h_{ss} and h_{cl} are hardening coefficients for solid solution hardening and hardening by clusters, respectively, and N_{cl} is the average number of atoms per cluster.

Table 2. Fitted parameters of hardening model.

	h_{ss}	$h_{cl}/(N_{cl})^{1/2}$	k (s^{-1})	n
Mg4Gd	350(10)	243(8)	$1.8(7) \times 10^{-7}$	0.8(3)
Mg9Gd	390(5)	269(5)	$1.5(4) \times 10^{-7}$	0.7(1)
Mg15Gd	342(8)	301(3)	$4.5(7) \times 10^{-6}$	0.8(1)
Mg13Tb	360(10)	286(4)	$1.1(2) \times 10^{-5}$	0.52(8)

The clusters in aged alloys develop by nucleation and subsequent growth. Since the studied alloys are coarse grained and exhibit low dislocation density, it is reasonable to assume that heterogeneous nucleation in limited number of suitable nucleation sites takes place. These sites are used at the early stage of clustering and so called site saturation occurs. Under these assumptions, the relative volume fraction of clusters is given by expression:

$$f = 1 - \exp\left[-(k(T)t)^n \right], \tag{5}$$

where $k(T)$ is the kinetic rate at temperature T and n is the kinetic exponent [3]. The quantity f is also identical to the relative fraction of solute atoms which precipitated from the solid solution and formed clusters. Hence, when $f = 0$ all solute atoms are in solid solution and no clusters are present in the sample, while the clusters are fully developed and no solutes remain in solid solution when $f = 1$.

Results obtained by fitting the measured data with proposed model of hardening are shown in table 2. The relative volume fraction of clusters f obtained from fitting is shown in figure 1b. As an example, fits of data measured on Mg15Gd and Mg13Tb alloys showing individual contributions HV_0, HV_{ss} and HV_{cl} to the total hardness are shown in figures 2a and 2b, respectively.

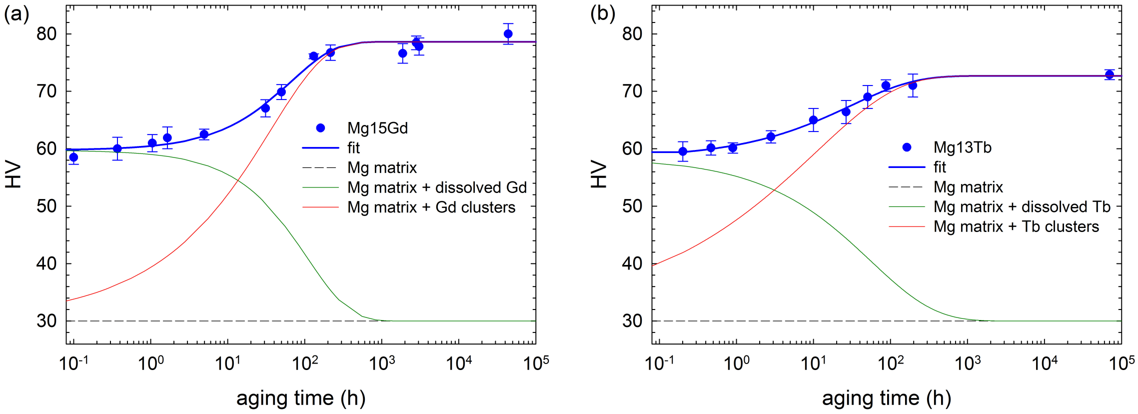

Figure 2. Development of microhardness and fit by the theoretical model described in the text: (a) Mg15Gd, (b) Mg13Tb.

Results obtained by positron lifetime spectroscopy are summarized in table 3. All quenched alloys exhibit two component positron lifetime spectra. The first component comes from free positrons while the second component represents a contribution of positrons trapped at defects. The lifetime of the second component $\tau_2 \approx 300$ ps agrees well with the theoretically calculated lifetime for a monovacancy in Mg [11]. However, experimental results suggest that positron lifetime for a monovacancy in Mg is ≈ 255 ps [12]. Therefore, positron lifetime measurements testify to presence of quenched-in vacancies or small vacancy clusters in the quenched alloys.

On the other hand, the alloys aged at ambient temperature for 2 months exhibit single component spectra with lifetime $\tau_1 \approx 225$ ps which agrees well with the bulk positron lifetime in Mg [11]. Hence, they are defect free within the sensitivity of positron lifetime spectroscopy.

Table 3. Results of positron lifetime measurements.

	quenched alloys				aged alloys (2 months)	
	τ_1 (ps)	I_1 (%)	τ_2 (ps)	I_2 (%)	τ_1 (ps)	I_1 (%)
Mg4Gd	219.7(5)	92.5(5)	290(10)	7.5(5)	225.5(2)	100
Mg9Gd	218.6(5)	88.4(5)	300(5)	11.6(5)	225.2(2)	100
Mg15Gd	214.6(7)	80.5(6)	295(5)	19.5(6)	225.4(2)	100
Mg13Tb	214.0(8)	84.3(7)	280(15)	15.7(7)	225.5(2)	100

Results of coincidence Doppler broadening measurements performed on Mg15Gd and Mg13Tb alloys are shown in figures 3a and 3b, respectively. Ratio curves of quenched alloys show peak located at $p \approx 8 \times 10^{-3}\ m_0c$ which testifies to enhanced concentration of Gd or Tb around quenched-in vacancy clusters. Amplitude of this peak significantly decreases after aging due to disappearance of quenched-in vacancy clusters.

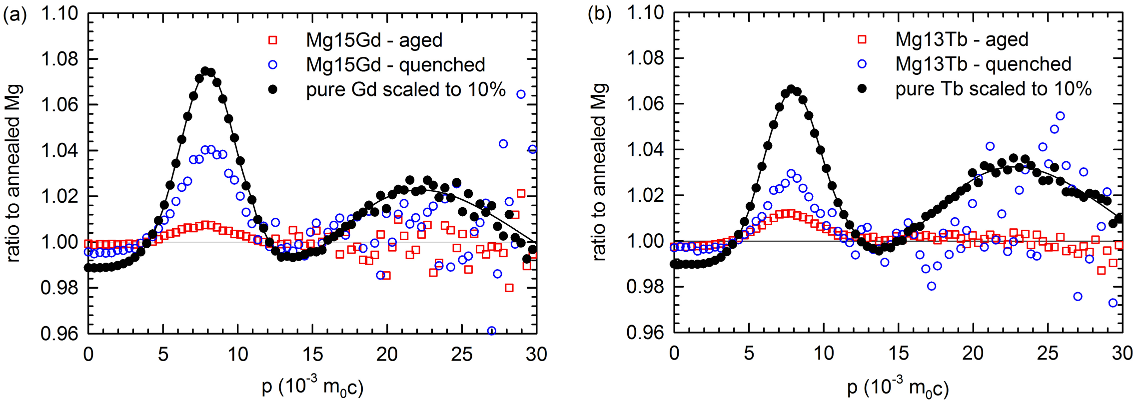

Figure 3. Coincidence Doppler broadening ratio curves: (a) Mg15Gd, (b) Mg13Tb.

Under the assumption that vacancy-Gd (or Tb) complexes consist of Mg monovacancy and a solute atom, concentration of quenched-in vacancy-Gd (or Tb) complexes can be calculated from positron lifetime data according to the simple trapping model [13]:

$$c_{pairs} = \frac{1}{\nu_v} I_2 \left(\frac{1}{\tau_1} - \frac{1}{\tau_2} \right), \tag{6}$$

where $\nu_v = 1.1 \times 10^{13}\ \mathrm{s}^{-1}$ is the specific positron trapping rate for vacancy in Mg [14].

Note that the specific positron trapping rate for a small cluster composed of N vacancies is $N\nu_v$. Therefore, trapping rate to vacancies of fixed concentration is the same independently whether they exist as isolated monovacancies or form small vacancy clusters providing that positron trapping is in transition limited regime [15], i.e. the mutual distance among vacancy clusters is significantly smaller than the mean positron diffusion length.

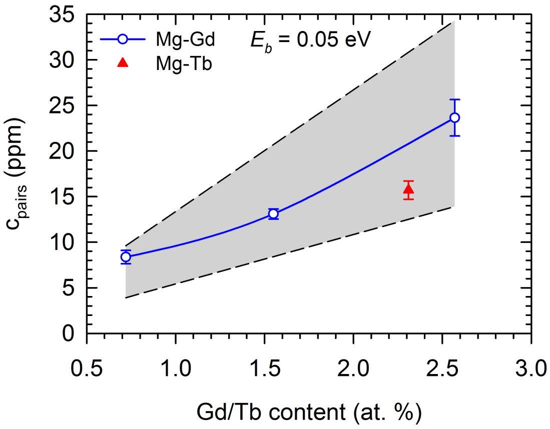

Figure 4. The concentration quenched-in vacancy-Gd (open circles) and vacancy-Tb (full triangle) pairs measured by positron lifetime spectroscopy. Shaded region shows the band for equilibrium concentration of vacancy-solute pairs at 500°C calculated by equation (7). Binding energy E_b between vacancy and Gd or Tb was assumed to be 0.05 eV.

Values calculated according to equation 6 can be compared to the equilibrium concentration of vacancy-Gd (or Tb) pairs at solution treatment temperature T given by expression:

$$c^*_{pairs} = c \exp\left(\frac{S_{v,f}}{k_B}\right) \exp\left(-\frac{E_{v,f} - E_b}{k_B T}\right), \tag{7}$$

where k_B is the Boltzmann constant, $S_{v,f} \approx 2k_B$ is the vacancy formation entropy [16]. The values of vacancy formation enthalpy $E_{v,f}$ reported in literature fall into the range 0.79-0.85 eV [17, 18, 12]. E_b is the binding energy between vacancy and Gd or Tb. The latter quantity is not known, but putting $E_b = 0.05$ eV, i.e. assuming small attractive interaction between vacancy and Gd or Tb atom, the equilibrium concentration of vacancy-Gd(Tb) pairs given by equation (7) falls into the shaded area in figure 4 which is in good agreement with experimental data.

4. Discussion

All studied Mg-RE alloys exhibit natural aging and the magnitude of hardening during aging as well as the concentration of quenched-in vacancy clusters increase with increasing concentration of RE alloying elements. It was found that early stages of precipitation are controlled by quenched-in vacancies. Positive binding energy between vacancy and solute atoms facilitates creation of solute-vacancy complexes during solution treatment at elevated temperature. However, since the binding energy between vacancy and Gd or Tb is comparable to the thermal energy most vacancies are not bound to Gd or Tb solutes during the solution treatment. In quenched samples free vacancies are quickly annealed out at room temperature but they can also bind to RE solutes. Vacancies associated with RE solutes are more stable and facilitate diffusivity of the solute RE atoms. Hence, the early stages of precipitation are strongly affected by the concentration of quenched-in vacancies bound to RE solutes. Agglomeration of solutes to small clusters proceeds by vacancy-assisted long-range diffusion. Solute clusters with defected structure containing vacancies are formed in the initial stage and further develop into precursors of the coherent D0_{19} precipitates.

Ab-initio theoretical calculations of positron lifetime for vacancy clusters with different sizes were performed to estimate the number of vacancies in vacancy-Gd (or Tb) complexes. Positron lifetimes were calculated within the so-called standard scheme [19] employing the atomic superposition method [20]. The electron-positron correlation was treated using the local density approximation according to the parametrization by Boroski and Nieminen [21]. The calculations were performed in 512 Mg atom based supercells. Vacancies and vacancy clusters were modeled simply by removing the corresponding number of atoms from the supercell.

Results of these calculation are presented in figure 5. Measured positron lifetime of defect component in quenched samples agrees well with the lifetime of ≈ 300 ps calculated for a Mg monovacancy. Note that similar lifetime was calculated for Mg monovacancy in reference [11].

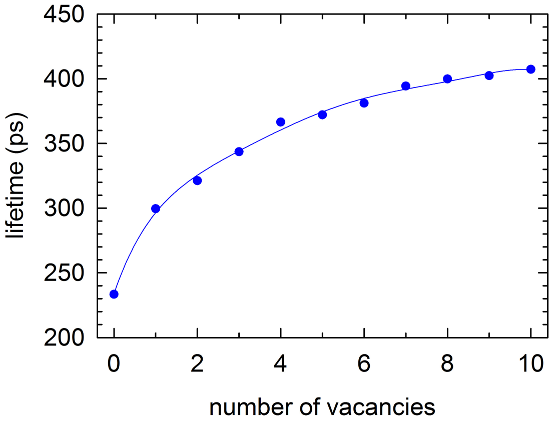

Figure 5. Calculated dependence of positron lifetime on the number of Mg vacancies in vacancy cluster. The solid line is just to guide the eyes.

On the other hand, the experimental lifetime value of ≈ 255 ps was determined by in-situ positron lifetime study of Mg samples annealed in the temperature range 0-600°C through fitting of the temperature dependence of the mean positron lifetime [12]. Low temperature measurements of quenched and electron irradiated Mg samples performed in reference [12] revealed defect component with positron lifetime of (350 ± 20) ps. Comparison with theoretical calculations suggests that in quenched and irradiated samples positron trapping occurs at complex small vacancy clusters consisting of 2-3 vacancies.

Nevertheless, the large difference between experimental and theoretical lifetimes for Mg monovacancy is very remarkable. In addition, the experimental value ≈ 255 ps determined in reference [12] is practically the same as the positron lifetime determined experimentally for dislocations in Mg which is ≈ 250 ps [22, 23, 24]. Therefore, further investigations are needed to definitively resolve these discrepancies and firmly assign the positron lifetime for vacancy in Mg. Hence, at the present stage of knowledge we can conclude that quenched Mg-Gd and Mg-Tb alloys studied here contain either monovacancies or small vacancy clusters (consisting of 2-3 vacancies) bound to Gd or Tb solutes.

The kinetics of natural aging is not the same for all studied alloys. The Mg15Gd and Mg13Tb alloys show significantly shorter incubation period of hardening than Mg4Gd and Mg9Gd alloys. This is most likely caused by higher concentration of alloying elements and thereby also higher concentration of quenched-in vacancies bound to RE solutes. However, further studies are required to elucidate the factors influencing the kinetics of natural aging in Mg-RE alloys.

5. Conclusions

Natural aging of Mg-Gd and Mg-Tb alloys associated with clustering of solute atoms was observed in this work. Theoretical model of hardening during natural aging showing good agreement with experimental data was developed.

Presence of quenched-in vacancy/vacancy cluster-Gd (or Tb) complexes in solution treated alloys was confirmed by positron annihilation spectroscopy. Quenched-in vacancies or vacancy clusters composed of up to three vacancies facilitate diffusion of Gd or Tb atoms in Mg matrix and disappear when the development of solute clusters is finished.

Acknowledgements

The research leading to these results has received funding from the People Programme (Marie Curie Actions) of the European Union's Seventh Framework Programme FP7/2007-2013/ under REA grant agreement N° 289163.

One of the authors (P. Hruška) acknowledges support by the Grant Agency of the Charles University (project no. 324015).

References

[1] Mordike B 2002 *Mat. Sci. Eng. A* **324** 103
[2] Vostrý P, Stulíková I, Smola B, von Buch F and Mordike B L 1999 *Phys. Status Solidi A* **175** 491
[3] Esmaeili S, Lloyd D J and Poole W J 2003 *Acta Materialia* **51** 3467
[4] Stulíková I, Faltus J and Smola B 2003 *Kovove Mater.* **45** 85
[5] Klobes B, Staab T E M, Haaks M, Maier K and Wieler I 2008 *Phys. Status Solidi RRL* **2** 224
[6] Banhart J, Lay M D H, Chang C S T and Hill J 2011 *Phys. Rev. B* **83** 014101
[7] Buha J 2008 *J. Mater. Sci.* **43** 1120
[8] Čížek J, Smola B, Stulíková I, Hruška P, Vlach M, Vlček M, Melikhova O and Procházka I 2012 *Phys. Status Solidi A* **209** 2135
[9] Bečvář F, Čížek J, Procházka I and Janotová J 2005 *Nucl. Instr. Meth. Phys. Res. A* **539** 372 – 385
[10] Čížek J, Vlček M and Procházka I 2010 *Nucl. Instrum. Methods A* **623** 982 – 994
[11] Robles J M C, Ogando E and Plazaola F 2007 *J. Phys.: Condens. Matter* **19** 176222
[12] Hautojärvi P, Johansson J, Vehanen A and Yli-Kauppila J 1982 *Appl. Phys. A* **27** 49
[13] West R 1979 *Positrons in Solids* ed Hautojärvi P (Berlin: Springer-Verlag) p 89
[14] Hood G M 1982 *Phys. Rev. B* **26** 1036
[15] Dupasquier A, Romero R and Somoza A 1993 *Phys. Rev. B* **48** 9235
[16] Wollenberger H 1983 *Physical Metalurgy* vol 2 (Amsterdam: North-Holland) p 1146
[17] Tzanetakis P, Hillairet J and Revel G 1976 *Phys. Status Solidi B* **75** 433
[18] Tzanetakis P 1978 *Thése* (Université de Grenoble)

[19] Puska M J and Nieminen R M 1994 *Rev. Mod. Phys.* **66** 841
[20] Puska M J and Nieminen R M 1983 *J. Phys. F: Met. Phys.* **13** 333
[21] Boroński E and Nieminen R M 1986 *Phys. Rev. B* **34** 3820
[22] Čížek J, Procházka I, Smola B, Stulíková I, Kužel R, Matěj Z and Cherkaska V 2006 *Phys. Status Solidi A* **203** 466
[23] del Río J, Gómez C and Ruano M 2012 *Philos. Mag.* **92** 535
[24] Dryzek J and Dryzek E 2011 *Magnesium Alloys - Corrosion and Surface Treatments* (Rijeka: InTech) p 289

D. Author's publication 4

Title	Investigation of Precipitation Effects in Mg-Tb and Mg-Tb-Nd Alloys
Authors	M. Vlček, J. Čížek, O. Melikhova, P. Hruška, I. Procházka
Journal	Acta Physica Polonica A
Volume	125
Year	2014
Pages	744–747

Vol. **125** (2014) *ACTA PHYSICA POLONICA A* No. 3

Proceedings of the 41st Polish Seminar on Positron Annihilation, Lublin, September 9–13, 2013

Investigation of Precipitation Effects in Mg–Tb and Mg–Tb–Nd Alloys

M. Vlček*, J. Čížek, O. Melikhova, P. Hruška and I. Procházka
Faculty of Mathematics and Physics, Charles University in Prague
V Holešovičkách 2, 180 00 Praha 8, Czech Republic

Investigation of precipitation effects in solution treated Mg–Tb and Mg–Tb–Nd alloy was performed. Solution treated alloys were compared with samples deformed by high pressure torsion to examine influence of deformation on precipitation effects. Dislocations present in samples processed by high pressure torsion can serve as diffusion channels for atoms and also as nucleation sites for precipitates. Therefore precipitation of some phases in high pressure torsion deformed samples was observed at lower temperatures than in solution treated ones.

DOI: 10.12693/APhysPolA.125.744

PACS: 78.70.Bj, 61.72.J–

1. Introduction

Mg–Tb is a novel hardenable alloy with good creep resistance at elevated temperatures with promising applications in aerospace and automotive industry. The solubility of Tb in Mg reaches maximum of 24 wt% at eutectic temperature 559 °C [1] and strongly decreases at lower temperatures. Therefore, supersaturated solid solution can be prepared by annealing at solution treatment temperature and subsequent fast quenching.

With increasing temperature, supersaturated solid solution α' decomposes according to the sequence [2]:

$$\alpha'(\text{hcp}) \to \beta''(\text{D0}_{19}) \to \beta'(\text{c-bco}) \to \beta(\text{bcc}, \text{Mg}_{24}\text{Tb}_5). \quad (1)$$

The β'' transient phase exhibits hexagonal D0_{19} structure and is fully coherent with Mg matrix. The semicoherent transition β' has c-base centered orthorombic structure (c-bco). The stable β phase exhibits body centered cubic (bcc) structure and is incoherent with Mg matrix. Lattice mismatch at the interface of semicoherent or incoherent particles and Mg matrix is compensated by open-volume misfit defects.

Addition of Nd to MgTb alloying system modifies the precipitation sequence to [3]:

$$\alpha'(\text{hcp}) \to \beta''(\text{D0}_{19}\ \text{clusters}) \to \beta''(\text{D0}_{19}\ \text{plates}) \to \beta'(\text{c-bco}) \to \beta_1(\text{fcc}, \text{Mg}_3\text{Gd type}) \to \beta(\text{fcc}, \text{Mg}_5\text{Gd type}) \to \beta(\text{bct}, \text{Mg}_{41}\text{Nd}_5\ \text{type}). \quad (2)$$

Industrial applicability of Mg-RE (rare-earth) alloys is limited by their low ductility which can be improved by grain size refinement [4]. Novel techniques for grain size refinement based on severe plastic deformation (SPD) were recently developed [5]. Finest grain size (typically ≈ 100 nm) is achievable by high pressure torsion (HPT) [5], where initially coarse-grained material is simultaneously deformed in torsion and compressed by pressure of several GPa.

SPD creates large amount of defects, mainly dislocations and vacancies [5]. In case of age hardenable alloys it is expected that presence of defects induced in the material by SPD will influence decomposition of supersaturated solid solution.

Positron lifetime (LT) spectroscopy [6] is well established technique ideally suited for investigation of open-volume misfit defects created by presence of semicoherent and incoherent phases in Mg matrix and also defects created in material by HPT deformation.

2. Experimental details

Samples of binary Mg–13 wt%Tb alloy (MgTb) were produced by squeeze casting under a protective Ar + 1%SF_6 atmosphere. As-cast samples were solution annealed at 530 °C for 6 h under Ar atmosphere and subsequently quenched into water of room temperature. Composition of solution treated sample was determined by chemical analysis as 13.3 wt% Tb and balance of Mg. The content of Tb is well under the solubility of Tb in Mg at 530 °C, which is 22 wt%.

Samples of ternary Mg–3.6 wt%Tb–2.1 wt%Nd (MgTbNd) alloy were also produced by squeeze casting under Ar + 1%SF_6 atmosphere. Solution treatment at 500 °C for 4 h was finished by quenching into water of room temperature. Selected samples of MgTb and MgTbNd alloys after the solution treatment were deformed by HPT at room temperature using hydrostatic pressure of 6 GPa and 5 revolutions. Both solution treated and HPT deformed samples were subjected to isochronal annealing with steps 20 °C/20 min. Each annealing step was finished by quenching into water of room temperature and then hardness and positron lifetime measurements were performed.

Positron LT measurements were performed using a digital positron LT spectrometer [7] with outstanding time resolution of 145 ps (FWHM ^{22}Na). $^{22}\text{Na}_2\text{CO}_3$ positron source deposited on a 2 μm mylar foil was used and at least 10^7 annihilation events were accumulated in each

---

*corresponding author; e-mail: vlcek@mbox.troja.mff.cuni.cz

LT spectrum. Decomposition of LT spectra into individual components was performed by a maximum likelihood code [8]. The goodness-of-fit expressed by the χ^2 value per degree of freedom was always below 1.03.

Vickers hardness (HV) was measured on polished samples using microhardness tester Struers Duramin 300 using a load of 100 g applied for 10 s. Each measurement was repeated at least ten times to improve precision of measurement and estimate statistical uncertainty of the hardness value.

3. Results

Evolution of HV of solution treated and HPT deformed MgTb samples during isochronal annealing is shown in Fig. 1. One can see in the figure that maximal hardness of solution treated samples is reached at (200±40) °C and it is associated with precipitation of β'' phase with $D0_{19}$ structure which was identified in the sample by selected area electron diffraction (SAED) [9]. At 260 °C hardness drops due to coarsening and dissolution of β'' particles. Subsequently hardness increases again and reaches local maximum at 280 °C. This is caused by precipitation of β' phase which was identified in the sample by SAED. Let us note that two stages corresponding to formation of β'' particles and subsequent precipitation of β' phase was found in the temperature dependence of electrical resistivity [9].

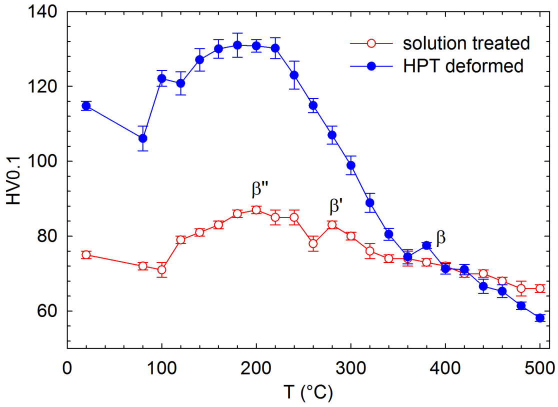

Fig. 1. Temperature dependence of HV for solution treated (open points) and HPT deformed (full points) MgTb alloy.

Initial hardness of HPT deformed samples is significantly higher than that of solution treated samples due to grain refinement and introduction of lattice defects during HPT deformation. Maximum hardness is reached at (180 ± 40) °C and at temperatures above 220 °C hardness decreases due to grain growth and recrystallization. At 360 °C process of recrystallization is finished and hardness is similar as hardness of solution treated samples.

Temperature dependence of the lifetimes resolved in positron lifetime spectra of solution treated samples is plotted in Fig. 2a. After solution treatment the MgTb alloy exhibits a single component spectrum with lifetime which agrees well with the bulk Mg lifetime $\tau_b =$ (224.8±0.5) ps [10]. Hence, within sensitivity of LT measurement the sample can be considered as a defect-free material. In temperature range 120–380 °C an additional component with lifetime $\tau_2 \approx 256$ ps appeared in the measured LT spectra. Lifetime of this component agrees well with the lifetime of positrons trapped in vacancy-like misfit defects at interfaces between semicoherent or incoherent precipitates and Mg matrix [10, 11]. The intensity I_2 of this component is plotted in Fig. 2b as a function of annealing temperature. For comparison temperature dependence of HV is plotted in the figure as well.

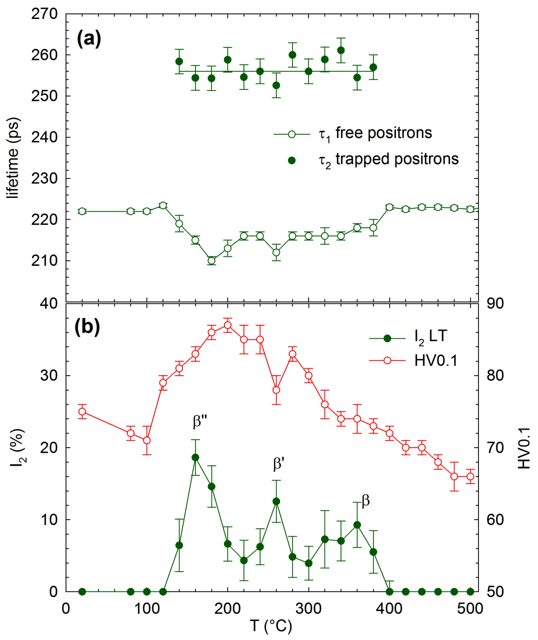

Fig. 2. Solution treated MgTb alloy subjected to isochronal annealing: (a) temperature dependence of positron lifetimes, (b) temperature dependence of HV (open points) and I_2 (full points) for solution treated MgTb alloy subjected to isochronal annealing.

There are two pronounced peaks in the temperature dependence of I_2. The highest value of I_2 is reached after annealing at (160 ± 20) °C. This peak occurs at lower temperature than the temperature of maximum hardening, i.e. (200 ± 40) °C, and it is associated with early stages of precipitation of β'' phase. Although β'' phase is coherent with matrix in early stages of precipitation, the structure of β'' particles is not perfect and contains vacancy-like defects which are trap positrons. When finely dispersed precipitates of β'' with well-defined orientation with respect to the Mg matrix are formed, they contain less vacancy-like defects. Therefore decrease in I_2 is observed. On the other hand, this condition is most favorable for precipitation strengthening mechanism and maximum hardness is achieved. Thus maximum value of I_2 intensity is reached at lower temperature than the maximum hardness although both are associated with the precipitation of β'' phase.

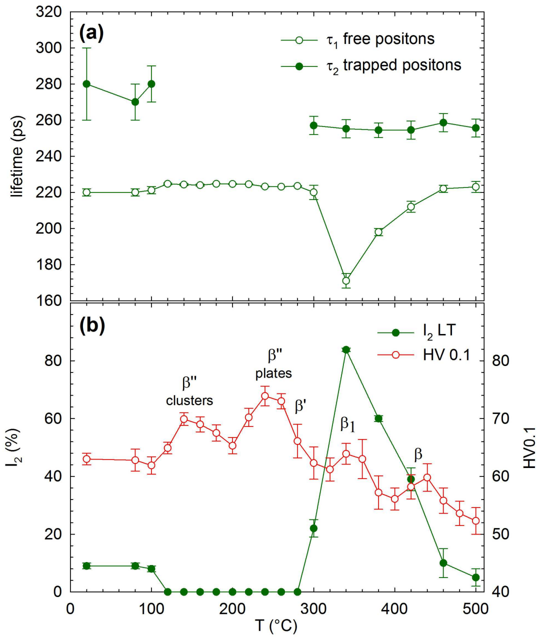

Fig. 3. Solution treated MgTbNd alloy subjected to isochronal annealing: (a) temperature dependence of positron lifetimes, (b) temperature dependence of HV (open points) and I_2 (full points) for solution treated MgTbNd alloy subjected to isochronal annealing.

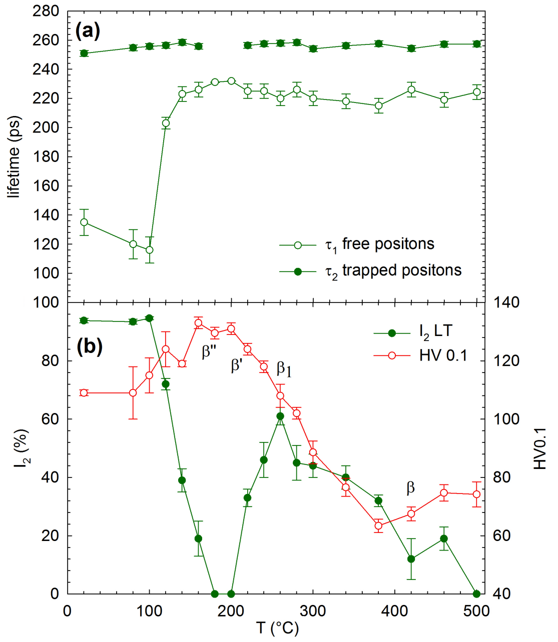

Fig. 4. HPT deformed alloy subjected to isochronal annealing: (a) temperature dependence of positron lifetimes, (b) temperature dependence of HV (open points) and I_2 (full points) for HPT deformed MgTbNd alloy subjected to isochronal annealing.

To examine the influence of addition of Nd to Mg–Tb alloying system, samples of MgTbNd alloy were investigated by HV and LT measurements. Temperature dependence of positron lifetimes, HV and I_2 for solution treated and HPT processed MgTbNd samples are shown in Figs. 3 and 4, respectively. After solution treatment MgTbNd alloy exhibits the lowest hardness. During isochronal annealing HV increases with increasing temperature and reaches maximum at (220 ± 20) °C. This hardening peak is associated with formation of plates of β'' phase. At slightly higher temperature particles of β' phase are formed which coexist with plates of β'' phase at temperature around 270 °C [3]. This leads to a decrease of hardness and subsequent annealing up to 500 °C does not produce any further pronounced hardening. Results of LT measurements of solution treated MgTbNd alloy revealed presence of a second component with lifetime of (280 ± 20) ps at temperatures up to 100 °C. This long-lived component can be attributed to positrons trapped at quenched-in complexes of vacancies and Nd or Tb atoms. Since quenched-in vacancies were not observed in the binary MgTb alloy the vacancies are likely associated with Nd atoms. At 120 °C this component disappears because vacancies bound to solutes are annealed out. From 120 °C up to 280 °C there is only one component present in LT spectra and virtually all positrons annihilate in the free state.

Hence, contrary to MgTb alloy particles of β'' particles in MgTbNd alloy exhibit well-defined structure without vacancy-like defects. Second component appears again at temperatures above 300 °C, however, now it has lifetime of (256 ± 5) ps which corresponds to positrons trapped at misfit defects at the precipitate–matrix interface. Presence of misfit defects implies that semicoherent or incoherent precipitates are formed in this temperature range. Maximum intensity of second component is reached at (340 ± 20) °C and is associated with formation of semicoherent β_1 phase. After further annealing Mg_5Gd-type β phase is formed at 390 °C and only few irregular particles of the $Mg_{41}Nd_5$-type phase are present after isochronal annealing up to 500 °C [3]. Although these phases are also not coherent with Mg matrix, they trap significantly smaller fraction of positrons than semicoherent β_1 phase. This decrease of fraction of positrons trapped at misfit defects at interfaces is caused by coarsening of particles at temperatures higher than 340 °C. As precipitates join together, their number density and also the surface area decrease resulting in a significant reduction of concentration of misfit defects at interfaces.

HPT processed samples exhibit significantly higher initial hardness due to grain refinement and lattice defects introduced during deformation. Maximum hardness associated with formation of plates of β'' phase is reached at (180 ± 20) °C. At temperatures above 200 °C hardness decreases due to grain growth and minimum hardness is reached at (380 ± 40) °C. Possible changes of hardness caused by precipitation of β' and β_1 are difficult to distinguish because they are overwhelmed by the major decrease in hardness due to grain growth occurring in the same temperature range. At temperatures over 380 °C there is slight increase in hardness caused by formation of β phase.

HPT deformation introduces dislocations into the processed material. This is testified by presence of the second component with lifetime of (256 ± 2) ps in the measured LT spectra at temperatures up to 100 °C. Lifetime of this component agrees well with the lifetime reported for positrons trapped at dislocations in Mg [10]. At temperatures below 100 °C range we can observe very high intensity I_2 of the second component since almost all positrons are trapped at defects. This is in agreement with expected high density of defects introduced by HPT processing. Intensity of I_2 starts to decrease at 120 °C and reaches zero at 180 °C where defects introduced by HPT deformation were annealed out. The component with lifetime of (256 ± 2) ps appears again after annealing at 220 °C and higher temperatures. In this temperature range it is associated with misfit defects at interfaces between Mg matrix and semicoherent or incoherent precipitates. Intensity I_2 of this component reaches local maximum at 260 °C and then gradually decreases until it finally disappears at 500 °C. Peak in intensity of the second component is associated with formation of semicoherent β_1 phase. Further annealing leads to coarsening and dissolution of β_1 precipitates followed by formation of coarse β phase particles. These processes cause the decrease of I_2.

4. Discussion

Comparison of temperature dependence of hardness of solution treated and HPT deformed MgTb alloy clearly shows that maximum hardening is achieved at lower temperatures in HPT deformed samples. Deformation during HPT processing introduces high density of dislocations which serves as nucleation centers for formation of second phase particles and also facilitates diffusion of solutes (pipe diffusion). This leads to precipitation of β'' at lower temperatures than in solution treated samples. Although β'' phase itself is coherent with matrix in the early stage of precipitation, β'' particles may contain vacancies. When precipitates of β'' with well defined structure and orientation with respect to the Mg matrix develop, vacancies gradually disappear.

In the binary MgTb alloy the β'' phase particles contain vacancy-like defects while in the ternary MgTbNd alloy no vacancy-like defects associated with the β'' phase have been detected. It indicates that in MgTbNd β'' phase particles exhibit well defined $D0_{19}$ structure already in early stages of precipitation while in MgTb β'' particles exhibit more defected structure in the early stages of precipitation. Semicoherent β_1 phase in MgTbNd alloy exhibits exceptionally strong trapping of positrons. Peak in intensity I_2 of the second component in LT spectra, corresponding to misfit defects at the interface between β_1 phase and Mg matrix, was also shifted to lower temperatures in HPT processed alloy. Thus β_1 phase also forms at lower temperatures in HPT deformed samples.

5. Conclusions

Maximal hardening in MgTb alloy is associated with precipitation of coherent β'' phase which is formed by thermally activated long-range diffusion of Tb. In HPT deformed alloy precipitation of β'' phase occurs at lower temperature than in the solution treated alloy due to dislocations introduced by severe plastic deformation. Presence of vacancies associated with β'' phase was confirmed by a rise of a component with lifetime of 256 ps in LT spectra at temperatures corresponding to the early stages of precipitation.

In solution treated and HPT deformed MgTbNd alloy maximum hardness is also associated with precipitation of β'' phase. Similar to MgTb, in HPT deformed MgTbNd alloy precipitation of β'' phase is also promoted by defects introduced by severe plastic deformation and takes place at lower temperatures. However, contrary to MgTb in MgTbNd samples β'' phase is not associated with presence of defects. The semicoherent β_1 phase exhibits exceptionally strong trapping of positrons and its precipitation is also shifted to lower temperatures in HPT deformed samples.

Acknowledgments

This work was supported by Grant Agency of Charles University (project no. 566012), the Czech Science Foundation (project no. P108/10/0648) and by the grant SVV-2013-267303.

References

[1] M. Drits, L. Rokhlin, E. Padezhnova, L. Guzei, *Met. Sci. Heat Treatm.* **20**, 771 (1978).

[2] G.W. Lorimer, in: *Proc. Magnesium Technology*, Institute of Metals, London 1986, p. 47.

[3] B. Smola, I. Stulíková, J. Černá, J. Čížek, M. Vlach, *Phys. Status Solidi A* **208**, 2741 (2011).

[4] R. Biringer, H. Gleiter, R.W. Cahn, *Encyclopedia of Materials Science and Engineering: Supplementary volume*, Vol. **1**, 1988, p. 399.

[5] R. Valiev, R. Islamgaliev, I. Alexandrov, *Prog. Mater. Sci.* **45**, 103 (2000).

[6] P. Hautojärvi, C. Corbel, in: *Proc. Int. School of Physics "Enrico Fermi"*, Eds.: A. Dupasquierm, A.P. Mills jr., IOS Press, Amsterdam 1995, p. 491.

[7] F. Bečvář, J. Čížek, I. Procházka, J. Janotová, *Nucl. Instrum. Methods Phys. Res. A* **539**, 372 (2005).

[8] I. Procházka, I. Novotný, F. Bečvář, *Mater. Sci. Forum* **255-257**, 772 (1997).

[9] O. Melikhova, J. Čížek, P. Hruška, M. Vlček, I. Procházka, M. Vlach, I. Stulíková, B. Smola, N. Žaludová, R. Islamgaliev, *Def. Diff. Forum* **322**, 151 (2012).

[10] J. Čížek, I. Procházka, B. Smola, I. Stulíková, V. Očenášek, *J. Alloys Comp.* **430**, 92 (2007).

[11] J. Čížek, I. Procházka, B. Smola, I. Stulíková, M. Vlach, V. Očenášek, O.B. Kulyasova, R.K. Islamgaliev, *Int. J. Mater. Res.* **100**, 780 (2009).